Experimental and Numerical Heat Transfer Studies of Nanofluids with an Emphasis on Nuclear Fusion Applications

Antonis Sergis
Imperial College London
Department of Mechanical Engineering

Supervised by Prof. Yannis Hardalupas from Imperial College London and
Dr. Thomas Barrett from the Culham Center for Fusion Energy (CCFE)

A thesis submitted for the degree of
Doctor of Philosophy
November 2013

Abstract

A nanofluid is a mixture of a low concentration of solid particles (10-100nm in size at concentrations below 10%vol.) and a carrier fluid (usually conventional coolants). These novel fluids exhibit anomalous heat transfer phenomena which cannot be explained using classical thermodynamic models. The fluids can be designed to offer unsurpassed heat transfer rates for heat transfer related applications at low costs of manufacturing. This PhD thesis describes the efforts to test whether these fluids can be utilised for high heat flux applications (similar to those encountered in proposed future fusion reactors) and also to discover the mechanisms which give rise to the phenomenal heat transfer enhancements observed. A broad metadata statistical analysis was performed on published literature which provided qualitative results regarding the heat transfer enhancement to be expected from nanofluids, indicated trends connecting by part mixture properties and heat transfer enhancement values exhibited and provided probable explanations of the heat transfer mechanisms involved. This study was performed to tackle the novelty and scientific uncertainty issues encountered in the field. Optical laser diagnostics experiments were performed on a high heat flux device (HyperVapotron) in isothermal conditions. The study provided extensive information regarding the flow structures formed inside the device using conventional coolants and nanofluids. This helped to both, understand the conventional operation of the device as well as review probable suitable geometries for the utilisation of the device using nanofluids. Finally, a Molecular Dynamics Simulation code was composed to model heat conduction through a basic nanofluid. The code results suggested the formulation of a new type of complex heat transfer mechanism that might

explain the augmentation of heat transfer encountered experimentally. A new low cost high throughput platform (HTCondor®) has been used to run the code in order to demonstrate the capabilities of the system for less financially able institutions.

Declaration of Originality

I would like to declare that this thesis presents my own original work and that all else is appropriately referenced.

Copyright Declaration

Publications

Up to the date of submission of this thesis, this is a list of the publications emerging from the work included:

1. Sergis, A. and Hardalupas, Y., *Anomalous heat transfer modes of nanofluids: a review based on statistical analysis.* Nanoscale Research Letters, 2011. 6(1): p. 391.
2. Barrett, T.R., Robinson, S., Flinders, K., Sergis, A., Hardalupas, Y., *Investigating the use of nanofluids to improve high heat flux cooling systems.* Fusion Engineering and Design, 2013. 88(9-10): p. 2594-2597.
3. Sergis, A., Hardalupas, Y. and Barrett, T.R., *Potential for improvement in high heat flux HyperVapotron element performance using nanofluids.* Nuclear Fusion, 2013. 53(11).
4. Sergis, A. and Hardalupas, Y., *Anomalous Heat Transfer Modes of nanofluids: A Statistical Analysis Approach Review*. HSTAM 2010 Conference, 2010. Limassol.
5. Barrett, T.R., Robinson, S., Flinders, K., Sergis, A., Hardalupas, Y., *Investigating the use of nanofluids to Improve High Heat Flux Cooling Systems*. 27th Symposium on Fusion Technology, 2012. Liege: SOFT.
6. Sergis, A., Hardalupas, Y. and Barrett, T.R., *Potential for Improvement in High Heat Flux HyperVapotron Element Performance Using nanofluids*. 24th IAEA Fusion Energy Conference, 2012. San Diego: IAEA.

Θα ήθελα να αφιερώσω αυτή την διατριβή στην γιαγιά μου Μαρία που μας άφησε λόγω γηρατειών στις 17 Ιουνίου 2012, στην οικογένεια και στους φίλους μου που με στήριξαν κατά την διάρκεια της έρευνας μου.

I would like to dedicate this thesis to my grandmother Maria who died of old age on the 17th of June 2012, to my loving family and friends who have been my support group throughout this investigation.

Acknowledgements

I would like to begin by thanking my sponsors (RCUK Energy Program, EURATOM, EPSRC and the associated CASE award as well as the contributing industrial collaborator CCFE) for all of their financial support. A big thank you to my supervisor Yannis (Prof. Yannis Hardalupas) that provided me the tools and trust to create and evolve throughout this project as an academic and as a person. He has been a real mentor to me that provided his advices unconditionally for everything academic and non-academic throughout these years. I would also like to thank my external supervisor Tom (Dr. Tom Barrett) for all of his guidance and help from CCFE. I am also thankful to Dr. Elizabeth Surrey and Dr. Joe Milnes for all of their help in forming up our IAEA conference and journal paper.

From Imperial, I would also like to thank Prof. Alex Taylor for always having his office door open to accommodate my requests and solve some of the problems encountered during the course. My friend Sebastian Henkel for all of his help and support including the wonderful style sheet used for this thesis. A big thank you to the precious help received from Steve Rochford for all of his associated help with HTCondor® along with Tim Machin and Dr. Nadiri Fusun that help to materialise it. Dr. Tamer Zaki and Dr. Edward Smith for donating the basic MDS code from Rapaport in Fortran 90 as well as Prof. David Heyes for all of his associated help. Our technicians Ian Wright, Guljar Singh, Stuart Marchant, Edward Benbow and Asanka Munasinghe as well as our industrial coordinator Harminder Flora for their remarkable work on building my laboratory tools and experimental rig. Serena Dalrymple for being an amazing secretary who provided all the help required with anything related to university paperwork. My friends and colleagues

that kept me company, always ready to lend a hand – and some provided a shoulder to lean on – during my time at Imperial – Dr. Panos Sphikas, Dr. Georgios Charalampous, Dr. Alexandros Charogiannis, Konstantinos Hadjiyannis, Elias Dodoulas, Michalis Hadjipanayis, Benoit Fond and Chris Abram.

The friends from UK – old and new – my dear Diego Vietes, Emanuel Filho, Yorgos Yeorgiou, Michalis Stylianou, my lovely Ester Maria Toumpouris and awesome Dr. Relja Arandjelovich for being there when I needed a nice time off, an advise or a stroll to cool down and reset.

Finally, I would like to thank my loving family with their unconditional, pure and wonderful love that made me climb mountains throughout my academic career and in my personal life – I could never have done it without you, you were the best I could ever have wished for. To my adoring grandmother Maria and grandfather Thimis who taught me, as well as the rest of my large extended family, that with proper education, even when you have nothing, this is the only tool you need to survive. My two crazy cousins – and by chance flat mates – "Queen" Electra Malaki and Eleni Agathokleous that amongst others gave me a roof to sleep when London showed me its dark face and tolerated my occasional frustrations with work. Eleni Agathokleous once more for the wonderfully inspired quote in Greek in the next section of the thesis – as the fashion goes in these kind of cases. My best friends which I consider the same as family – Maria Savvidou and Thanasis (or "Athanasios" as he insists on but will never going to get his way) Taliadoros for their huge support sorting myself, my work and my actions out.

It has been a wonderful trip these last four years and I would not mind repeating it. I learned a lot, laughed a lot, met a lot of people and harvested from the best times, learned and roughened up from the bad times and will always be thankful to the ones (both named and those unnamed) that help me reach the end.

Καταρχάς, θα ήθελα να ευχαριστήσω τους χορηγούς μου (RCUK Energy Program, EURATOM, EPSRC και το αντίστοιχο CASE award καθώς και την συμμετέχων βιομηχανία CCFE). Ένα μεγάλο ευχαριστώ στον επιτηρητή μου Yannis (Prof. Yannis Hardalupas) που μου πρόσφερε τα εργαλεία και την εμπιστοσύνη να δημιουργήσω και να

εξελιχθώ μέσα από αυτή την εργασία.Ήταν ένας πραγματικός μέντορας που μου χάρισε τις συμβουλές του άνευ όρων κατά την διάρκεια της έρευνας μου στον ακαδημαϊκό – και όχι μόνο – τομέα. Θα ήθελα επίσης να ευχαριστήσω τον εξωτερικό μου επιτηρητή Tom (Dr. Tom Barrett) για όλη την καθοδήγηση και βοήθεια μέσω της CCFE. Είμαι επίσης ευγνώμων στην Dr. Elizabeth Surrey και στον Dr. Joe Milnes για όλη την βοήθεια τους στην διεκπεραίωση του χειρόγραφου για το συνέδριο και σύγγραμα της IAEA.

Από το Imperial, θέλω επίσης να ευχαριστήσω τον Prof. Alex Taylor που πάντα είχε την πόρτα του ανοιχτή για να εξυπηρετήσει τις διάφορες ανάγκες και προβλήματα που έπρεπε να αντιμετωπιστούν στην πορεία της εργασίας μου. Τον φίλο μου Sebastian Henkel για την βοήθεια και στήριξη που μου πρόσφερε, συμπεριλαμβανομένης της όμορφης φόρμας αυτής της διατριβής. Ένα μεγάλο ευχαριστώ στον Steve Rochford για την πολύτιμη βοήθεια που μου πρόσφερε με το σύστημα HTCondor® καθώς και τον Tim Machin και την Dr. Nadiri Fusun που το έκαναν πραγματικότητα. Τον Dr. Tamer Zaki, Dr. Edward Smith που δώρησαν την βασική έκδοση του MDS κώδικα σε Fortran 90 από τον Rapaport καθώς και τον Prof. David Heyes για όλη την σχετική βοήθεια που πρόσφερε. Τους τεχνικούς μου Ian Wright, Guljar Singh, Stuart Marchant, Edwart Benbow και Asanka Munasinghe καθώς και τον βιομηχανικό μας σύνδεσμο Harminder Flora για την αξεπέραστη δουλειά τους στην κατασκευή και προετοιμασία του εργαστηρίου μου. Στην εξαιρετική γραμματέα του τμήματος μου Serena Dalrymple για όλη την βοήθεια της με τα γραφειοκρατικά θέματα του πανεπιστημίου. Τους φίλους και συνάδελφους μου που μου κράτησαν συντροφιά, ήταν πάντα έτοιμοι να προσφέρουν μια χείρα βοηθείας – κάποιοι μέχρι και ένα ώμο για να στηριχτώ – καθ'όλη την διάρκεια που πέρασα στο Imperial – Dr. Panos Sphikas, Dr. Georgios Charalampous, Dr. Alexandros Charogiannis, Konstantinos Hadjiyannis, Elias Dodoulas, Michalis Hadjipanayis, Benoit Fond και Chris Abraam.

Τους φίλους από το Ηνωμένο Βασίλειου – παλιούς και νέους – τον αγαπητό Diego Vietes, Emanuel Filho, Yorgos Yeorgiou, Michalis Stylianou, την αγαπημένη Ester Maria Toumpouris και τον καταπληκτικό Dr. Relja Arandjelovich που ήταν εκεί όταν χρειαζόμουν να ξεσκάσω, όταν χρειαζόμουν μια συμβουλή ή μια βόλτα για να ηρεμήσω και να επανεκκινηθώ.

Τέλος, θα ήθελα να ευχαριστήσω την πολυαγαπημένη μου οικογένεια για την απεριόριστη και αγνή αγάπη τους που με ώθησε να ανεβώ βουνά σε όλη την ακαδημαϊκή και προσωπική μου ζωή – δεν θα τα κατάφερνα χωρίς εσάς, είστε το καλύτερο που θα μπορούσε να μου είχε συμβεί. Στην γιαγιά μου Μαρία και τον παππού μου Θυμή που δίδαξε σε εμένα και στην υπόλοιπη οικογένεια μας ότι το μόνο εργαλείο που χρειάζεσαι για να επιβιώσεις είναι η μόρφωση. Στις τρελιάρες ξαδέρφες μου – και τυχαία συγκάτοικους μου – "Πριγκίπισσα" Electra Malaki και Eleni Agathokleous που μεταξύ άλλων μου πρόσφεραν στέγη όταν το Λονδίνο αποφάσισε να μου δείξει το σκοτεινό του πρόσωπο και ανέχτηκαν τις περιστασιακές μου απογοητεύσεις με την εργασία μου. Την Eleni Agathokleous για ακόμη μια φορά για το υπέροχο εμπνευσμένο απόσπασμα στα Ελληνικά που ακολουθεί αυτό το τμήμα της διατριβής - όπως είθισται σε αυτές τις περιπτώσεις. Στους κολλητούς μου φίλους που θεωρώ πλέον οικογένεια – Maria Savvidou και Thanasis (ή "Athanasios" όπως επιμένει αλλά ποτέ δεν θα καταφέρει να περάσει το δικό του) Taliadoros για την τεράστια υποστήριξη τους στο να ξεκαθαρίσω ποιος είμαι και τι κάνω στην ζωή και στην δουλειά μου.

Ήταν ένα ωραίο ταξίδι τα τελευταία τέσσερα χρόνια και δεν θα με πείραζε να το επαναλάμβανα. Έμαθα πολλά, γέλασα πολύ, γνώρισα πολλούς ανθρώπους και είσπραξα από τις καλές στιγμές, έμαθα και τραχύνεψα από τις κακές και θα είμαι για πάντα ευγνώμων σε αυτούς (κατονομαζόμενους και μη) που με βοήθησαν να φτάσω μέχρι το τέλος.

"Ένα τελευταίο ευχαριστώ στην σπονδυλική μου στήλη, για όλη την υποστήριξη που μου πρόσφερε όλα αυτά τα χρόνια"

Ελένη Αγαθοκλέους

Contents

List of Figures

List of Tables

Nomenclature

Latin Symbols

A	$\frac{1}{3}\sum_{j=a,b,c}\frac{k_{pj}-k_{BF}}{k_{pj}+(n-1)k_{BF}}$ when ellipsoid is defined by $\frac{x^2}{a^2+u}+\frac{y^2}{b^2+u}+\frac{z^2}{c^2+u}=1$ $\begin{pmatrix} u=0 & outside\ surface\ of\ solid\ ellipsoid \\ u=L & outside\ surface\ of\ solid\ ellipsoid\ layer \end{pmatrix}$ a,b and c are constants indicating the points where the ellipsoid is crossing the x, y and z axis correspondingly
Ab	absorbance
CCR(r_i)	cross correlation function value for the molecule i located at a distance r from the central "oil droplet" molecule
d	number of dimensions (here d=2 since a 2D system is used)
D	randomness function value
D_F	diffusion factor/coefficient
d_p	particle diameter
D_{self}	self-diffusion coefficient
E_k	kinetic energy of system
E_u	potential energy of system
f	volume concentration of the solid ellipsoids without surrounding layers
f_e	$r_v f$
$\mathbf{f}_{ij}$	force vector between the i^{th} and j^{th} pair of atoms

Latin Symbols

F_{TP}	Thermophoresis force
g(r)	radial distribution function value of the r^{th} ring from the central atom
I	probing signal intensity
I_0	probing signal intensity before travelling through the cuvette
J	diffusion flux
k	heat transfer coefficient
k_{pe}	equivalent thermal conductivity of equivalent nanoparticle
k_{pj}	equivalent thermal conductivities along the axes of the complex ellipsoid
L	domain size length
m	atomic mass
M_{jobs}	maximum number of jobs to assign on each administration machine
n'	$\frac{3}{\psi}$
N(r)	number of atoms in the r^{th} ring from the central atom
N_a	number of atoms in the domain
N_{admin}	number of administration machines in operation
n_{iw}	number of interrogation windows in area of interest (number of velocity vectors)
N_{nodes}	number of available nodes
P	system pressure
r_c	cut-off distance at which is assumed that the attractive tail of the model is no longer significant
R_{ext}	external radius
$\mathbf{r}_{ij}$	distance vector between the i^{th} and j^{th} pair of atoms
R_{int}	internal radius
r_v	volume ratio of nanolayer to nanoparticle
$\ddot{\boldsymbol{r}}_i$	acceleration vector of the i^{th} atom
state`$_i$	system state after a simulation running time t_{run}
state$_i$	initialisation state of the system
T	initial temperature of the system
t'	integral time variable
t_{d1}, t_{d2}	reference times where the diffusivity investigation initiates (t_{d1}) and ends (t_{d2})
t_i	native randomisation routine input argument

Latin Symbols

t_{real}	real-time native randomisation input argument
t_{run}	simulation running time
$\mathbf{u}_{ij}$	potential energy vector between the i^{th} and j^{th} pair of atoms
$\Delta V(r)$	elemental volume (corresponding ring area in a 2D domain) of the r^{th} ring from the central atom
$\mathbf{V}$, $\mathbf{v}$	velocity vectors
V_{norm}	normalisation speed
$\langle\lvert\bar{V}'\rvert\rangle$	groove spatially averaged RMS of normalised velocity fluctuations
$\langle\lvert\bar{V}\rvert\rangle$	groove spatially averaged normalised speed
$\langle\lvert\overline{V_{REL}}'\rvert\rangle$	groove spatially averaged RMS of normalised velocity fluctuations further normalised by $\langle\lvert\bar{V}\rvert\rangle$
$\hat{v}_{NP}$	unit velocity vector of the central atom of the assembled nanoparticle
$\hat{v}_i$	unit velocity vector of the i^{th} atom
y	atomic property y

Greek Symbols

α	offset between probing and reference intensity signals
β	$\frac{nanolayer\ thickness}{NP\ radius}$
γ	arbitrary constant
ε	strength of interaction
θ	angle
λ_{grid}	expected number of atoms in each grid cell
μ_{eff}	effective viscosity
μ_{bf}	Basefluid viscosity
μ_{y_i}	mean of the 1^{st} up to the i^{th} value of population property y
μ_{y_n}	mean of the 1^{st} up to the n^{th} value of population property y (n>i)
ρ	overall number density of system
ρ`	density
$\sigma^2_{y_i}$	variance of the 1^{st} up to the i^{th} value of population property y
$\sigma^2_{y_n}$	variance of the 1^{st} up the n^{th} value of population property y (n>i)
Φ_m	mass concentration of nanoparticles
Φ_p	particle/atomic concentration

Greek Symbols

Ψ	sphericity

Subscripts

BF	basefluid (host fluid)
Cal	calibration
eff	effective
f	fluid
NF	nanofluid
NP	nanoparticle
p	solid particle
R	reference
RMS	root mean square

Abbreviations

ANL	Argonne National Laboratory
BET	Brunnauer-Emmet-Teller
CAD	Computer Aided Design
CFD	Computational Fluid Dynamics
CHF	Critical Heat Flux
CPU	Central Processing Unit
DLS	Dynamic Light Scattering
EDL	Electrical Double Layer
HHF	High Heat Flux
HT	Heat Transfer
HV	HyperVapotrons
ITER	International Thermonuclear Experimental Reactor
JET	Joint European Torus
MAST	Mega Amp Spherical Tokamak
MDS	Molecular Dynamics Simulation
ND	Non Dimensional
NDU	Non Dimensional Units
NF	Nanofluids
NP	Nanoparticle

Abbreviations

PBHT	Pool Boiling Heat Transfer
PCA	Principle Component Analysis
PDF	Probability Density Function
PFC	Plasma Facing Components
PIV	Particle Image Velocimetry
POD	Proper Orthogonal Decomposition
RAM	Random Access Memory
RDF	Radial Distribution Function
RMS	Rood Mean Square
SEM	Scanning Electron Microscope
TEM	Transfer Electron Microscope/Microscopy
VACF	Velocity Autocorrelation Function

Chapter 1

Introduction

1.1 Motivation and project tasks

A nanofluid is a mixture of a small concentration of solid particles (10-100nm in size at concentrations below 10%vol) and a carrier fluid (usually conventional cooling fluids). These novel fluids exhibit anomalous heat transfer phenomena which cannot be explained using classical thermodynamic models. The fluids can be designed to offer unsurpassed heat transfer rates for heat transfer related applications at low manufacturing costs.

The adoption of the design and operation of future fusion power depends strongly on the efficiency of the power generation cycle and its comparison with current schemes. The most important aspect of the fusion technology substituting current means of mass power generation are the economics involved in the lifetime operation of the power plant which will ensure its viability. The heat transfer from the fusion reactor is a large contributor to the overall plant performance and is hence significant that the primary heat exchangers to be highly efficient. The optimisation of the heat exchangers so far has been limited to changes of the geometrical design of the components of HyperVapotrons and their operational regimens (volumetric flows, pumping pressures). This work attempts to optimise the primary heat transfer exchangers proposed by the fusion community by re-designing the coolant flow in the device.

This PhD thesis describes the efforts to test whether nanofluids can be utilised for high heat flux applications in a probable fusion primary heat exchanger and also to discover the mechanisms which give rise to the phenomenal heat transfer enhancements observed. The following subsections describe the literature review performed on HyperVapotrons and Molecular Dynamic Simulations to set the scene for the chapters to follow. The short literature reviews included in this chapter are complemented by a large piece of work containing a very broad [1-165] metadata statistical analysis review on nanofluids which can be found in chapter 2of the thesis.

1.2 HyperVapotrons[1]

HyperVapotrons (HV) are durable, high efficient two phase heat exchangers which are able to withstand high heat fluxes (HHF), of the order of 20-30MW/m^2, for extended periods of time. They were developed by Thomson CSF during the 50s' to cool down the anodes of high power tetrodes employed for communication purposes in klystron microwave tubes [170, 171]. They have high geometric flexibility and can be moulded to the shape of the heat exchanging surface they are attached to. These factors make them viable for nuclear fusion applications as plasma facing components (PFC). HyperVapotrons have been used extensively on the Joint European Torus (JET) for all actively cooled beam dumps and are considered as a candidate to form the first wall for the International Thermonuclear Experimental Reactor (ITER) [171].

HyperVapotrons are elongated modules which consist of three main features. A high velocity free stream rectangular channel which is joined over a substrate with grooves running perpendicular to the free stream flow and finally, a longitudinal groove running along each rib of the device. The device is oriented in a way that the grooved substrate is facing the oncoming heat flux. HyperVapotrons employ the "Vapotron" effect – a complex, highly effective two-phase heat transfer mode which allows some parts of the device to operate at a temperature which is higher than the CHF [172]. A typical cut out

[1] Parts of the work produced in this section were published in the public domain under references [166-169].

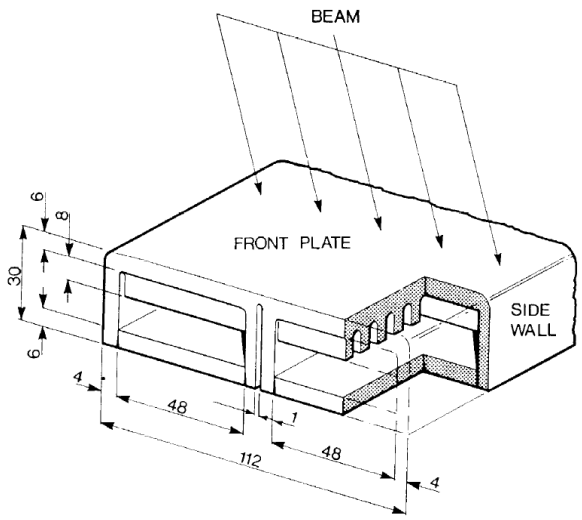

Figure 1.1. Standard JET flat HV design – all dimensions given in mm.

design can be seen in Figure 1.1 as found in [171]. The operation of the device is characterised into three modes according to the heat flux power received under fixed operating conditions (pressure and flow rate). These consist of a low power single phase heat transfer mode, an intermediate power two-phase soft boiling regime mode and a high power hard boiling mode at which parts of the device (plasma facing wall) operate above the CHF point [171]. Irregular vortices form along the grooves which appear to play an important role in the overall performance of the device. Upon the latter two modes of operation and at the onset of boiling, vapour bubbles form inside the grooves followed by an injection of the vapour in the free stream which then gets conveyed downstream and condensates.

Various computational fluid dynamics (CFD) and experimental studies have been performed by research groups around the world to assess the applicability of CuCrZr HyperVapotrons in fusion applications [170-195]. The experiments are generally focusing on the overall thermal performance of various geometries under various thermal loading scenarios and operating conditions. The CFD studies in general try to recreate the experiments in an effort to model the device operation and hence are able to predict the thermal performance under expanded operation regimes and geometries – without the need of further experimentation – for design optimisation.

In the literature, only a handful of experimental and computational investigations provide information regarding the flow fields inside a HyperVapotron. An experiment has been performed in the past [195] to provide qualitative information regarding the flow vortical structure observed in a single groove of a HyperVapotron. However, this experiment remained a qualitative investigation and the data cannot be used to evaluate the corresponding CFD investigations that either followed or preceded the experiment [172, 192]. An experimental visualisation of the vapotron effect under all of the thermal power modes of operation has also been performed [173] however, there is no detailed analysis of the recorded data to be able to evaluate the complex vaporisation, steam convection and condensation processes presented in the computational studies. It is hence evident that the hydrodynamic flow structures that may promote the Vapotron phenomenon have not been studied in detail experimentally and hence the physics of heat transfer, which are strongly related to the coolant flows, are not yet fully understood.

1.3 Molecular Dynamics Simulations (MDS)[1]

The uncertainty on the physical mechanism responsible for increased heat transfer points to the need for an investigation from first principles of the conductive heat transfer mode mechanism through a simplified, single particle nanofluid. This is achieved via a Molecular Dynamics Simulation code, which is composed to study the dynamic dispersion of a nanoparticle and compare this to the corresponding dispersion of a fluid molecule. The code is deployed at a computational scale of the order of millions of Central Processing Unit (CPU) hours with a minimum domain size of 1600 atoms. The model makes no assumptions regarding the macroscopic thermodynamic quantities of the fluid while the domain set up is such that preserves the simplicity of molecular collisions in order to understand and extract from first principles the associated macroscopic thermodynamic quantities via a statistical analysis. The system is chaotic and is allowed to evolve without any thermostatic or energy regulation control on the domain. The backbone of the

[1] Parts of the work produced in this section were published in the public domain under references [168, 169].

developed code is based on the available MDS models across the academic community (in particular from [196]).

Chapter 7 describes the methodology and the deployment of the MDS code on the computational domain, which is novel in its own right. It continues with the verification of the operation of the MDS code and the presentation of initial results that provide an explanation of the physics leading to enhanced heat transfer in nanofluids. Chapter 8 contains a nanoparticle size parametric study of nanofluids at the molecular level using the methodology described in chapter 7. This chapter attempts to explain the enhancement observed by the formulation of a new type of heat transfer mechanism present in nanofluids.

1.4 Thesis overview

Due to the novelty of nanofluids as smart coolants and the fact that the scientific community does not seem to have reached a definite answer to explain how nanofluids convey heat, it was decided to perform a wide range metadata statistical analysis of the majority of the publicly published work. The broad metadata statistical analysis performed on published literature (Section 2.1) provided qualitative results regarding the heat transfer enhancement to be expected from nanofluids as well as indicating trends linking by part mixture properties and heat transfer enhancement values exhibited. The study also helped to determine the most probable complex heat transfer mechanisms that might explain the enhancements observed. The nanofluids review formed the theoretical part of the project and provided the required motivation for the experimental processes followed.

The problem solving process was split into two large groups – experimental and numerical investigations. Along with the nanofluids literature review (section 2.1), a secondary literature review on HyperVapotrons (section 1.2) determined the experimental tasks of the thesis. It was evident that preliminary testing of nanofluids into the HyperVapotron devices was a complex four part problem:

a) The first part was to design an experimental rig which provides optical access into the HyperVapotron. In this way, planar velocity measurements with Particle Image Velocimetry (PIV) can be obtained. This facility allows the reproduction and hence modeling of the cold flow conditions encountered in a HyperVapotron device (section 3.3). This offered challenges as the pumping network had to be able to handle both, the large volumetric flows required with the added complications of measuring accurately and with high spatial resolution the flows using a PIV system.

b) The second part of the problem was the lack of a basic point of reference for comparison. The scientific community is lacking extensive information regarding the flow structures of conventional coolants inside the particular devices that explain their nominal operation. Without this information it is impossible to proceed with a comparison of the operational profile of the device using a nanofluid instead of a conventional coolant. As such, it was decided to proceed via velocity measurements of the flow of the conventional coolant to create the reference comparison dataset before proceeding with the exchange of the nominal coolant into a nanofluid (chapters 4 and 5).

c) The third problem came from the determination of an acceptable level of nanofluid type and quality given the practical concerns of experimentation at the local facilities and the budget limitation of the project. It was decided to use an Al_2O_3-water nanofluid to take advantage of the lower nanofluid material costs as well as the abundance of literature material on the current nanofluid as it is favoured by the broad scientific community of the field (Table 2.1 and Table 2.2). A lower quality level nanofluid creation method (multi-step creation process) was the only option in the PIV studies as the amount of nanofluid to be created were both prohibitive in terms of cost and availability. An investigation assessed the quality of the nanofluids produced given the mixing method employed (section 3.1).

d) The fourth and last problem came from the application of the PIV methodology itself to nanofluids. There is a lack of experimental data in the literature describing laser beam interactions in a PIV experiment and light scattering in nanofluids. As such, before advancing to the nanofluids PIV velocity measurements, it was decided to perform investigations on the scattering and absorption profiles of laser

beams in nanofluids (section 3.2). This will ensure that the proposed PIV approach will be applicable to the study.

The numerical investigation consists of a MDS code. The code models a simple single nanoparticle nanofluid (Chapters 7 and 8). What differentiates the code from the rest of the numerical studies found in the literature is the lack of assumptions that can predetermine the macroscopic physical heat transfer mechanisms of nanofluids and hence interfere with the obtained results. The code is built on an established solid molecular dynamics base model (Lennard-Jones molecular interaction model) which reduces the macroscopic thermodynamic phenomena into an ensemble of soft sphere interactions. The problem is then scaled up into the macroscopic thermodynamic regime via the collection of molecular interaction and location data which are subsequently statistically processed to extract the quantities required. The code provides information regarding the physical processes of heat transfer which take place as well as allowing the application of parametric studies to define the trends linking "tuneable" mixture properties with heat transfer.

1.5 Thesis outline

Chapter 2 contains a broad metadata statistical analysis review for nanofluids while chapter 3 describes the experimental methodology followed in this study. For the ease and aid of the reader, the experimental and numerical chapters of the thesis (chapters 4 to 8) are written in a comprehensive, partially self-contained, segmented format. Each chapter starts with a short introduction, followed by a results and discussion section and ends with conclusions. All of the published material produced in this project is clearly specified at the beginning of each section in the footnotes part of the page. The thesis concludes with a short chapter summarising the main outcomes of the thesis and proposes the future research needs foreseen by the current author. Finally, the electronic version of the thesis accommodates a dynamic cross referencing capability which aids the readers to move easily between the referred items in the text.

Chapter 2

Nanofluids Literature Review[1]

2.1 Foreword

The nanofluids literature review was composed in the first year of this PhD study (2009). The process took about one year to complete and considered 130 peer reviewed journal publications. Buonjiorno J. et al. (2009)[3] in one of his publications estimates that the total number of publications bearing the word "nanofluid" up to 2008 to be around 650. The estimation was performed using SciFinder scholar – a chemistry related publication tracking tool. The filtering process to arrive to the mentioned results is not explained. Up to the time of initiating the nanofluids literature review study (i.e. mainly publications up to and including year 2008), the Thomson Reuters Web of Science website (http://apps.webofknowledge.com/) indicates that there are 372 publications bearing the word "nanofluid". However, the results emanate from the entire spectrum of databases held by the tool and unavoidably there are publications in which the engineering and thermodynamic aspect of heat transfer in nanofluids was not investigated. As such the total number of publications at the time of the study is expected to be less than the initially quoted number. Filtering through the publications to narrow the categories into peer

[1] The work produced in this section was published in the public domain under references [1, 2].

reviewed journal publications brings the total number to 240. Further filtering of the sample to include only peer reviewed publications related to engineering and thermodynamics, limits the final sample to 153 publications. The statistical analysis of the sample produced is therefore considered to be complete and exhaustive.

2.2 Section introduction

Nanofluids are fluids that contain small volumetric quantities (around 0.0001-10%) of nano sized suspensions of solid particles (100nm and smaller in size). This kind of fluids exhibit anomalous heat transfer characteristics and their use as advanced coolants along with the benefits over their conventional counterparts (pure fluids or micron-sized suspensions/slurries) is investigated.

Nanofluids were invented by U.S. Choi of the Argonne National Laboratory (ANL) in 1993, during an investigation around new coolants and cooling technologies, as part of the "Advanced Fluids Program" project taking place at (ANL). The term "nanofluids" was subsequently coined to this kind of colloidal suspensions by Choi in 1995 [4].

Since then, thriving research was undertaken to discover and understand the mechanisms of heat transfer in nanofluids. The knowledge of the physical mechanisms of heat transfer in nanofluids is of vital importance as it will enable the exploitation of their full heat transfer potential.

Several literature review papers were issued by researchers in the last years [5-9] . However, it is the current authors' belief that previous reviewers failed to present all the observations and results obtained from the literature in a clear and understanding method. The main problems arise from the fact that the application of nanofluids as coolants is a novel practice with no established physical foundations explaining the observed anomalous heat transfer characteristics. In addition, due to the recent growth of this area, there are no procedures to follow during testing for the evaluation of the thermal performance. As a consequence, traditional methods of performing a literature review may be inadequate in

presenting an unbiased, objective and clear representation of the bulk of the available literature.

It was therefore decided to perform a statistical analysis of the findings of the available publications in the literature in order to alleviate the problems faced by previous reviewers. The statistical analysis would enable the depiction of observations on comprehensive charts (histograms and scatter diagrams) hence making possible the extraction of conclusions in a more solid and mathematically rigorous manner. The present literature review gives the same weight to all of the observations available in the literature. This review addresses the following questions:

a) What are the General Heat transfer characteristics of nanofluids?
b) What are the trends linking the heat transfer performance of certain nanofluids with their by-part mixture parameters?
c) What are the most prevailing theories explaining the anomalous heat transfer behaviour observed in nanofluids?

Section 2.3 of this thesis describes the nanofluid characteristics followed by section 2.4 where the methodology of statistical analysis is described. Sections 2.5 and 2.6 present the results of the analysis obtained. Section 2.7 of this review contains brief information regarding a different type of fluids – "Nanoemulsions" – that has started emerging in the literature recently and might in the future be incorporated into the broader category of nanofluids. Finally, section 2.8 contains the main conclusions reached by the current review.

2.3 Characteristics of nanofluids

This section characterises the most common nanofluid preparation methods by providing information about the last stages of the fluid creation. Note that the "quality" of a nanofluid represents the extent of achievability of the desired properties of the mixture. The desired properties of a nanofluid are:

a) Even, durable and stable suspension of the solid nanoparticles in the host fluid (Basefluid).
b) Low or no formation of agglomerates.
c) No chemical change of the basefluid (i.e. the solid particles must not chemically react with the host fluid).

Nanofluids follow either single or multi-step creation methods. The single-step creation approach refers to a direct evaporation method (Vacuum Evaporation onto a Running Oil Substrate – VEROS). This method attains the best quality nanofluids; however, there are substantial limitations on the flexibility to create customised nanoparticle volumetric concentrations and basefluid type samples.

The multi-step method provides more flexibility, but, in general, with a penalty in the quality of the attained mixture. Nanofluids can be created either by diluting a very dense solution of the required nanofluid with the matching basefluid or by mixing directly the nanoparticles of choice with the desired basefluid. The first procedure provides more flexibility than the single-step method as the nanoparticles' volumetric concentration can be made to order; however, the quality of the resulting nanofluid is lower than the one achieved via the single-step method.

The second approach of the multi-step method is the most widely used amongst researchers, since it provides maximum flexibility to control the volumetric concentration of the nanoparticles, along with the basefluid type to be customised given the nanoparticle material, shape and size. On the other hand, this procedure delivered the lowest quality of nanofluids in comparison to all the other methods [10].

The most common liquids used as basefluid are conventional coolants, such as deionised water, engine oil, acetone, ethylene glycol (EG). The most common nanoparticle materials used are Aluminium (Al), Aluminium Oxide (Al_2O_3), Copper (Cu), Copper Oxide (CuO), Gold (Au), Silver (Ag), Silica Dioxide (SiO_2), Titanium Oxide (TiO_2) and Carbon Nanotubes (CNT – either single walled, double walled or multi walled).

2.4 Methodology of statistical analysis

In order to tackle the topics mentioned in Section 2.2 of this thesis, the present researchers resolute to following a statistical investigation of a large sample of findings collected from the available literature. The analysis was performed in three levels. The first level consists of the bulk of the findings from all the published work and enables the demonstration of a general view of the thermal performance of nanofluids. The second level focuses on the most commonly studied nanofluid types and compositions and makes it possible to extract trends linking the various nanofluid properties with their thermal performance. The third and final level narrows the sample to include a selection of findings from simple geometry experiments (consisting of travelling hot wire and pipe flow type, instead of complex geometries), ignoring theoretical and numerical investigations, thus providing an insight into what appear to be the controlling parameters of thermal performance of nanofluids. Additionally, the final level of analysis reveals what is currently missing from the literature and indicates what aspects need to be investigated further to reach a more conclusive result regarding the links between thermal performance and nanofluid properties.

Table 2.1. Most common nanoparticle materials along with their indicative price ($) per 100g.

Material	**Indicative price ($/100g)**
Al (Aluminium)	380
Al_2O_3 (Aluminium Oxide)	70
Cu (Copper)	500
CuO (Copper Oxide)	75
Au (Gold)	5,500
Ag (Silver)	400
SiO_2 (Silica Dioxide)	70
TiO_2 (Titanium Oxide)	80
Carbon Nanotubes	930-12,500

Table 2.2. The four most probable nanofluids found in the literature.

Type of nanofluid used	**Sample percentage**	**Number of corresponding Observations**
Al_2O_3 – Water	33.9	85
Al_2O_3 – EG	8.8	22
CuO – Water	6.8	17
TiO_2 – Water	6.8	17
Total	56.3	141

Findings were gathered regarding the observed enhancement for several heat transfer modes (conduction, convection, pool boiling heat and critical heat flux) and compared to the heat transfer performance of the basefluid alone. Additional information was recorded linking the observed enhancement to the material of the basefluid and nanoparticles, nanofluid composition (nanoparticle concentration), nanoparticle size, temperature of nanofluid, viscosity (enhancement), type of experimental set up, flow status (i.e. laminar or turbulent), possible gravitational effects (e.g. for convective heat transfer), as well as any other interesting observations. Finally, the proposed mechanisms for the observed heat transfer anomalies were identified (the assembled database which was used for the presented review can be found in Table 2.3 - Table 2.10).

The methodology for the capturing of the findings (numerical and theoretical) from each publication and ensure repeatability of data collection and analysis is as follows:

a) It was decided to limit the data gathering for volumetric concentrations of nanoparticles (Φ) up to 10% (focus group) as larger concentrations impart practical considerations due to the large viscosity increase of the fluid.
b) Information was presented on diagrams only when adequate number of cases was available in order to be able to approximately describe the shape of the resulting graph.
c) In cases where Dynamic Light Scattering (DLS) or a Brunnauer-Emmet-Teller (BET) sizing method was used in conjunction with a Transfer Electron Microscopy (TEM) or Scanning Electron Microscopy (SEM) method, the latter sizing values were preferred over the former ones as they provide better accuracy (DLS and BET methods both take into account the hydrodynamic size of particles with the

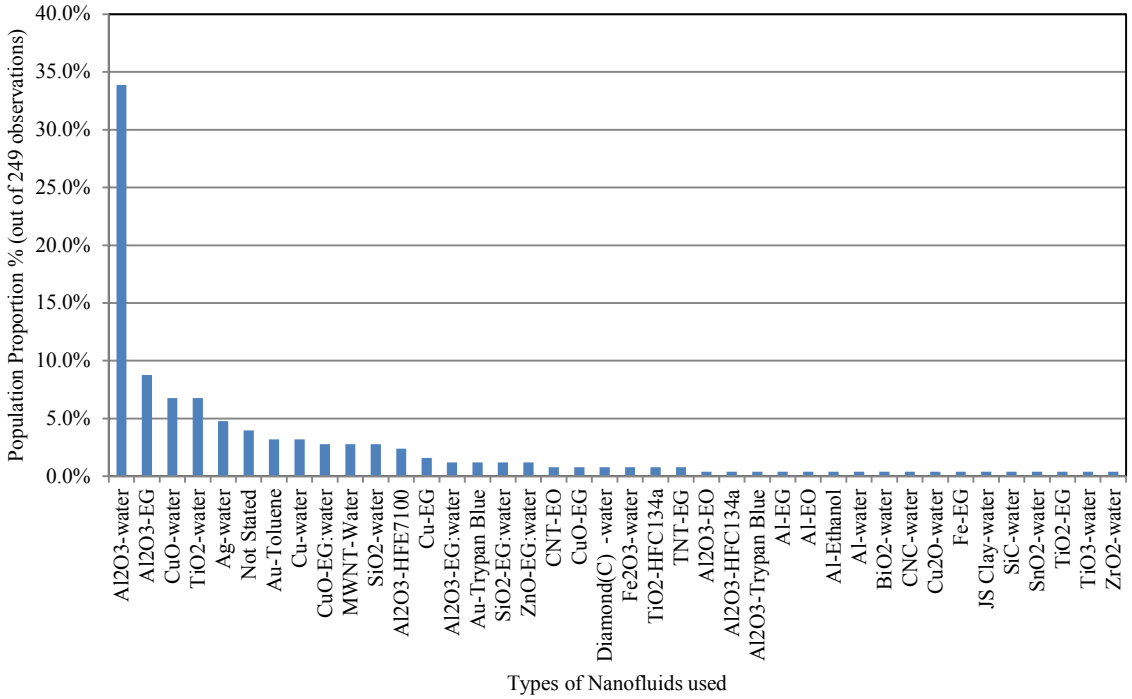

Figure 2.1. Nanofluid type distribution.

assumption of sphericity instead of their actual dimensions. This incurs problems when the nanoparticles are clustered/agglomerated or not spherical).

d) In the cases where the Pool Boiling Heat transfer (PBHT) or Critical Heat Flux (CHF) were considered, values from experiments representing a real and practical engineering application were recorded over the rest.

e) In the rare case where nanoparticle concentrations were represented as mass fraction quantities, a volumetric conversion, according to Equation (2.1) was used [11].

f) When the mode of heat transfer was not clearly stated or was not evident from the experiment (for example if heat transfer mode was purely via conduction/convection), then the experimental values were sorted into the convection/mixed convection heat transfer class (when both modes are present, it is expected that the effects of convection would prevail over the effects of conduction).

$$\Phi = \frac{1}{\frac{(1-\Phi_m)\rho`_p}{\Phi_m \quad \rho`_f}+1} \tag{2.1}$$

where,

Φ : volumetric concentration of nanoparticles

Φ_m : mass concentration of nanoparticles

$\rho`$: densities (p for nanoparticles, f for base fluid)

Table 2.1 displays an average price list of different nanoparticle materials, while Table 2.2 and Figure 2.1 show the nanofluid types in the literature. It is evident that the cost of particular type(s) of nanoparticles heavily controlled the available study. As a consequence, the statistical results of this section are heavily inclined towards indicating the thermal performance of Al_2O_3 - water type nanofluids.

2.5 Thermal performance studies

Previous investigators chose to carry out their studies either via the experimental or the analytical route. For the former one, the majority of researchers selected simple experiments (e.g. simple heated pipe/duct flow or stationary flow experiments) using various combinations of nanofluid concentrations and materials under different heat input conditions. The simple experiments provided more insight into the actual physics of heat transfer in nanofluids whilst the more complex experiments usually gave information concerning the practical usage of particular nanofluid compositions and types for certain applications, with little or no referral to the employed theories for heat transfer.

Analytical-computational methods involve the formulation of semi-empirical correlations in order to predict the behaviour of nanofluids. The most common analytical methods are based on the renovated Maxwellian [12], Equation (2.2), or renovated Hamiltonian-Crosser equation models [13], Equation (2.3), to be able to predict the effective heat conduction in a nanofluid. Additional components are usually added to the equations to take into account the Brownian motion heat transfer mechanism.

$$k_{eff} = \frac{k_{pe}+2k_{BF}+2(k_{pe}-k_{BF})(1+\beta)^3\Phi}{k_{pe}+2k_{BF}-(k_{pe}-k_{BF})(1+\beta)^3\Phi} k_{BF} \quad (2.2)$$

$$k_{eff} = \left(1 + \frac{n`f_eA}{1-f_eA}\right) k_{BF} \quad (2.3)$$

where,

k : heat transfer coefficient (eff for effective, BF for basefluid)

k_{pe} : equivalent thermal conductivity of equivalent nanoparticle

β, n`, f_e, A : constants defining shape, consistency and properties of nanoparticles (a more detailed explanation can be found in the nomenclature section of this thesis)

Equations (2.2) and (2.3) rely on the molecular layering theory, i.e. the presence of Nanolayers with reduced thermal resistance covering the surface of each nanoparticle. The Renovated Hamiltonian-Crosser model equation is assumed to be more accurate, as the shape of the solid nanoparticles is taken into account (sphericity), while the renovated Maxwellian model only assumes spherical particles and works well for nanoparticle diameters that are less than 10nm [12]. For the other heat transfer modes (apart of heat conduction), the formulation of further equations to include additional parameters (e.g. density changes, buoyancy forces, gravitational forces etc.), has its foundations on Equation (2.2) and Equation (2.3).

The critical issue with numerical simulations and semi-empirical correlations is that the majority of researchers predetermined, to some degree, the physical mechanisms underlying behind the anomalous heat transfer characteristics in nanofluids. For example, some semi-empirical correlations are based on fitting experimental measurements determined for specific applications. As a result, with the physical understanding of the heat transfer mode mechanisms is unknown, it becomes trivial to sightlessly rely on such simulations and equations to hold valid for a general range of nanofluid compositions, types and application (e.g. as coolants in various heat exchanger designs).

2.6 Heat transfer characteristics

In the following section, the heat transfer characteristics of nanofluids are considered [2, 5-8, 10-127]. Information was collected from the literature and processed to reveal the thermal performance of nanofluids for different heat transfer modes (purely conductive, convective/mixed, PBHT and CHF). Information, regarding the mechanisms that various researchers employed to describe the anomalous heat transfer, was also collected to allow the evaluation of the most statistically occurring patterns for each heat transfer mode.

Finally, a cross-correlation of the findings between the different levels of analysis (as discussed in Section 2.4) was also considered in order to evaluate the observations and reveal any possible trends linking the thermal performance characteristics of nanofluids with their by part properties (i.e. consistency and application). Furthermore, the focused samples of Level 3 of the analysis provided further information about the parameters controlling the thermal performance characteristics of nanofluids.

2.6.1 General observations – Level 1 analysis

Level 1 of the analysis considers the entire sample record collected from the literature. It aims to present a general idea of the thermal performance of nanofluids for different heat transfer modes.

Heat transfer characteristics

Heat transfer enhancement studies purely via conduction (130 observations)

Strong evidence of thermal conductivity enhancement exists, as indicated by the histogram of the findings of Figure 2.2. An enhancement lying between 5-9% was observed for 30% of the sample. The variation around the 5-9% enhancement range is large. However, the majority of the remaining observations are in the 1-4% and 10-24% enhancement ranges, representing around 45% of the sample. The remaining data (around 25% of the sample)

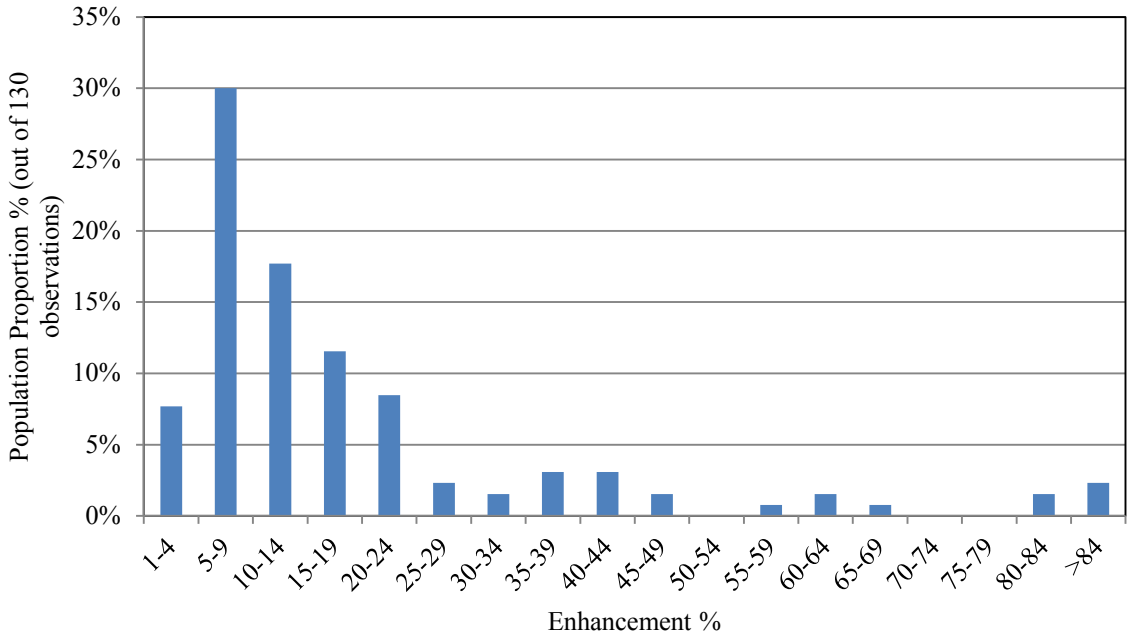

Figure 2.2. Probability function of enhancement of heat transfer due to conduction.

indicate enhancement above 29% and some even larger than 84%. Therefore, there is a need for additional understanding of the origin of the resulting enhancement of heat transfer due to conduction.

Heat transfer enhancement studies via convection/mixed heat transfer mode (91 observations)

Strong evidence of heat transfer enhancement by nanofluids for convective or mixed heat transfer mode is indicated by the histogram of Figure 2.3. Most data indicate a convective heat transfer coefficient enhancement between 10-19% (18% of the sample). However, the spread of the enhancement results is very large. The majority of the results (around 45% of the sample) indicated unspecified enhancement. There is also weak statistical indication of nanofluids causing deterioration of the heat transfer coefficient (11% of the sample) and an even smaller percentage of the sample indicating no enhancement at all (3% of the sample). Therefore, the statistical analysis for convective heat transfer is less consistent than for conduction, which supports the need for more research.

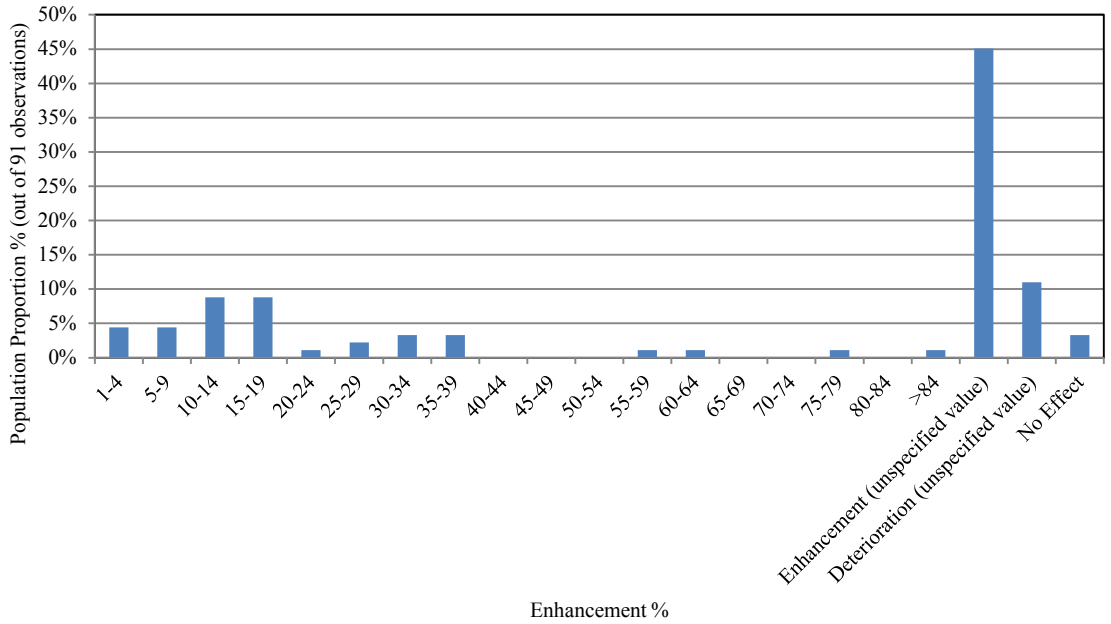

Figure 2.3. Probability function of enhancement of heat transfer due to convection/mixed heat transfer modes

Pool boiling heat transfer enhancement studies (22 observations)

Strong evidence of enhancement of heat transfer due to PBHT is indicated in the histogram of Figure 2.4. Most data reporting specific values show an improvement of the PBHT coefficient between 40-44% (9% of the sample). However, the majority of the results (45% of the sample) indicate an unspecified enhancement, while there is an indication of deterioration with moderate statistical importance (23% of the sample) and a weak statistical percentage of the considered sample indicating no enhancement at all (5% of the sample). However, the number of publications for PBHT is low and, as a consequence, the findings have lower confidence level. In addition, the complexity of the physics of PBHT can cause large variation in the observed enhancement and the lack of understanding does not allow the assessment of optimised operation with PBHT.

Critical heat flux enhancement studies (23 observations)

Strong evidence of enhancement of CHF in boiling applications is indicated by the histogram of Figure 2.5. Most observations show an improvement of the CHF coefficient

lying between 100-200% (35% of the sample). There is a weak statistical percentage of the considered population indicating deterioration (4% of the sample). However, the spread of the results is large and the confidence level of the findings is low. Since several publications have reported very large enhancement of CHT, it is important to understand the origin of CHT enhancement in nanofluids.

Proposed physical mechanisms for the anomalies of heat transfer

An outline of all the proposed mechanisms for each type of heat transfer study is presented. These mechanisms (or a combination of more than one mechanism) are used by researchers in the literature to explain the augmentation of the heat transfer coefficient in nanofluids. The proposed mechanisms are briefly explained first before the findings of the statistical analysis are presented. The findings are considered jointly for conduction and convection and for PBHT and CHF.

Conduction/convection/mixed mode heat transfer studies (85 observations)

The proposed mechanisms for the enhancement of heat transfer in conduction, convection

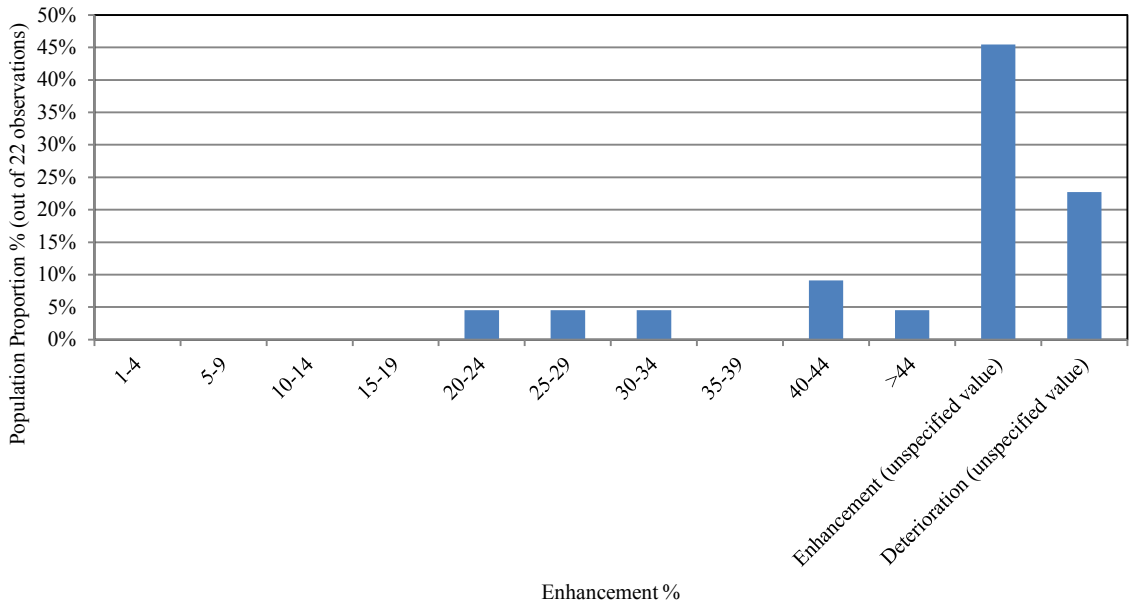

Figure 2.4. Probability function of enhancement of heat transfer due to PBHT.

or for mixed conditions in the literature are described below. Example references of papers containing the explanation of the theory are also provided.

Brownian motion

Many researchers believe that there is an apparent enhancement of heat transfer due to Brownian motion of nanoparticles. Their speculations rely on the fact that nanoparticles provide larger surface area for molecular collisions. The higher momentum of nanoparticles (higher mass concentrations compared to the host fluid molecules) are believed to carry and transfer thermal energy more efficiently at greater distances inside the basefluid before they release it in a colder region of the fluid (small packets of energy) [128].

Interfacial layer theory (Kapitza resistance)

The Kapitza resistance is a thermal boundary resistance arising from thermal energy carrier scattering at an interface (scattering of phonons and electrons). The type of carrier scattered will depend on the materials governing the interfaces. In liquid-solid interfaces

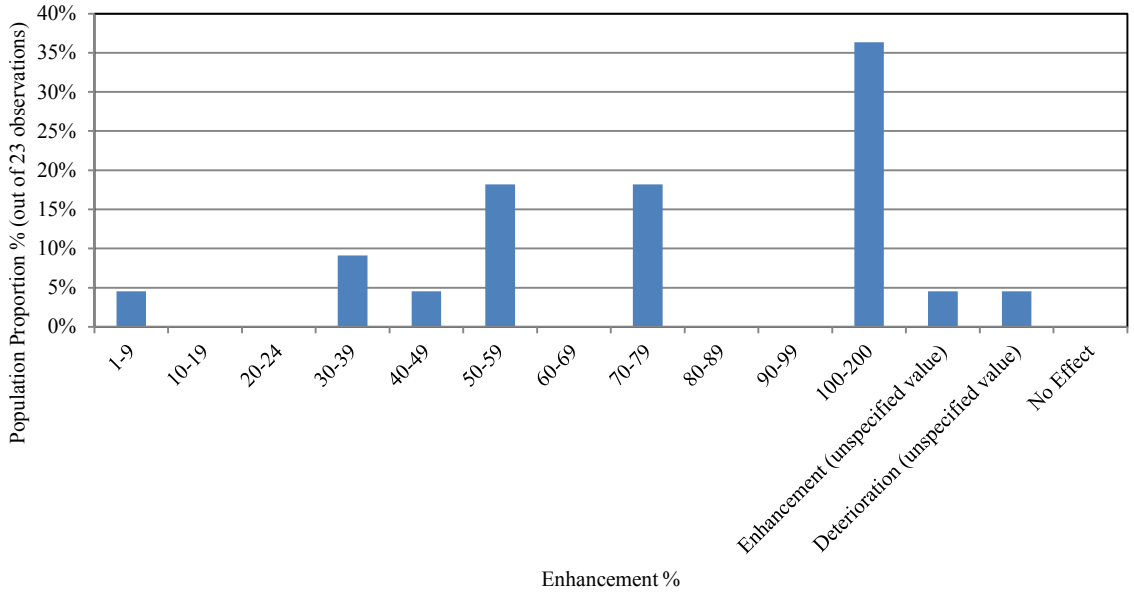

Figure 2.5. Probability function of enhancement of heat transfer due to CHF.

(e.g. nanoparticle – base fluid interfaces), the boundary resistance is believed to decrease hence the overall thermal resistance of the system (e.g. a nanofluid in this case) is believed to reduce [129].

Aggregation and diffusion

This mechanism suggests that there is a formation of a linear assembly of nanoparticle chains upon their suspension in the host fluid. The occurrence of this chain assembly is speculated to provide a faster path for heat transfer through the nanofluid (faster heat diffusion) [79].

Electrical Double Layer theory

EDL is a mechanism which proposes an alteration of the strength of intermolecular interaction forces that in effect change the mean free path of the nanoparticles and hence augmenting the heat transfer of molecules [121].

Flattening of velocity profile due to viscosity

This mechanism proposes that the viscosity change of nanofluids leads to a more uniform velocity profile for flows in pipes and ducts than the expected parabolic velocity profile (Poiseuille flow). The increased near wall velocity is believed to provide an increase in the convective heat transfer coefficient observed in these applications [130].

Near field radiation

Some researchers believe that there is infrared Radiation Emission and Absorption augmentation at the nanoscales (near field radiation). This enhances heat transfer between the heating surface and the nanoparticles, the basefluid molecules and the nanoparticles and between the nanoparticles themselves by a factor of 2-3 compared to the far field radiation estimates [131].

Thermophoretic forces

Thermophoretic forces on nanoparticles arise from the presence of temperature gradients in the fluid causing the concentration of nanoparticles to change around heating and cooling sides relative to the mean value. The consequence of this nanoparticle redistribution is the alteration of the heat transfer coefficient accordingly [61].

Shear thinning behaviour of flows

Some researchers believe that nanofluids exhibit non-Newtonian characteristics with shear thinning behaviour. The viscosity is believed to reduce at the solid boundaries of a flowing

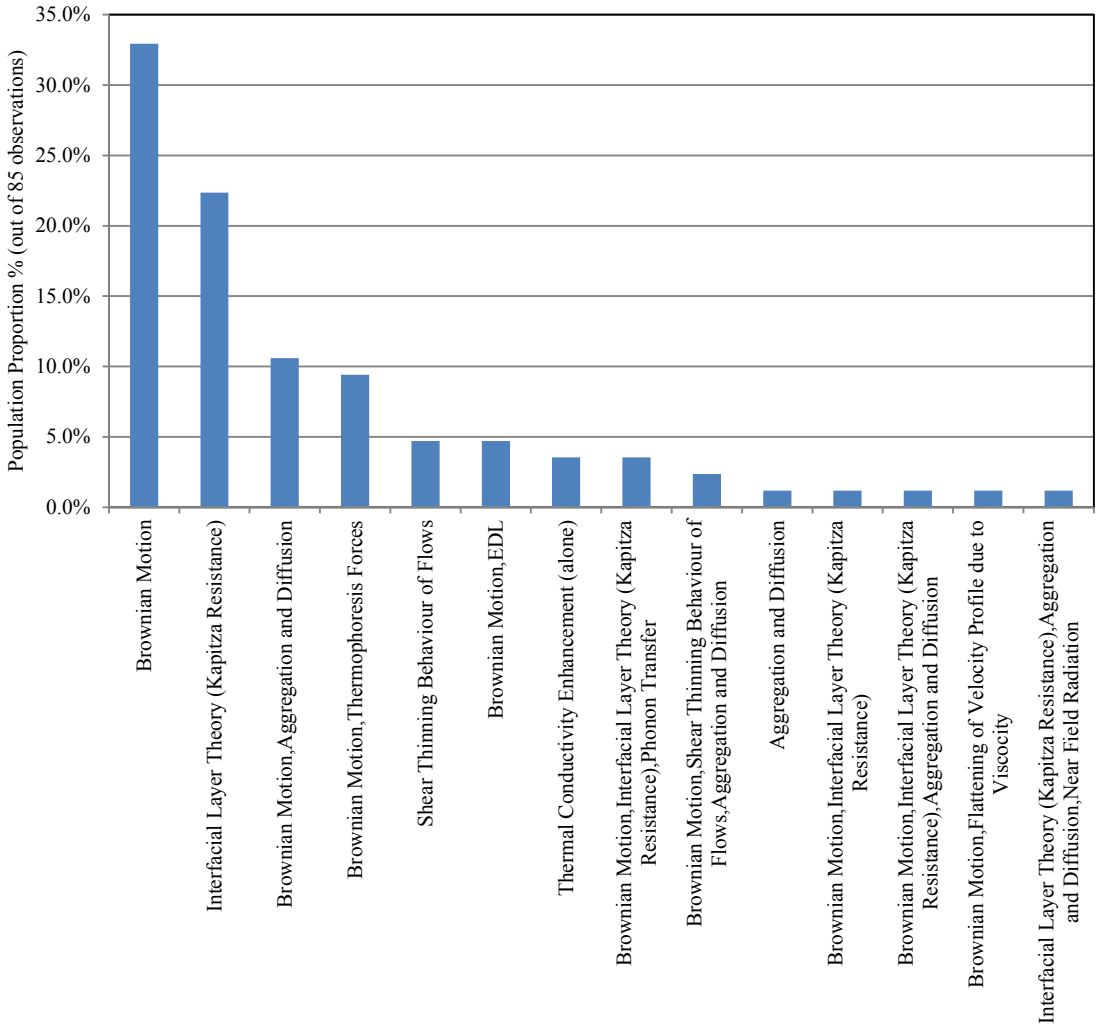

Figure 2.6. Probability function of proposed mechanisms to explain anomalous heat transfer (conduction/convection/mixed mode heat transfer studies).

nanofluid, because the shear rate of the nanofluids increases along the walls. This promotes increased heat transfer between the wall and the liquid because the thermal boundary layer width is reduced. It also provides a beneficial lubrication effect [132].

Phonon transfer

A few researchers suggested that nanofluids have an increased heat transfer rate due to specialised phonon and electron interaction and scattering at the nanoscales (ballistic heat transport) [133].

Thermal conductivity enhancement alone

Some researchers have accounted for the increase of the thermal conductivity alone (without providing more information) to account for the observed enhancement of heat transfer [96].

Figure 2.6 presents the histogram of the proposed mechanisms to explain the anomalous heat transfer for conduction, convection and mixed cases in the literature. The observations from Figure 2.6 are summarised below to the three most commonly proposed mechanisms:

a) Brownian motion (33% of the sample).
b) Interfacial Layer theory (Kapitza Resistance) (22.4 % of the sample).
c) A combination of the Brownian motion and the aggregation and diffusion theories (11% of the sample).

Pool boiling heat transfer and critical heat flux enhancement studies (40 observations)

The proposed mechanisms for the enhancement of PBHT and CHF in the literature are described below.

Deposition of nanoparticles on heating surface

The vast majority of researchers assume that, for this heat transfer mode, the use of nanofluids leads to a modification of the heating surface. The alteration promotes higher frequency of bubble departure with smaller bubble size. At the same time, there is an increased wettability that inhibits the dry patch development on the heating element, leading to increased CHF [59].

Passive/active mode of heat transfer

The passive mode mechanism suggests that nanoparticles provide additional nucleation sides for vapour bubble formation and boiling. The active mode mechanism suggests that nanoparticles provide appropriate surface area for converting infrared radiation into heat. These two modes are suspected to increase the overall heat transfer coefficient of nanofluids [27].

Long range structural disjoining pressure

Confinement of nanoparticles in the meniscus area, supplying liquid to the formation of the vapour bubble at the dry patch, is believed to promote an increased wettability and inhibition of the dry patch development [81]. This leads to increased CHF.

Electrical Double Layer theory

The EDL mechanism was also proposed to explain conduction/convection heat transfer enhancement. It is based on a change of the strength of intermolecular interaction forces that modifies the mean free path of the nanoparticles [121].

Thermal conductivity enhancement alone

This mechanism was also proposed to explain conduction/convection heat transfer enhancement. It makes use of the increase of the thermal conductivity alone (without

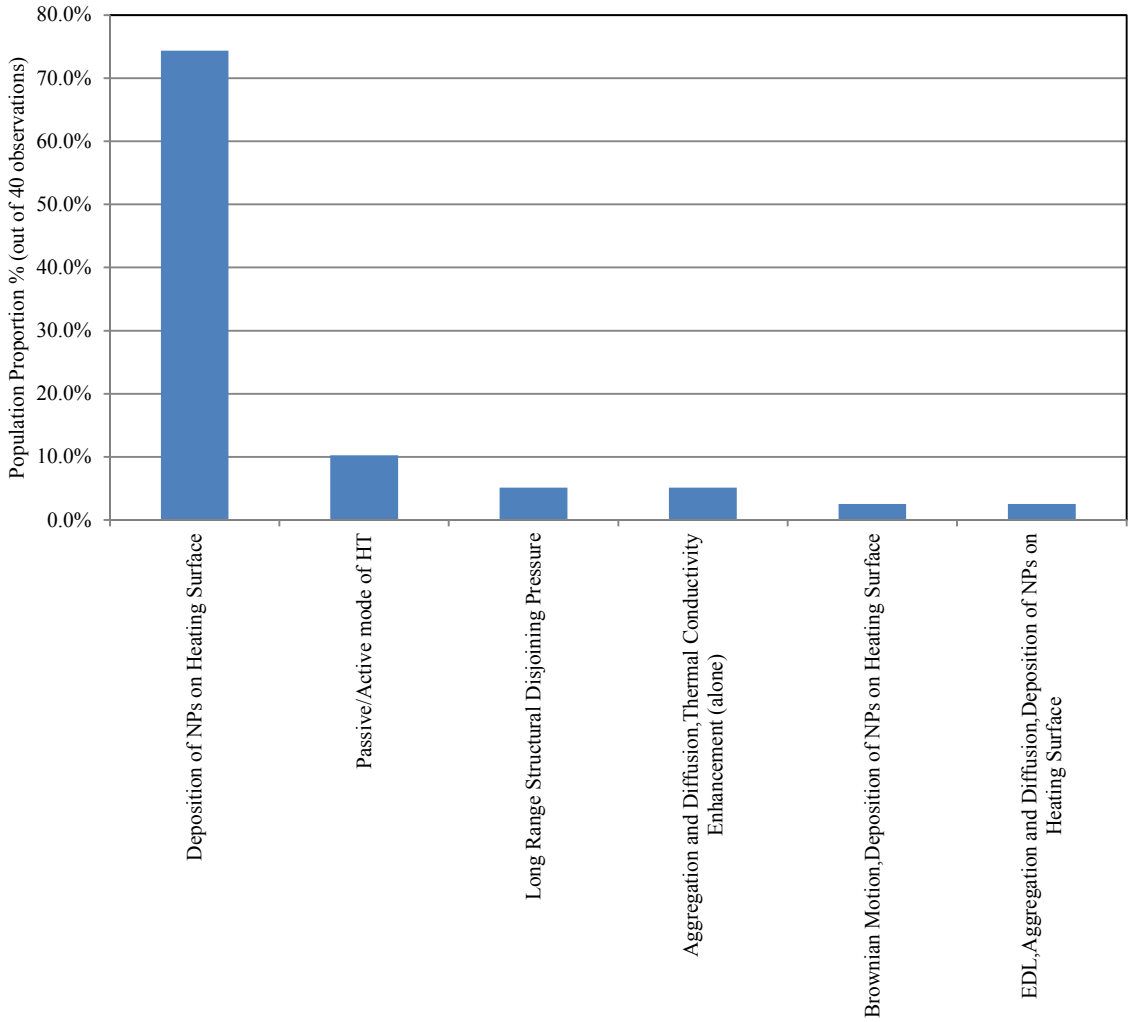

Figure 2.7. Probability function of proposed mechanisms to explain anomalous heat transfer (PBHT and CHF heat transfer studies).

providing more information) to account for the observed enhancement of heat transfer [96].

Figure 2.7 presents the histogram of the proposed mechanisms to explain the anomalous heat transfer for pool boiling and CHF in the literature. The observations from Figure 2.7 are summarised below to the two most commonly proposed mechanisms:

a) Alteration of the heating surface due to the deposition of nanoparticles (75% of the sample).
b) Passive/active heat transfer mode theory (10% of the sample).

In summary, a general overview of the thermal performance for each heat transfer mode was presented. It is evident that the vast majority of publications in the literature indicated that nanoparticles are found to augment the heat transfer coefficient of a given basefluid for every mode of heat transfer.

The most popular mechanisms for explaining the anomalous heat transfer were also presented. All of the proposed mechanisms have not been verified experimentally and as a result these proposals still remain notions of what is theoretically employed by researchers to explain the phenomena.

2.6.2 Evaluation of trends of specific nanofluids – Level 2 analysis

Level 2 of the statistical analysis contains a narrowed down sample of publications. The criterion for selecting the publications of the secondary group of Level 2 was the nanofluid material composition. It was decided to select the nanofluid material consistencies that were most commonly used in the literature. This enables the in-depth comparison between observations recorded from different research groups found in the literature, hence allowing the definition of possible trends linking the thermal performance characteristics of nanofluids with their by part properties (such as consistency, temperature of nanofluid, etc.). The formation of the secondary group also provides correlation information between the two analysis levels (namely levels 1 and 2) that assists the evaluation of the statistical analysis findings.

Nanofluid types considered (249 observations)

A histogram of nanofluid types employed in the literature was presented in Figure 2.1 and was considered again here to discover which types have been studied most and hence, allow the creation of secondary focus groups**.** The selected sample was narrowed to the following nanofluids: Al_2O_3-water, Al_2O_3-EG, CuO-water and TiO_3-water (see Table 2.2). The processing of the Level 2 analysis sample indicated that the number of publications for the latter two types of nanofluids was too small to obtain conclusions with reasonable

statistical significance. Hence, it was decided to consider only the results for the former two nanofluids (i.e. the Al_2O_3-water and Al_2O_3-EG).

Heat transfer characteristics

The statistical analysis 2 of the thermal performance was performed for each heat transfer mode, when the sample was large enough (more than 10 observations) to justify the statistical findings. Histograms of this analysis are not presented here, but the findings are summarised below.

Heat transfer enhancement via conduction

Al_2O_3-water nanofluids (41 observations)

Strong evidence of thermal conductivity enhancement is present. Heat transfer enhancement was observed mainly between 5-9% (34% of the sample). The variation around the 5-9% enhancement regime was small with the majority of the remaining observations in the enhancement range of 10-14% (32% of the sample).

Al_2O_3-EG nanofluids (11 observations)

Strong evidence of thermal conductivity enhancement is present. Heat transfer enhancement lying between 5-9% was similarly observed (36% of the sample). The variation around the 5-9% enhancement range was again small with the majority of the remaining observations in the 10-14% range (27% of the sample).

The findings for the two nanofluids are complimentary and in agreement with the findings for all types of nanofluids as obtained from the analysis of Level 1 and presented in Figure 2.2.

Heat transfer enhancement studies via convection/mixed heat transfer mode (91 observations)

Al_2O_3-water nanofluids (36 observations)

There is strong evidence of heat transfer enhancement with most publications indicating an unspecified value of enhancement (39% of the sample).

Al_2O_3-EG nanofluids (11 observations)

Strong evidence of heat transfer enhancement is present. Most observations indicate an enhancement between 1-4% and 10-14% (27% of the sample for each range). The spread is small with all results indicating an enhancement around the 1-19% enhancement range. It should be noted that the findings for the two nanofluids is in agreement with the findings of analysis Level 1, as presented in Figure 2.3.

Proposed physical mechanism for anomalous heat transfer

Conduction/convection/mixed mode heat transfer studies

Al_2O_3-water nanofluids (29 observations):

a) Brownian motion (28% of the sample).
b) Brownian motion combined with the aggregation and diffusion theory (28% of the sample).
c) Interfacial layer theory (Kapitza resistance) (17% of the sample).

Al_2O_3-EG nanofluids (13 observations):

a) Brownian motion (85% of the sample).
b) Interfacial layer theory (Kapitza resistance) (15% of the sample).

The most popular proposed mechanism is the Brownian motion of the nanoparticles. This is in agreement with the findings of Level 1 analysis presented in Figure 2.6. Some differences exist for the second and third most popular mechanisms, but both are the same as for the Level 1 analysis.

Pool boiling heat transfer and critical heat flux (12 observations)

The sample for the Al_2O_3-EG nanofluids was too small to give a credible statistical result. Hence, only the Al_2O_3-water nanofluid sample is presented. The most popular proposed mechanisms are:

a) Alteration of the heating surface due to deposition of nanoparticles (83.3% of the sample).
b) Brownian motion combined with the alteration of the heating surface due to deposition of nanoparticles (8.33% of the sample).
c) Deposition and aggregation theory combined with the diffusion and thermal conductivity (alone) (8.33% of the sample).

The alteration of the heating surface by the deposition of nanoparticles is the most popular proposed mechanism for the explanation of enhanced PBHT and CHF. This is in agreement with the findings of Level 1 analysis presented in Figure 2.7.

Scatter diagrams based on Level 2 analysis – indication of trends

Level 2 analysis allowed the formation of various scatter diagrams and two of the most representative diagrams are selected and can be seen in Figure 2.8 and Figure 2.9. Figure 2.8 presents the effect of nanoparticle concentration and size on conducting heat transfer for Al_2O_3-water nanofluids. Figure 2.9 shows the effect of nanoparticle concentration and size on the viscosity of the mixture for Al_2O_3-water nanofluids. The scatter diagram analysis provided vital information on the links between nanofluids parameters and their thermal performance. The following trends were derived:

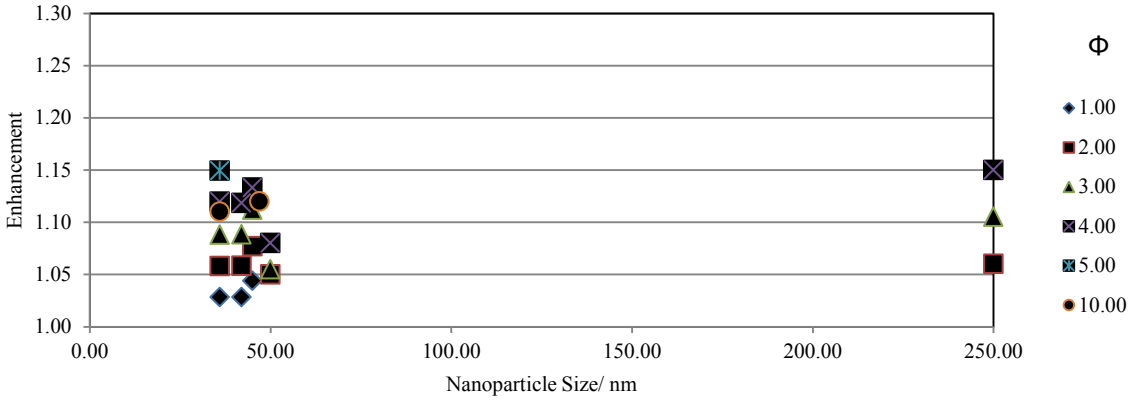

Figure 2.8. Sample of one of the scatter diagrams used to extract the trends. The diagram depicts various results of conductive heat transfer enhancement for the Al_2O_3-water type nanofluid at various concentrations (Φ) and at a temperature range of 290-310K.

a) The level of enhancement for the purely conductive case indicated an increasing trend with increasing nanofluid temperature and nanoparticle concentration, while there is a slight hint of the enhancement increasing with nanoparticle size (see Figure 2.8).
b) The effective viscosity of the mixture is enhanced and the findings show an increasing trend with decreasing fluid temperature, increasing volumetric concentration. There is also a slight hint of an effective viscosity increase with decreasing nanoparticle size (see Figure 2.9).
c) The level of enhancement for the convection/mixed heat transfer mode indicated an increasing trend with increasing temperature, volumetric concentration and decreasing nanoparticle size. Unfortunately, this trend can only be deduced by taking account the entire sample of scatter diagrams produced hence there is not a single representative diagram to display supporting it (contrary to the conductive and viscosity enhancement trends considered).

The trends appear to hold true up to the level where the nanofluid defining qualities (regarding particle suspension and chemical consistency properties as listed in section 2) are still satisfied and the nanoparticle concentrations remain in between the boundaries set in the methodology of observation collection (0.0001-10 vol%). It should be noted that the

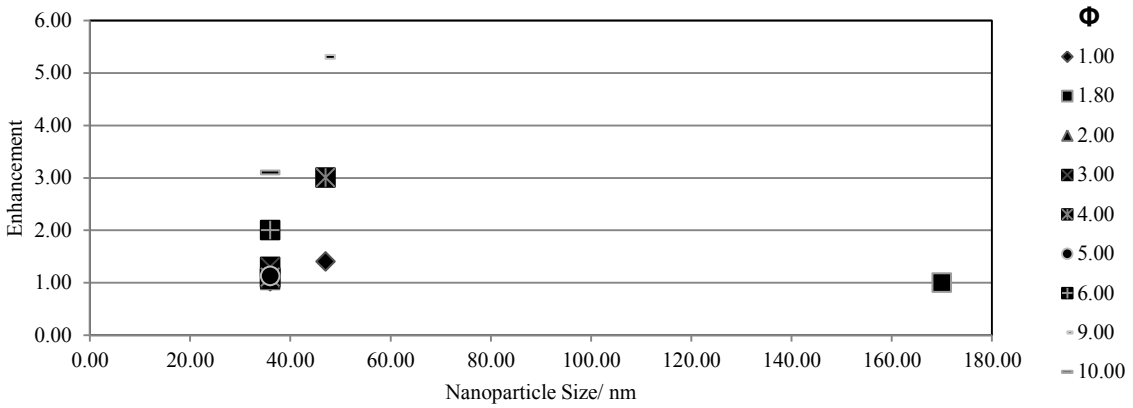

Figure 2.9. Sample of one of the scatter diagrams used to extract the trends. The diagram depicts various results of viscosity enhancement for the Al_2O_3-water type nanofluid at various concentrations (Φ) and at a temperature range of 290-310K.

observed trends cannot be quantified to evaluate the contribution of each by part property of the nanofluids. The observed trends will be discussed in the next subsection.

Unfortunately, the sample size was not large enough to extract trends regarding PBHT and CHF. Moreover, due to sample size limitation it was also impossible to determine nanoparticle material effects on thermal performance characteristics.

Discussion of findings from Level 2 analysis

The thermal performance assessment study of the second level agrees to a large degree with the findings of the first level. The cross correlation between the two levels ensures that the narrowed sample still falls into the reliability limits of the study.

The heat transfer enhancement studies for the Al_2O_3-water/EG generally indicated strong enhancement for the conduction and convection/mixed modes. More specifically, for the conduction heat transfer enhancement, the two nanofluids performed the same. For the convection/mixed heat transfer mode, the results for the two nanofluids do not correlate to the same level of enhancement for the statistically most popular proposed mechanism to explain the anomalous heat transfer. Both types of nanofluids agree on the Brownian motion of nanoparticles being most popular mechanism to explain the phenomena while small deviations appear regarding the secondary and tertiary most popular mechanisms.

In the light of this evidence, it can be concluded that the narrowing of the sample to perform the second level of the analysis can still be accounted creditable, as it generally agrees with the findings from the overall sample of Level 1. The findings regarding the thermal performance indicate that the basefluid material has little influence on the heat transfer enhancement in the conduction mode. On the contrary, the basefluid material seems to affect the performance for the convection/mixed heat transfer mode as discrepancies on the performance studies for the two materials were observed.

The observed trends on the effect of nanofluid properties to heat transfer of the trend formation can be accounted to the following for each subsection:

Trends for conduction enhancement

The findings indicate that conduction enhancement increases with increasing particle size, increasing nanoparticle concentration and mixture temperature. For this "less active" (compared to the convection/mixed) mode, Brownian motion becomes less pronounced; it appears that this trend is reasonable by referring partially to the second most popular mechanism found in the literature, namely aggregation and diffusion. By increasing the nanoparticle size and concentration, the highly conductive nanoparticles can diffuse the heat faster into the liquid as the thermal energy coefficient for solids is much larger than that of liquids. The increase of particle size provides longer and more effective ground for heat diffusion through each nanoparticle, while the increase of concentration increases the volume of the highly conductive solid available for heat transfer in the nanofluid. The enhancement increases with increasing temperature. This is accounted for by conventional heat transfer mechanisms. The increased temperature leads to statistically more energetic molecules. The statistical thermo mechanics for liquids and solids dictates that the intermolecular interactions will increase (collisions become more frequent and the energy involved per collision increases due to the average molecular speed augmentation). As a consequence, the heat transfer due to conduction is enhanced with increasing temperature. It should be noted that there must be a critical value of nanoparticle size and concentration beyond which the observed trend will reverse. However, there is no information available that will be able to demonstrate this assessment.

Trends for convection/mixed enhancement

The convection/mixed heat transfer mode is more "energetic" than conduction. Hence, Brownian motion of nanoparticles is more pronounced. The liquid molecules are allowed to move under the influence of buoyant forces arising from density variations inside the liquid. The heat transfer enhancement follows an increasing trend with decreasing nanoparticle size, increasing nanoparticle concentration and increasing temperature. For the latter, the same principle holds true as for conduction enhancement. For the former, at a given volumetric concentration of nanoparticles, the decrease in nanoparticle size results in an increase in the particle surface area available for collisions and at the same time an increase in the number of nanoparticles and a decrease in the corresponding mass per particle in a given volume of a nanofluid (the mass reduction per particle is much smaller compared to the gain of free surface area available for collisions). The increased surface area and number of nanoparticles results into an increased number of collisions between the basefluid molecules and the nanoparticles as well as between the nanoparticles themselves. Moreover, the decreased particle mass and increased collision count and hence overall collision energy involved leads to an increase of the mean free path (according to the most prevailing mechanism found in the literature) and energy content per nanoparticle. Brownian motion is hence augmented giving rise to large local density variations (and hence large buoyancy force variations) that, in turn, provide an enhancement in the convective/mixed heat transfer coefficient.

Trends for effective viscosity of nanofluid mixture

The effective viscosity follows an increasing trend with decreasing nanoparticle size, increasing nanoparticle concentration and decreasing temperature. For the latter, the decrease of temperature results in less energetic i.e. more sluggish liquid molecules. The decreasing temperature results in a decreasing kinetic energy of each molecule. The attractive/repulsive intermolecular forces become more pronounced giving rise to an enhancement in viscosity. Additionally, the decrease in particle size for a given volumetric concentration and volumetric amount of a nanofluid results in larger nanoparticle surface

area and number count, which consequently results in a rise in the shear stress observed between the solid-solid and solid-liquid interfaces inside the fluid – contrary to the shear thinning mechanism accounted by some researchers. This effect is also augmented by increasing the volumetric concentration of nanoparticles, since the overall nanoparticle surface area and number count of nanoparticles are increased as well.

2.6.3 Focus on simple experiments – Level 3 analysis

It was decided to investigate further the available information by considering publications, which reported simple and well-documented experiments. The simplicity of the experiments will allow focusing on the effects of nanoparticles, while other parameters introduced by the complexity (e.g. geometry) of the experiment will be eliminated. It is expected that these publications will enable a more generic view of the anomalous heat transfer characteristics of nanofluids, while it will also allow other researchers to reconstruct experiments in order to carry out further investigations on the notions and suggestions of previous studies.

It was decided to focus on publications that:

a) Include a physical experiment (i.e. eliminate those with computer simulations).
b) Consider simple experiments, where concise documentation is available, consisting of:
    i. Heat exchange via flow through a duct/pipe (simple pipe flow).
    ii. Heat exchange in stationary flow, i.e. transient hot wire experiments.

It was hence possible to construct new limited data sets and produce new histograms that enable the extraction of more targeted quantities. Results are presented where the sample size was sufficient to have a statistical importance (at least 10 observations).

Transient hot wire experiments

The transient hot wire experiments involve conventional conductivity measurements in a stationary fluid by means of the transient hot-wire apparatus method. This experimental procedure is considered to be one of the most accurate and simple methods used to deduce the thermal conductivity of nanofluids. The experiments are believed to provide an insight in the performance criteria without unnecessary experimental complexities that might affect the results acquired. Heat transfer studies and analysis to determine the proposed mechanisms for heat transfer were performed similarly to Level 1 and 2 of this investigation. No histograms are presented, however the numerical results are tabulated in the subsections following.

Heat transfer results

Heat transfer enhancement purely via conduction (17 observations):

There is strong indication that nanoparticles can enhance the heat transfer via conduction. All observations indicated an enhancement. Statistically, most observations indicate an enhancement in the range of 10-14% (41% of the sample) with a moderate spread. The performance indication is different to the 5-9% most occurring enhancement regime indicated by Level 1 but overall lies in the 1-24% general enhancement regime also indicated by Level 1.

Critical heat flux enhancement (13 observations):

All observations indicate an enhancement. Most observations show statistically an improvement of the CHF coefficient in the range of 100-200% (46% of the sample). This figure agrees with the performance value of the same heat transfer mode observed in Level 1.

Proposed mechanisms for heat transfer anomalies

Conduction/convection/mixed mode heat transfer (16 samples):

The statistics indicate that a large percentage of researchers explain the heat transfer enhancement by the interfacial layer theory and the Brownian motion theory in combination with the thermophoretic effect on nanoparticles (37.5% of the sample for each category). The Brownian motion theory comes third most popular (25% of the sample). Differences are found compared to the findings of the 1st level of analysis concerning the most occurring proposed mechanism for heat transfer anomalies.

Pool boiling heat transfer and critical heat flux enhancement (17 observations):

The analysis indicates that the majority of researchers (82.4%) account for the heat transfer enhancement through the alteration of the heating surface due to deposition of nanoparticles. The second proposed mechanism is the aggregation and diffusion in combination with the thermal conductivity enhancement alone theories (11.8% of the sample). The third most favoured mechanism refers to the EDL in combination with the aggregation and diffusion and the alteration of the heating surface due to the deposition of nanoparticles theories (5.9% of the sample). The most probable mechanism agrees with the findings of the first level however, the second and third most probable mechanisms do not agree with the first analysis level.

Simple pipe flow experiments

To investigate the convection/mixed heat transfer mode it was decided to narrow the sample to the experiments involving flow in a heated pipe. Temperature measurements are made and in conjunction with the already established physics governing flow in heated pipes it is possible to extract convective heat transfer performance data. This kind of experiments represents the simplest experimental arrangements around the convective mode performance assessment found in the literature. The outline of the section is similar

to the analysis performed for the transient hot wire experiments. No histograms are present but instead the results are presented in their numerical form.

Heat transfer results

Heat transfer enhancement via conduction (19 observations):

There is strong indication that nanofluids can enhance the conductive heat transfer mode. All observations indicated an enhancement. Most observations indicate a heat transfer enhancement in the range 5-9% (42% of the sample). This performance value agrees with the one found in analysis Level 1.

Heat transfer enhancement via convection/mixed heat transfer mode (28 observations):

The majority of the publications shows heat transfer enhancement in the range of 10-14% (14% of the sample). However, the spread of the enhancement results is large. There is also moderate statistical evidence that the addition of nanoparticles does not change the thermal performance of the heat transfer via convection/mixed mode (36% of the sample). The findings agree partially with the ones found in Level 1 (Level 1 produced a probable enhancement of 10-19%).

Rheological studies (23 observations)

There is strong indication that nanoparticles enhance the effective viscosity of the considered nanofluids (78% of the sample indicates an increase). Most publications have on average a viscosity enhancement between 5-14% (34% of the sample) and moderate evidence showing that the addition of nanoparticles has no effect on the effective viscosity of nanofluids (22% of the sample). The rheological studies of this section contain the vast majority of experiments of this kind in the entire observation sample hence a comparison with Level 1 cannot be performed.

Proposed mechanisms for the heat transfer anomalies

Conduction/convection/mixed mode heat transfer studies (13 observations)

The statistics indicate that the majority of researchers explain the enhancement of heat transfer through the Brownian motion of nanoparticles in combination with the aggregation and diffusion theory (53.8% of the sample), followed by the second most statistically occurring, which is the Brownian motion theory alone (30.8% of the sample). Therefore, the majority of the researchers believe that the Brownian motion is the main mechanism and this is in agreement with the results of Level 1.

Discussion of findings from Level 3 analysis

The thermal performance analysis of the narrowed down sample agreed moderately well with the analysis performed in Level 2 and the entire population of observations analysed in Level 1.

Specifically, for the transient hot-wire experiments, the conduction mode enhancement was found to lie close to the arithmetical values found in Level 1 and Level 2, while, for CHF, the enhancement was also found in agreement with the previous two levels of analysis. For conduction/convection/mixed heat transfer, the most popular proposed mechanisms are in relatively good agreement with those of Level 1 and 2 (the two most probable mechanisms are followed by a third – the thermophoretic effect theory). The deposition of nanoparticles on the heating surface was identified as the most popular mechanism in explaining the heat transfer anomalies for PBHT and CHF, which is also in good agreement with the findings of Level 1 and 2 analysis.

For the simple pipe flow experiments, the heat transfer enhancement via pure conduction and convection/mixed modes were in good agreement with those of Level 1 and Level 2 analysis. The most popular mechanism to explain the observations was the augmented Brownian motion in combination with the aggregation and diffusion mechanism, which again are in good agreement with the results of the levels 1 and 2 analysis.

Apart from the examination of the heat transfer performance, the current study examined the correlation between several controlling parameters and nanofluid thermal performance in order to investigate if the trends were the same as those of Level 2 analysis. The five parameters under investigation were the nanofluid type (basefluid and nanoparticle materials), the nanoparticle size, shape and concentration along with the flow type (stationary/turbulent/laminar flow) and nanofluid temperature. The analysis yielded no correlation between the parameters associated with this sample even though the sample size appears arithmetically sufficient.

The reason for the absence of any correlation between the observations and their by part properties was further investigated. It was discovered that the combination of the different parameters resulted in a variety of different experimental conditions, thus any comparison of any individual parametric effect was impossible as the sample became too small to study. At the same time, it was possible to indirectly deduce that the investigated five parameters play an important role in the emerging thermal performance of nanofluids. Finally, the 3rd level of analysis pointed out that despite the large sample of observations collected from publications for this literature review, no study was performed to take into account simultaneously all five parameters and their effects on the thermal performance of nanofluids.

2.7 Nanoemulsions

Nanoemulsions are a type of fluids that bear similarities with nanofluids. They emerged recently in the literature and have been attracting attention from the research community. Nanoemulsions usually comprise of an insoluble mixture of droplets with a single or a soluble mixture of fluid(s) as the base/carrier fluid, i.e. fluid-in-fluid mixtures. This is in contrast to the broader definition of the two phase nature of nanofluids (solids-in-fluid mixtures). The most common formation of nanoemulsions arises from a stable suspension of droplets of one of the main constituents into the other(s) at various concentrations where the stability of the emulsion is still ensured.

The droplets have sizes of the nanoscale order and their stability is ensured by means of surfactants (contrary to nanofluids where the stability can also be ensured without the need of a surfactant). This kind of fluids exhibited heat transfer augmentation effects in conduction studies. Thermal enhancement up to 52% was reported upon testing a nanoemulsion mixture of water-in-FC72 oil [134], while experimentation with nanoemulsions of oil in a binary mixture of H_2O/LiBr [135] and water in n-decane [136] indicate augmentations of 3.6% and very little augmentation to suggest any heat transfer potentials respectively.

One of the most appealing aspects of nanoemulsions is that they can be mass produced using cheap emulsification techniques and the emulsion can hold the carrier fluid's electrical properties while the suspension stability (under specific conditions) can be larger compared to their conventional two phase nanofluid counterparts. One of their major drawbacks is that the heavy use of surfactants to achieve mixture stability leads to hysteresis phenomena in the thermal performance of these fluids. An additional issue – this time to be foreseen from the literature review analysis on nanofluids – is that the stability of the nanoemulsion is probably going to be endangered in high temperature heat transfer as the conventional surfactant chemical composition at those temperatures changes irreversibly (surfactants are destroyed). All in all, the area of thermal nanoemulsion performance is rather immature to reach to conclusions regarding the thermal performance of such fluids, since not enough experiments have been performed up to date to quantify creditable statistics.

2.8 Conclusions

A literature review was performed, which statistically analysed a large amount of literature regarding the anomalous heat transfer modes exhibited by nanofluids. Three levels of analysis were selected. The first one allowed the extraction of results concerning general heat transfer characteristics and performance of nanofluids. The second one focused on revealing any possible trends linking the heat transfer performance of certain nanofluids

with their by part parameters. The third level revealed the parameters that appear to control the thermal performance of nanofluids and indirectly indicated the current research needs to enable reaching a more conclusive result. All three levels of analysis agreed to a large degree on the choice of proposed mechanisms to explain the anomalous heat transfer, as well as on the thermal performance of nanofluids for different heat transfer modes. This indicates that both diminished sample sets of Level 2 and Level 3, created from the bulk population of publications, were reliable to proceed with the extraction of statistical results.

The statistical analysis of thermal performance indicated that there is a notable enhancement for conduction, convection/mixed, PBHT and CHF heat transfer modes. The level of enhancement varies for each sub set with the purely conductive mode showing the least enhancement (around 5-9% most frequently observed), the convection/mixed mode a moderate enhancement (around 10-14%), the PBHT mode a higher enhancement of 40-44%, while the CHF demonstrated the highest enhancement (100-200%). For some of the considered heat transfer modes, heat transfer coefficient deterioration or no effect were also recorded; however, these occurrences were low.

For the explanation of the enhancement related to conduction, convention/mixed heat transfer modes, the most popular theories revolve around the Brownian motion of nanoparticles, the interfacial liquid layering (Kapitza resistance) theory, the aggregation and diffusion theory or simply a combination of all three.

For PBHT and the CHF, the most commonly proposed mechanisms are the alteration of the heating Surface by deposition of nanoparticles along with the passive/active mode theories (i.e. heat transfer via the augmentation of infrared radiation in the near field range).

The sample set of the Level 2 analysis indicated that for the purely conductive mode, the basefluid material has negligible effect to the enhancement of heat transfer. It was also possible to define trends, linking properties of nanofluids with their thermal performance as follows:

a) The level of enhancement for the purely conductive case indicated an increasing trend with increasing nanofluid temperature and nanoparticle concentration, while there is a slight hint of enhancement with increasing nanoparticle size.

b) The level of enhancement for the convection/mixed heat transfer mode indicated an increasing trend with increasing temperature, volumetric concentration and decreasing nanoparticle size.
c) The effective viscosity of nanofluids increases with decreasing temperature of the fluid and increasing volumetric concentration. There is also a slight hint of the effective viscosity increase with decreasing nanoparticle size.

The trends remain valid up to the degree where the nanofluid defining qualities (regarding particle suspension and chemical consistency properties as listed in section 2.3) are still satisfied and the nanoparticle concentrations remain in between the boundaries set in the methodology of observation collection (0.0001-10 vol%). The most popular mechanisms proposed in the literature to explain the heat transfer anomalies observed supported the trend behaviour observed.

Based on the findings of the statistical analysis of the literature, some recommendations for future research are provided below:

a) The final level of analysis, Level 3, outlined the five apparent parameters controlling thermal performance. Those are the nanofluid type (basefluid and nanoparticle materials), the nanoparticle size, shape and concentration, the flow type (stationary/turbulent/laminar flow) and lastly the nanofluid temperature. Level 3 analysis indicated that no parametric study has been performed that takes into account all five parameters noted above in order to evaluate their contribution on the thermal performance of nanofluids.
b) The review demonstrated that, even though attempts were frequently made to ensure that the quality criteria of the prepared nanofluids were satisfied prior the experiments, no attempt has been presented to re-examine the nanofluids after or during experiments – with the exceptions of some cases of pool boiling or CHF investigations or micro channel clogging investigations due to nanofluids. As a result, it is doubtful whether the nanofluid properties (e.g. nanoparticle size) remain the same during or after experiments.

c) No study has been performed to quantify any erosion effects during long term operation of nanofluids heat / cooling circuits.
d) The mechanism responsible for the observed heat transfer enhancement has not been verified experimentally. This is an important step for the optimisation of the performance of nanofluids and the development of appropriate computational models to describe their behaviour.
e) A larger amount of experimental studies are related to conduction and less is available for convection, pool boiling and CHF modes. Therefore, more emphasis on the effect of the nanofluids on the flow structures for these modes should also be considered in comparison to the basefluid.

Finally, a brief consideration of a type of fluid that bears similarities to nanofluids and might in the future be part of the broader nanofluid category has been examined. Nanoemulsions are single-phase liquid-into-liquid mixtures that can potentially be of interest due to their abnormal thermal performance. Unfortunately, not enough experiments have been performed to allow statistical analysis of their performance.

2.9 Up to date comparison

The literature review statistical analysis, was initiated in 2009, took account, almost in its entirety, the literature available on nanofluids and required a year to complete. It is hence necessary to review the current and up to date literature to discover any possible discrepancies between the results obtained in the past with those currently present in the literature. It is also important to include work which has been distinguished for the gravity imposed throughout the years and might have not been possible to include at the time the statistical analysis took place.

A limited selection of 10 representative pieces of work is used to perform a short traditional literature review in this subsection [3, 137-145]. Beginning from the first chronological papers in our selection, the work of Xuan Y. et al. (2000)[144] formed correlations for predicting the thermal conductivity factor of nanofluids using experimental

data from transient hot wire measurements. Xuan Y. et al (2003)[145] investigated the convective heat transfer in nanofluids and discovered that the classical heat transfer correlations of pure fluids do not apply to nanofluids. The authors stressed the importance of performing more investigations on the fundamental features of heat transfer and flow performance of nanofluids. Additionally, the study indicated that the nanofluids tested exhibited remarkable enhancement of heat transfer with no pumping losses compared to their pure base fluids. Keblinsky P. et al. (2002)[140] suggested that the thermal properties of Nanofluids are ballistic rather than diffusive combined with clustering effects. Pustovalov V.K. (2005)[142] performed an experiment and managed to obtain analytical solutions for heat transfer inside and around metallic nanoparticles. Buonjiorno J. (2006)[138], in an order of magnitude analysis, proposed that the Brownian motion and Thermophoresis slip mechanisms are important and can be held accountable for giving rise to the anomalous heat transfer phenomena observed in nanofluids. Keblinsky P. et al. (2006)[141] proposed through a molecular dynamic simulation study that the Brownian motion does not seem to be responsible for the increased heat transfer observed in nanofluids. Eapen J. et. al (2007)[139] suggested that clustering and percolating amorphous like structure are responsible for giving rise to the thermal conductivity enhancement observed. Buonjiorno J. et al. (2009)[3] proposed that the heat transfer enhancement of nanofluids is not anomalous but could be explained and predicted by the effective medium theory. Venerus D.C. et al. (2010)[143] proposed that the effective viscosity of nanofluids changes significantly with nanoparticle concentration and concludes that, even by considering the heat transfer enhancement encountered in nanofluids, the associated pumping losses make nanofluids fail as coolants for engineering applications. The same authors suggest that the effective medium theory cannot explain some of the phenomena observed in their study. Finally, Babaei H. et al. (2013)[137] indicate that Brownian motion is insignificant in giving rise to the enhanced thermal conductivity encountered in nanofluids.

It is evident that the scientific community has yet to reach a definite and solid answer regarding the mechanisms that give rise to the phenomena observed in nanofluids. This is apparent from the work reviewed in this section. The disparity between the

different labs and research groups suggests that the statistical method followed in 2009 was and appears to still be the only impartial method to quantify the results from the large range of literature currently available. It will be most suitable to end this subsection by using a quote from the work of Venerus D.C. et al. (2010)[143]; "*The study of nanofluids as heat transfer fluids remains both an active and controversial field of research*".

Table 2.3. Index number table.

Index number	Proposed augmentation mechanism theory	Experimental apparatus
-	none mentioned	
1	Brownian motion augmentation theory	Flow in tube or microchannel
2	Shear thinning behaviour of flows	transient hot-wire in stationary fluid
3	Interfacial layer theory (Kapitza resistance)	Specialised instrument for measuring thermal conductivities/viscosities etc.
4	Electrical Double Layer (EDL)	Theoretical/numerical investigation
5	Phonon transfer	Specialised application
6	Aggregation and diffusion	Flow over flat heated plates
7	Flattening of velocity profile due to viscosity	Quenching
8	Thermal conductivity enhancement alone	Heated wire
9	Deposition of nanolayer on heating surface	
10	Passive/active mode of heat transfer	
11	Long range structural disjoining pressure	
12	Near field radiation	
13	Thermophoresis forces	

Table 2.4. Experiments focusing on heat transfer of carbon nanotube – nanofluids.

Paper Reference No	k_{eff}/k_{NF} Conduction	keff/kNF Convection/ mixed	NP material	NP size, (nm unless specified)	BF material	Φ,(vol% unless specified)	T test, (K)	Experimental Apparatus Index No	Mechanism Index No	μ_{NF}/μ_{BF}	Flow Status	Effects of Gravity	PB HT	CH T	Notes
[146]	1.20	-	MWNT	10-20nm*1-2μm	water	2%wt	303	1	1	1	1,2	-	-	-	-
[146]	1.59	-	MWNT	10-20nm*1-2μm	water	1%wt	332	1	1	1	1,2	-	-	-	-
[147]	1.07	-	MWNT	15nm*30μm	DW	1%vol	-	2	-	-	-	-	-	-	-
[147]	1.13	-	MWNT	15nm*30μm	EG	1%vol	-	2	-	-	-	-	-	-	-
[147]	1.20	-	MWNT	15nm*30μm	DE	1%vol	-	2	-	-	-	-	-	-	-
[132]	1.18	-	MWNT	-	water	0.1%vol	-	1	2	<1	1,2	-	-	-	-
[132]	1.37	3.50	MWNT	-	water	0.5%vol	-	1	2	<1	1,2	-	-	-	-

Table 2.5. Experiments focusing on conduction heat transfer.

Paper Reference No	k_{eff}/k_{NF} Conduction	k_{eff}/k_{NF} Convection/ mixed	NP material	NP size, (nm unless specified)	BF material	Φ,(vol% unless specified)	T test, (K)	Experimental Apparatus Index No	Mechanism Index No	μ_{NF}/μ_{BF}	Flow Status	Effects of Gravity	PBHT	CHT	Notes
[49]	1.35	-	ZnO	77	3:2 mass EG: Water	4.0000	368	3	-	-	-	-	-	-	
[49]	1.42	-	ZnO	29		4.0000	368	3	-	-	-	-	-	-	
[49]	1.49	-	ZnO	29		7.0000	363	3	-	-	-	-	-	-	
[49]	1.60	-	CuO	29		6.0000	363	3	-	-	-	-	-	-	
[49]	1.69	-	Al_2O_3	53		10.0000	365	3	-	-	-	-	-	-	
[148]	1.07	-	Al_2O_3	150	water	1.0000	344	2	1	-	-	-	-	-	
[148]	1.10	-	Al_2O_3	11	water	1.0000	344	2	1	-	-	-	-	-	
[148]	1.15	-	Al_2O_3	47	water	1.0000	344	2	1	-	-	-	-	-	
[148]	1.29	-	Al_2O_3	47	water	4.0000	344	2	1	-	-	-	-	-	
[91]	1.11	-	Al_2O_3	36	water	10.0000	294	2	-	-	-	-	-	-	not large differences generally found in this experiment with varying T, Φ and material
[91]	1.12	-	Al_2O_3	47	water	10.0000	294	2	-	-	-	-	-	-	
[91]	1.11	-	CuO	29	water	10.0000	294	2	-	-	-	-	-	-	average temperature used (very narrow T range)hence very narrow change in results found (average will be used again). Note LARGE viscosity increase with ΔT around 10K
[80]	1.05	-	TiO_2	21	water	2.0000	294	2	-	+5-15%	-	-	-	-	
[149]	1.24	-	Cu_2O		water	-	294	2	-	-	-	-	-	-	
[150]	-	-	-	-	-	-	-	-	1	-	-	-	-	-	theoretical/numerical investigation
[75]	1.11	-	Al_2O_3	150	water	1.0000	334	2	3	-	-	-	-	-	averaged values used
[75]	1.12	-	Al_2O_3	80	EG	1.0000	334	2	3	-	-	-	-	-	
[75]	1.12	-	Al_2O_3	80	water	1.0000	334	2	3	1.82	-	-	-	-	
[75]	1.18	-	TiO_2	15	EG	5.0000	334	2	3	-	-	-	-	-	
[75]	1.37	-	Al	80	Engine Oil	3.0000	334	2	3	-	-	-	-	-	
[75]	1.45	-	Al	80	EG	5.0000	334	2	3	-	-	-	-	-	
[75]	2.60	-	CNT	0	Engine Oil	1.0000	334	2	3	-	-	-	-	-	
[75]	-	-	TiO_2	15	water		334	2	3	1.85	-	-	-	-	
[72]	>1	-	-	-	-	-	-	-	-	-	-	-	-	-	theoretical/numerical investigation
[121]	1.08	-	Au	17	water	0.0003	335	4	1, 4	-	-	-	-	-	-
[121]	1.10	-	Al_2O_3	150	water	4.0000	344	4	1, 4	-	-	-	-	-	-
[121]	1.12	-	Al_2O_3	47	water	1.0000	344	4	1, 4	-	-	-	-	-	-
[121]	1.24	-	Al_2O_3	47	water	1.0000	344	4	1, 4	-	-	-	-	-	-
[115]	1.14	-	Cu	10	EG	0.5500	-	-	3	-	-	-	-	-	-
[115]	1.18	-	Fe	10	EG	0.5500	-	-	3	-	-	-	-	-	
[151]	1.15	-	Al_2O_3	35	EG	5.0000	-	-	-	-	-	-	-	-	
[151]	1.20	-	CuO	35	EG	4.0000	-	-	-	-	-	-	-	-	
[151]	1.40	-	Cu	10	EG	0.3000	-	-	-	-	-	-	-	-	

[54]	>1	-	CuO	80*20	water	0.4000	-	1	-	>1 small	1,2	-	-	-	turbulent and laminar flow must be present (see pressure diagrams - kick after a point indication of flow turning into turbulent with increased pressure losses). Furthermore, increase in performance observed under specific conditions (e.g. Low flow rates and high temperatures)
[152]	1.05	-	Al_2O_3	150	water	5.0000	-	-	3	-	-	-	-	-	-
[152]	1.24	-	Al_2O_3	80	water	5.0000	-	-	3	-	-	-	-	-	theoretical/numerical investigation
[153]	1.12	-	Al_2O_3	38	water	5.0000	-	-	-	-	-	-	-	-	layering theory investigated and found inadequate to account for the results obtained
[124]	>1	-	CuO	28.6	water	4.0000	-	-	1	>1	-	-	-	-	theoretical/numerical investigation
[66]	1.07	-	SiO_2	9	water	14.6000	294	2	-	-	-	-	-	-	very high concentrations used up to 30%. Used the lowest ones investigated to have a more concise records for comparison with the other papers reviewed. Moreover paper supports that there is no solid indication of anomalous increase in the thermal conductivities of NF
[154]	1.15	-	Al_2O_3	38.4	water	1.0000	320	-	1,3,5	-	-	-	-	-	-
[154]	1.22	-	Al_2O_3	38.4	water	4.0000	320	-	1,3,5	-	-	-	-	-	theoretical/numerical investigation
[154]	1.35	-	Cu	10	EG	2.0000	303	-	1,3,5	-	-	-	-	-	
[154]	1.20	-	CuO	15	EG	5.0000	-	-	3	-	-	-	-	-	
[154]	1.80	-	Cu	3	EG	5.0000	-	-	3	-	-	-	-	-	
[155]	2.50	-	CNT	2*54	OIL	1.0000	-	-	3	-	-	-	-	-	
[84]	1.23	-	Al_2O_3	35	water	5.0000	-	-	3	-	-	-	-	-	-
[84]	1.25	-	CuO	35	water	4.2000	-	-	3	-	-	-	-	-	-
[84]	1.30	-	Al_2O_3	35	EG	6.0000	-	-	3	-	-	-	-	-	average value used
[34]	1.30	-	Al	90	water	5.0000	324	3	1, 6	-	-	-	-	-	-
[120]	1.03	-	Au Citrate	15.0000	toluene	0.0001	304	-	-	-	-	-	-	-	Surface Coating
[120]	1.05	-	Au Thiolate	3.5000	toluene	0.0050	334	-	-	-	-	-	-	-	
[120]	1.05	-	Au Citrate	15.0000	toluene	0.0003	304	-	-	-	-	-	-	-	
[120]	1.05	-		15.0000	toluene	0.0001	334	-	-	-	-	-	-	-	
[120]	1.07	-	Au Thiolate	3.5000	toluene	0.0080	334	-	-	-	-	-	-	-	
[120]	1.07	-		3.5000	toluene	0.0110	304	-	-	-	-	-	-	-	

[120]	1.08	-	Au Citrate	15.0000	toluene	0.0003	334	-	-	-	-	-	-	-	
[120]	1.09	-	Au Thiolate	3.5000	toluene	0.0110	334	-	-	-	-	-	-	-	
[156]	>1	-	-	-	-	-	-	-	1,3	-	-	-	-	-	theoretical/numerical investigation - small size, large Φ, large enhancement
[110]	>1	-	-	-	-	-	-	-	1	-	-	-	-	-	
[157]	>1	-	-	-	-	-	-	-	1	-	-	-	-	-	theoretical/numerical investigation - Brownian dynamics simulation - small size, large Φ, large enhancement
[41]	1.05	-	Al_2O_3	50	water	2.0	298	-	-	-	-	-	-	-	suspected aggregation at lower NP sizes in this experimental work performed, that's why the conductivity increase for increasing NP size. Authors explain this by implying that the decrease in the NP size leads to increased phonon scattering - decreased NP conductivity
[41]	1.06	-	Al_2O_3	50	water	3.0	298	-	-	-	-	-	-	-	
[41]	1.06	-	Al_2O_3	250	water	2.0	298	-	-	-	-	-	-	-	
[41]	1.08	-	Al_2O_3	50	water	4.0	298	-	-	-	-	-	-	-	
[41]	1.09	-	Al_2O_3	50	EG	2.0	298	-	-	-	-	-	-	-	
[41]	1.09	-	Al_2O_3	250	EG	2.0	298	-	-	-	-	-	-	-	
[41]	1.09	-	Al_2O_3	50	EG	3.0	298	-	-	-	-	-	-	-	
[41]	1.11	-	Al_2O_3	250	water	3.0	298	-	-	-	-	-	-	-	
[41]	1.14	-	Al_2O_3	250	EG	3.0	298	-	-	-	-	-	-	-	
[41]	1.15	-	Al_2O_3	250	water	4.0	298	-	-	-	-	-	-	-	
[122]	1.02	-	Al_2O_3	45	EG	1.0	295	-	-	-	-	-	-	-	3ω method used
[122]	1.03	-	Al_2O_3	45	EG	2.0	295	-	-	-	-	-	-	-	
[122]	1.04	-	Al_2O_3	45	water	1.0	295	-	-	-	-	-	-	-	
[122]	1.08	-	Al_2O_3	45	EG	3.0	295	-	-	-	-	-	-	-	
[122]	1.08	-	Al_2O_3	45	water	2.0	295	-	-	-	-	-	-	-	
[122]	1.10	-	Al_2O_3	45	EG	4.0	295	-	-	-	-	-	-	-	
[122]	1.11	-	Al_2O_3	45	water	3.0	295	-	-	-	-	-	-	-	
[122]	1.13	-	Al_2O_3	45	water	4.0	295	-	-	-	-	-	-	-	
[82]	>1	-	-	-	-	-	-	-	1	-	-	-	-	-	theoretical/numerical investigation
[53]	1.1	-	Ag	60	water	0.3	424	2	1, 13	1.1	1	-	-	-	-
[53]	1.15	-	Ag	60	water	0.6	424	2	1, 13	1.4	1	-	-	-	-
[53]	1.25	-	Ag	60	water	0.9	424	2	1, 13	1.6	1	-	-	-	-
[53]	1.40	-	Ag	60	water	0.3	464	2	1, 13	1.5	1	-	-	-	-
[53]	1.80	-	Ag	60	water	0.6	464	2	1, 13	1.9	1	-	-	-	-
[53]	2.30	-	Ag	60	water	0.9	464	2	1, 13	2.2	1	-	-	-	-

Table 2.6. Experiments focusing on convection heat transfer.

Paper Reference No	k_{eff}/k_{NF} Conduction	k_{eff}/k_{NF} Convection/ mixed	NP material	NP size, (nm unless specified)	BF material	Φ,(vol% unless specified)	T test, (K)	Experimental Apparatus Index No	Mechanism Index No	μ_{NF}/μ_{BF}	Flow Status	Effects of Gravity	PBHT	CHT	Notes
[158]	-	>1	Al_2O_3	-	engine oil	4.4wt	-	5	-	-	-	-	-	-	4WD rotary blade coupling
[158]	-	>1	CuO	-		4.4wt	-	5	-	-	-	-	-	-	

[101]	1.03	-	CuO	-	60:40 EG/ water	1.0	293	1	-	1.14	-	-	-	-	theoretical/numerical investigation
[101]	1.06	-	CuO	29		2.0	293	1	-	1.27	-	-	-	-	
[101]	1.09	-	CuO	29		3.0	293	1	-	1.69	-	-	-	-	
[101]	1.09	1.18	SiO_2	50		6.0	293	1	-	1.33	-	-	-	-	
[101]	1.09	-	SiO_2	20		6.0	293	1	-	1.41	-	-	-	-	
[101]	1.09	-	SiO_2	100		6.0	293	1	-	1.21	-	-	-	-	
[101]	1.12	-	CuO	29		4.0	293	1	-	2.12	-	-	-	-	
[101]	1.15	-	CuO	29		5.0	293	1	-	2.60	-	-	-	-	
[101]	1.21	1.75	CuO	29		6.0	293	1	-	3.49	-	-	-	-	
[101]	1.22	1.36	Al_2O_3	53		6.0	293	1	-	1.80	-	-	-	-	
[37]	-	>1	Al_2O_3	varying	water	4.0	-	1	-	-	-	-	-	-	theoretical/numerical investigation - 2 phase approach showed the smaller the diameter the greater the HTC
[65]	-	1.15	Al_2O_3	<100	water	4.0	314	1	6	0.00	-	-	-	-	theoretical/numerical investigation - 1 phase approach
[68]	-	-	TiO_2	21	water	0.2	-	1	-	-	2	-	-	-	negligible HT conduction increase
[18]	-	>1	Al_2O_3	45	50:50 EG/ water	-	-	2,3	-	<1	-	-	-	-	-
[57]	-	>1	Al_2O_3	36	water	2.8	-	5	-	-	2	-	-	-	jet impingement experiment
[159]	-	>1	Cu	42	water	1.0	-	-	-	-	2	-	-	-	theoretical/numerical investigation - 2 phase model
[160]	-	1.12	Al_2O_3	20	water	0.2	-	1	1,6	-	1	-	-	-	values recorded here for an averaged Pecklet number
[160]	-	1.13	Al_2O_3	20	water	0.5	-	1	1,6	-	1	-	-	-	
[160]	-	1.15	Al_2O_3	20	water	1.0	-	1	1,6	-	1	-	-	-	
[160]	-	1.22	Al_2O_3	20	water	1.5	-	1	1,6	-	1	-	-	-	
[160]	-	1.30	Al_2O_3	20	water	2.0	-	1	1,6	-	1	-	-	-	
[160]	-	1.35	Al_2O_3	20	water	2.5	-	1	1,6	-	1	-	-	-	
[42]	1.15	-	Al_2O_3	-	water	5.0	-	1	-	-	1	-	-	-	geometry dependent augmentation/deterioration
[42]	1.156342	geometry dependent	Al_2O_3	-	HFE 7100	5	-	1	-	-	1	-	-	-	
[77]	-	1.03	ZrO_2	50	water	1.32	-	1	-	-	1	-	-	-	-
[77]	-	1.27	Al_2O_3	50	water	6	-	1	-	7.2	1	-	-	-	-
[60]	-	1.08	Al_2O_3	30	water	0.3	-	1	1,7	-	1	-	-	-	-
[20]	-	>1	Al_2O_3	-	HFC134 a	0.1%wt	-	5	-	<1	-	-	-	-	MO: mineral oil used for lubrication inside HFC134a refrigerant fluid along with NPs. Conventionally Polyol-ester (POE) is used as a lubricant

[20]	-	>1	TiO_2	-		0.1%wt	-	5	-	<1	-	-	-	-	MO: mineral oil used for lubrication inside HFC134a refrigerant fluid along with NPs. Conventionally Polyol-ester (POE) is used as a lubricant. Same effect when using the same size Al_2O_3 NP
[73]	-	>1	Al_2O_3	-	water	0.1	-	5	-	-	-	-	-	-	theoretical/numerical investigation - 2 phase approach, smaller diameter, better effects, larger skin friction
[40]	1.04	1.11	Al_2O_3	150	water	4%wt	-	1	-	-	1	-	-	-	fully developed region values used here
[40]	1.06	1.25	Al_2O_3	45	water	4%wt	-	1	-	-	1	-	-	-	
[161]	-	>1	Al_2O_3	10	water	2	-	1	1	1	1	-	-	-	theoretical/numerical investigation - 2 phase approach - fully developed region values recorded here
[161]	-	>1	Al_2O_3	10	water	4	-	1	1	1	1	-	-	-	
[161]	-	>1	Al_2O_3	10	water	7	-	1	1	1	1	-	-	-	
[97]	-	1.12	Al_2O_3	100	water	1	-	1	1,6	1.419	1	-	-	-	
[97]	-	1.187	Al_2O_3	100	water	4	-	1	1,6	1.92	1	-	-	-	
[63]	-	1.32	Al_2O_3	170	water	1.8	300	1	-	1	1	-	-	-	average values used
[96]	-	>1	TiO_2	95	water	0.6	300	1	8	-	1	-	-	-	theoretical/numerical investigation 1phase and Langrange & Euler methods used
[96]	-	>1	TiO_2	145	water	0.6	300	1	8	-	1	-	-	-	
[96]	-	>1	TiO_2	210	water	0.6	300	1	8	-	1	-	-	-	
[162]	-	1.3	Cu	-	water	10	-	5	-	-	-	-	-	-	theoretical/numerical investigation
[162]	-	>1	Ag	-	water	-	-	5	-	-	-	-	-	-	
[162]	-	>1	Al_2O_3	-	water	-	-	5	-	-	-	-	-	-	
[162]	-	>1	CuO	-	water	-	-	5	-	-	-	-	-	-	
[162]	-	>1	TiO_2	-	water	-	-	5	-	-	-	-	-	-	
[22]	1.028192	1	Al_2O_3	36	water	1	300	1	-	1.025	1,2	-	-	-	No boiling values recorded
[22]	1.030973	1	Al_2O_3	36	HFE 7100	1	300	1	-	1.025	1,2	-	-	-	
[22]	1.058043	1	Al_2O_3	36	water	2	300	1	-	1.050	1,2	-	-	-	
[22]	1.061947	1	Al_2O_3	36	HFE 7100	2	300	1	-	1.050	1,2	-	-	-	
[22]	1.087894	1	Al_2O_3	36	water	3	300	1	-	1.075	1,2	-	-	-	
[22]	1.09292	1	Al_2O_3	36	HFE 7100	3	300	1	-	1.075	1,2	-	-	-	
[22]	1.119403	1	Al_2O_3	36	water	4	300	1	-	1.100	1,2	-	-	-	
[22]	1.125369	1	Al_2O_3	36	HFE 7100	4	300	1	-	1.100	1,2	-	-	-	
[22]	1.149254	1	Al_2O_3	36	water	5	300	1	-	1.124	1,2	-	-	-	
[22]	1.157817	1	Al_2O_3	36	HFE 7100	5	300	1	-	1.125	1,2	-	-	-	
[93]	1.028333	-	Al_2O_3	42	water	1	294	6	-	-	-	-	-	-	theoretical/numerical investigation
[93]	1.058333	-	Al_2O_3	42	water	2	294	6	-	-	-	-	-	-	
[93]	1.088333	-	Al_2O_3	42	water	3	294	6	-	-	-	-	-	-	
[93]	1.118333	-	Al_2O_3	42	water	4	294	6	-	-	-	-	-	-	

[123]	-	<1	Al_2O_3	43.5	water	1	-	5	-	-	-	-	-	-	
[123]	-	<1	CuO	11.05	water	1	-	5	-	-	-	-	-	-	
[123]	-	<1	JS Clay discs	25diax1thickness	water	1	-	5	-		-	-	-	-	
[114]	-	>1	Cu	100	water	-	-	6	-	-	1	-	-	-	

Table 2.7. Experiments focusing on natural convection heat transfer.

Paper Reference No	k_{eff}/k_{NF} Conduction	k_{eff}/k_{NF} Convection/ mixed	NP material	NP size, (nm unless specified)	BF material	Φ_s(vol% unless specified)	T test, (K)	Experimental Apparatus Index No	Mechanism Index No	μ_{NF}/μ_{BF}	Flow Status	Effects of Gravity	PBHT	CHT	Notes
[28]	-	>1	-	-	-	-	-	2	-	-	-	significant	-	-	theoretical/numerical investigation
[52]	-	>1	Al_2O_3	60	water	0.3-2%	-	1	-	1	-		-	-	
[100]	-	>1	Al_2O_3	-	water	-	-	2	-	-	-		-	-	
[100]	-	>1	Cu	-	water	-	-	2	-	-	-		-	-	
[100]	-	>1	TiO_3	-	water	-	-	2	-	-	-		-	-	
[67]	-	>1	-	-	-	-	-	5	-	-	-		-	-	
[90]	-	>1	Ag	-	water	-	-	5	-	-	-		-	-	
[90]	-	>1	Al_2O_3	-	water	-	-	5	-	-	-		-	-	
[90]	-	>1	Cu	-	water	-	-	5	-	-	-		-	-	
[90]	-	>1	CuO	-	water	-	-	5	-	-	-		-	-	
[90]	-	>1	TiO_2	-	water	-	-	5	3	-	-		-	-	
[163]	-	>1	Cu	10	water	-	-	2	1,3,6	-	-		-	-	

Table 2.8. Experiments focusing on PBHT and CHF heat transfer.

Paper Reference No	k_{eff}/k_{NF} Conduction	k_{eff}/k_{NF} Convection/ mixed	NP material	NP size, (nm unless specified)	BF material	Φ_s(vol% unless specified)	T test, (K)	Experimental Apparatus Index No	Mechanism Index No	μ_{NF}/μ_{BF}	Flow Status	Effects of Gravity	PBHT	CHT	Notes
[25]	-	-	Ag - silver sphere	35	water	0.5%wt	364	7	9	-	-	-	<1	-	initially washed sphere quenched from 974K
[25]	-	-		35	water	1%wt	364	7	9	-	-	-	<1	-	
[25]	-	-		35	water	2%wt	364	7	9	-	-	-	<1	-	
[25]	-	-		35	water	4%wt	364	7	9	-	-	-	<1	-	
[25]	-	-		25	water	0.125%wt	364	7	9	-	-	-	>1	-	
[25]	-	-		25	water	0.25%wt	364	7	9	-	-	-	>1	-	
[25]	-	-		25	water	0.5%wt	364	7	9	-	-	-	>1	-	
[25]	-	-		25	water	1%wt	364	7	9	-	-	-	>1	-	
[27]	-	-	Al_2O_3	220	Trypan Blue	-	-	5	10	-	-	-	>1	-	-
[27]	-	-	Au (Shells)	170		-	-	5	10	-	-	-	>1	-	-
[27]	-	-	Au (spheres)	30		-	-	5	10	-	-	-	>1	-	-
[27]	-	-	Au (Rods)	14*45		-	-	5	10	-	-	-	>1	-	-
[59]	-	-	Al_2O_3	47	water	0.1	-	8	9	-	-	-	-	1.78	unwashed heating surface values used here. Max values used. When CHT>1 then PBHT is inferred to be >1 as well
[59]	-	-	SiO_2	90	water	0.1	-	8	9	-	-	-	-	2.00	
[59]	-	-	TiO_2	85	water	0.1	-	8	9	-	-	-	-	2.75	
[59]	-	-	TiO_2	85	water	1	-	8	9	-	-	-	-	2.70	
[164]	-	-	Al_2O_3	47	water	0.1	374	8	9	-	-	-	-	1.75	

[164]	-	-	TiO_2	85	water	0.1	374	8	9	-	-	-	-	2.15	
[81]	-	-	-	-	-	-	-	8	11	-	-	-	-	>1	theoretical/numerical investigation
[50]	-	-	Al_2O_3	30	water	1.25%wt	-	8	9	-	-	-	1.4	-	aggregation is observed with an effective particle size of around 270nm
[103]	-	-	Al_2O_3	25	water	2%wt	-	8	6,8	-	-	-	1.3	-	
[103]	-	-	SnO_2	55	water	3%wt	-	8	6,8	-	-	-	1.2	-	
[102]	-	-	Al_2O_3	38.8	water	0.1	304	7	9	-	-	-	-	1.50	Stainless Steel Sphere - SS, Zircalloy Sphere – Zry quenched from 1304K
[54]	-	-	Al_2O_3	38.8	water	0.1	304	7	9	-	-	-	-	2.37	
[102]	-	-	Diamond	165.4	water	0.1	304	7	9	-	-	-	-	1.08	
[102]	-	-	diamond	165.4	water	0.1	304	7	9	-	-	-	-	0.60	
[102]	-	-	SiO_2	32.9	water	0.1	304	7	9	-	-	-	-	1.32	SS sphere
[102]	-	-	SiO_2	32.9	water	0.1	304	7	9	-	-	-	-	1.54	Zry sphere
[95]	-	-	TiO_2	21	HCF 141b	0.05	-	8	-	-	-	-	<1	-	Heating surface washed after each trial
[165]	-	-	Al_2O_3	-	water	0.05 g/l	334	8	-	-	-	-	1	2.00	Heating surface washed after each trial
[6]	-	-	Al_2O_3	20	water	1	371	8	9	-	-	-	1.4	-	heavily agglomerated NF. If greatly sub cooled NF used there is degradation of heating wire
[24]	-	-	CuO	30	water	1%wt	-	8	9	-	-	-	1.25	1.50	Atmospheric Pressure
[24]	-	-	CuO	30	water	1%wt	-	8	4,6,9	-	-	-	2.5	3.00	Lowered Pressure
[56]	-	-	Al_2O_3	47	water	0.001	-	8	9	-	-	-	-	1.70	Saturated CHT
[56]	-	-	Al_2O_3	47	water	0.1	-	8	9	-	-	-	-	1.70	
[56]	-	-	TiO_2	23	water	0.1	-	8	9	-	-	-	-	2.00	
[87]	-	-	Al_2O_3	22.6	water	0.08%wt	374	8	9	-	-	-	-	1.50	
[87]	-	-	Al_2O_3	46	water	0.08%wt	374	8	9	-	-	-	-	1.45	
[87]	-	-	BiO_2	38	water	0.01%wt	374	8	9	-	-	-	-	1.33	

Table 2.9. Experiments focusing on rheological studies.

Paper Reference No	k_{eff}/k_{NF} Conduction	k_{eff}/k_{NF} Convection/ mixed	NP material	NP size, (nm unless specified)	BF material	Φ,(vol% unless specified)	T test, (K)	Experimental Apparatus Index No	Mechanism Index No	μ_{NF}/μ_{BF}	Flow Status	Effects of Gravity	PBHT	CHT	Notes
[109]	-	1.08	TNT	10X100	EG	1		-	1,2,6	1.35	-	-	-	-	high shear viscosity recorded here
[109]	-	1.15	TNT	10X100	EG	1.75		-	1,2,6	1.75	-	-	-	-	
[55]	-	-	Fe_2O_3 - PEO dispersant	30	water	3	299	-	2	1.015	-	-	-	-	high shear viscosity recorded here, averaged values
[55]	-	-	Fe_2O_3 - PVP dispersant	30	water	3	299	-	2	1.07	-	-	-	-	
[118, 127]	-	-	Al_2O_3	36	water	3	290	3	-	1.3	-	-	-	-	the effect of rising temperature reduces the effective viscosity. However, the values for augmented temperature for viscosity are not recorded here as they are
[118, 127]	-	-	Al_2O_3	36	water	6	290	3	-	2	-	-	-	-	
[118, 127]	-	-	Al_2O_3	36	water	10	290	3	-	3.1	-	-	-	-	
[118, 127]	-	-	Al_2O_3	47	water	1	290	3	-	1.4	-	-	-	-	
[118, 127]	-	-	Al_2O_3	47	water	4	290	3	-	3	-	-	-	-	
[118, 127]	-	-	Al_2O_3	47	water	9	290	3	-	5.3	-	-	-	-	
[118, 127]	-	-	CuO	29	water	1	290	3	-	1.35	-	-	-	-	

[118, 127]	-	-	CuO	29	water	4	290	3	-	2.5	-	-	-	-	a result of unstable and damaged NF due to the surfactant change of composition
[118, 127]	-	-	CuO	29	water	9	290	3	-	4	-	-	-	-	

Table 2.10. Various experiments not falling into the previous categories.

Paper Reference No	k_{eff}/k_{NF} Conduction	keff/kNF Convection/ mixed	NP material	NP size, (nm unless specified)	BF material	Φ,(vol% unless specified)	T test, (K)	Experimental Apparatus Index No	Mechanism Index No	μ_{NF}/μ_{BF}	Flow Status	Effects of Gravity	PBHT	CHT	Notes
[106]	1.4	-	CNC	15	water	4.2wt%	299	2	-	1.11	-	-	-	-	-
[21]	1.05	-	SiO_2	10	water	16	-	-	-	-	-	-	-	-	-
[21]	1.08	-	SiO_2	15	water	16	-	-	-	-	-	-	-	-	-
[21]	1.16	-	SiO_2	30	water	16	-	-	-	-	-	-	-	-	-
[119]	>1	>1	-	-	-	-	-	-	3,6,12	>1	-	-	-	-	theoretical/numerical investigation
[61]	-	>1	Al_2O_3	42.5	water	-	-	-	1,13	-	-	-	-	-	
[8]	-	1.60	SiC	170	water	3.7	320	1	1,13	>1	2	-	-	-	lower viscosity rather than using Al2O3
[26]	-	1.01	Al_2O_3	150	EG	0.5	294	-	1	-	-	-	-	-	theoretical/numerical investigation
[26]	-	1.03	Al_2O_3	150	EG	0.5	300	-	1	-	-	-	-	-	
[26]	-	1.03	Al_2O_3	150	EG	0.5	309	-	1	-	-	-	-	-	
[26]	-	1.05	Al_2O_3	150	EG	0.5	324	-	1	-	-	-	-	-	
[26]	-	1.06	Al_2O_3	150	EG	2	300	-	1	-	-	-	-	-	
[26]	-	1.11	Al_2O_3	11	EG	1	294	-	1	-	-	-	-	-	
[26]	-	1.12	Al_2O_3	150	EG	3	300	-	1	-	-	-	-	-	
[26]	-	1.13	Al_2O_3	11	EG	1	309	-	1	-	-	-	-	-	
[26]	-	1.16	Al_2O_3	11	EG	1	324	-	1	-	-	-	-	-	
[26]	-	1.17	Al_2O_3	60	EG	2	300	-	1	-	-	-	-	-	
[26]	-	1.35	Al_2O_3	60	EG	5	300	-	1	-	-	-	-	-	
[35]	-	1.10	Al_2O_3	80	water	2	-	-	1	-	-	-	-	-	
[35]	-	1.15	Cu	100	water	2	-	-	1	-	-	-	-	-	
[35]	-	1.55	Cu	100	water	5	-	-	1	-	-	-	-	-	
[69]	-	>1	Al_2O_3	20	water	2	-	5	1,9	-	-	-	>1	-	averaged values used. Thermosiphon experiment
[36]	-	>1	CuO	30	water	4	329	5	-	>1	2	-	-	-	-
[89]	-	-	Al	60	Ethanol	2	310	5	-	>1	-		>1	-	-
[74]	1.039539	>1	CuO	30	water	2	-	5	-	1.3	2	-	-	-	-
[74]	1.059308	>1	Al_2O_3	20	water	2.9	-	5	-	2.9	2	-	-	-	-
[74]	1.059308	>1	CuO	40	water	3	-	5	-	-	2	-	-	-	-
[74]	1.059308	>1	TiO_2	-	water	2.4	-	5	-	2	2	-	-	-	-
[74]	1.067545	>1	Al_2O_3	11	water	4	-	5	-	-	2	-	-	-	-
[74]	1.102142	>1	CuO	30	water	4	-	5	-	2	2	-	-	-	-
[74]	1.186161	>1	CuO	30	water	8	-	5	-	5.6	2	-	-	-	-

Chapter 3

Experimental Methodology

This chapter contains a description of the experimental methodology followed during this project. The experimental processes followed to determine the nanofluid quality can be found in section 3.1 followed by an absorbance experiment to determine the laser light interaction with the nanofluid in section 3.2. Section 3.3 contains a description of the experimental rig used for the PIV experiments while section 3.4 contains in detail the method and the analysis followed to acquire and process the experimental results.

3.1 Nanofluids quality assessment[1]

The nanofluids quality assessment is required to evaluate the mixing process employed, in particular the optimum sonication time required to produce a nanofluid of an acceptable quality. There are no specific guidelines on the sonication time in the literature; the sonication times vary from a few minutes to more than 12 hours in some cases [59, 146]. An Al_2O_3-water nanofluid with a nanoparticle volumetric concentration of 1% was tested.

[1] Parts of the work produced in this section were published in the public domain under references [166, 167].

The study was aiming to determine the optimum sonication time at which the fluid presented the best qualities as outlined in section 2.3 hence, five samples were prepared each with varying sonication times from 1 up to 5 hours using Method 1 (details of the preparation method can be found in the Appendix A). A visualisation of the agglomeration degree and characteristic agglomeration size was the primary focus of this study. An additional volumetric analysis of the sample would also be desirable using a DLS technique, however, this was currently beyond the experimentation limits of the study. Visualisation of the emerging diluted nanofluid was performed by placing a drop of nanofluid at 1ppm concentration on a carbon film and air drying it. The sample was then visualised using a JOEL 2010 TEM operating at 200kV according to [102]. The microscope was also able to perform in situ spectroscopic measurements in order to detect any impurities present in the sample.

Analysis of the nanofluid samples indicated that 5 hours of sonication create smaller and fewer agglomerates than shorter sonication times which was in agreement with the literature [197]. The visualisation comparison between a sample with a sonication time of 1 hour and 5 hours can be found in Figure 3.1 (figure appearing in [167]). The purity of the nano clusters was also determined to 94.8% (traces of Cu and C were detected however these were of the order of less than 2.6% for each element).

Despite the maximum practical time of sonication allowed, the samples still presented up to some degree agglomeration and sedimentation over extended relaxation times (no agitation) as no surfactant was used to stabilise the two-phase mixture. As such, the last step of the dilution process to a concentration of 1ppm for visualisation was performed following an agitation process. The results of this investigation verified the preparation process of the nanofluids that was used in the subsequent PIV experiments and indicate possible nanofluid deterioration issues to be taken into account in the experimental rig design (mainly a continuous nanofluid agitation process had to be included in the rig design to ensure nanofluid stability).

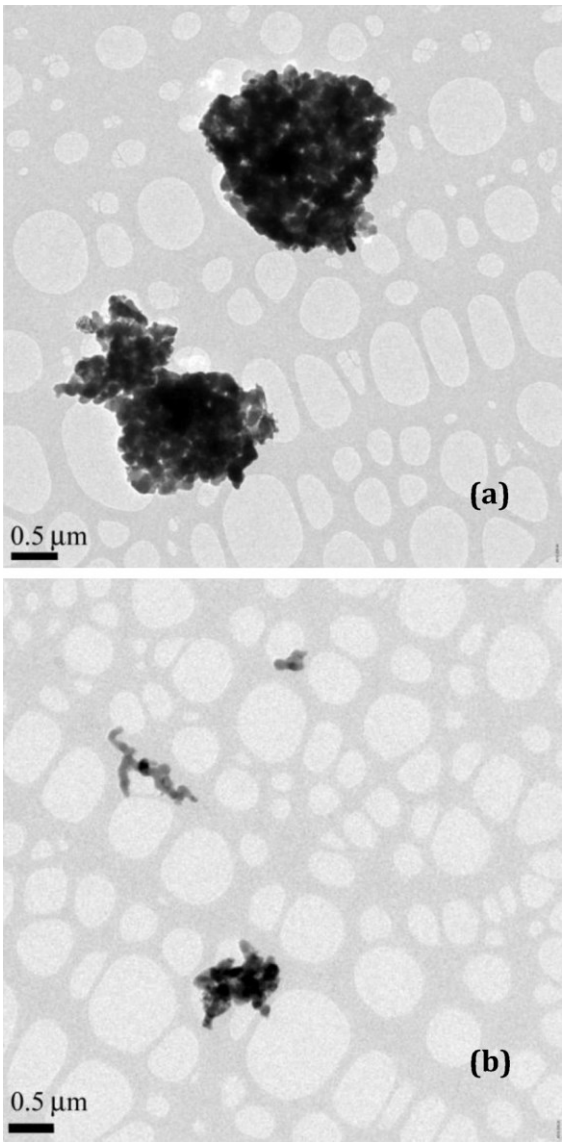

Figure 3.1. TEM images of Al_2O_3 agglomerates under a 3k magnification for a sonication time of 1 hour and 5 hours - images (a) and (b) correspondingly.

3.2 Nanofluid laser absorbance assessment

The literature is lacking of data regarding PIV experimentations with nanofluids. It was decided to assess these parameters via a Beer-Lambert absorbance experiment. The Beer-Lambert law relationship states that the absorbance of coherent light from a medium has a linear relationship with the molar concentration of the light scatterers inside the medium for the same light path distances. The law is valid, amongst other assumptions, for homogenous single phase mixtures with the light scatterers being in the molecular scale

and with the mixture exhibiting no visible turbidity. These assumptions do not hold true for the nanofluid tested. For the nanofluid case, the scatterers are the actual nanoparticles inside the tested water based nanofluids and hence it was crucial to test if their concentration is correlated with the Beer-Lambert law for absorbance. The data is vital to aid understanding and judging the applicability range of the PIV laser based method to be used in chapters 4 to 6.

A multistep nanofluid creation method was followed to create the samples as described in section 3.1 with a sonication time of 5hrs. The final sample was placed into a high optical quality spectrometer type cuvette (VWR, Type 100-OS macro cells with PTFE lids, Special Optical glass, Optical path Length: 40mm, Height: 45mm, Volume 1400µl, product number: 634-9016) where the laser measurements took place (probing signal path).

A Nd-Yag pulsed laser (Litron Nano T PIV) was used at a beam wavelength of 532nm. The pulse width of the laser was 7-9ns. The laser beam was split using a standard beam splitter into two beams in order to provide a reference signal (beam traversing through air) and a probing signal (beam traversing through the nanofluid). Two beam samplers where then used to sample the intensity of the probing and reference signal in order to avoid saturating the photodiode sensors (Figure 3.2). The complication of creating and recording a reference signal from each pulse is necessary as the power level and length of each successive laser pulse is inherently varying hence an averaging process to reduce random errors would have been impossible without it.

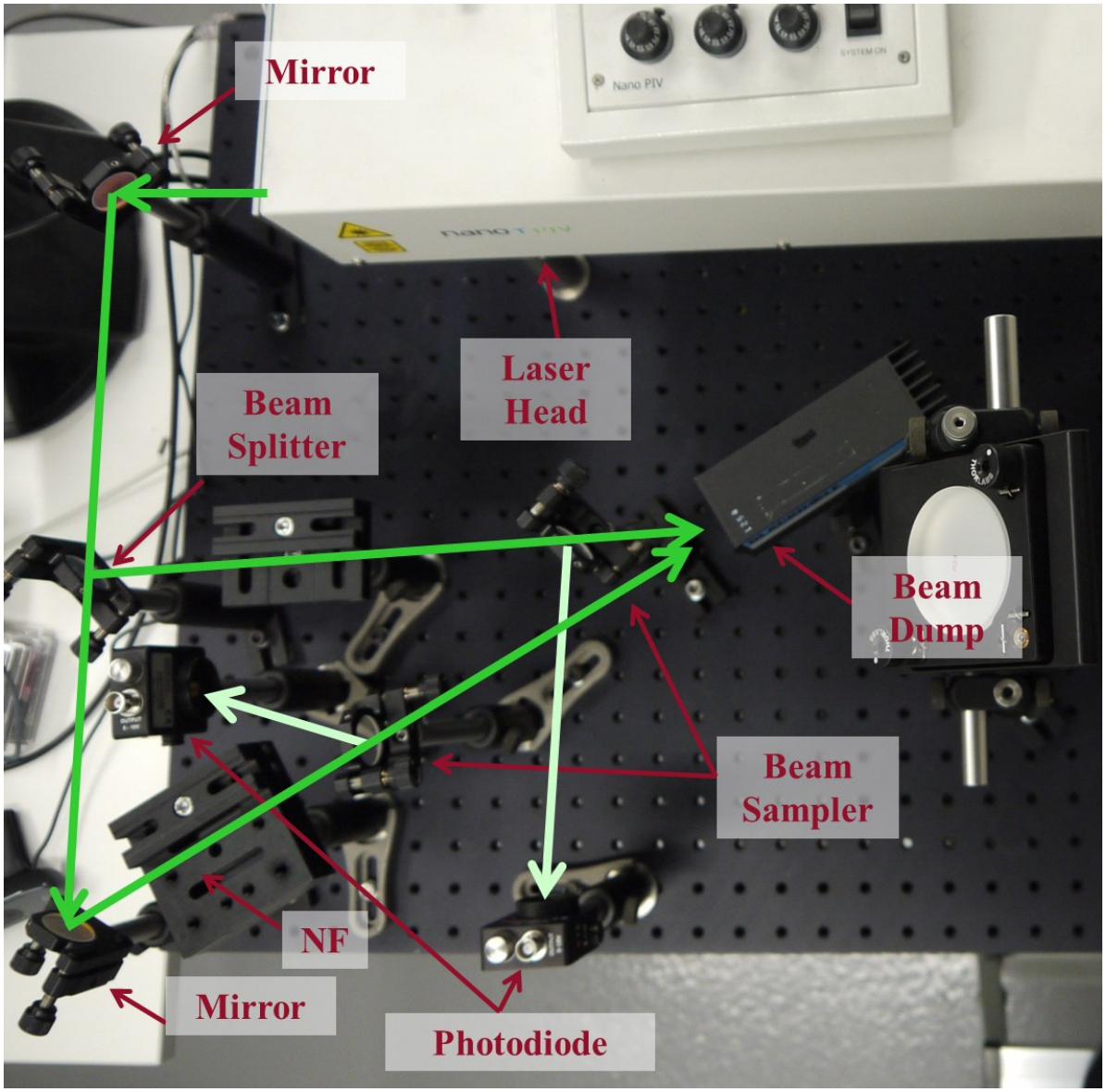

Figure 3.2. Laser light paths for the absorbance experiment. High and low intensity laser beams are depicted in darker and brighter green colours respectively.

The reference signal and probing signal intensities from the same pulse were recorded separately but simultaneously via two sensitive high speed photodetectors (Thorlabs High-Speed Photodetectors, Biased Si Detectors: 200-1100nm wavelength, 1ns Rise Time, 0,8mm^2 Sensor Area, Model number: DET10A/M) connected to an oscilloscope (Tektronix DPO4054).The oscilloscope was using the same triggering signal as the laser in order to synchronise the recording interval of the oscilloscope with the pulse output. An averaging process was used to collect the intensity readings from the photodetectors in volts.

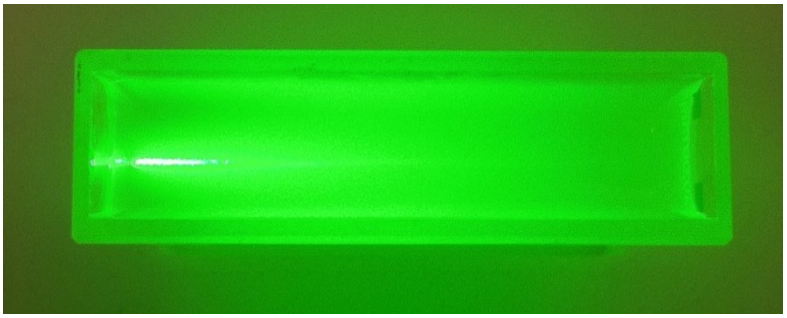

Figure 3.3. Laser beam path through the nanofluid filled cuvette (beam enters the cuvette from the left hand side).

A formula had to be defined in order to verify the Beer-Lambert law from the quantities recorded. The absorbance in liquids is represented by equation (3.1).

$$\mathrm{Ab} = -\log\left(\frac{I}{I_0}\right) = \gamma l \Phi \tag{3.1}$$

where,

Ab : absorbance

I : probing signal intensity reading

I_0 : probing signal initial power before travelling through the cuvette

γ : arbitrary constant

l : light path length

The paths of light for the laser pulses are less than a meter long in air and the optical components used to steer the beam are of high optical efficiency. It can hence be assumed that the loss of power to the surroundings of the travelling beams is negligible compared to the loss of power from the beam that passes through the nanofluid.

An offset exists between the two recorded intensities from the photodiodes. The offset (α) is arising mostly due to systematic errors and experimental set up constants on the optical component arrangement and alignment – for example the difference in the angle of incidence of the laser pulses on the photodiodes, the beam splitter intensity split up, the beam sampler orientation, the different impedance of the cables connecting the photodiodes to the oscilloscope etc. Random errors are reduced to a minimum by the use of averaging quantities. The systematic errors/constants are expected to create a fixed offset value α which can be determined via a calibration process. It can hence be inferred that with the absence of a cuvette (and therefore both the reference and probe pulses travelling

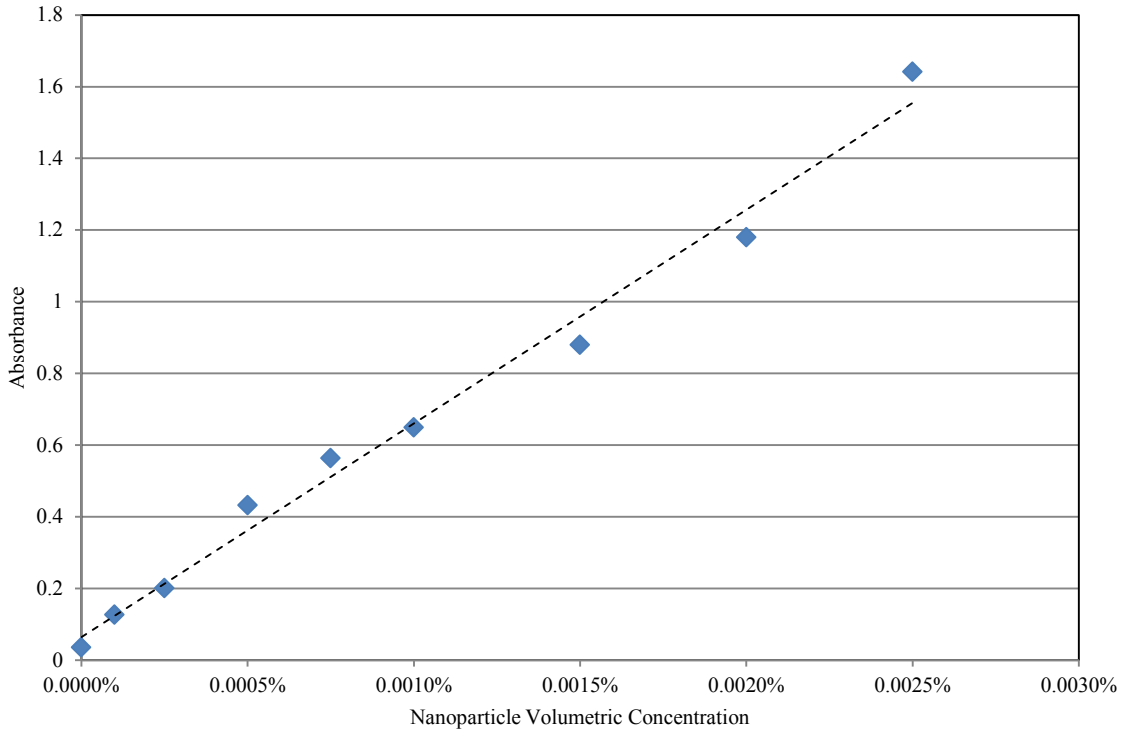

Figure 3.4. Plot of coherent laser light intensity absorbance with nanoparticle concentration for an Al_2O_3-water nanofluid.

through air) the reference signal intensity can be related to the probing signal intensity, which in this case is equal to the overall power of the probing beam before going through the cuvette. The offset between the two intensity readings recorded can be calculated via equation (3.2).

$$\alpha = I_{R_{cal}} - I_{cal} \tag{3.2}$$

where,

α : offset between the reference signal and attenuated signal through the nanofluid

$I_{R_{cal}}$: calibration reference signal intensity

I_{cal} : calibration probing signal intensity which is equal to I_0 for the calibration process

With the value for α calculated via equation (3.2) it is possible to calculate the pulse signal I_0 from equation (3.3).

$$I_0 = I_R + \alpha \tag{3.3}$$

where,

I_R : reference signal

Substituting equation (3.3) into equation (3.1) and simplifying results in equation (3.4).

$$Ab = \log\left(\frac{I_R+\alpha}{I}\right) = \gamma l \Phi \tag{3.4}$$

Samples with nanoparticle volumetric concentrations ranging from 0.0001% up to 0.0050% are tested. The limit of opacity for a laser beam with a maximum intensity of 120mJ (max attainable pulse output from the laser) is reached at a volumetric concentration of 0.003% at which the probing signal intensity was undetectable. It is expected that the limit of the allowable nanoparticle concentrations for the PIV measurement to be lower than the limit of opacity due to the sensitivity of the method used. The results are plotted in Figure 3.4 and satisfy the Beer-Lambert law linear relationships of light scattering and nanoparticle concentration. There is an uncertainty involved with the measurement however; the complexity of the experiment makes it very hard to calculate without spending a considerable amount of time in repeating the measurements and taking factors like laser beam and triggering jitter into account. These factors are of very low uncertainty and are not expected to change much the outlook of the experimental results. The linearity of the results though cannot be disputed.

3.3 PIV experimental rig[1]

The set up was designed to accommodate a HyperVapotron model, replicate the cold flow fields encountered in a real HyperVapotron device and allow the optical accesses required for the PIV measurements. Computational Fluid Dynamics (CFD) simulations aided the designing process for the HyperVapotron model and tank jet mixing apparatus.

[1] Parts of the work produced in this section were published in the public domain under references [166-169].

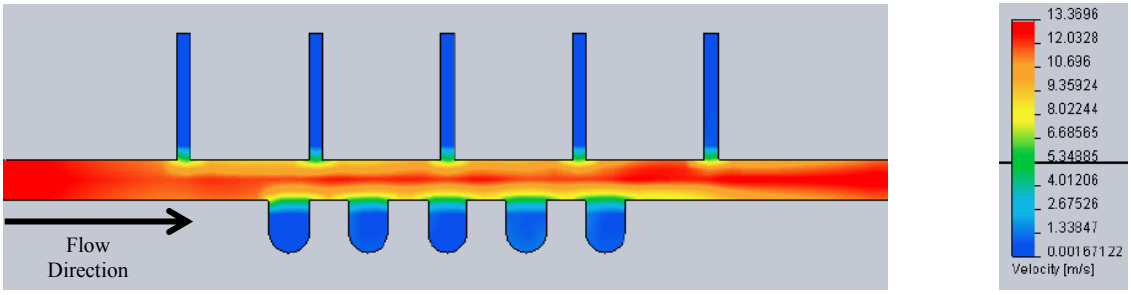

Figure 3.5. CFD graphics showing velocity profile inside one of the exact replicas of the mock HV designs containing the slotted rear plate (top side).

3.3.1 CFD calculations

The literature indicated that the thermal performance of the HyperVapotron devices shows linkage in between the channel height and width along with the fin height employed [167, 171, 172, 184, 191, 195]. However, there was no obvious non dimensional quantity to use in order to scale the proposed models. It was hence decided to follow the literature trends and keep the HyperVapotron channel width and fin size constant while altering the channel height. A fin height of 4mm is most commonly used in the literature and this was also used on the PIV model. The number of grooves was limited to five to be able to keep the cost of manufacturing low.

During the rig design process it was required to perform a range of CFD

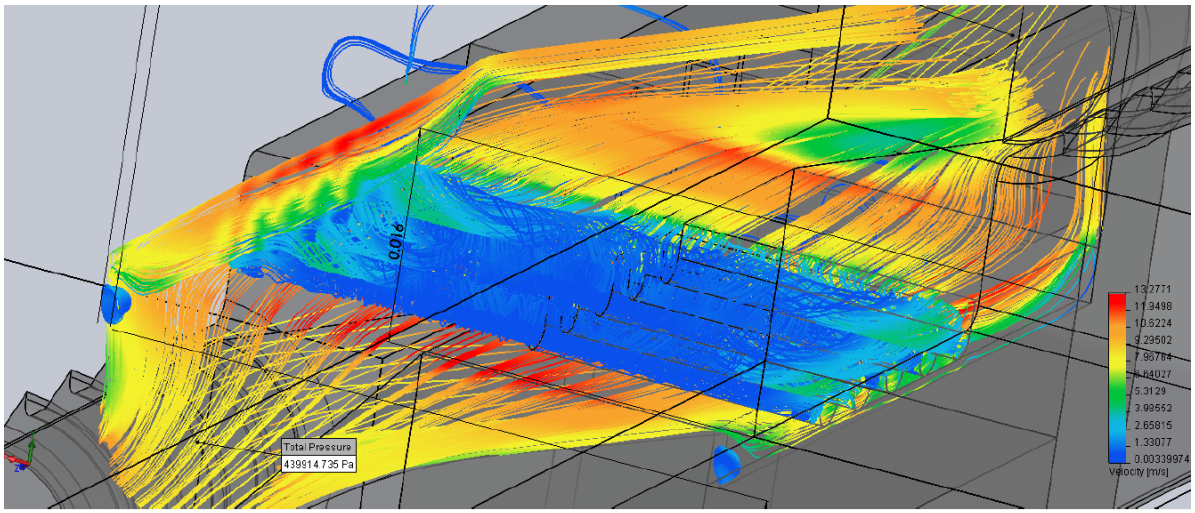

Figure 3.6. CFD simulation graphics showing velocity contoured streamlines inside a cut out from one of the mock up test sections considered (MAST design).

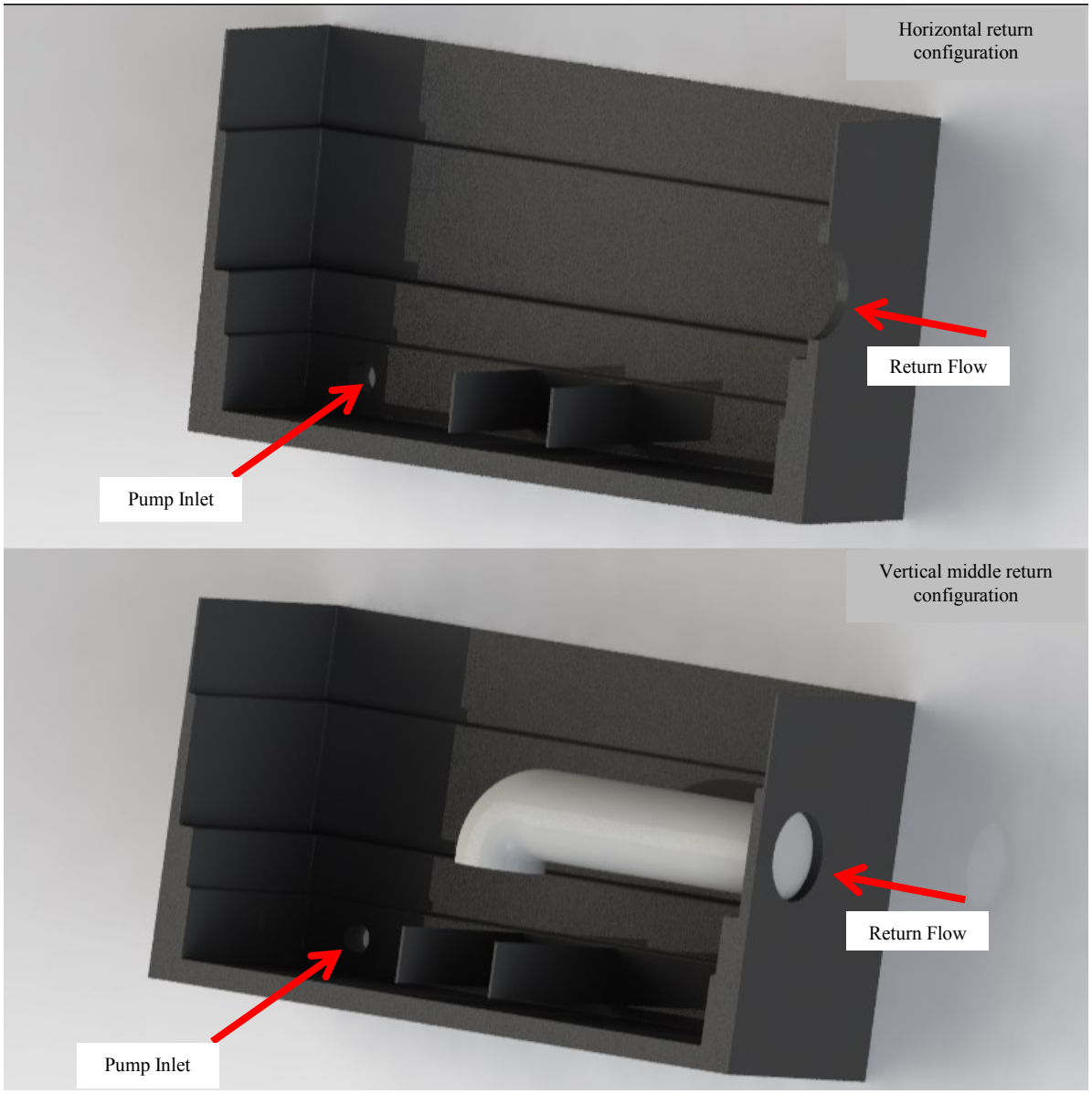

Figure 3.7. Tank cut-out with return configurations considered.

calculations in order to assess qualitatively the proposed designs and the requirements and limitations of the rig according to the experimental laboratory provisions. Three HyperVapotron designs that were encountered most often in the literature were designed in a Computer Aided Design Software (SolidWorks CAD, Student Edition Versions 2008 to 2012 were used throughout the project duration). Exact replicas of the 3.4mm, 5mm and 10mm channel height with a fixed fin height and spacing designs were considered and tested using SolidWorks Flow Simulation package (CFD package). A smart adaptive refinement mesh of at least 147 thousand cells and a spatial resolution of at least 0.85mm

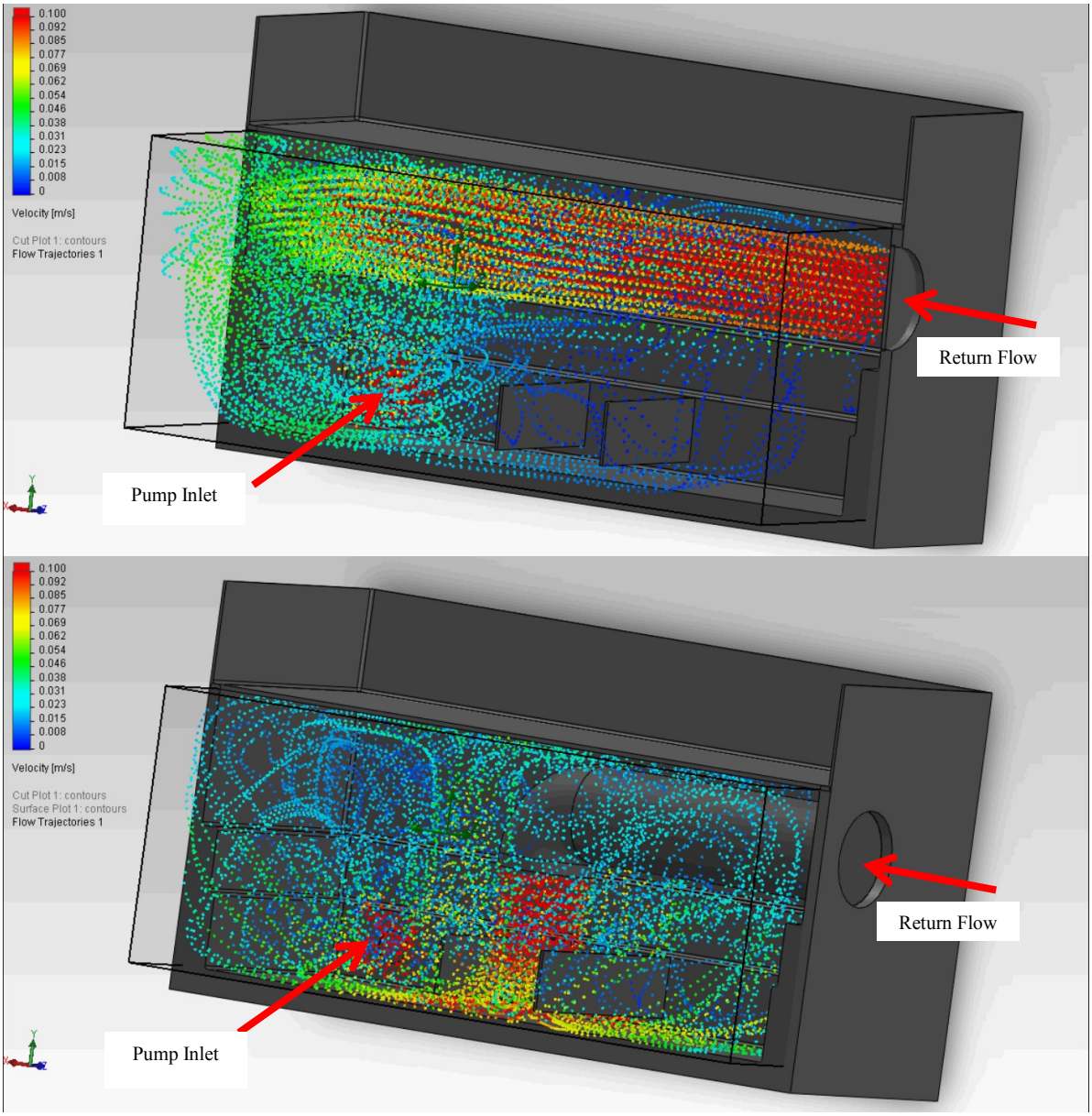

Figure 3.8. Tank cut-out CFD analysis. Top image depicts the streamline velocity profiles of the tank with a horizontal return configuration and bottom image depicts the same information on a tank with a vertical return configuration.

was used to perform the qualitative analysis on each model with the cell number and spatial resolution changing according to the conditions and configuration tested. The analysis indicated that the rear plate slots contained on the underside of the rear flat plate of the devices was of negligible significance to the established flow field (Figure 3.5). As a result, in order to reduce experimental complexities and manufacturing cost, it was decided to omit the slots. This aids the laser sheet beam entry region into the model for the PIV experiments.

Table 3.1 Boundary conditions for test section CFD calculations.

Geometry	Solver	Medium	Temperature/ K	Inlet velocity/ ms^{-1}	Inlet velocity profile	Inlet/Outlet turbulence parameters				Mesh parameters			Pressure at the outlet
						Intensity	Length scale/ mm	Model	Boundary layer	Cube side size/ mm		Type	
										Smallest	Largest		
JET	Navier-Stokes, k-ε turbulence model	Water	293.2	3 6 10	Uniform	2%	0.67	I-L	Turbulent	1.8	0.85	Cubic control volumes, adaptive size according to geometry complexity	Static pressure of 1 standard atmosphere
MAST				3 6 10									

Table 3.2 Boundary conditions for tank CFD calculations.

Geometry	Solver	Medium	Temperature/ K	Outlet volumetric flow rate/ m^3s^{-1}	Inlet velocity profile	Inlet/Outlet turbulence parameters				Mesh parameters			Pressure at the inlet
						Intensity	Length scale/ mm	Model	Boundary layer	Cube side size/ mm		Type	
										Smallest	Largest		
Tank	Navier-Stokes, k-ε turbulence model	Water	293.2	0.0025	Uniform	0.1%	6	I-L	Turbulent	6.4	25.5	Cubic control volumes, adaptive size according to geometry complexity	Static pressure of 1 standard atmosphere

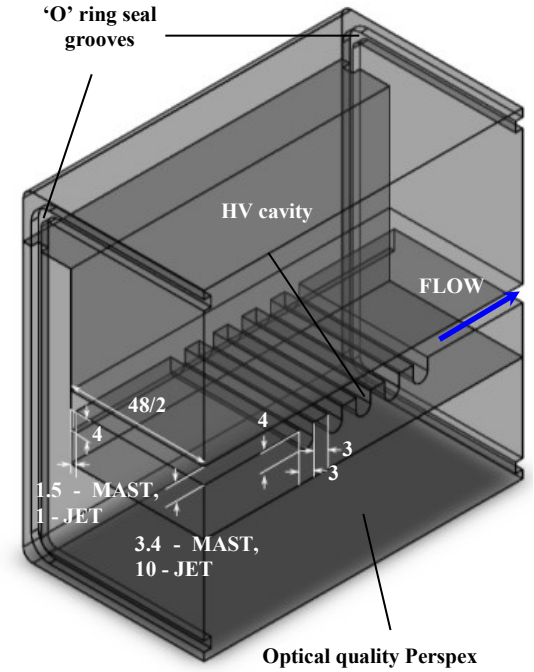

Figure 3.9. Centre-line sectional view of the HV test sections under consideration. Dimensions are in mm.

Additionally, the CFD analysis provided information about the pressure profiles to be expected in the models (helped to define the structural tolerances and pumping requirements during the design process) while it also verified that the mock ups produced similar flow fields as those found in the literature (Figure 3.6). Furthermore, studying the CFD results allowed limiting the final number of mock ups to two; the 3.4mm and the 10mm one which are currently used on the MAST and JET reactors accordingly (the 5mm section showed no important flow profile differences compared to the other two).

Finally, the CFD tool was used to analyse the in-tank return configurations to allow a jet impact mixing process to take place. This was required as the two phase mixtures used for both the PIV and nanofluid experimentation required continuous agitation to ensure good particle suspension and distribution qualities. A replica of the tank internal components and exact dimensions was created and two return configurations were tested (Figure 3.7). The first configuration had a horizontal side return while the second one a vertical middle return arrangement. For both configurations tested, the inlet to the pump was located at the left lower corner of the tank. The streamlines and mixing velocity profiles of the water in a tank cut out sketch can be found in Figure 3.8. The analysis

indicated that the second configuration created more turbulent mixing compared to the first and hence this modification was preferred on the final design. More details on the boundary conditions followed to set up the CFD investigations can be found in Table 3.1 and Table 3.2.

3.3.2 Rig design

Taking account of the CFD calculations it was possible to produce the final designs of the experimental rig to be used. The proposed designs – even though trying to keep them as simple as possible – were still quite complicate to manufacture. The complexity arises from the level of accuracy required to recreate the proposed HyperVapotron dimensions along with the complexity of making the entire experimental rig water tight. An additional complexity that needed to be handled was that the rig had to be designed to be as modular as possible to allow flexibility for further future experimentation using interchangeable alternative test sections without the need of further modifications. The CAD tool was used extensively to design all parts of the rig.

Two high optical quality transparent test sections were designed to model the JET and MAST related HyperVapotron geometries (Figure 3.9). The test sections require a well-conditioned, “top hat” inlet velocity profile. In addition, the operational scenarios tested and the experimental process followed, required a high volumetric flow rate to be delivered at the test section with minimal vibrations. To achieve that, the rig was split into two main functional components, namely the pumping station and the measurements station, both connected into a closed circuit loop using flexible hoses to dampen out the vibrations being transferred from the former to the latter.

The pumping station comprises of a collection tank, a powerful pump able to deliver the high volumetric flow rates of water required, additional flow volumetric and pressure control vanes, electrical circuitry and pressure gauges to finely tune and monitor the delivery of flow under the operational regimes tested. Additional pumps and plumbing

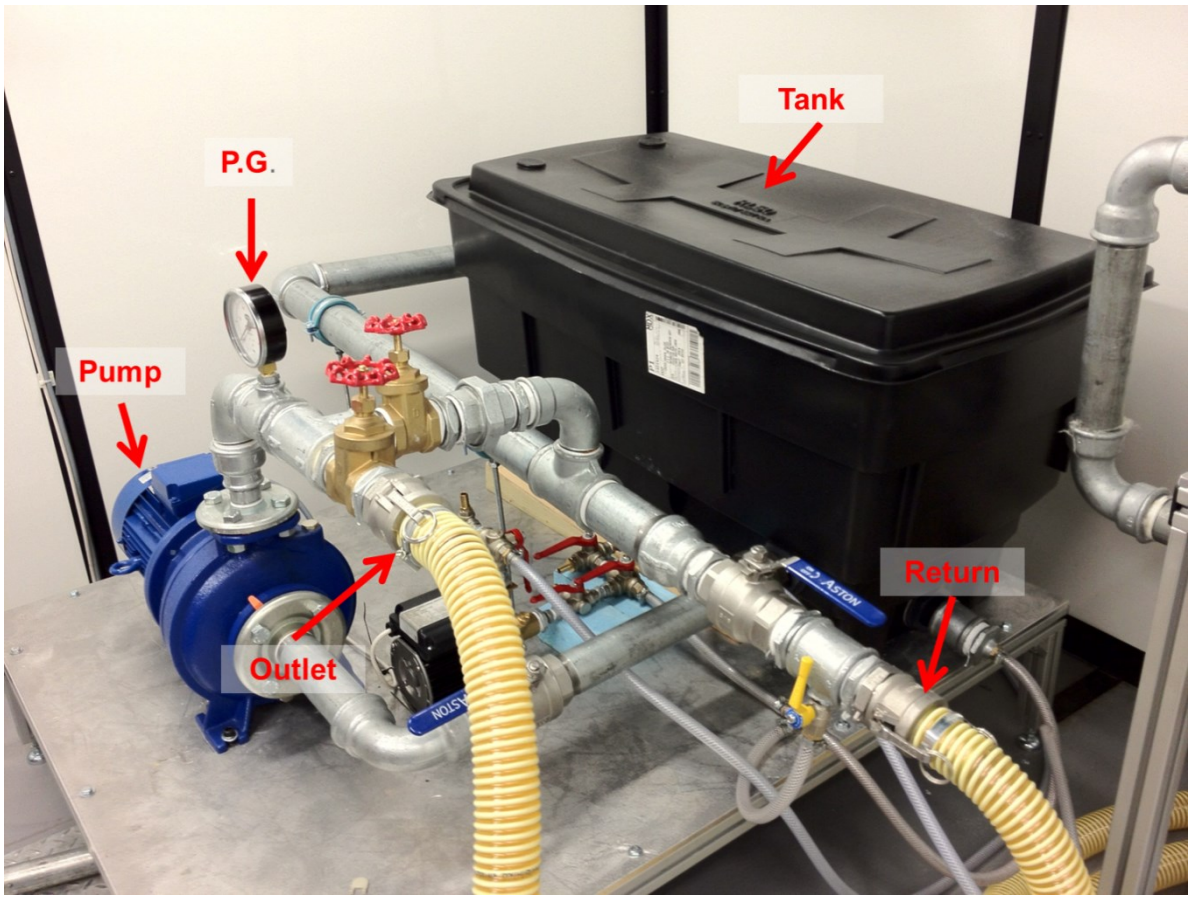

Figure 3.10. Pumping station with main component captions.

networks also occupy the same space and aid the practical and functional issues of emptying and cleaning the rig (Figure 3.10).

The measurements station (Figure 3.11) is vibrationally isolated from the pumping station and comprises of four main components: a flow conditioning channel, the actual HyperVapotron test section, a diffuser and a turbine flow meter. Additional components such as pressure gauges and control valves aid to regulate the experimental process while complimentary components (isolation vanes, air vanes, secondary pump etc.) are installed to serve practical considerations upon filling up, cleaning and decommissioning the rig.

A flow conditioning channel prior the actual test section is required to ensure laminar and close to uniform flow profiles upon the fluid entry into the test section chambers (Figure 3.12). The conditioning channel consists of an initial diffusing section (minor diffusion is expected upon changing the circular shape of the inlet pipe into a square one having the same side length as the inlet pipe diameter), followed by a screen, a

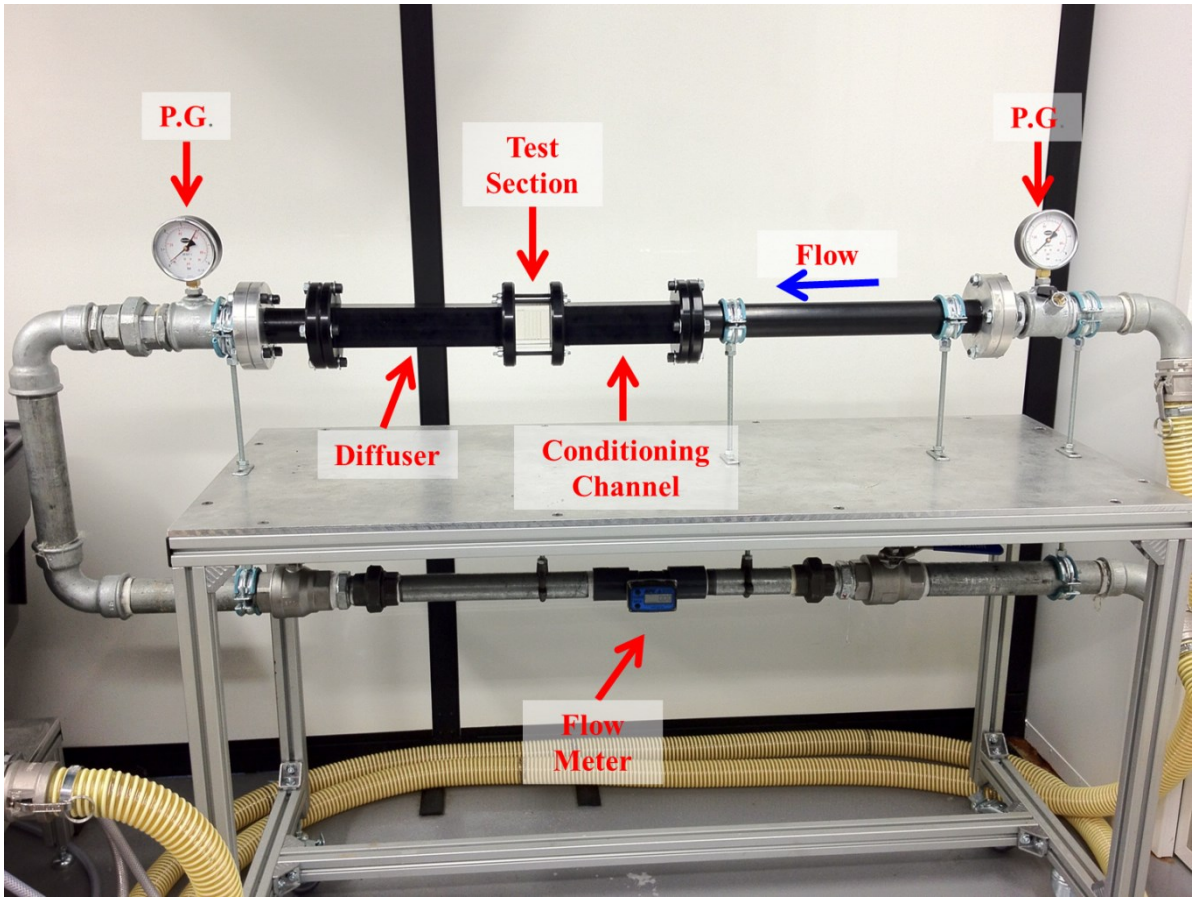

Figure 3.11. Measurements station with main components captions

honeycomb filter and an additional 3 screens leading to a contraction section. All screens have different design criteria to break up any possible persistent vortical flow structures (namely, different grid spacing and blocking factors). A straight pipe spanning 10 pipe diameters [198] is fitted at the inlet to allow a developed flow prior the test channel (Figure 3.13). 3D printing (rapid prototyping) was used to produce the blue, red and green parts out of a water proof resin in Figure 3.12 and Figure 3.13. The metallic parts of the rig are manufactured from aluminium which is later anodised to withstand water corrosion. The anodisation had a matt black colour to minimise laser light reflections during the PIV experiment. The rest of the pipe work components are fabricated from galvanised steel or other non-water corrosive materials to ensure longevity of the components.

The design and choice of the required parameters governing the lengths, locations and design for each specific component are based on literature provided for the designs of aerodynamic test sections [199-205]. The flow treatment channel was designed to be

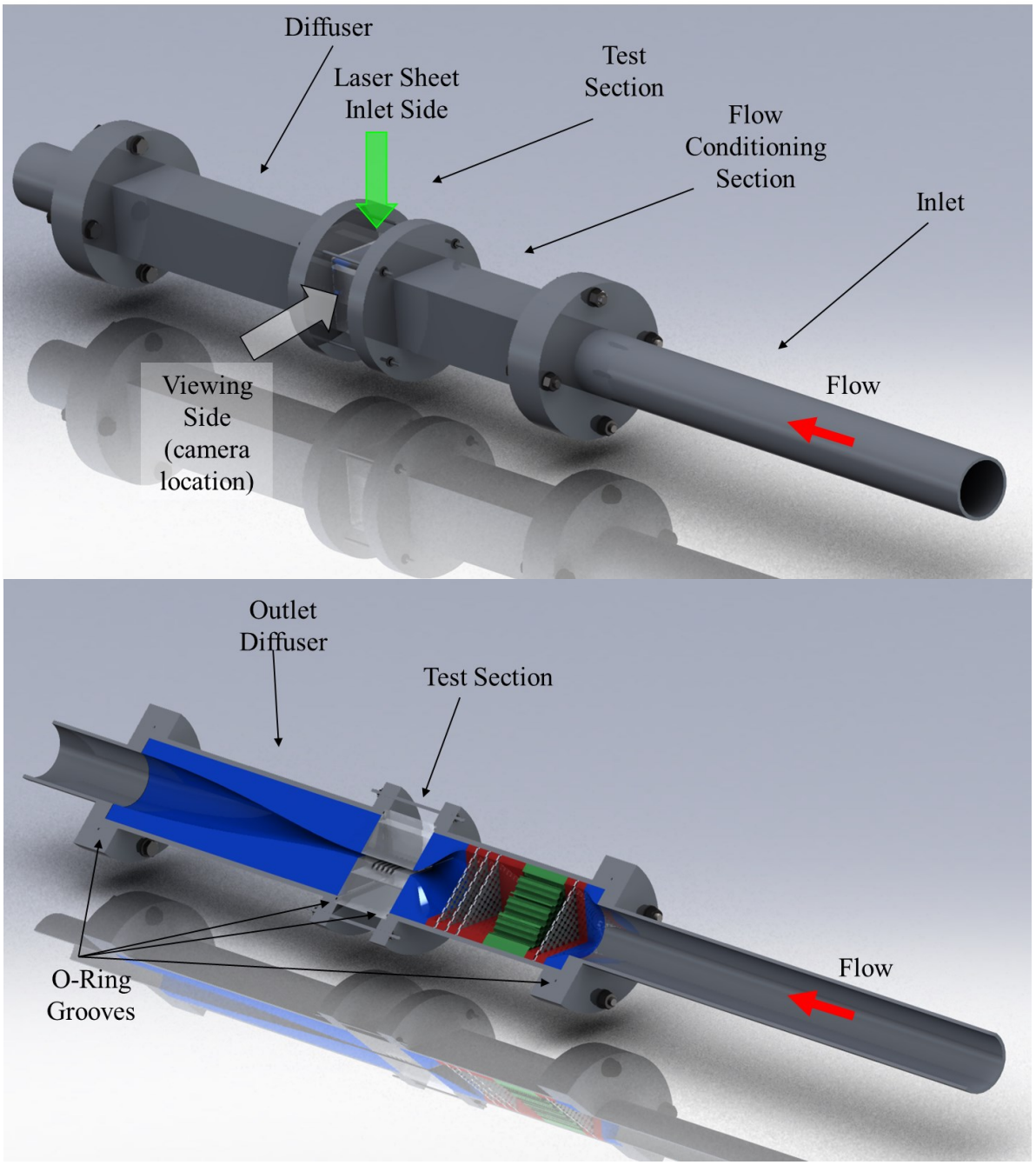

Figure 3.12. Measurements station general optical arrangement on the top image and a cut-out of the main components on the lower image.

highly modular and simple to manufacture following a sandwich approach to aid easy interchanging of components along with the provided flexibility for maintenance or further refinement if it is required (unfortunately the computational power required to calculate the flow parameters throughout the conditioning channel is currently beyond the available computational capacity of the hardware the CFD software is installed upon). To overcome

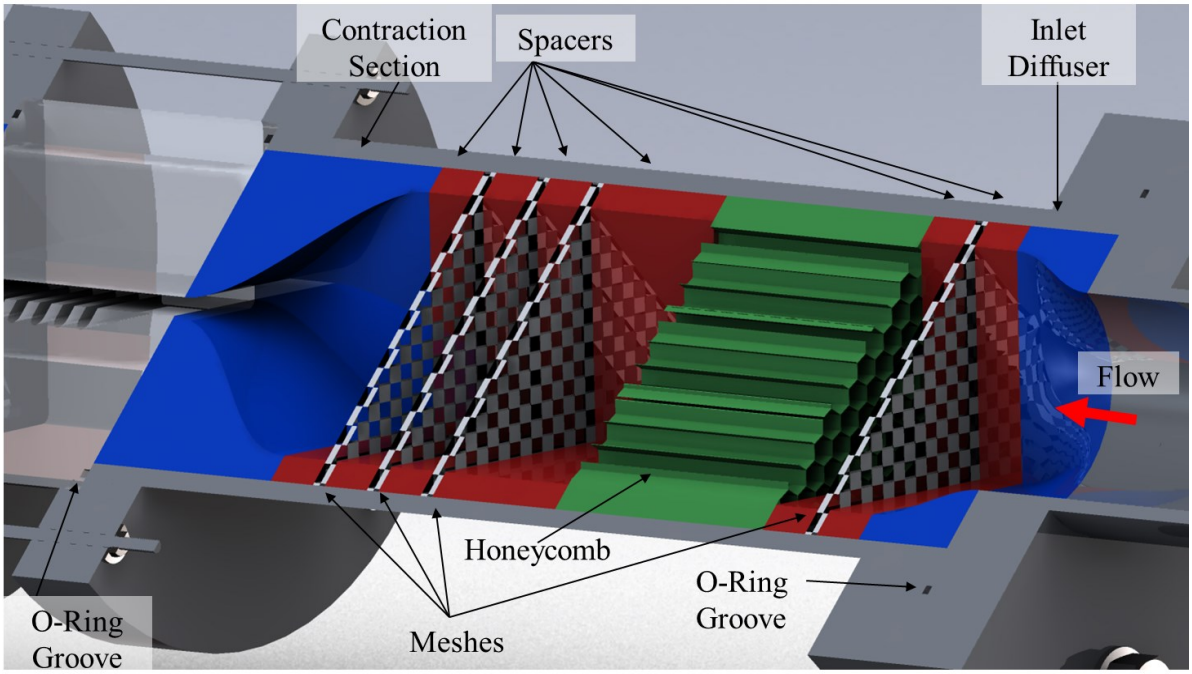

Figure 3.13. Cut-out section details of the conditioning channel.

the intricate problems of sealing the square duct while keeping modularity it was decided to fit the entire flow channel into an aluminium tube. The outer tube bares airtight fitted cylindrical flanges at the ends thus transforming the complicated square cross-section sealing problem into an easier circular one. The duct-into-duct approach results into fewer sealing points, reduced manufacturing and assembly complexity as well as it gets around the porosity leakage issue faced by the rapid prototyping components.

Manufacturing, assembly and sealing fittings needed to be concerned as well and be accounted for in the design. The primary sealant to be used is a customisable O-ring chord in a face-slot arrangement. The test section is sandwiched between the conditioning channel and the diffuser section. The test section is secured in place via compression screws. It was decided to secure the section in a compression instead of a tension state as the polarising planes of perspex material would be least affected and hence avoid any interaction with the PIV measuring process. The modularity of the section provides flexibility to establish the rig as a PIV testing tool for subsequent experimentation. This is mainly achieved by the interchange ability of parts as well as the chosen square cross-sectional dimensions of the test section, conditioning channel and diffuser inserts. British

Standards template sizes were chosen for most components (where possible) to minimise technician labour work and speed up the manufacturing process.

Both the pumping and measurements stations contain isolation valves and electronic pump emergency stop operators to aid easy component interchange ability, test section hot-swapping as well as component isolation in case of maintenance, leakage or accident. The test section hot-swapping ability is important as it allows the two HyperVapotron geometries to be exchanged without switching off the primary pumping circuit hence the tracers and nanoparticles are prevented from settling down inside the tank. The electrical loading of the pump is finely tuned by a standard high precision electronic controller and in combination with the various mechanical vanes and the turbine flow meter it is possible to fine tune the volumetric delivery of fluid to the measurements station with a minimum accuracy of 6.1% for all operational conditions (more details in Table 5.1).

3.4 Experimental methodology[1]

This section describes the methodology followed to carry out the PIV measurements as well as the associated data processing required to extract the results presented in chapters 4 to 6.

3.4.1 Particle Image Velocimetry (PIV)

PIV is a well-established method for obtaining quantitative, high resolution flow visualisation measurements. The method relies on the use of a pulsed laser source to illuminate a thin sheet of tracers/seeders dispersed in the flow (a Litron Nano T PIV Nd-Yag laser was used) and a CCD camera (non-intensified LaVision Imager Intense camera with a resolution of 1376x1040 pixels) to record the tracer 'seeding' particles as they move inside the test section. A Nikkor 50mm F/2.8 lens with manual focus was attached to the

[1] Parts of the work produced in this section were published in the public domain under references [166-169].

camera. Additionally, a 10nm bandwidth 532nm wavelength bandpass filter was attached to the lens to remove light wavelengths other than the one the laser produced and hence improve the recording quality. The overall quantity of the flow 'seeding' particles is small to avoid changing the fluid properties of the working medium. A volumetric ratio of less than 0.0025% of tracers to water was used in this experiment. Al_2O_3 particles with 1μm nominal diameter were used for 'seeding', which ensured appropriate tracking of the fluid flow for velocity measurements. The laser beam path steering arrangement can be found in Figure 3.14 [206].

A hybrid method was employed for the nanofluid study where the seeding particles (1μm Al_2O_3) were mixed in the nanofluid [94]. The scattered light collected for PIV processing was originating from the seeding particles. The size of the nanoparticles was smaller than the wavelength of light used to illuminate them, hence the photon interaction with them lay into the Rayleigh scattering regime and hence was adding noise to the scattered light signal from the tracers received by the recording imaging equipment (hence the emerging limitation on nanoparticle concentration) [168].

The laser pulses are a few nanoseconds long (7-9ns) to avoid image "ghosting" and are emitted in pairs. The time delay between the two pulses is adjusted in the range of 5-40ms, according to the flow velocity magnitude expected in the flow and is finely tuned by real time image analysis. The process can be repeated thousands of times (1000 datasets are recorded for each operating scenario and geometry in this case) in order to collect device operational statistics. Each pulse pair is emitted at a rate of 1Hz hence, in the time domain of the examined flow, each dataset collected from a pair of pulses is statistical independent from the rest and does not follow the evolutionary timescale of events taking place inside the device since the timescale of the hydrodynamic events is shorter than the pulse pair separation time. The recorded images of the flow had real dimensions of 35.6x26.9mm and the resulting spatial resolution was 30μm. In retrospect, the Kolmogorov length scale, which is an indicator of the smallest turbulent scale to be found in the solution, was found to be of the order range of 40 to 50 μm for the water cases [207]. Using the Nyquist-Shannon sampling theorem, the spatial resolution of the PIV measurement is able to capture in full structures of twice the sampling resolution, namely

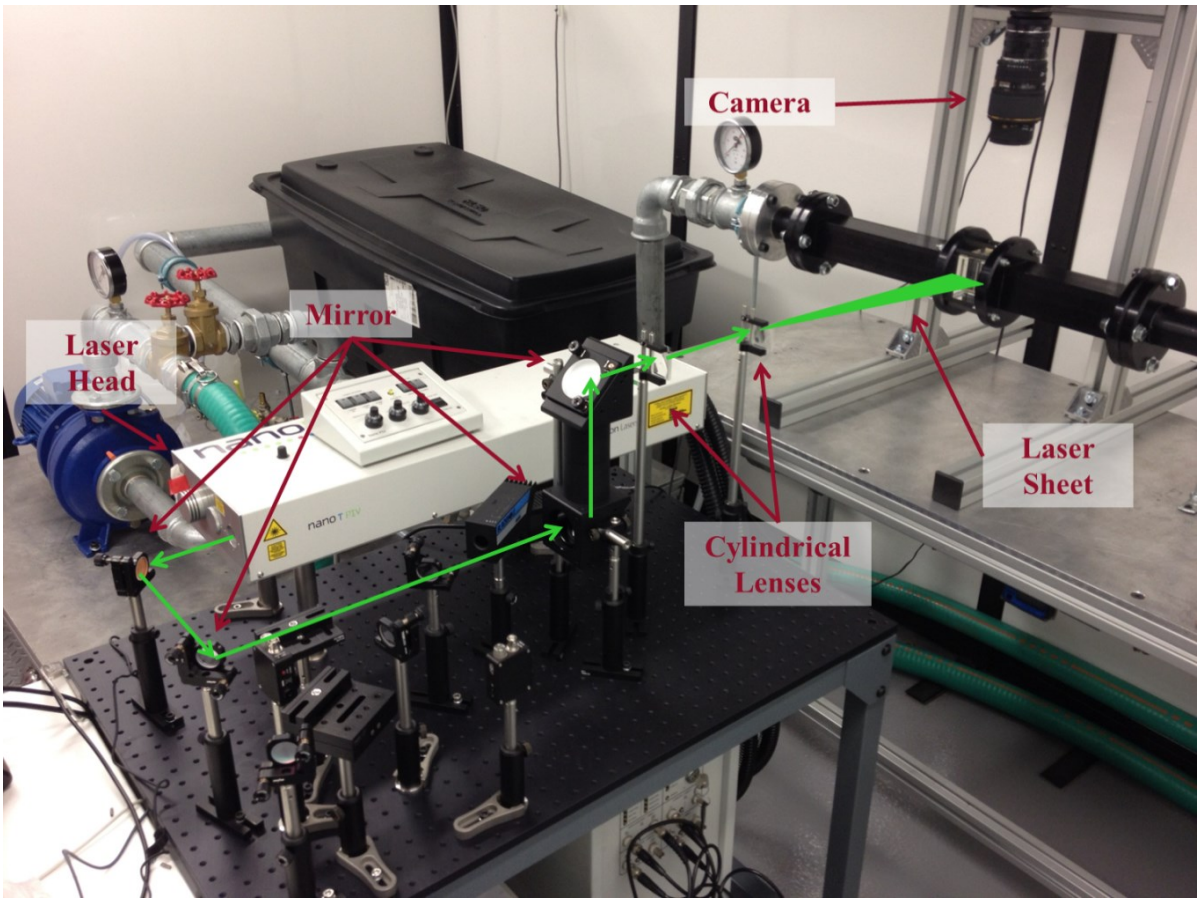

Figure 3.14. Laser light paths for the PIV experiment. Laser beam paths are depicted in green colour.

structures which form and have a minimum size of 60μm which is of the same order of magnitude as the smallest turbulent structure length scale to be found in the flow. This means that the spatial resolution of the technique used is sufficient to capture the smallest flow field features of the flow and hence the results present an exhaustive two dimensional view of the region of interest.

Commercial software (LaVision DaVis 7.2) is used to process the recorded images and estimate the 'seeding' particle displacement, which is then translated into the fluid flow velocity. Initially, a shift and intensity correction routine is followed to stabilise the raw images and normalise the intensities of scattered light recorded. A cross correlation method was then used at which the interrogation window followed a multi pass refinement process from 512x512 pixels down to 8x8 pixels with an overlap of 50% to calculate the vector field. A multi pass post processing is then followed at which the quality of the first calculation is evaluated and filters are successively and repeatedly applied to remove noise

and improve the accuracy of the calculation. Three filtering processes are followed. The first deletes vectors at which their cross correlation function peak ratio is less than a given value. Secondly a median filter is applied to strongly remove and iteratively replace vectors at which their RMS difference with their neighbouring vectors is larger than a value of the average RMS value of the neighbouring vectors. Vector groups can be removed with this process and replaced by interpolated ones. A smoothing filter is finally applied to improve the accuracy of the vector distribution. Multiple passes of these filters are applied with variable filtering parameters. At the final pass vectors with a cross correlation function peak ratio of less than 3 are deleted. The median filter will also delete vectors at which their value is more than twice the RMS value of their neighbouring vectors. Groups of a maximum of 20 vectors can be removed and replaced by interpolated ones. Finally, a smoothing filter of 3x3 pixels is applied. The sample vector yield is close to 100%.

For the nanofluid experiment (chapter 4 and 6), a two stage method was followed to produce an Al_2O_3-water nanofluid at a nanoparticle volumetric concentration of 0.0001%. This was the upper limit to allow the optical laser diagnostics to obtain velocity measurements [168]. This limit was as predicted lower than the limit of opacity found in section 3.2. Method 2 was followed to prepare the nanofluid required (more details on the preparation method can be found in the Appendix A).

The distributions of the mean flow velocity and the standard deviation of the corresponding flow velocity fluctuations were estimated from the instantaneous flow velocity images. For the water experiment, a total of 1000 statistical independent samples, which led to statistical uncertainties of the order of ±2.2% and ±3.2% for the temporal and spatial mean speeds inside the groove (groove speed) of JET and MAST respectively within a 95% confidence level. For the nanofluid experiment a total of 1000 image pairs were also collected which led to statistical uncertainties of the order of ±3.8% and ±3.5% for the mean groove speed of JET and MAST respectively within a 95% confidence level.

3.4.2 Further processing of PIV results

Apart from the measurement of the flow velocity statistics described above, which was used to describe the flow structure of each flow geometry, additional routines and processing tools were developed in order to investigate further the morphology of the instantaneous large scale vortical structures observed within the grooves of the examined flow geometries (chapter 5 and 6). Please note that the experimental method focused on the middle groove of each geometry as this section of the flow is expected to suffer the least from end effects. The methodology hence was adjusted to obtain high quality quantitative results in the particular section of the device while providing less detailed results regarding the flow fields inside the rest of the grooves of the models used (only general features of the flow are provided for the secondary grooves).

Proper Orthogonal Decomposition

Proper Orthogonal Decomposition (POD) is the mechanical engineering equivalent of Principal Component Analysis (PCA) in mathematics. It is a multivariate eigenvector based analysis at which an orthogonal transformation is used to decompose series of correlated velocity data, recorded by each laser pulse pair, into a set of uncorrelated components / modes (Eigen-components / modes each orthogonal to the next). The components are given an "energy level", namely a weighing factor towards their contribution to the correlated series. The higher the energy level the highest the effect of a particular Eigen-mode to the overall average of the series. The Eigen-components are presented in a series with the same number count as the total dataset number used; the first being the most energetic and the last being the least energetic. The decomposition images produced have the mean flow of the entire series subtracted, so as to be able to get a clearer view of the out-of-the mean components.

Commercial software (LaVision DaVis 7.2) was used to decompose the velocity data series for each geometry and for each operational condition tested. The decomposed velocity field is used to understand better which instantaneous flow structures are more influential for the operation of the device. The data can be used to analyse how the design

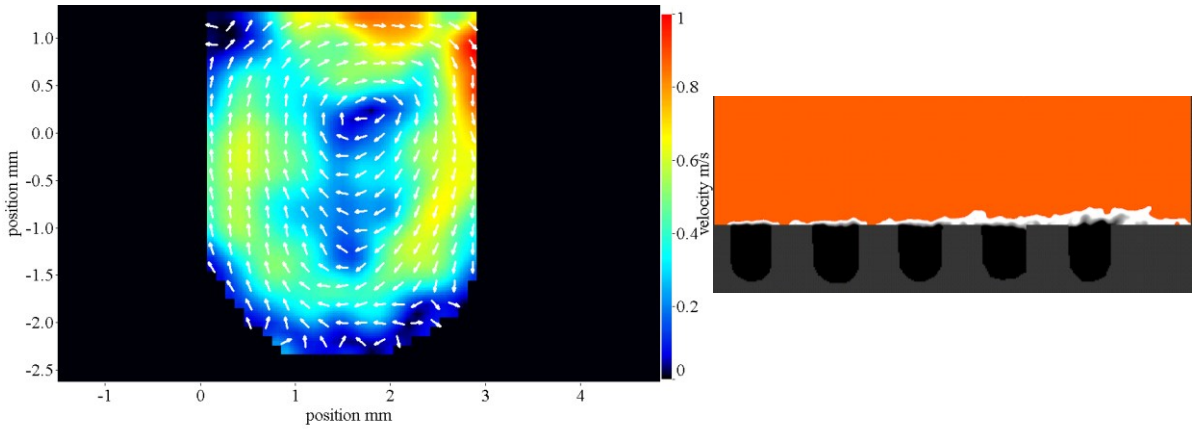

Figure 3.15. Instantaneous images of the velocity vector field inside the middle groove (on the left) and a view of the entire test section with the wake formation highlighted on top of the grooves (on the right). Both instantaneous images are under a 3m/s target free stream speed in the JET geometry.

and operation of the flow geometry affects the formation of the instantaneous vortical structures. The analysis was focused on the flow field of the middle groove of each of the flow geometries, as it is expected to be more representative of the flow inside the majority of the multiple grooves present inside a real device, which may not be strongly influenced by hydrodynamic end effects.

Image recognition routines

Due to the large number of recorded images, additional routines were developed in Matlab so as to automatically analyse the locational characteristics of the vortices inside the grooves of each test section as well as to detect a breakup of an instantaneous vortical structure. The routines also investigate possible evolution of wakes at the entrance of the grooves inside the free stream channel and assess how these might affect the locational and formational stability of the vortical structures inside the grooves. Also, the possibility of the flow inside one groove affecting the flow inside the next will be examined. The challenge of forming the data processing routines was not straightforward as the high irregularity of both the vortical structures and the wake made it impossible to use traditional methods of detection based on fluid quantities (see Figure 3.15). Averaging methods and interrogation windows had to be formed to be able to resolve the instantaneous flow features.

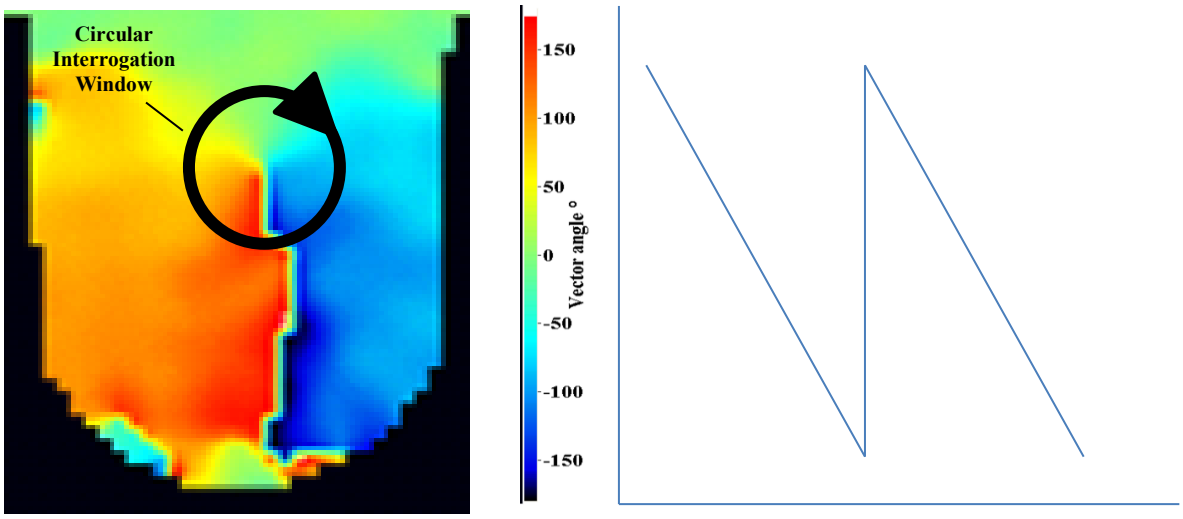

Contours of vector angles in the middle groove of the test section

Scanning angle pattern

Figure 3.16 Schematic of the recognition logic of the centroid of a vortical flow structure.

The routines for the detection of wake presence in the freestream are formed in a way to automatically register the presence of a wake and mark the corresponding groove number that is located below it for every data set. The routine loads a PIV processed matrix, which contains the values of flow velocity with a resolution of 30μm for the entire viewing area. The code then makes use of rectangular overlapping interrogation windows and scans the full length of the free stream area closer to the groove openings at which the wake is formed. An average speed is calculated for every interrogation window and compared to the next. If the average speed in the window is less than 80% of the target free stream velocity (a threshold that has been defined by studying the wake attributes) the interrogation window is flagged. If the flagged windows span a continuous distance of more than two groove widths (namely if a wake is long enough to affect more than one groove) then the routine identifies a wake and the corresponding grooves of the dataset are marked. The wake formation and its extend aids to understand the physics of the flow better by identifying the conditions of a wake presence and how it affects the instantaneous and average behaviour of the flow inside the grooves.

The routine for the detection of locational stability of the vortical structure required advanced methods of image recognition to increase the sensitivity of the detection of the vortex centroid, while accommodating large irregularities in its shape. The geometrical

irregularity of the vortex formation makes it impossible to use traditional flow quantities, such as the flow vorticity, to detect the vortex centroid. Alternative image analysis routines had to be devised that recognised vortical patterns according to a relative size and morphology and allowed a large degree of vortex formation irregularity. The angles of the fluid inside a circular interrogation area are examined and the average vector angle change of the fluid in each quadrant of is resolved. A matrix from each dataset containing the velocity vector angles at a resolution of 30μm is used. A fixed pattern is observed close to the vortex centroid at which the average vector angle is decreasing and a "jump" is detected when a clockwise circular scanning is completed, as seen in Figure 3.16.

The morphological features of a vortex described by a velocity vector angle plot (such as the one in Figure 3.16) contain distinctive features; the pattern followed by the vector angles, as described earlier and a "dead" undefined region of vector angles which are located inside the vortex "eye". Taking account of these features and allowing for irregularities, an elaborate design for the interrogation window is required (Figure 3.17). An averaging process is applied to calculate the average velocity vector angle in successive quadrants at a time of the interrogation window bounded by the external radius (R_{ext}) and internal radius (R_{int}) of the interrogation window (hatched area in Figure 3.17). The internal radius corresponds to the characteristic size of the eye of the vortex, while the external radius represents an average characteristic size of the vortices to be recognised (this plays an important role in the overall locational accuracy of the calculated vortex centroid). If the vortex had a geometrically perfect circular shape, the average vector angle from successive quadrants (θ) would have been in steps of 90º. Allowing for irregularities though, θ can be reduced to allow deformed and skewed vortices to be detected.

The comparison starts from quadrant "1" and ends in quadrant "1" hence making in total four angle comparisons. The interrogation window scans the entire area of the grooves searching for the vortex velocity vector angle pattern and flags up the locations when this criterion is satisfied. Control criteria are in place to abort a scanning if the pattern is quickly found to be missing from the interrogation window (this can happen as soon as the scanning is completed inside the 2nd quadrant and onwards) hence improving computational efficiency. The circular interrogation windows are overlapped to increase

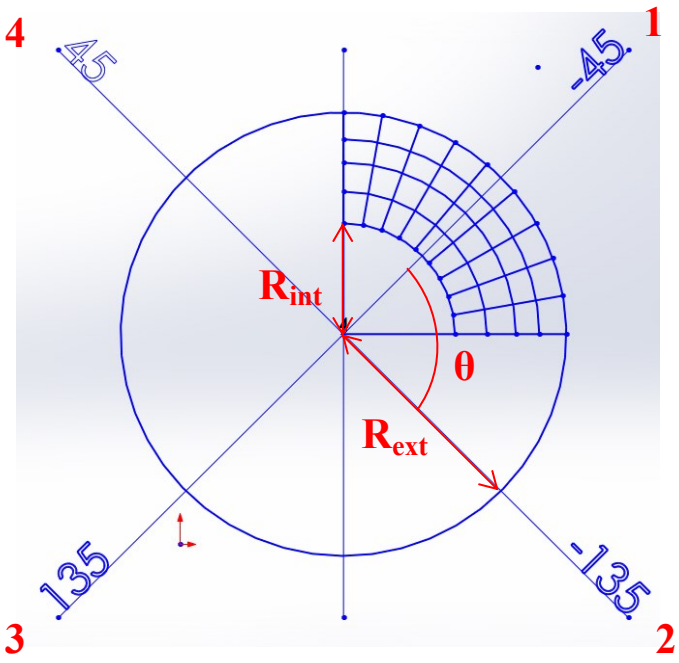

Figure 3.17. Circular interrogation window with polar coordinates of the average sector angles in degrees.

the accuracy of the calculation. The overlap distance is as small as $1/10^{th}$ of R_{ext}. To accommodate different vortex sizes, a generally larger R_{ext} is used. This increases the locational accuracy of vortex detection away from the walls of the groove. However, it makes nearly impossible to identify vortices near the walls of the grooves. A "trial and error" process indicated a suitable value for R_{ext} which ensures a large overall accuracy. When a pattern is identified, the center of the interrogation window is logged. As soon as the entire groove is scanned, a collection of points is attained for which the interrogation window has detected a centroid pattern. The geometrical center of the entire collection of points is calculated, which yields a good approximation of the vortex real centroid (accuracy is below 500μm).

3.5 Summary

In this chapter the experimental methodology followed in the thesis is described. The nanofluid quality assessment defined the optimum mixture preparation methods and

provided information regarding the nanofluid structure used for the experiments. The nanofluid laser absorbance experiment provided data on how laser light interacts with nanofluids which provided quantitative information regarding the mixture concentrations and laser light scattering profiles to be used with the PIV measurements. Finally, the experimental rig used for the PIV measurements as well as the methodology of data processing followed was described.

Chapter 4

Preliminary HyperVapotron Particle Image Velocimetry Experiments on Water and Nanofluids[1]

4.1 Introduction

This chapter reports on a preliminary experimental PIV analysis to measure the flow field in two HyperVapotron variant geometries from the JET and MAST experiments using the methodology described in chapter 3. The results from this section helped to develop the in depth experimental and analytical process followed in chapters 5 and 6. Past studies have yielded qualitative experimental results, but the measurements reported here provide quantitative data to aid the understanding of the initial flow field inside the HyperVapotron (i.e., before a heat flux is applied). Further, the experiment is conducted using both water and Al_2O_3-water nanofluid as the flow medium. Thus, these velocity measurements offer a first indication for potentially enhanced heat transfer in HyperVapotron devices when nanofluids are used as the coolant. The improved understanding of the HyperVapotron flow regime and

[1] The work produced in this chapter was published in the public domain under references [166-169].

the cooling advantage of nanofluids could assist the design of advanced high heat flux components for future fusion machines.

4.2 Results and discussion

4.2.1 Measured fluid flow velocity field in HyperVapotrons

By using the PIV methodology, the flow velocity was measured inside the central groove of the JET and MAST HyperVapotron variant models and key results are plotted in Figure 4.1. Note that in the vector plots the arrows represent local flow direction but not velocity magnitude; the superimposed coloured contour plots represent the normalised velocity magnitude. All velocities quoted represent the absolute velocities normalised by the maximum free stream velocity magnitude recorded.

Table 4.1 Measured normalised speed characteristics - described by equations (4.1) - (4.3).

		$\langle\lvert\bar{V}\rvert\rangle$	$\langle\lvert\bar{V}'\rvert\rangle$	$\langle\lvert\overline{V_{REL}}'\rvert\rangle$ / %	Vortex breakup occurrences / %
JET	Water	0.1205	0.0413	34	0
	nanofluid	0.0858	0.0490	57	17
MAST	Water	0.0833	0.0422	51	3
	nanofluid	0.0773	0.0418	54	5

$$\langle|\bar{\boldsymbol{V}}|\rangle = \frac{\sum_i^{n_{iw}}|\boldsymbol{V}_i|}{n_{iw}V_{norm}} \tag{4.1}$$

$$\langle|\bar{\boldsymbol{V}}'|\rangle = \frac{1}{V_{norm}}\sqrt{\frac{\sum_i^{n_{iw}}(|\boldsymbol{V}_i|-\langle|\bar{\boldsymbol{V}}|\rangle)^2}{n_{iw}-1}} \tag{4.2}$$

$$|\overline{\boldsymbol{V_{REL}}'}| = \frac{\langle|\overline{\boldsymbol{V}'}|\rangle}{\langle|\bar{\boldsymbol{V}}|\rangle} \tag{4.3}$$

where,

$\langle|\bar{\boldsymbol{V}}|\rangle$: Groove spatially averaged normalised speed

$\langle|\bar{\boldsymbol{V}}'|\rangle$: Groove spatially averaged RMS of normalised velocity fluctuations

$\langle|\overline{\boldsymbol{V_{REL}}'}|\rangle$: Groove spatially averaged RMS of normalised velocity fluctuations further normalised by $\langle|\overline{\boldsymbol{V}}|\rangle$).

n_{iw} : number of interrogation windows in area of interest (number of velocity vectors)

V_{norm} : normalisation speed

Focusing first on the PIV results with pure water, the results confirm the presence of irregular vortices inside the grooves that are thought to delay the onset of cavity boiling. In general, one transverse vortex exists per HyperVapotron groove, which is consistent with previous studies [192]. The vortex is seen to interact dynamically with the free stream. "Lumps" of high velocity fluid (up to twice the spatial average speed inside the groove) detach from the free stream flow and move inside the groove (see instantaneous planar flow velocity distribution in Figure 4.1). These high kinetic energy packets of fluid appear to re-energise and at the same time distort the geometrical symmetry of the vortex formation. It appears that the more energetic the vortex is the better the vortex stability for the test sections involved. The fluid exchange from free stream to vortex is much more pronounced in the JET HyperVapotron geometry (compare Figure 4.1c, j and k). For about the same inlet free stream velocity, the local time-averaged normalised velocity of the vortex of the JET HyperVapotron model is higher than the one from the MAST, as also indicated by the spatially averaged groove normalised speed of the MAST model which is 31% lower compared to the JET model (0.12 compared to 0.08, see Table 4.1). The JET HyperVapotron geometry produces a more uniformly circular vortex compared to the MAST vortex, while the vortex centroid is on average located at the top half of the groove for both geometries (see Figure 4.1a and h). The stability of the vortex is evaluated using the RMS of the local groove velocity fluctuations (Figure 4.1b, i and Table 4.1) along with the quantification of the random vortex breakup occurrences (for example Figure 4.1g). It is found that the vortex stability of the MAST model is lower compared to the JET model by 17% of the relative RMS value. Additionally, the probability of the vortex breakup occurrences for the MAST model was 3% whilst for the JET model no vortex breakup occurrences were recorded in the sample observed.

The above results in pure water represent the first detailed experimental measurements of the velocity field in HyperVapotron devices. Despite similar inlet free stream velocity and

geometry of their cavities, the measured flow field in the MAST and JET cavities is very different. The free stream channel height appears to play an important role in the hydrodynamic behaviour of the device, which is a useful result, as it has previously been argued that for a given inlet free-stream velocity, the channel height can be changed (for example, to suit facilities with lower flow available) without affecting the heat transfer coefficient in the cavities. However, the relative effects of the observed flow phenomena on thermal performance are not clear. The slower rotational velocity (and therefore convective heat transfer coefficient) of the MAST vortex would be expected to promote nucleate boiling at lower heat fluxes, increasing overall heat transfer efficiency but at the expense of a reduction in the device CHF. The stable MAST vortex may lead to more predictable performance, but in practice the greater channel-cavity fluid exchange observed in the JET geometry may yield advantages for thermal performance. Further work carried out in chapters 5 and 6 will aim to elucidate understanding of the relationship between the principal HyperVapotron flow structures and its heat transfer performance, by further experimental studies.

The PIV results of the HyperVapotron flow field for the low concentration Al_2O_3-water nanofluid are also presented in Figure 4.1. For the MAST geometry, the velocity results are almost identical between the water and nanofluid runs, as seen from Figure 4.1h-o and Table 4.1. This suggests that the small concentrations of nanoparticles in the flow do not influence the flow structures promoting the HyperVapotron cooling effect. This being the case, one can expect no adverse effect on HyperVapotron operation due to nanofluids. Thus, it is expected that the superior heat transfer properties of the nanofluid, as indicated by previous research, can be realised in the MAST HyperVapotron, including the reputed factor of 2-3 increase in CHF [1].

In contrast however, for the JET model a significant shift in flow pattern was observed in the nanofluid compared to pure water. The magnitude of the vortex interaction with the free stream flow is reduced (Figure 4.1f and g) for the nanofluid. The vortex spatially normalised averaged speed of the nanofluid flow reduces by 29% relative to pure water (0.12 m/s compared to 0.08 m/s, see Table 4.1 and Figure 4.1d). The vortex becomes more circular (Figure 4.1d). The stability of the vortex is significantly reduced, as indicated by the 23%

increase of the spatially averaged relative normalised RMS value as well as the vortex pattern present in the RMS distribution (Figure 4.1e). Additionally, the occurrence of vortex breakup events is increased to 17% (Table 4.1). Finally, the centroid location of the vortex has lowered to the bottom half of the groove for the nanofluid (Figure 4.1d). Such a fundamental change in the macroscopic flow regime is somewhat surprising, given the low concentration of nanoparticles introduced and especially given that the flow in the MAST HyperVapotron is unresponsive to these particles. Again, whether the induced flow structures are positive or negative to HyperVapotron thermal performance is currently not clear. The mechanism for these changes is also unknown and could be due to the subtle change in local effective fluid viscosity [1], surface nanoparticle coating or a result of a thinning of the boundary layer profile. What is certain is that the adoption of nanofluids will require careful design of high heat flux components, as existing water-cooled geometries may be non-optimal for a nanofluid flow. Further, it is proposed here that the flow structure altering property of nanofluids can be exploited, to establish better hydrodynamic patterns which enhance the thermal performance of the HyperVapotron.

HyperVapotrons are known to be highly flexible devices but their robustness to flow perturbations has never before been demonstrated. In practice their shape and orientation are commonly moulded to fit to complicated surface geometries requiring cooling and as such a uniform “top hat” free stream velocity profile in the grooved part (as enforced in the above study) is practically unachievable. In order to assess the practical implications of assemblies of HyperVapotrons, a worst case scenario study was performed. An artificial perturbation in the free stream flow at the entrance of the test section was introduced while keeping the average mass flow rate approximately the same as before. The perturbation (in the form of a high velocity jet) was placed near the groove entrance of the geometries to be able to study the effects of the groove vortex interaction with the free stream. The results associated with the JET geometry were significantly altered (deviations of up to 50% in velocity parameters and vortex shape were recorded). This might have significant effects on the designed thermal operating regime of the device. However, the MAST geometry performed better with minimal disruption on the vortex pattern and associated velocities compared to the results in Figure 4.1. The narrower free stream section of MAST (hence larger shear stresses) naturally

suppresses any large free stream perturbations enforcing an almost top hat free stream profile. As such, it can be concluded that the MAST device is expected to have superior practical applicability and robustness of operating conditions compared to the JET geometry for both water and nanofluid runs.

Several recent papers have been presented in the literature, which make use of advanced CFD modelling to predict the thermal performance of HyperVapotrons for ITER with water [193, 194, 208, 209]. These results are generally in agreement with experimental results from thermal studies at various high heat flux research institutes. Even though substantial information can be extracted regarding the thermal performance under a given thermal loading for different geometries, the computational work has not been evaluated due to the lack of high resolution experimental data to compliment the hydrodynamic properties of the investigations performed and hence provide a further insight on the physics of the Vapotron effect. The current study attempts to partially address this omission by performing two-dimensional experiments in a cold flow with water and a nanofluid on two geometries. The reported results provide velocity measurements with high spatial resolution (30μm), which identified the flow structures that may promote the vapotron effect. The main focus of the study performed was to:

a) Reveal the hydrodynamic characteristics of the isothermal flow and the formation of vortices inside the grooves of a HyperVapotron device without disruption by single phase heat transfer, boiling and vapour ejection.
b) Investigate how the geometry of each model affects the hydrodynamic properties of the device.
c) Compare the hydrodynamic structures under normal operation with those formed upon using a nanofluid.

The effect of the three dimensional nature of the flow, as well as the two phase flow observed upon boiling heat transfer, is important and requires further studies in the future.

However, the current study indicates that the hydrodynamic structure of the flow with nanofluids changes relative to water. It is expected that changes of the fluid flow will also lead to changes in the convective heat transfer characteristics and it is important to quantify

independently this influence before the added complication due to heat transfer. Therefore, the evaluation of the computational models must start with the evaluation of their ability to predict the change of the flow when nanofluids are introduced before their ability to predict the changes in heat transfer are evaluated. The current results can help the evaluation and better assessment of the computational results.

In order to take advantage of the gross effects of nanofluids, further work is required to improve understanding of the HyperVapotron flow regime and the relationship between the flow phenomena and thermal performance of the device. It will also be essential to study the mechanisms for the flow structure alterations due to the addition of nanoparticles, so that predictive models can be developed to guide the engineering design of the HyperVapotron.

Up to present, there are no conclusive studies to evaluate erosion effects that nanofluids might impart to such devices or any studies indicating nanofluid deterioration after extensive use (nanoparticles erosion). There are also no extensive studies on any other complications arising from pumping and distributing a nanofluid instead of the usual coolant. Any erosion and pumping issues arising from substituting a normal coolant with a nanofluid will be important and must be taken into account upon using them. An on-going study on erosion has been initiated [167].

4.3 Conclusions

The enhanced heat transfer properties of nanofluids make them attractive as coolants for fusion heat sinks such as the HyperVapotron device, but in the past the mechanisms responsible for their anomalous performance have been unexplained. This study has proposed that the thermal performance of the HyperVapotron with nanofluids might improve for two reasons: the bulk nanofluid thermal properties and the establishment of better hydrodynamic patterns that promote more efficient HyperVapotron cooling. Accordingly, computational and experimental analyses have been performed to study the molecular and flow field behaviour, respectively, of a nanofluid.

A preliminary experiment to measure the flow velocity field in a HyperVapotron by PIV has been carried out for water and for a low concentration Al_2O_3-water nanofluid. The results using pure water confirmed the presence of irregular vortices inside the narrow cavity, with the 3.4mm channel MAST geometry exhibiting a less circular, slower rotating, less stable vortex than the 10mm channel JET variety. It can be inferred that the change in channel height has an effect on the heat transfer coefficient of the device. The results using a dilute Al_2O_3-water nanofluid are very different for the MAST and JET designs. The flow field in the MAST variant is largely unaffected by the presence of nanoparticles, suggesting that the HyperVapotron will operate in high heat fluxes as intended but will also benefit from the well-known thermal enhancement of nanofluids. In contrast, the flow in the JET design is fundamentally altered, with the nanofluid vortex exhibiting much less stability and a slower rotation. Further work (chapters 5 and 6) is carried out to understand how specific flow structures affect thermal performance, but from this section it is clear that even very small concentrations of nanoparticles can dramatically alter the flow regime and this effect could be exploited to create flow structures which enhance HyperVapotron thermal performance.

A flow perturbation study was performed to assess the robustness of the flow regime in both geometries. The MAST geometry proved superior in handling free stream flow non uniformities compared to the JET geometry, where the device operation was highly disrupted. There are positive signs that the heat transfer performance of HyperVapotrons can be enhanced by using a nanofluid coolant, both by a mechanism of nanoscale thermal diffusion as well as by modification of large scale flow structures. This improved understanding of both HyperVapotron devices and the cooling advantages of nanofluids could assist the design of advanced high heat flux components for future fusion machines.

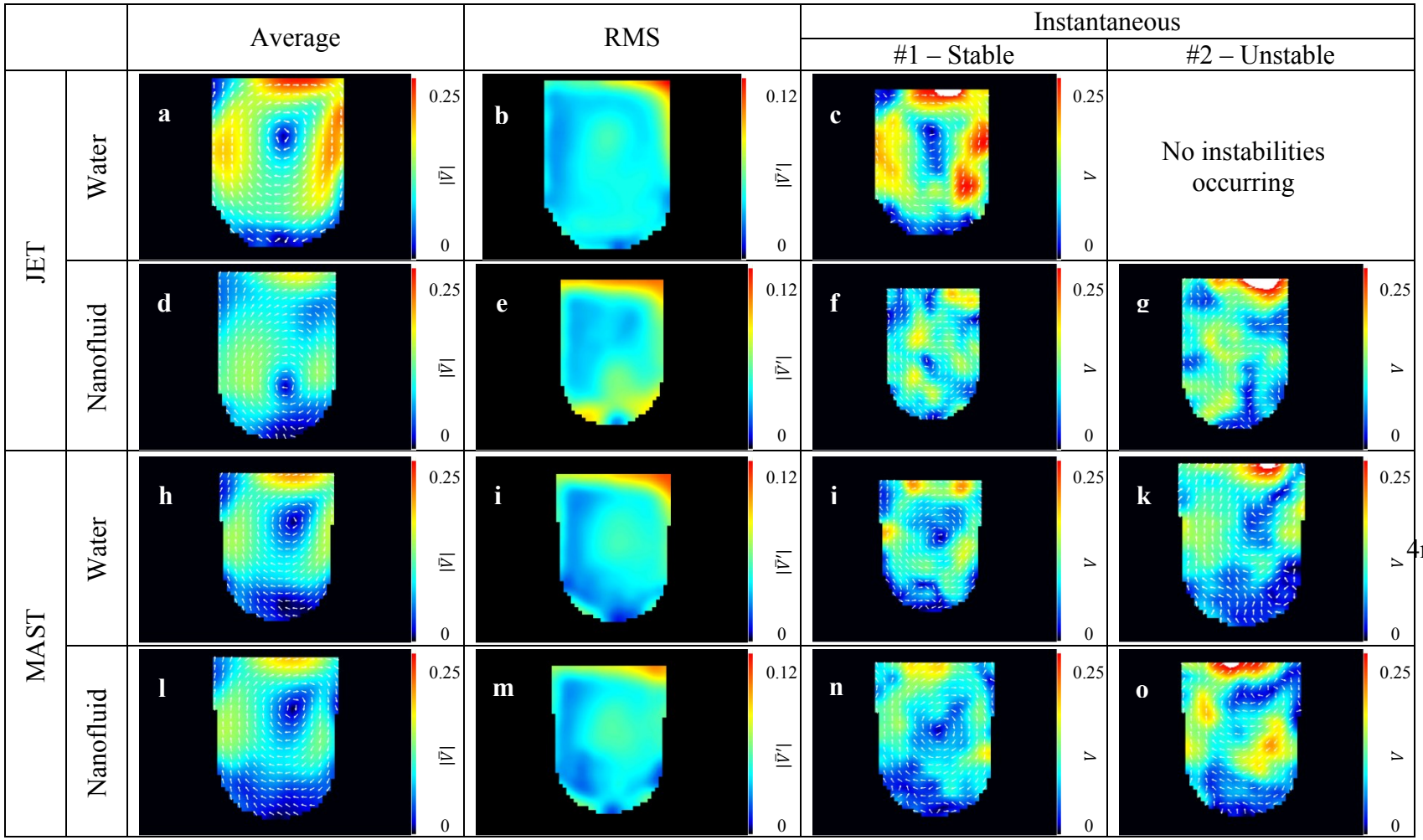

Figure 4.1. Mean normalised velocity, RMS of normalised velocity fluctuations and example instantaneous vortex formations with water and water-based nanofluids.

Chapter 5

HyperVapotron Particle Image Velocimetry – Water Experiments

5.1 Introduction

A high spatial resolution (30μm) PIV experimental study has been carried out on two replicas of HyperVapotron geometries taken from MAST and JET using the methodology described in chapter 3. The models were tested under three isothermal operating conditions to collect coolant flow data for contributing in the understanding of the Vapotron phenomenon and assess how the design and operational conditions might affect the thermal performance of the devices. It was discovered that the MAST in-groove speeds are lower and the flow structures less stable but less sensitive to free stream speed perturbations compared to the JET geometry. The MAST geometry was found to suffer from hydrodynamic end effects. A wake formation was discovered at the top of the groove entrance for the JET geometry while this is absent from the MAST geometry. The wake does not affect significantly the mean operation of the device but it may affect the coolant pumping load of the device. The in depth study presented in this chapter is a result of the preliminary experimentation knowledge attained and documented in chapter 4.

5.2 Results and discussion

The results related to the velocity field are presented normalised by the corresponding free stream velocity for each condition. The tabular results of Table 5.2 represent the averaged temporal and spatial quantities of the middle groove while the data in Figure 5.2 represent its averaged temporal quantities. The related uncertainties in setting the flow rates are given by Table 5.1. The velocity and POD field analysis study was focused on the 3rd groove, which is expected to be the least affected by hydrodynamic end effects. The POD presents the first four Eigen-modes of the decomposition as there are no distinguishable features to extract from the fifth mode and onwards. An example of the Eigen-mode energy levels for JET at an operating free stream velocity of 10m/s can be seen in Figure 5.1. Similar energy levels were observed for the rest of the operational points and MAST. The vortex locational analysis was extended to include both the entire section as well as the middle groove (3rd groove) in more detail. The investigation was one dimensional and the results took account of the locational coordinate perpendicular to the free stream flow. The wake interaction study took account of the entire test section only.

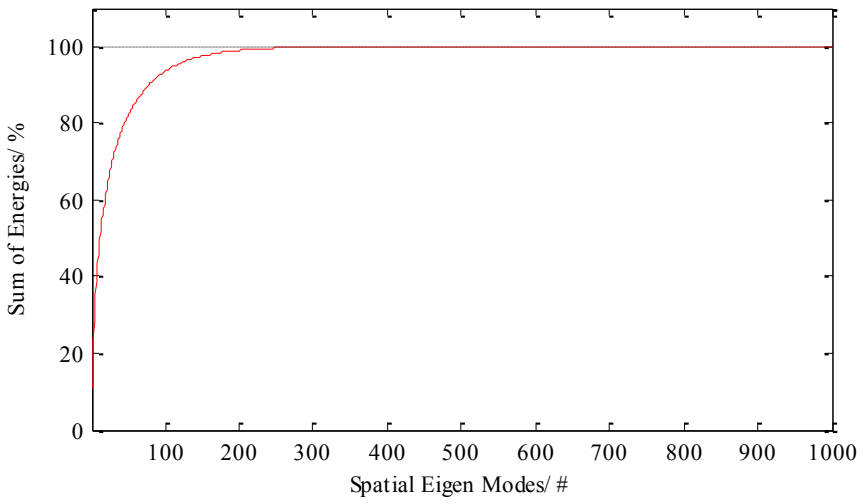

Figure 5.1. Sum of energies of the spatial Eigen modes for JET at a free stream speed of 10m/s.

5.2.1 JET related geometry

Velocity field

The normalised tabular data for the Velocity field and breakup occurrences of the vortex for the 3rd groove of the JET test section can be found in Table 5.2 while a comparison of the various operating conditions with the current ones (free stream speed of 6m/s) is provided in Table 5.3 (percentage differences). There is no significant change (<10%) in the non-dimensional (ND) groove speeds observed with higher or lower velocities than the current operating conditions (free stream velocity of 6m/s). The non-dimensional temporal and spatial averaged speeds appear to be lower for the 3m/s and 10m/s cases compared to the 6m/s (by 3% and 1% respectively). The RMS values for the 3m/s and 10m/s cases are higher by 8% and 1% compared to the 6m/s case.

Table 5.1 Uncertainties in setting up target flow rates.

Geometry	Target free stream speed/ (m/s)	Target volumetric flow rate/ (l/min)	Flow meter uncertainty / (%)
JET	3	88	4
	6	176	4
	10	293	3
MAST	3	32	6
	6	63	5
	10	105	4

The relative RMS of velocity fluctuations for the 3m/s and 10m/s cases also appear to be higher by 4% and 1% respectively compared to the 6m/s case. The breakup occurrences of the vortex for the 3m/s, 6m/s and 10m/s were small and limited to below 5% (3%, 2% and 5% respectively). It appears that the operation of the geometry at 3m/s, 6m/s and 10m/s to be similar.

There is no significant change of the groove vortex morphology for the 6m/s and 10m/s cases as seen in Figure 5.2. The vortex appears to have higher velocity gradients close to the side walls and lower close to the bottom boundary. The non-dimensional average velocity for operating conditions of 3m/s shows a slightly increased non-dimensional speed

close to the right boundary. The RMS plots are similar for all three cases with a minor exception of the right top corner for the 10m/s case which appears to have an overall slightly lower RMS value than the rest.

Proper orthogonal decomposition

The POD Eigen-modes for JET can be found in Figure 5.3. The first Eigen-mode shows the effects of the separation vortex occurring at the left top corner of the groove with a strong diagonal flow in the middle of the groove and a secondary vortex at the lower right section of the groove (the Eigen-mode energy levels are 8%, 9% and 7% for the 3m/s, 6m/s and 10m/s cases respectively). The effects of these features (size of vortices and diagonal flow) decrease with increasing free stream velocity. The 2^{nd} to 4^{th} Eigen-modes do not provide any additional information regarding the flow field.

Groove vortex locational characterisation

Table 5.4 contains the characterisation of the vortex centroid location in the groove. The vortex in the third groove appears to be stabilised around its average position for all three cases with the probability that the centroid remains around its average temporal position (within a 0.5mm bounded area above and below the mean average centroid) being around 95%-96%. Upon deviation from the temporal equilibrium position, the vortex is statistically more probable to be situated near the lower boundary of the groove compared to the higher boundary. The probability of the vortex centroid location remaining around its temporal average position decreases marginally with increasing free stream velocity. The vortex locational stability appears to be larger for the 6m/s case.

A similar picture is presented by the overall groove vortex characterisations in grooves one to five with the overall section exhibiting vortex stabilisation about its temporal equilibrium position with a probability ranging from 88%-96%.

Wake interactions with vortices

Table 5.5 contains the vortex centroid locational characterisation for the entire test section in the presence of wake in the free stream. There is wake formation at the free stream channel boundary at the top side of the grooves for the JET geometry. The instantaneous wake can grow to occupy up to about 10-15% of the free stream channel height. The probability of wake occurrence is large for the JET and follows a decreasing trend for an increasing free stream velocity (67%, 43% and 34% for the 3m/s, 6m/s and 9m/s respectively). The wake is most probable to start from the upstream groove and conveyed downstream. The probability of the existence of a wake on top of the downstream grooves follows an increasing trend.

The wake has negligible effect on the overall vortex breakup occurrences for the entire section. It is also found to induce minor (below 10%) vortex centroid stabilisation around its average position due to the lower groove opening free stream velocities, which "shield" the groove from free stream perturbations. The fact that the probability of the wake formation decreasing with increasing free stream speed is owing to the increased shear stresses, which act as a dampening parameter to free stream irregularities.

5.2.2 MAST related geometry

Velocity field

The normalised tabular data for the Velocity field and breakup occurrences of the vortex for the 3rd groove of the MAST test section can be found in Table 5.2 while a comparison of the various operating conditions with the current ones (free stream speed of 6m/s) is provided in Table 5.3 (percentage differences). There is moderate change in the non-dimensional average groove speeds compared to the current operating conditions. The average non-dimensional groove speed at 3m/s is by 16% higher and, at the 10m/s case, 10% lower compared to the normal operating conditions (free stream of 6m/s). This indicates an overall average groove speed reduction with the increase of the free stream velocity. There is significant change on the non-dimensional RMS value for 3m/s (an increase of around 22%), while, for the 10m/s,

there is a decrease of 7% compared to the 6m/s case. The relative RMS values appear to be small with an increase of 2% for both free stream speeds, compared to the operating conditions. The vortex breakup occurrences seem to remain the same for higher or lower free stream speeds in between 7%-10% (10%, 7% and 8% for the 3m/s, 6m/s and 10m/s respectively). The operation of the MAST geometry is affected significantly by changing the free stream velocity.

There is no significant change of the groove vortex morphology (see Figure 5.2) for the 6m/s and 10m/s cases. The vortex appears to have higher velocity gradients on the side walls and lower on the bottom boundary. The 3m/s non-dimensional average velocity plot shows a slightly increased non-dimensional speed on the top boundary. The RMS plots are similar for all three cases with the exception of the right top corner of the 3m/s case where the RMS values appear higher.

Proper orthogonal decomposition

The first four POD Eigen-modes for MAST can be found in Figure 5.4. A separation vortex and diagonal middle flow appear to be present for only the 6m/s and 10m/s cases as seen from the 1st and 2nd Eigen-modes (the energy levels of the 1st Eigen-modes are 10%, 13% and 13% for the 3m/s, 6m/s and 10m/s cases respectively. For subsequent Eigen-modes the energies reduce significantly). It appears that the narrower channel height suppresses the separation vortex for low free stream velocities. Subsequent Eigen-modes provide little additional information compared to the mean flow.

Groove vortex locational characterisation

Table 5.4 contains the analysis of the vortex centroid locational characterisation. The vortex, similarly to the JET geometry, appears to be stabilised around its average temporal position for all three cases with the probability that the centroid being around its average position (within a 0.5mm bounded area above and below the average centroid) being around 86%-88%. Upon deviation from the temporal equilibrium position, the MAST vortex is statistically more probable to be near the lower boundary of the groove compared to the

higher boundary. The probability of the vortex centroid location being around its average temporal position remains about the same with increasing free stream velocity.

A similar behaviour is presented by the overall groove vortex characterisation in grooves one to five with the overall section exhibiting vortex stabilisation about its temporal equilibrium position with a probability ranging from 72%-82%.

Wake interactions with vortices

No wake was formed in the MAST geometry due to the higher shear stresses encountered in the free stream section, which act to suppress the free stream non-uniformities.

Comparison of the MAST to the JET geometry

The groove speeds for the MAST geometry seem to be more sensitive to free stream speed variations, while this is not the case for the JET geometry. The comparison of the tabulated velocity field data between MAST and JET can be found in Table 5.6. The non-dimensional average groove speed is lower in the MAST geometry for all three cases (18%, 30% and 35% for the 3m/s, 6m/s and 10m/s cases respectively). The RMS of the velocity fluctuations is higher for the 3m/s and 6m/s cases by 14% and 3%, while it is lower for the 10m/s case (3%). The relative RMS values appear to be in general higher than the JET geometry by around 15-18%, while the breakup occurrences of the vortex are similar and marginally higher for the MAST geometry (2%, 3% and 3% for the 3m/s, 6m/s and 10m/s cases respectively).

The MAST geometry exhibits lower speeds close to the side boundaries with the non-dimensional average velocity field being overall more uniform compared to the JET geometry. The RMS of the velocity fluctuations is also similar with the exception of a higher right corner RMS value for the 3m/s case. The MAST and JET locational stability is not affected significantly by the free stream velocity changes. The locational stability of MAST is lower compared to JET.

Focusing on the entire section locational characteristics of each groove for both geometries (Table 5.4), the central grooves for MAST appear to form more locational stable vortices compared to the end grooves for the water runs. This is not the case with the JET

geometry at which all grooves appear to be more insensitive to end effects compared to the MAST geometry. A wake appears to form close to the top boundary of the grooves for the JET geometry for a significant amount of operational time of the device. The wake can occupy the free stream by as much as 10-15%. Examining the locational stability of the grooves with a wake, no significant disruption is evident on the normal operation of the device. Moreover, the wake acts as a buffer zone which seems to be shielding the groove from free stream flow perturbations. On the contrary, the MAST geometry has no wake formation for all operating conditions. It is believed that any free stream perturbations are suppressed by the high shear stresses encountered inside the narrow free stream channel of the device. Evidence of instability suppression are also found in previous studies performed [168], where the MAST geometry appeared to behave more stably, when exposed to severe free stream perturbations.

5.3 Conclusions

A PIV study was carried out to quantify the velocity field under isothermal conditions and reveal, in high spatial resolution (30μm), the flow structures that promote the Vapotron effect during cooling of fusion reactors. The study considered two geometries (JET and MAST variants) under three operating conditions defined by the free stream speed enforced in each test section (3m/s, 6m/s and 10m/s). The comparison was performed with the operating conditions currently in service at JET and MAST (6m/s free stream speed) to investigate the effects of the free stream channel speed to the groove flow structure characteristics.

The groove speeds for the MAST geometry are more sensitive to free stream speed changes compared to the JET geometry. Generally, the non-dimensional average groove speeds of MAST are lower and the relative values of the RMS of velocity fluctuations are higher compared to the JET geometry. This indicates that the vortex inside the MAST geometry is less stable and spinning at a lower speed. The vortex shape is similar between the two geometries. The MAST and JET vortex centroid locational stability seems to be insensitive to free stream velocity changes. The locational stability of the MAST vortex is

overall lower compared to JET. A wake forms inside the JET geometry. The wake does not affect significantly the vortex locational characteristics of the device, but might have an effect on the pumping loading of the device. The wake formation inside the MAST device is suppressed by the high shear stresses encountered in the free stream channel.

The flow in the grooves of the MAST geometry is affected significantly by end effects, while the JET geometry appears to be insensitive to them. As such, hydrodynamic end effects are likely to have an impact on the local thermal performance of the MAST geometry. Non-uniformities of the thermal loading performance and thermal tolerances of PFC are extremely important and must be accounted for upon designing and operating high heat flux components.

This study was performed under cold flow, isothermal conditions and presents high spatial resolution data regarding the flow structures that promote the Vapotron effect. The data is important as it provides evaluation benchmarks for future HyperVapotron CFD analyses, as well as contributing in better understanding of the physics behind the Vapotron effect. Future work needs to be carried out to collect more information regarding the non-isothermal effects on the flow structures recorded.

Table 5.2. Measured normalised speed characteristics - described by equations (4.1) - (4.3).

Free stream speed / ms^{-1}	JET				MAST			
	$\langle\lvert\bar{V}\rvert\rangle$	$\langle\lvert\bar{V}'\rvert\rangle$	$\langle\lvert\overline{V_{REL}'}\rvert\rangle$ / %	Vortex breakup occurrences / %	$\langle\lvert\bar{V}\rvert\rangle$	$\langle\lvert\bar{V}'\rvert\rangle$	$\langle\lvert\overline{V_{REL}'}\rvert\rangle$ / %	Vortex breakup occurrences / %
3	0.118989	0.045314	38.1	2.6	0.110381	0.058569	53.1	9.7
6	0.122133	0.041868	34.3	2.4	0.094863	0.048105	50.7	7.0
10	0.120528	0.042246	35.1	4.7	0.085252	0.044969	52.7	7.8

Table 5.3. Comparison of measured normalised speed characteristics with current operating conditions given as percentage changes - described by equations (4.1) - (4.3).

Free stream speed / ms^{-1}	JET				MAST			
	$\Delta\langle\lvert\bar{V}\rvert\rangle$ / %	$\Delta\langle\lvert\bar{V}'\rvert\rangle$ / %	$\Delta\langle\lvert\overline{V_{REL}'}\rvert\rangle$ / %	ΔVortex breakup occurrences / %	$\Delta\langle\lvert\bar{V}\rvert\rangle$ / %	$\Delta\langle\lvert\bar{V}'\rvert\rangle$ / %	$\Delta\langle\lvert\overline{V_{REL}'}\rvert\rangle$ / %	ΔVortex breakup occurrences / %
3	-2.6	8.2	3.8	0.2	16.4	21.8	2.4	2.7
10	-1.3	0.9	0.8	2.3	-10.1	-6.5	2.0	0.8

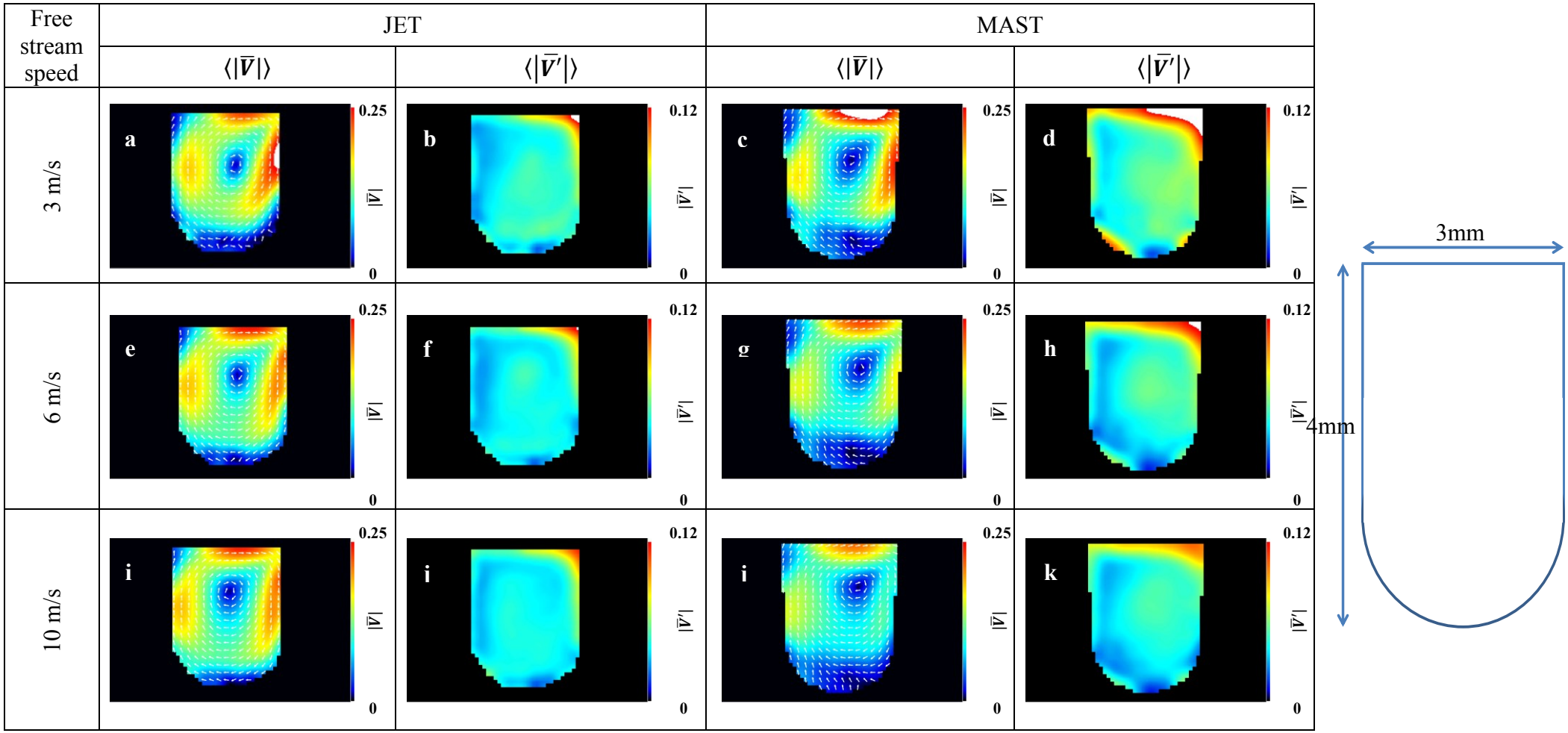

Figure 5.2. Mean normalised velocity and RMS of normalised velocity fluctuations for the JET and MAST geometries.

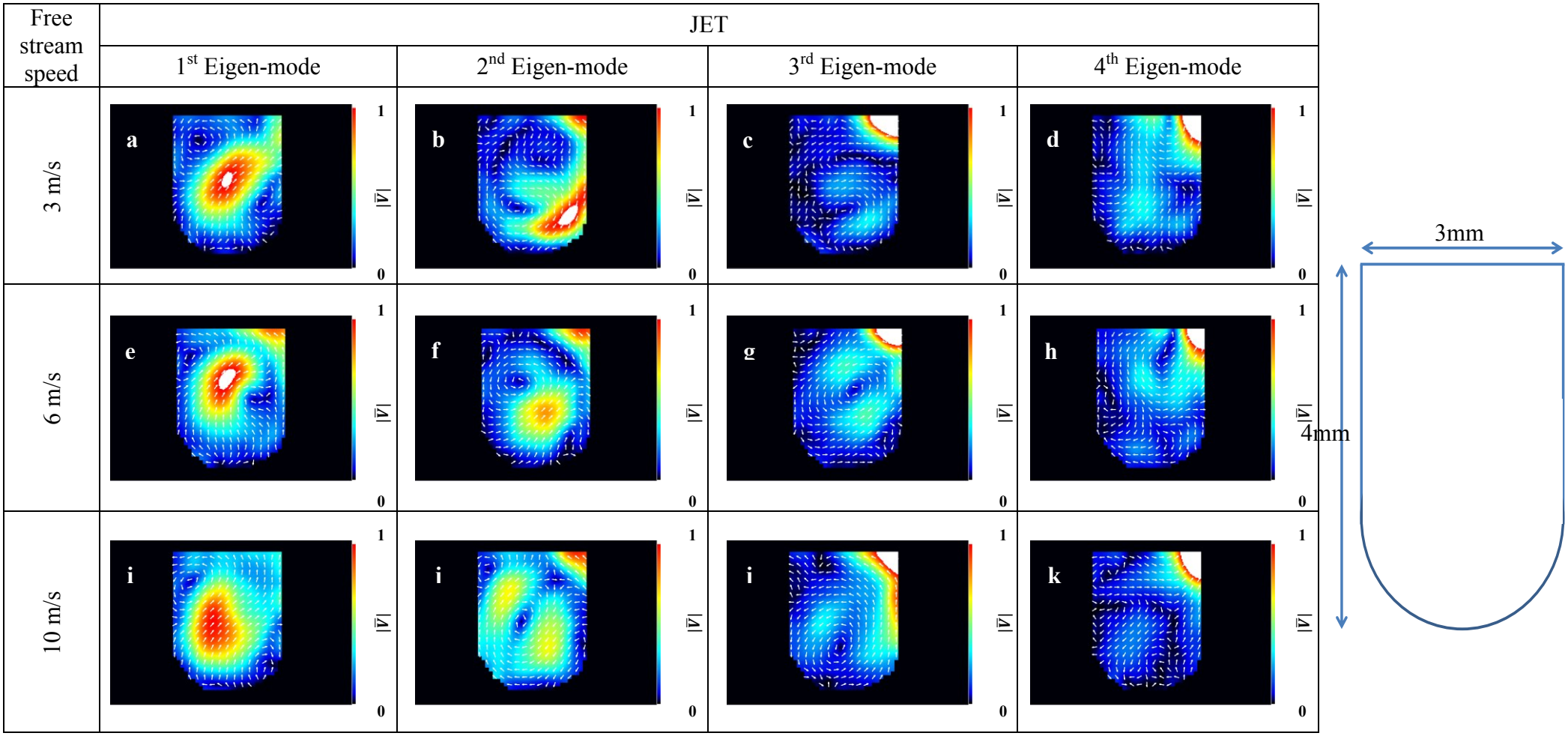

Figure 5.3. POD - first four most energetic Eigen-modes of the normalised velocity field for the JET geometry.

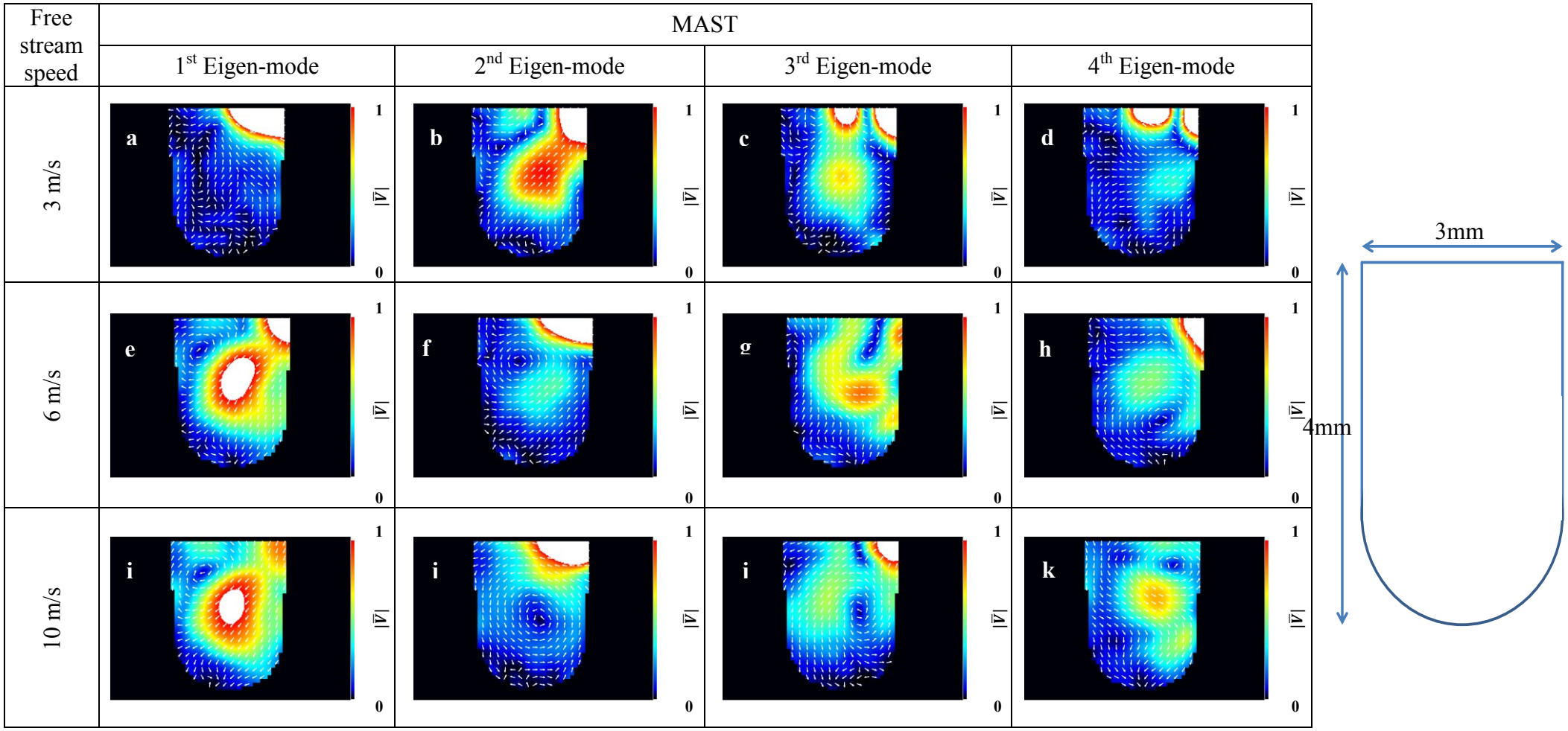

Figure 5.4. POD - first four most energetic Eigen-modes of the normalised velocity field for the MAST geometry.

Table 5.4. Vortex centroid locational stability analysis.

Geometry	Speed/ (m/s)	Groove No	Centroid Position															
			Counts								Statistics							
			Entire Section				Single Groove				Entire Section				Single Groove			
			Low	Average	High	No Vortex	Low	Average	High	No Vortex	Low	Average	High	No Vortex	Low	Average	High	No Vortex
JET	3	1	138	818	26	18	13	955	6	26	0.138	0.818	0.026	0.018	0.013	0.955	0.006	0.026
		2	33	736	221	10					0.033	0.736	0.221	0.010				
		3	15	959	4	22					0.015	0.959	0.004	0.022				
		4	18	955	4	23					0.018	0.955	0.004	0.023				
		5	32	912	18	38					0.032	0.912	0.018	0.038				
		Total	236	4380	273	111					0.047	0.876	0.055	0.022				
	6	1	11	934	19	36	10	964	2	24	0.011	0.934	0.019	0.036	0.010	0.964	0.002	0.024
		2	13	970	7	10					0.013	0.970	0.007	0.010				
		3	21	963	2	14					0.021	0.963	0.002	0.014				
		4	5	965	1	29					0.005	0.965	0.001	0.029				
		5	9	946	8	37					0.009	0.946	0.008	0.037				
		Total	59	4778	37	126					0.012	0.956	0.007	0.025				
	10	1	18	890	20	72	1	950	2	47	0.018	0.890	0.020	0.072	0.001	0.950	0.002	0.047
		2	13	972	10	5					0.013	0.972	0.010	0.005				
		3	10	943	0	47					0.010	0.943	0.000	0.047				
		4	5	924	0	71					0.005	0.924	0.000	0.071				
		5	10	966	2	22					0.010	0.966	0.002	0.022				
		Total	56	4695	32	217					0.011	0.939	0.006	0.043				
MAST	3	1	No established vortex				26	863	14	97	No established vortex				0.026	0.863	0.014	0.097
		2	176	704	41	79					0.176	0.704	0.041	0.079				
		3	31	898	27	44					0.031	0.898	0.027	0.044				
		4	65	858	19	58					0.065	0.858	0.019	0.058				
		5	33	863	45	59					0.033	0.863	0.045	0.059				
		Total	305	3610	837	248					0.061	0.722	0.167	0.050				
	6	1	403	498	49	50	37	885	8	70	0.403	0.498	0.049	0.050	0.037	0.885	0.008	0.070
		2	48	885	12	55					0.048	0.885	0.012	0.055				
		3	51	887	9	53					0.051	0.887	0.009	0.053				
		4	22	949	9	20					0.022	0.949	0.009	0.020				
		5	51	823	83	43					0.051	0.823	0.083	0.043				
		Total	575	4042	162	221					0.115	0.808	0.032	0.044				
	10	1	176	651	47	126	24	883	15	78	0.176	0.651	0.047	0.126	0.024	0.883	0.015	0.078
		2	119	807	30	44					0.119	0.807	0.030	0.044				
		3	25	908	13	54					0.025	0.908	0.013	0.054				
		4	10	964	2	24					0.010	0.964	0.002	0.024				
		5	57	783	94	66					0.057	0.783	0.094	0.066				
		Total	387	4113	186	314					0.077	0.823	0.037	0.063				

Table 5.5. Vortex centroid locational stability analysis with wake formation.

Geometry	Speed/ (m/s)	Groove No	Centroid Position								
			Counts				Statistics				
			Entire Section				Entire Section				
			Low	Average	High	No Vortex	Low	Average	High	No Vortex	Wake Presence
JET	3	1	0	0	0	0	0.000	0.000	0.000	0.000	0.000
		2	0	6	5	0	0.000	0.545	0.455	0.000	0.011
		3	2	84	0	3	0.022	0.944	0.000	0.034	0.089
		4	8	222	1	3	0.034	0.949	0.004	0.013	0.234
		5	7	306	7	15	0.021	0.913	0.021	0.045	0.335
		Total	17	618	13	21	0.025	0.924	0.019	0.031	0.669
	6	1	0	0	0	0	0.000	0.000	0.000	0.000	0.000
		2	0	7	0	0	0.000	1.000	0.000	0.000	0.007
		3	1	58	0	1	0.017	0.967	0.000	0.017	0.060
		4	1	133	0	4	0.007	0.964	0.000	0.029	0.138
		5	1	217	1	9	0.004	0.952	0.004	0.039	0.228
		Total	3	415	1	14	0.007	0.958	0.002	0.032	0.433
	10	1	0	0	0	0	0.000	0.000	0.000	0.000	0.000
		2	0	6	0	0	0.000	1.000	0.000	0.000	0.006
		3	0	34	0	3	0.000	0.919	0.000	0.081	0.037
		4	1	97	0	11	0.009	0.890	0.000	0.101	0.109
		5	0	184	0	7	0.000	0.963	0.000	0.037	0.191
		Total	1	321	0	21	0.003	0.936	0.000	0.061	0.343

Table 5.6. Comparison of the measured normalised speed characteristics of MAST to the JET geometry given as percentage changes - described by equations (4.1) - (4.3)..

Free stream speed/ ms^{-1}	MAST			
	$\Delta\langle\lvert\bar{V}\rvert\rangle$ / %	$\Delta\langle\lvert\bar{V}'\rvert\rangle$ / %	$\Delta\langle\lvert\overline{V_{REL}{}'}\rvert\rangle$ / %	ΔVortex breakup occurrences / %
3	-17.9	14.4	15.0	1.7
6	-30.3	3.1	16.4	3.0
10	-35.4	-2.9	17.7	3.3

Chapter 6

HyperVapotron Particle Image Velocimetry – Nanofluid Experiments

6.1 Introduction

A cold isothermal nanofluid flow is established inside two HyperVapotron models representing the geometries used at JET and MAST using the methodology described in chapter 3. A hybrid PIV method is then employed to map in high resolution (30μm) the flow fields inside each replica. The flow structures obtained with a nanofluid are compared to the ones attained by the use of the traditional coolant (water) in order to detect any departure from the hydrodynamic design operational regime of the device. It was discovered that the flow field of the JET model is considerably affected when using nanofluids, while the flow in the MAST geometry does not change significantly by the introduction of nanofluids.

6.2 Results and discussion

The flow velocity results with a nanofluid are presented in this section and follow the same approach as the one performed earlier with water as the working fluid to aid comparison between the two (chapter 4 and 5). The PIV velocity maps of the middle groove are presented

along with their corresponding RMS values around the mean (averaged in time – temporal) to quantify the morphological features of the flow in the grooves. Tables are provided to quantify the velocity vector maps averaged in time and space (temporal and spatial averaging) to provide information regarding the activity of the vortex inside the groove. The POD analysis aids to identify any significant temporal structures that affect the instantaneous behaviour of the flow in the groove. The morphological and geometrical temporal stability of the flow structures are also quantified to provide further information regarding the instantaneous nature of the flow fields.

The results are non-dimensionalised by the target free stream speed for each condition tested. The uncertainty in setting the free stream target lay in between 3-6% and was the same as that found in Table 5.1. The resolution used for the calculated velocity results was 30μm, while the uncertainty of the vortex locational characterisation analysis tool was below ±500μm, as presented earlier in chapter 5.

The velocity and POD results focus on the third (middle) groove of each test section as it is expected to suffer the least from hydrodynamic end effects that might be present. The POD analysis contains the first four Eigen-modes of the decomposition, as subsequent modes are less energetic or/and provide no additional information regarding the flow patterns observed. The energy level distribution of the POD decomposition for every test section and running condition was similar to those observed with water (Figure 5.1), namely a sharp peak containing most of the energy in the first five to ten modes.

The vortical flow structure locational analysis expanded to additionally include a view of the flow field inside the entire test section. The analysis resolves the state of the vortex namely, identifies whether a vortex is present and calculates its geometrical center hence collecting statistics on the instantaneous vector fields. A flow wake analysis from the grooves was also employed and took into account the flow field inside the entire test section. The routine scans the open boundary of each groove for any wake formations. The wake formations are analysed (span of wake and location is logged) and linked to the corresponding vortex status inside the grooves the wake is situated above. Both of the latter investigations are one dimensional with the coordinate system being perpendicular to the free stream flow and aim to firstly describe the instantaneous operation of the grooves and secondly indicate any effects a wake might be having on them.

The study focuses on the comparison of the flow features obtained with the use of a nanofluid and water in order to provide information regarding changes of the operational regimes of the device with the change of the coolant.

6.2.1 JET related geometry

Velocity field

The normalised tabular data for the velocity field and breakup occurrences of the vortex formation inside the middle groove can be found in Table 6.1. A comparison of the flow information for operation with nanofluids relative to the current operating conditions of the HyperVapotron device at JET and MAST (water with a target free stream speed of 6m/s) are found in Table 6.2.

There is a decrease of the average non-dimensional groove speed by 2%, 24% and 34% for 3m/s, 6m/s and 10m/s free stream speeds with the nanofluid flow. Using Einstein's effective viscosity equation for micron sized suspensions (6.1) and taking account of the very low concentrations of nanofluids used (0.0001%) the changes in the effective viscosity of the nanofluid as a bulk fluid property over the basefluid viscosity are found negligible (2.5×10^{-4}%).

$$\mu_{eff} = (1 + 2.5\Phi)\mu_{bf} \tag{6.1}$$

where,

μ_{eff} : effective viscosity

μ_{bf} : basefluid viscosity

The decrease might hence be linked with local effective viscosity effects exhibited by nanofluids or surface nanoparticle coating as described in section 2.1 which appear to reduce the interaction of the groove flow with the freestream flow and hence the exchange of energy in between the two regions. In comparison, the change in the average non-dimensional free stream speeds for the 3m/s and 10m/s under the water run was minimal and limited to below 3%. The RMS values of the velocity fluctuations for the 3m/s, 6m/s and 10m/s cases are higher (104%, 27% and 5% respectively). The change in the 3m/s and 10m/s case with water

was limited to 8% and under. The relative RMS of velocity fluctuations also appears to be higher than the water runs (37%, 23% and 21% for the 3m /s, 6m /s and 10m /s cases), while the corresponding changes for the water runs were limited to below 4%. The occurrences of the vortex break up inside the middle groove also appear generally higher by 7%, 17% and 30% for the 3m/s, 6m/s and 10m/s cases respectively, while the changes for the water flow conditions are limited to 2% and under .

There are significant changes in the vortex morphology for the nanofluid run (Figure 6.1). The vortex center is lower for all three cases, while the velocity gradients are less steep compared to the water runs with an almost uniform non-dimensional average velocity profile for all three cases. There appears to be a trend on the velocity gradient on the top boundary for all three cases. The 3m/s case appears to exhibit high non-dimensional velocities on the top boundary, while, for the 6m/s and 10m/s cases, those decrease. The RMS of velocity fluctuations (Figure 6.1) also appear significantly altered for the 3m/s case exhibiting high RMS values overall but also especially for the top and bottom boundary of the groove. The RMS values follow a decreasing trend for increasing free stream target speed, which is evident from the RMS field images (Figure 6.1 and Table 6.1).

In general, the use of nanofluid has a substantial effect on the operation of the JET geometry. The non-dimensional average groove speed decreases, the RMS, relative RMS values and breakup occurrences of the vortex increase. The morphological features of the flow structures also appear to change significantly. The changes are considerably larger than those observed for each operational condition with water.

Proper orthogonal decomposition

The Eigen-modes for the JET geometry can be found in Figure 6.2. Unlike the corresponding POD analysis for operation with water (chapter 5), there are not many distinctive features that can be obtained by the POD analysis for operation with nanofluid. The first Eigen-mode for the 6m/s and 10m/s cases indicates the presence of a vortex, however, this does not appear to be similar to the separation vortical structure obtained with water as it is located closer to the lower boundary of the groove. This instantaneous vortex formation does not seem to play an important role in the main composition of the mean vortical structures (the corresponding energy levels of the first Eigen-mode for the 6m/s and 10m/s cases is 8% and 13%). The

remaining Eigen-modes do not contain any further distinguishable flow features apart from background random fluctuations.

Vortex locational characterisation

The instantaneous vortical structures in the third groove appear to be stabilised around their temporal average position for all three flow conditions with the probability that the centroid is around the temporal equilibrium position (within a 0.5mm bounded area above or below the average temporal location of the centroid) being around 62%-81% (Table 6.3). The vortex stability is significantly affected by the use of a nanofluid as the corresponding water results indicate a probability of being close to the temporal equilibrium position of 95%-96% (chapter 5). Upon deviation from the temporal equilibrium position the vortex is statistically more probable to be situated near the lower boundary of the groove compared to the higher boundary for the 6m/s and 10m/s cases, while for the 3m/s the vortex appears to be stabilised at the top part of the groove. The probability of the vortex centroid location being close to its temporal average position decreases with increasing free stream velocity. The vortex locational temporal stability appears to be largest for the 3m/s case.

Similar results are found when considering the statistics of the vortex centroid location in the entire test section for the 3m/s and 6m/s with the overall test section vortex center locational stability in grooves one to five being around their temporal equilibrium position with a probability of 68%-76%. This was significantly different to the general vortex temporal stability of the test section using water which lied in between 88%-94%. It was not possible to record any data for the entire section in the 10m/s case, since the signal-to-noise ratio of the images was too low. It should be noted that a vortex was not established in the first groove for the 6m/s case, which shows the sensitivity of the flow structure to the boundary conditions. The free stream velocity in the real application is not as well conditioned as for the experiment here and it is expected that the turbulence levels of the free stream would be much higher in the real case. It is expected that the formation of the vortical structures in the grooves then could vary a lot more than in the current experiment and cause larger deviations from an ideal operation.

Wake interaction with vortices

Similarly to the operation with water (chapter 5), a wake was also detected for the run with nanofluid (Table 6.4). The probability of the occurrence of a wake at the free stream wall for the 3m/s and 6m/s nanofluid cases is 16% and 4% respectively. At the corresponding water conditions, the probability of wake occurrences was significantly higher at 67% and 43%. It was not possible to quantify the effect for the 10m/s nanofluid case. The wake has minor stabilisation effects on the vortex location for the nanofluid cases, which is similar to water. The wake size and probability of occurrence are reduced compared to water conditions. Owing to the fact that the temporal average vortex centroid for the JET geometry for nanofluid operation is lowered significantly compared to water, it can be concluded that the wake is triggered by interactions between the vortical structures in the grooves with the free stream flow.

6.2.2 MAST related geometry

Velocity field

The normalised tabular data for the velocity field and occurrences of vortex breakup can be found in Table 6.1. A comparison of the nanofluid operation to the current operating conditions of the HyperVapotron device at JET and MAST (water with a target free stream speed of 6m/s) are found in Table 6.2.

There are only small changes of the operational behaviour of the MAST geometry for all cases investigated compared to the water runs. The average non-dimensional groove speed increases from the water operating conditions by 1% for the 3m/s case while for the 6m/s and 10m/s cases there is a decrease of 7% and 17% respectively. The equivalent change with water operation is an increase of 16% and a decrease of 10% for the 3m/s and 10m/s cases. The RMS of velocity fluctuations is increased by 21% for the 3m/s and decreases by 1% and 9% for the 6m/s and 10m/s cases, which is similar to the changes observed with water. The relative RMS values are higher than the water runs by 10%, 3% and 5% for the 3m/s, 6m/s and 10m/s cases. The vortex breakup occurrences display insignificant changes compared to

the current operating conditions (increase of 1% for the 3m/s and a decrease of 1% and 2% for the 10m/s case). These changes are similar to the breakup occurrences when using water for all cases. The morphological features of the vortical structures have no visible differences compared to operation with water.

There is little change of the operational behaviour of the MAST geometry for all investigated cases with nanofluid, which indicates that the functionality of the HyperVapotron device is not compromised by the use of nanofluids throughout the range of considered free stream speeds.

Proper orthogonal decomposition

The POD decomposition of the MAST geometry using nanofluid can be found in Figure 6.3. A separation vortex and a strong diagonal flow are observed from the first Eigen-modes at the 6m/s and 10m/s cases (the corresponding energy levels of the 1st Eigen-mode for the 6m/s and 10m/s are 13% and 15% respectively). Secondary vortical structures do not appear to be important in the main structural composition of the mean flow. These features are similar to the ones found in the POD analysis performed on the same geometry with water (chapter 5).

Vortex locational characterisation

The vortex in the third groove of the test section appears to be stabilised around its temporal average position for all three flow cases with the probability that the centroid is around the temporal equilibrium position (within a 0.5mm bounded area above and below the average temporal centroid) being around 87%-91% (Table 6.3). The corresponding values for water indicated a stability about the temporal equilibrium position ranging from 86%-89%, which is similar to the nanofluid. Upon deviation from the temporal equilibrium position the vortex is statistically more probable to be situated near the lower boundary of the groove. The probability of the centroid location of the vortical structure being close to its temporal average position remains about the same with increasing free stream velocity. The vortex behaviour in the MAST geometry with nanofluid appears to be insensitive to free stream velocity changes.

Similar results are found when considering the flow structures in the entire test section for the 3m/s, 6m/s and 10m/s cases with the vortex stability in the overall test section, namely in grooves one to five, being around their temporal equilibrium position with a probability of 71%-83% which is analogous to what was observed for water (72%-82%). A vortical structure was not established in the first groove for the 6m/s case.

Wake interaction with vortices

Similarly to the water runs, no wake was formed for the MAST geometry with nanofluids.

6.2.3 Comparison of the MAST to the JET geometry with water and nanofluids

The comparison of the JET and MAST geometries with water under the same operating conditions has been presented in chapter 4 and 5. This section focuses on the comparison of the flow structures found in the JET and MAST geometries with water and those found with a nanofluid. The operation of the JET geometry is significantly affected when nanofluids are used instead of water. The average groove velocities decrease significantly, while the vortical structures become more unstable, since the RMS and the relative RMS of velocity fluctuations and the vortex breakup occurrences increase. Morphologically, the JET vortex also exhibits substantial changes when the nanofluid is used; the most notable one is the average centroid location of the vortex forming lower than the one with water. The geometry appears to be more sensitive to free stream speed changes, while this was not the case with the use of water. Secondary flow features that formed the mean profile of the structures appear to have been eliminated or reduced significantly for the JET geometry with nanofluids, as the POD analysis indicates. The overall JET test section investigation indicated significant changes for the temporal equilibrium stability of the model compared to that of water. A wake is equally present in the JET model with the use of nanofluids, but its occurrence is greatly limited compared to water. It is evident that by the use of nanofluids, the vortex centroids move further inside the groove and hence the interaction of the vortex

with the free stream is reduced. It can, hence, be concluded that the wake appears to be triggered by the vortical structures inside the upstream grooves and conveyed downstream.

The operation of the MAST geometry is more stable during the use of nanofluids. The velocity field, the POD analysis and the vortex morphological and locational characterisation studies indicated similar operational features with water. A free stream wake formation was not present with nanofluid, which is the same as for water. It can be concluded that the wake formation, despite the fact that the vortex centroids for the MAST geometry are located close to the groove entrance (and hence the interaction of the vortex with the free stream is high) is suppressed by the increased shear stresses encountered in the narrower free stream section of the geometry.

Focusing on the overall test section vortex characterisation for both geometries, it is evident that with the nanofluid both, the JET and MAST geometries are affected by hydrodynamic end effects, whilst this was not the case for the JET geometry for operation with water. In general, the operational design of the MAST geometry seems to be unaffected by the use of nanofluids, while the operation of the JET geometry is severely affected by them.

Erosion effects may also be critical in the use of nanofluids instead of conventional coolants. Erosion effects can be present in three ways; erosion of the device(s) and plumb work the fluid is streaming into, erosion of the solid nanoparticles used to form the nanofluid or both. There are no conclusive studies to quantify these effects and this is something that must be taken into account before considering the beneficial thermal properties of nanofluids in HyperVapotrons. A study to take account of these effects is under way [167].

6.3 Conclusions

A hybrid PIV method was employed to visualise in high resolution the cold isothermal nanofluid flow structures forming inside two HyperVapotron models representative of the JET and MAST devices currently in operation. The flow structures inside a HyperVapotron are expected to be important in the overall thermal performance of the device. The focus of the study was to quantify possible hydrodynamic changes arising from the change of the

traditional working fluid (water – chapters 4 and 5) to a nanofluid, which in its turn might link to a change in the overall thermal performance of the device before considering the thermal properties of nanofluids alone. The study for both geometries was conducted under three operating regimes defined by the average free stream channel speed of the device at 3m/s, 6m/s and 10m/s.

It is apparent from this work that small nanoparticle concentration nanofluids cause large changes to the hydrodynamic flow fields of HyperVapotrons. It was observed that the JET operational design is greatly affected by exchanging the traditional working fluid (water) with a nanofluid. The non-dimensional average in-groove speed decreases while the RMS and relative RMS of velocity fluctuations and breakup occurrences of the vortical structure in grooves increase. The morphology and wake formation also change considerably while hydrodynamic end effects become important for the device although they were insignificant when using water. In general, the flow structures in the JET geometry with a nanofluid appear to become more unstable compared to operation with water. This indicates that the nanofluid is expected to alter the thermal performance of the device as the changes in the flow field are substantial.

On the contrary, the MAST geometry seems to be more robust to working fluid changes with the device exhibiting similar flow structure characteristics as water. This indicates that the hydrodynamic operational regime of the device remains at the same locus as the original design. However, the Vapotron phenomenon is an exceptionally complex heat transfer process which is controlled by various parameters that cannot be currently modelled. Further study is hence required to fully quantify the effects of nanofluids on the overall thermal performance for both HyperVapotron geometries.

Table 6.1. Measured normalised speed characteristics with a water based nanofluid - described by equations (4.1) - (4.3).

Free stream speed / ms^{-1}	JET				MAST			
	$\langle\lvert\bar{V}\rvert\rangle$	$\langle\lvert\bar{V}'\rvert\rangle$	$\langle\lvert\overline{V_{REL}'}\rvert\rangle$ / %	Vortex breakup occurrences / %	$\langle\lvert\bar{V}\rvert\rangle$	$\langle\lvert\bar{V}'\rvert\rangle$	$\langle\lvert\overline{V_{REL}'}\rvert\rangle$ / %	Vortex breakup occurrences / %
3	0.119753	0.085485	71.4	9.3	0.095817	0.057995	60.5	8.4
6	0.092792	0.052946	57.1	19.6	0.087924	0.047561	54.1	6.2
10	0.080322	0.044058	54.9	32.0	0.079165	0.043777	55.3	5.3

Table 6.2. Comparison of measured normalised speed characteristics with a water based nanofluid and current operating conditions with water given as percentage changes - described by equations (4.1) - (4.3).

Free stream speed / ms^{-1}	JET				MAST			
	$\Delta\langle\lvert\bar{V}\rvert\rangle$ / %	$\Delta\langle\lvert\bar{V}'\rvert\rangle$ / %	$\Delta\langle\lvert\overline{V_{REL}'}\rvert\rangle$ / %	ΔVortex breakup occurrences / %	$\Delta\langle\lvert\bar{V}\rvert\rangle$ / %	$\Delta\langle\lvert\bar{V}'\rvert\rangle$ / %	$\Delta\langle\lvert\overline{V_{REL}'}\rvert\rangle$ / %	ΔVortex breakup occurrences / %
3	-1.9	104.2	37.1	6.9	1.0	20.6	9.8	1.4
6	-24.0	26.5	22.8	17.2	-7.3	-1.1	3.4	-0.8
10	-34.2	5.2	20.6	29.6	-16.5	-9.0	4.6	-1.7

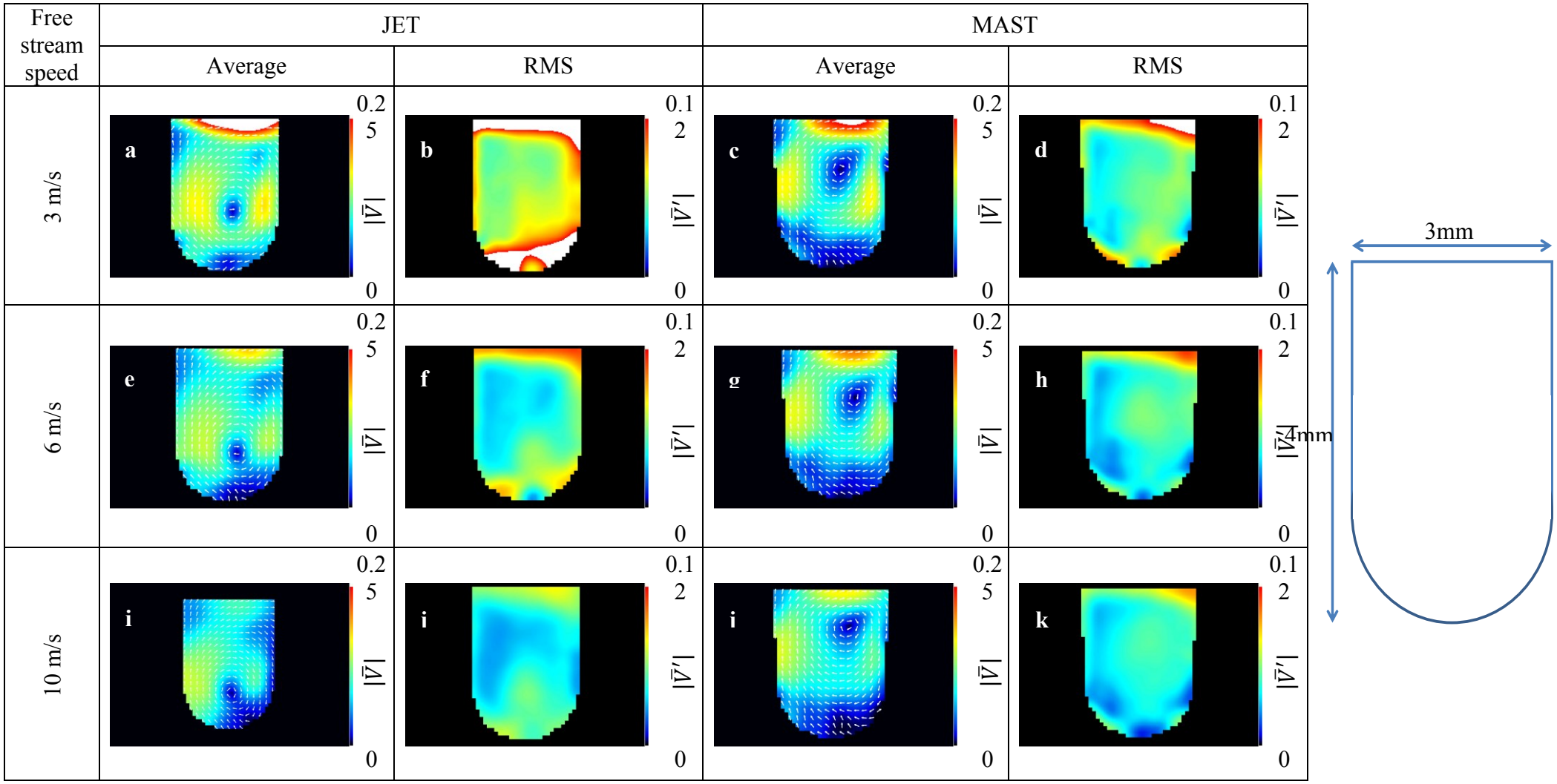

Figure 6.1. Mean normalised velocity and RMS of normalised velocity fluctuations with nanofluid for the JET and MAST geometries.

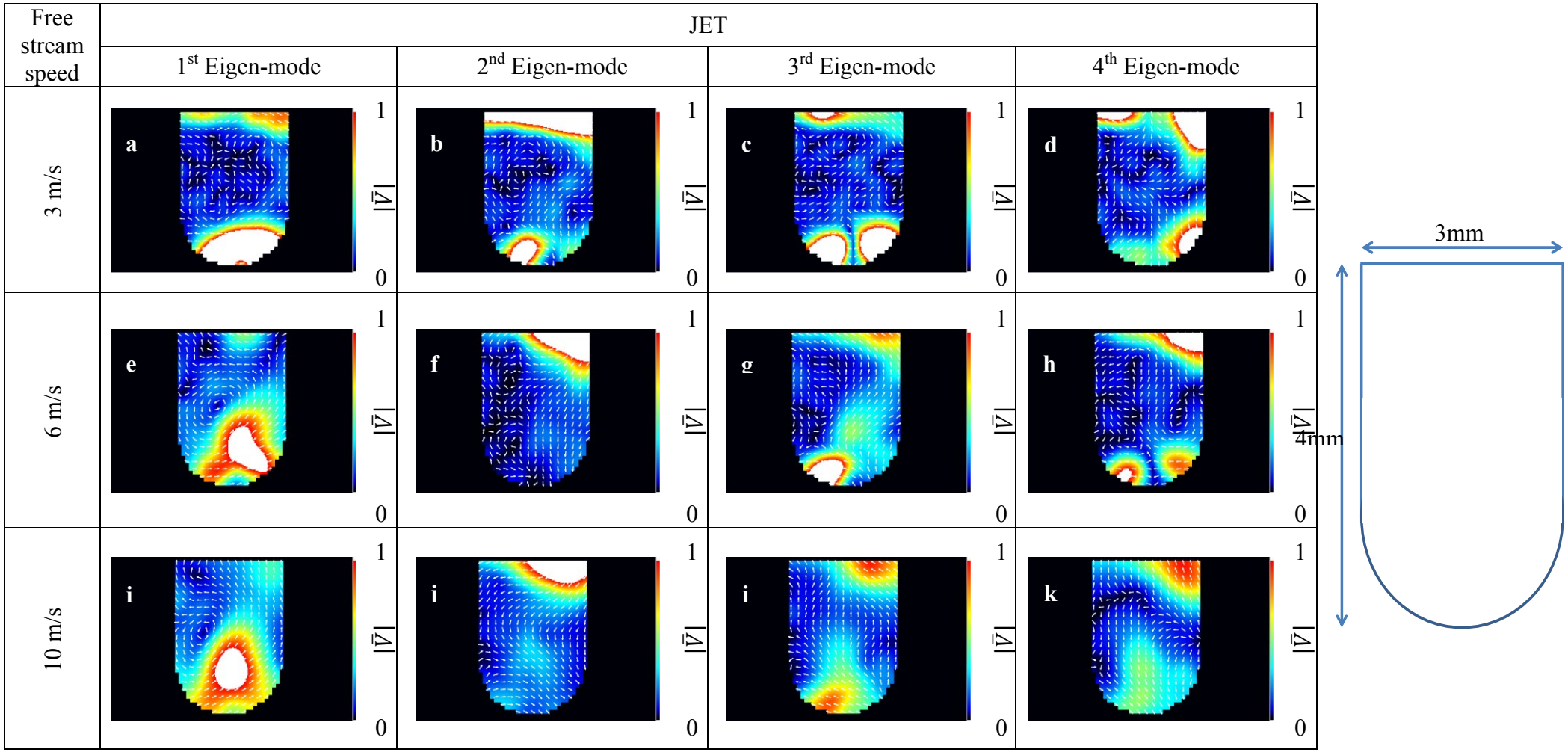

Figure 6.2. POD analysis – first 4 most energetic Eigen modes of the normalised velocity fields with nanofluid for the JET geometry.

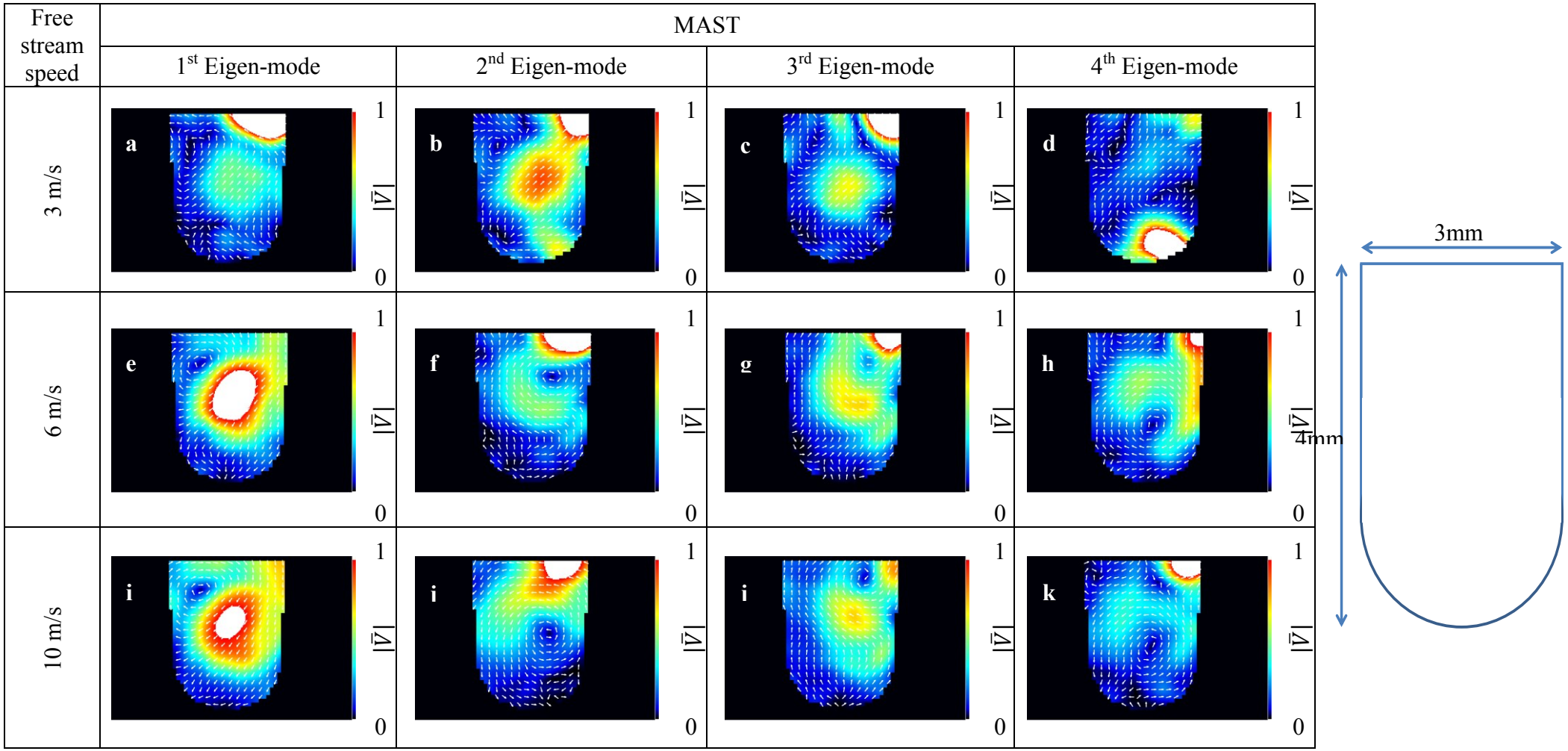

Figure 6.3. POD analysis – first 4 most energetic Eigen modes of the normalised velocity fields with nanofluid for the MAST geometry.

Table 6.3. Vortex centroid locational stability analysis for operation with nanofluid.

Speed/ (m/s)	Groove No	Centroid Position															
		Counts								Statistics							
		Entire Section				Single Groove				Entire Section				Single Groove			
		Low	Average	High	No Vortex	Low	Average	High	No Vortex	Low	Average	High	No Vortex	Low	Average	High	No Vortex
3	1	252	646	93	9					0.252	0.646	0.093	0.009				
	2	266	664	18	52					0.266	0.664	0.018	0.052				
	3	97	776	32	95					0.097	0.776	0.032	0.095				
	4	53	865	22	60					0.053	0.865	0.022	0.060				
	5	96	831	25	48					0.096	0.831	0.025	0.048				
	Total	764	3782	190	264	42	814	51	93	0.153	0.756	0.038	0.053	0.042	0.814	0.051	0.093
6	1	No established vortex								No established vortex							
	2	110	771	45	74					0.110	0.771	0.045	0.074				
	3	76	736	15	173					0.076	0.736	0.015	0.173				
	4	7	973	1	19					0.007	0.973	0.001	0.019				
	5	38	903	3	56					0.038	0.903	0.003	0.056				
	Total	231	3383	888	498	54	732	18	196	0.046	0.677	0.178	0.100	0.054	0.732	0.018	0.196
10	1	Measurement not possible								Measurement not possible							
	2																
	3																
	4																
	5																
	Total					37	615	28	320					0.037	0.615	0.028	0.320
3	1	172	679	138	11					0.172	0.679	0.138	0.011				
	2	193	705	28	74					0.193	0.705	0.028	0.074				
	3	33	905	12	50					0.033	0.905	0.012	0.050				
	4	53	870	22	55					0.053	0.870	0.022	0.055				
	5	31	847	61	61					0.031	0.847	0.061	0.061				
	Total	482	4006	261	251	35	871	10	84	0.096	0.801	0.052	0.050	0.035	0.871	0.010	0.084
6	1	No established vortex								No established vortex							
	2	89	846	23	42					0.089	0.846	0.023	0.042				
	3	35	913	6	46					0.035	0.913	0.006	0.046				
	4	14	958	7	21					0.014	0.958	0.007	0.021				
	5	49	813	101	37					0.049	0.813	0.101	0.037				
	Total	187	3530	1059	224	28	901	9	62	0.037	0.706	0.212	0.045	0.028	0.901	0.009	0.062
10	1	201	635	46	118					0.201	0.635	0.046	0.118				
	2	106	835	24	35					0.106	0.835	0.024	0.035				
	3	28	917	21	34					0.028	0.917	0.021	0.034				
	4	2	969	5	24					0.002	0.969	0.005	0.024				
	5	67	795	75	63					0.067	0.795	0.075	0.063				
	Total	404	4151	171	274	25	911	11	53	0.081	0.830	0.034	0.055	0.025	0.911	0.011	0.053

Table 6.4. Vortex centroid locational stability analysis with wake formation for operation with nanofluid.

Geometry	Speed/ (m/s)	Groove No	Centroid Position								
			Counts				Statistics				
			Entire Section				Entire Section				
			Low	Average	High	No Vortex	Low	Average	High	No Vortex	Wake Presence
JET	3	1	0	0	0	0	0.000	0.000	0.000	0.000	0.000
		2	1	0	0	0	1.000	0.000	0.000	0.000	0.001
		3	0	2	0	0	0.000	1.000	0.000	0.000	0.002
		4	1	38	1	2	0.024	0.905	0.024	0.048	0.042
		5	15	84	2	9	0.136	0.764	0.018	0.082	0.110
		Total	17	124	3	11	0.110	0.800	0.019	0.071	0.155
	6	1	0	0	0	0	0.000	0.000	0.000	0.000	0.000
		2	0	0	0	0	0.000	0.000	0.000	0.000	0.000
		3	0	1	0	0	0.000	1.000	0.000	0.000	0.001
		4	0	4	0	1	0.000	0.800	0.000	0.200	0.005
		5	1	35	0	2	0.026	0.921	0.000	0.053	0.038
		Total	1	40	0	3	0.023	0.909	0.000	0.068	0.044
	10	1	Measurement not possible								
		2									
		3									
		4									
		5									
		Total									

Chapter 7

Molecular Dynamic Simulations Methodology[1]

7.1 Introduction

This chapter describes the developed methodology used to design and run a MDS code in order to simulate from first principles the behaviour of a single nanoparticle dispersing in a temperature gradient of a nanofluid. Previous theoretical investigations, including MDS studies, have not been conclusive in providing a definitive explanation regarding the thermal heat transfer mechanisms employed by nanofluids. This has been the case as the investigators frequently modelled the problem using several assumptions regarding the nature of the fluid and the heat propagation it employs (section 2.1). As a result, it is believed that the outcome of this type of investigations might have been affected by the modelling processes followed. There is hence a necessity to break up the task into its simplest form and with the least amount of assumptions create a model to study the heat propagation mechanisms in nanofluids from first principles.

The current study documents the prologue of a larger scale parametric study to investigate the elusive conductive heat transfer mechanisms employed by nanofluids.

[1] Parts of the work produced in this section were published in the public domain under references [168, 169].

HTCondor® was used to perform a simultaneous large scale deployment of the MDS code across a maximum of 4000 cores for a prolonged running interval. Five million CPU hours were used to design, benchmark and obtain the showcase results presented in this chapter. The showcase results obtained were successfully validated using three widely documented tests from the associated literature. It was discovered that the nanoparticle appears to travel a larger distance when compared to the distance travelled by a fluid molecule (recovery region). The findings were confirmed by calculating the Green-Kubo self-diffusivity coefficient halfway through the simulation at which an enhancement of 156% was discovered in favour of the nanoparticle. This might be the physical mechanism responsible for the experimentally observed thermal performance enhancement in various nanofluids. Future work will reveal in more detail the mechanisms involved in the conductive heat transfer mode studied.

7.2 General domain set-up

This section includes the methodology followed to assemble, test, benchmark and run the MDS code routines.

7.2.1 MDS core code

The core of the MDS code, taken from the literature [196], is written in Fortran 90 and compiled via Microsoft Visual Studio 2008 on a Windows platform (Windows XP and later on Windows 7). The simplified Lennard-Jones potential model, equation (7.1), is used to simulate the forces between atoms in the domain, equation (7.2). Equation (7.2) can be derived upon integrating equation (7.1). Equation (7.3) can be derived from equation (7.2) by substitution and represents the force vector an atom experiences in the domain.

$$\boldsymbol{u}(\boldsymbol{r}_{ij}) = 4\varepsilon\left[\left(\frac{\sigma}{\boldsymbol{r}_{ij}}\right)^{12} - \left(\frac{\sigma}{\boldsymbol{r}_{ij}}\right)^{6}\right] + \varepsilon,\ |\boldsymbol{r}_{ij}| \leq r_c = 2^{\frac{1}{6}}\sigma \tag{7.1}$$

$$\boldsymbol{f}_{ij} = \begin{cases} \left(\frac{48\varepsilon}{\sigma^2}\right)\left[\left(\frac{\sigma}{\boldsymbol{r}_{ij}}\right)^{14} - \frac{1}{2}\left(\frac{\sigma}{\boldsymbol{r}_{ij}}\right)^{8}\right]\boldsymbol{r}_{ij}, & |\boldsymbol{r}_{ij}| \le r_c \\ 0, & otherwise \end{cases} \tag{7.2}$$

$$m\ddot{\boldsymbol{r}}_i = \boldsymbol{F}_i = \sum_{\substack{j=1 \\ (j\neq i)}}^{N_a} \boldsymbol{f}_{ij} \tag{7.3}$$

where,

$\mathbf{f}_{ij}$: force vector between the i^{th} and j^{th} pair of atoms

m : atomic mass

N_a : number of atoms in the domain

$\mathbf{r}_{ij}$: distance vector between the i^{th} and j^{th} pair of atoms

$\ddot{\boldsymbol{r}}_i$: acceleration vector of the i^{th} atom

$\mathbf{u}_{ij}$: potential energy vector between the i^{th} and j^{th} pair of atoms

ε : strength of interaction

σ : characteristic length scale

r_c : cut-off distance at which we assume that the attractive tail of the model is no longer significant

It can be concluded from equations (7.2) and (7.3) that the controlling dimensional parameters of the system are σ, m and ε. Non-dimensionalisation of the system is achieved by substituting r with rσ for the units of length, e with eε for the units of energy and t with $t\sqrt{m\sigma^2/\varepsilon}$ for the units of time. As a result, the equation of motion is reduced to non-dimensional units in equation (7.4).

$$\ddot{\boldsymbol{r}}_i = 48\sum_{j(\neq i)}\left(\boldsymbol{r}_{ij}^{-14} - \frac{1}{2}\boldsymbol{r}_{ij}^{-8}\right)\boldsymbol{r}_{ij} \tag{7.4}$$

The model is used in its 2D form with periodic boundaries on the x and y axes forming the surface of a torus. To ensure that any wraparound effects are avoided (a paradox of having a perturbation from an atom travelling around the smallest wrap-around dimension(s) of the torus and returning to self-affect/excite the atom), the domain dimensions are chosen to be much larger than the cut-off distance of the molecules (the cut-off distance is the distance that defines the extent of the interaction force field for each molecule in the domain). The system is initialised with each atom uniformly distributed in the assigned domain area using a desired density and initial system temperature. The initialisation process aims, firstly, to define the average intermolecular spacing, according to user-

selected number of atoms and density and, secondly, to assign random velocity components to each atom, thus ensuring that the system depicts a collection of atoms at a given time. An equilibration process is applied only once on the first iteration uniformly across the domain and after the velocity vector assignment to ensure that the system is initialised at the given initial temperature. The system is subsequently left to reach a steady state without any more invasive controls on the energy content of the system. The integration of the equations of motion is solved numerically using the 'leapfrog' method.

The domain is initialised with a fixed density of 0.8 Non-Dimensional Units (NDU) and a temperature of 1NDU across the simulations performed. This translates to a square domain size length (L) according to equation (7.5) and an initial indicative velocity magnitude sum used for the first iteration, equilibration, given by equation (7.6).

$$L = \sqrt{\frac{N_a}{\rho}} \tag{7.5}$$

$$T = \frac{1}{dN_a}\sum_i \boldsymbol{v}_i \tag{7.6}$$

where,

d : number of dimensions (here d=2 since a 2D system is used)

T : initial temperature of the system

ρ : overall number density of system

The system reaches steady state in this configuration after the 5000th iteration, which corresponds to a non-dimensional time of 25 units. A time step of 0.005 NDU is selected which, for example, if the system is chosen to simulate liquid argon this will correspond to a real time of approximately 10^{-14} seconds – a typical value used for MDS simulations to ensure stability and accuracy. The link between the numerical MDS calculations presented in this thesis and a real ensemble of monoatomic molecules will be that of liquid argon.

Monoatomic molecules are preferred throughout this investigation while the fabrication of the nanoparticle will also translate to an assembly of monoatomic molecules with altered force relations. This path is preferred instead of modelling the exact chemistry of nanofluids as the domain modelling remains simple requiring less assumptions to set up which might, in their turn, affect the overall solution.

7.2.2 MDS code extensions

Several code extensions were used to build upon the core code and customise it to the needs of the study. The most important ones are listed in this section.

Boundaries and temperature gradient

The core model represented an infinite system, namely a system at which there are no boundaries in any dimension as those are handled by a wraparound function. It was desired to use a semi-infinite system with one dimension being infinite (horizontal x-axis direction), while bounding the system in the vertical dimension (y-axis). This system transformation in space can be envisaged by a shape change from a full toric surface into a cylindrical surface. This was required in order to be able to apply a finite temperature gradient in a bound coordinate and investigate the molecular motion across it without the implications of a wraparound coordinate.

"Walls" are created at the extremes of the y-coordinate. The walls are stochastic, which means that the walls do not have any physical constituency (they are not represented by a fixed chain of atoms or forces at a given location), but an arbitrary theoretical one. The wall theoretical location is marked (i.e. the end of a half domain length with the coordinate system centered at the geometrical center of the domain). The code will detect if any atoms are about to cross the imaginary wall boundary and before updating their location during the next iteration, their location and their y-velocity components will be corrected so as to reflect off the "wall" and return into the domain. This is a hard-wall correction, which does not represent a true physical process and hence leads to minor energy leakages. Never-the-less it is a simple and typical model used for this type of applications, which will allow heat to be extracted or added to the system.

A linear temperature gradient is achieved across the y-direction by regulating the "temperature" of the walls. Keeping the temperature of the lower wall to 1NDU, it is possible to induce a temperature gradient in the system by increasing the temperature of the top wall. The regulation of wall temperature is achieved by the hard wall routines. Every time an atom reflects on the fixed boundaries, its velocity magnitude components can be altered to represent an isotropic energy transfer to the atom. The history of the

velocity magnitudes prior the reflection is logged and an indicative "single atomic temperature" purely based on the kinetic energy of the atom is calculated. If the temperature is different than the prescribed "wall temperature", the code decides if the atom will lose energy (atom hotter than wall) or gain energy (atom is colder than wall) to equilibrate the atomic temperature with the wall temperature during a wall collision. The energy transfer is performed isotropically by matching the overall atomic velocity magnitude to the wall temperature, while preserving the reflection angles and hence the reflected velocity component angles.

Input files and property recording/file saving

Due to the nature of the study, the design of the system had to be flexible to accommodate the large number of simulations to be performed, the computational platforms the simulations were performed on, as well as the parametric studies and postprocessing to be completed. It was hence inherently needed to be able to change on demand the input conditions of the system without the need of recompiling. A routine that reads out all the input properties to be applied to the system from a text file was created to accommodate this need. Extensions were also formed to record system properties into files under a standardised format determined by the postprocessing routines written in Matlab. The flexibility of capturing the system properties for various timings was again something critical hence special saving routines were composed to deal with it. A network saving routine was also constructed which uses operating system call functions to be able to increase the data recording options across different computational platforms used or to be used in the future.

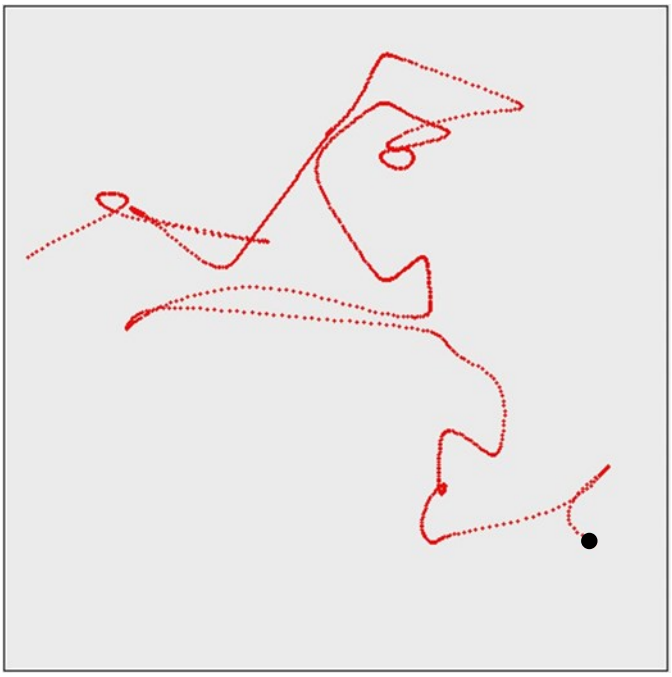

Figure 7.1. Particle tracking routine results.

Atomic trajectory tracking

Atomic tracking routines were essential to visualise the atoms and their interaction with each other. Several lines of code are composed in conjunction with Matlab to be able to record the trajectory of individual atoms. The routines are also able to create plots as stills or video animations to be able to evaluate the correctness of the developed routines (especially the hard wall routines and future multi nanoparticle studies). An example image produced from the atomic tracking routine can be found in Figure 7.1 which depicts an atom performing Brownian motion. The location of the atom (its final position in black colour) is logged at every iteration. The previous locations are marked in red colour and present a time lapse of the atomic motion through the time duration of interest. The temporal spacing of the atomic logging process is constant hence the spacing between each successive red dot indicates the speed at which the molecule was moving between the two time lapse traces (as the distance increases the speed of the molecule increases and vice versa).

7.2.3 Nanoparticle assembly and handling processes

Two approaches were followed to assemble the nanoparticle. The first approach – which required less computational power and complexity – was the "oil droplet" model. Following the validation of the core parts of the extension, it was possible to advance to the final "solid particle" model at which a more elaborate procedure is followed to assemble the nanoparticles while the computational time for the simulations increases significantly. The final assembly routines are based on [210].

The "oil droplet" model

The initial attempts to form a more crystal like particle followed a simple "oil droplet" approach. An atom was selected from the domain and its interatomic attraction value ε was increased from the nominal 1 NDU to a larger value. This enabled the formation of more rigid bonds between the atoms forming the "oil droplet". The larger the ε value, the greater the effects of bond strength variations around the atom. This model was simple and did not require much computational power to conclude hence, the initial model of nanoparticle assembly tested and helped forming the final extensions for both the Fortran 90 and the Matlab code.

The model, however, had limitations which required a more detailed approach. The main limitations arising from the preliminary model were the inability to form a crystallic solid with a fixed size as well as performing any solid-solid and solid-fluid interactions. Cross-correlation routines, equation (7.7), were used to define the boundaries of the "oil droplet".

$$CCR = \hat{\boldsymbol{v}}_i \cdot \hat{\boldsymbol{v}}_{NP} \tag{7.7}$$

where,

$\hat{\boldsymbol{v}}_i$: unit vector of the i^{th} atom

$\hat{\boldsymbol{v}}_{NP}$: unit vector of the central atom of the assembled nanoparticle

$CCR(r_i)$: cross correlation function value for the molecule i located at a distance r from the central "oil droplet" molecule

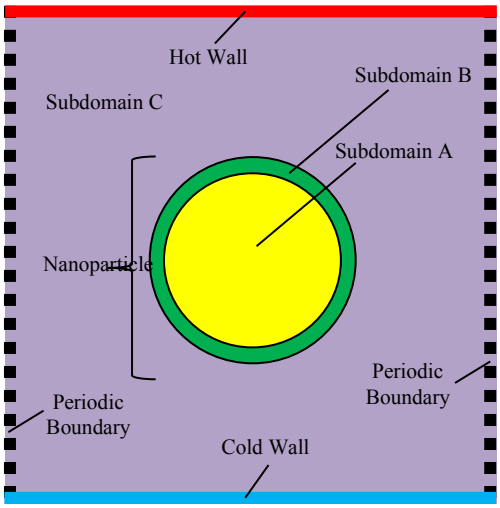

Figure 7.2. Domain set up schematic indicating main features.

A spatial velocity cross correlation function was used to correlate the velocity field of the center of the "oil droplet" to the surrounding molecules at a fixed time. The CCR(r) gives peaks of the directional vector matching of the "oil droplet" central atom velocity vector with that of its neighbouring atoms. The CCR(r) ranges from -1 to +1, with +1 being a case of perfect velocity directional matching and -1 an antiphase velocity vector directional matching of 180º. The peaks of the CCR(r) are expected to mark the atoms which on average move in the same direction as the atom at the center of the "oil droplet" hence identifying a cluster formation. A lower threshold peak value magnitude of less than 1 was used to acknowledge a match in order to allow for small directional mismatching due to the motion of atoms inside the "oil droplet" domain. Other quantities apart from the unit vectors were also introduced in parallel (such as velocity magnitude and local temperature matching) using simpler approaches than equation (7.7); however, the correlation functions gave small and indistinct peaks. This indicated that the "oil droplet" formed was highly volatile and unstable with no defined boundaries in between the droplet and the rest of the fluid atoms as there was an absence of the needed intermolecular forces and interactions to create them. The shape and mass of the droplet was changing continuously from collisions with other fluid atoms or the walls while the fluid-"oil droplet" interactions were performed similarly to fluid-fluid interactions in order to simplify the scripts and reduce the computational power required.

The "solid particle" model

The limitations of the "oil droplet" model led to the development of a more elaborate, computationally demanding and highly complex assembly routine. The solid particle is assembled by the formation of 3 subdomains inside the main domain. The core of the particle subdomain A, the surface of the particle subdomain B and the outside of the particle where the fluid atoms exist – subdomain C (Figure 7.2). The atoms in each subdomain are assigned a different value for their interatomic potential force parameter ε. Subdomain A atoms have an ε_A of 5NDU, subdomain B an ε_B of 2NDU and subdomain C an ε_C of 1 NDU (as commonly used in other MDS simulations [210]). A surface domain is required to limit "evaporation" effects occurring by collisions on the surface of the particle and loss of mass.

A radial selection of atoms is executed to assemble the nanoparticle. This is done by selecting an atom which is regarded as the central atom of the nanoparticle from which the subdomains are radially and concentrically created according to the nanoparticle size chosen by the user (subdomain B is kept at a fixed width of 1NDU). Equation (7.4) is altered to accommodate the effective interatomic attraction parameter $\varepsilon_{eff,}$ equations (7.8) and (7.9), of the combination of forces involved by the interaction of atoms in different subdomains with each other. There are 3! force combination pairs involved (A-A, B-B, C-C, A-B, A-C, B-C as denoted by their subdomain characterisation letters) arising from the various subdomain characteristics and according to the given location of the atomic pairs i-j under consideration.

$$\ddot{\boldsymbol{r}}_i = 48\varepsilon_{eff} \sum_{j(\neq i)} \left(\boldsymbol{r}_{ij}^{-14} - \frac{1}{2}\boldsymbol{r}_{ij}^{-8} \right) \boldsymbol{r}_{ij} \tag{7.8}$$

$$\varepsilon_{eff} = \varepsilon_i \varepsilon_j \tag{7.9}$$

The routine assembles nanoparticles, which are stable, while the surface evaporation is limited by the use of a surface subdomain. An automatic replenishment of lost nanoparticle constituent atoms is performed at each iteration, in order to ensure that the generated nanoparticles retain their size and mass. A crystal-like core is expected to be formed (subdomain A), which still allows limited motion between the bound atoms thus simulating more realistically the energy transitions through the nanoparticle.

7.2.4 Evaluation of developed MDS code

The evaluation of the MDS code was performed using data from [196]. Convergence tests were additionally performed to detect system instabilities. The system properties under the convergence tests were the temperature, equation (7.6), kinetic energy, equation (7.8), potential energy, equation (7.9), total energy, equation (7.10) and system pressure, equation (7.11).

$$E_k = \frac{1}{2N_a}\sum_{i=1}^{N_a} \boldsymbol{v}_i^2 \tag{7.10}$$

$$E_u = \frac{4}{N_a}\sum_{1\le i<j\le N_a}(\boldsymbol{r}_{ij}^{-12} - \boldsymbol{r}_{ij}^{-6}) \tag{7.11}$$

$$P = \frac{1}{A}\left[N_a T + \frac{1}{d}\langle\sum_{i=1}^{N_a} \boldsymbol{r}_i \cdot \boldsymbol{F}_i\rangle\right] \tag{7.12}$$

where,

E_k : non-dimensional kinetic energy of system

E_u : non-dimensional potential energy of system

P : non-dimensional system pressure

For the heated system, it was discovered that with all of the core extensions in place the system properties reach a steady state on average after 20-30 thousand iterations which corresponds to a non-dimensional time of 100-150 units (where the temperature of the system reaches a plateau). Without any energy input (hot wall temperature the same as cold wall temperature) a significant energy leakage was present. The energy leakage was following an exponential trend with the system being drained of 50% of its initial total energy in a duration of 100 thousand iterations and 98% of its total energy in a duration of 1 million iterations. The leak was compensated for and the system reached steady state with the application of a temperature surplus compared to the initialisation state as small as 0.16NDU on the hot wall (for comparison the minimum temperature difference used for the parametric studies performed was 1NDU). The leakage is arising from the implementation of the hard wall model.

The validity of the system with the addition of the extensions was also verified via two test processes. The first was a comparison of the randomness distribution functions, equation (7.11) and Figure 7.3, [211, 212] which provides information regarding the atomic distribution in the domain. The domain is sub divided into regions (grid division)

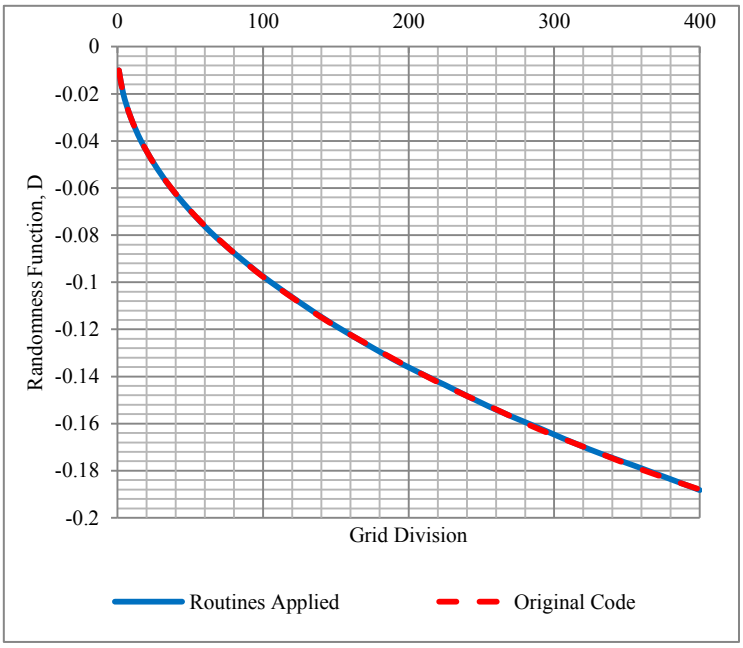

Figure 7.3. Comparison of the randomness distribution functions for changing grid division in a 10,000 particles domain after 100,000 iterations with and without the extensions.

and the atomic number inside each grid is compared to the expected one in order to form an atomic distribution map for different grid subdivisions. This test was performed without the nanoparticle assembly routines active as the system atomic distribution is altered with the formation of nanoparticles hence comparisons with the reference cases (core code with no extensions) is no longer possible. A good agreement with the reference core code was achieved after the extensions are activated hence it can be concluded that the extensions have no effect on the normal operation of the domain.

$$D = \frac{\sigma_{grid}^2 - \lambda_{grid}^{\frac{1}{2}}}{\lambda_{grid}} \tag{7.13}$$

where,

D : randomness function value

σ_{grid} : standard deviation of atomic numbers in each grid cell counted

λ_{grid} : expected number of atoms in each grid cell

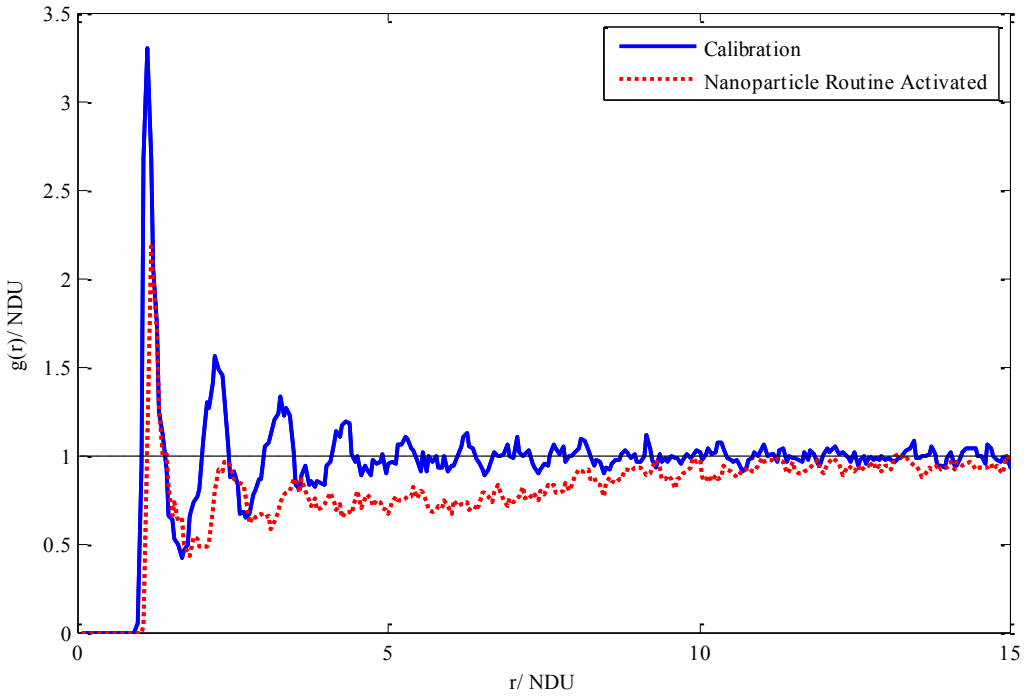

Figure 7.4. Comparison of the RDF plot for the calibration and nanoparticle cases.

The radial distribution function (RDF) was also employed as a validation test. This function provides information regarding the atomic concentration ring bands as seen by an atom at their center, equation (7.12). The peaks and crests of the function, their spacing and amplitude provide a full profile regarding the structure of the domain (all of the thermodynamic quantities of the system can be resolved using the RDF function). The results (Figure 7.4) were in agreement with similar ones found in the literature for the Lennard-Jones model [196, 210, 213] for the "calibration" RDF function plot where the system is used with all but the nanoparticle assembly extensions activated. For the "Nanoparticle" RDF function plot all the extensions are activated and the RDF function is similar to the RDF functions found in the literature regarding crystallic solid dendrimers in fluid/gas mixtures [210, 213-215]. An averaging process of 1000 iterations is used to assemble the RDF functions for both samples. It is evident that the process used to assemble the nanoparticle is creating a compound structure arrangement resembling that of a solid. The process of nanoparticle assembly involves "freezing" the selected atom arrangement and imposing a crystallic intermolecular force profile. As a result, this produces a crystalline structure with less density than the surrounding fluid atoms as

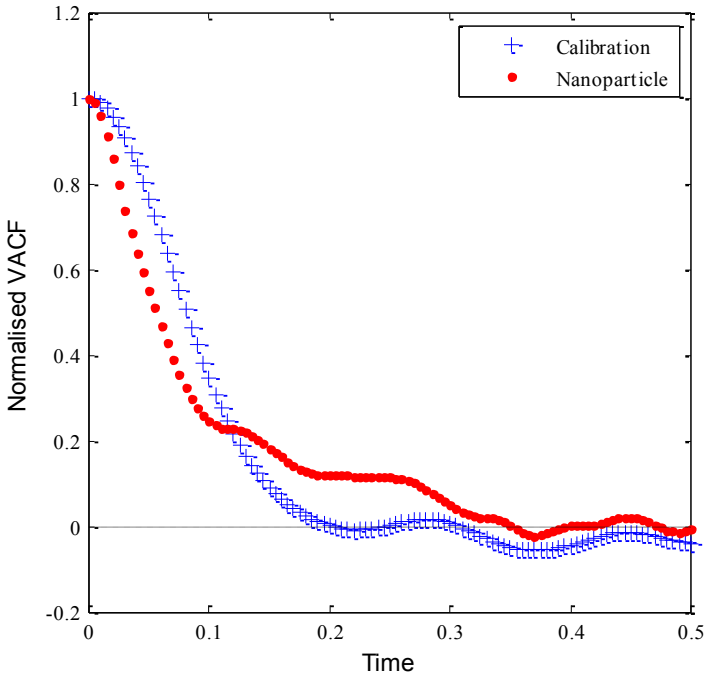

Figure 7.5. Comparison of the normalised VACF for the calibration and nanoparticle cases.

indicated in Figure 7.4. The structure has similar RDF profile to that of a dendrimer. The RDF tends to a value which is slightly sub-one NDU for longer radial distances indicating a marginally reduced density (of about 5%) compared to the theoretical one. This is due to the small deficit of molecules left in the fluid domain because a number of them were used for the nanoparticle assembly. The nanoparticle for this investigation had a radius of 7 NDU of length which corresponds to a mapped real nanoparticle size of 2nm. A fixed temperature gradient, for both cases, of 0.02 NDU of temperature per NDU of length is also imposed.

$$g(r) = \left(\frac{N(r)}{\Delta V(r)}\right) \div \rho \tag{7.14}$$

where,

g(r) : RDF value of the r^{th} ring from the central atom

N(r) : number of atoms in the r^{th} ring from the central atom

ΔV(r) : elemental volume (corresponding ring area in a 2D domain) of the r^{th} ring from the central atom

The mapping of the nanoparticle size is performed by comparing the relative sizes between the atoms/molecules forming a nanoparticle and its carrier fluid in a real nanofluid and applying this size comparison between the fluid atoms and the assembled nanoparticle in

the MDS. For this study, a size mapping relation corresponding to a gold-water nanofluid is applied as the relevant gold to water molecular size ratio matches the relevant nanoparticle to fluid atom sizes found in the MDS code.

The final test performed was to investigate the trends of the normalised Velocity AutoCorrelation Function (VACF) for the nanoparticle and compute the self-diffusion coefficient to verify its agreement with the literature, equation (7.15). The normalised Velocity Autocorrelation Function ($VACF_N$) is described by equation (7.16) and the self-diffusion coefficient can be calculated by the Green-Kubo relationship – equation (7.17).

$$VACF = \langle \boldsymbol{V}(t_1) \cdot \boldsymbol{V}(t_1 + t') \rangle,\ t_1 \leq\ t' \leq t_2 \tag{7.15}$$

$$VACF_N = \langle \frac{\boldsymbol{V}(t_1) \cdot \boldsymbol{V}(t_1 + t')}{|\boldsymbol{V}^2(t_1)|} \rangle, t_1 \leq\ t' \leq t_2 \tag{7.16}$$

$$D_{self} = \frac{1}{3} \int_{t_1}^{t_2} \langle \boldsymbol{V}(t_1) \cdot \boldsymbol{V}(t_1 + t') \rangle dt' \tag{7.17}$$

where,

D_{self} : self-diffusion coefficient

t_{d1},t_{d2} : reference times where the diffusivity investigation initiates (t_{d1}) and ends (t_{d2})

t` : integral time variable

V : particle/atomic velocity vector

The domain has a size of 56x56 atoms with a temperature gradient of 0.02 NDU of temperature per NDU of length. The results are averaged across 1385 simulations.

Figure 7.5 displays a normalised VACF plot for the first 0.5 out of the 5 non-dimensional time units considered in the investigation starting from the 50,000th iteration step (about half way through the simulation corresponding to a non-dimensional time of 250). Two data sets are plotted, one without a nanoparticle formation (calibration) and one with a nanoparticle of 2nm in diameter in place. Both data sets indicate an exponential decay of the normalised VACF, which is in agreement with the literature [210, 216-217].

The self-diffusion coefficient for each iteration step was computed by using the trapezium rule with a linear unit step interval ("trapz" function in Matlab) to calculate the integral of the VACF from a translated time of zero non-dimensional time units (t_{d1}) up to the point where each plot first crosses the x-axis.

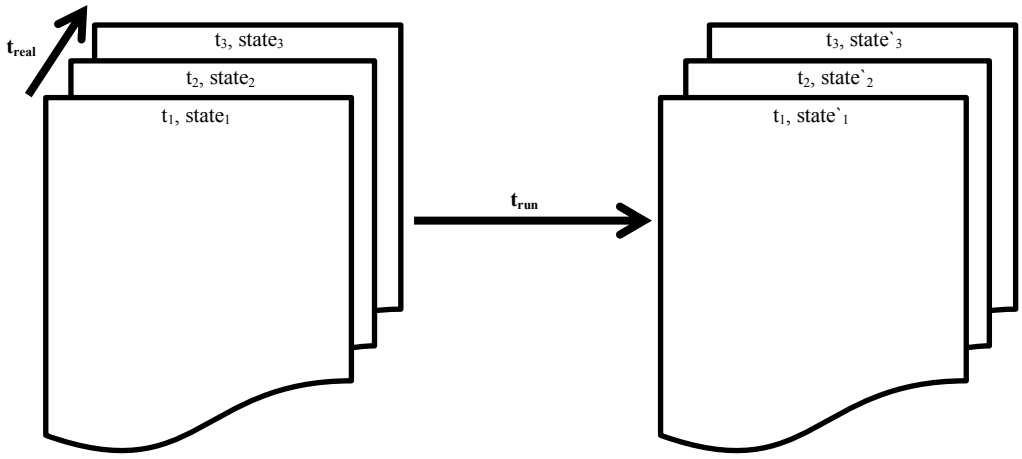

Figure 7.6. Diagram of randomization routines process followed.

7.2.5 Debugging and final version – randomisation routines

Care was required to compose suitable randomisation routines that will allow the extraction of results as well as enabling the debugging process. The validation tests were performed on a small number of simulations – a couple of runs of the order of thousands up to millions of iterations to assess the system status with variable system parameters. During the design and validation process, the randomisation routines are required to create a random initialisation state in time of the system, which should be repeatable. This was achieved by fixing the native randomisation routine input argument (t_i) and hence setting up a random but frozen initialisation state of the system in time ($state_i$). The evolution in time of identical systems (simulation running time t_{run}), given the identical initialisation arguments (t_i), was the same; hence it was possible to study the effects each routine imposed on the system by studying the evolutionary system changes ($state`_i$) compared to the standard basic timeline evolution of the domain (baseline).

In order to extract realistic statistical results on macroscopic thermodynamic phenomena from the code, a more elaborate randomisation process of the initialisation state needed to be performed. In the real world, the atoms in a domain are continuously moving (unless the domain is frozen to either its absolute zero temperature or in time) in a chaotic manner. Hence the system ($state_i$) is different at every instance (t_i chosen to initiate the experiment must be a unique number). If it was possible to record full resolution snapshots of a thermodynamic system through time the probability of getting exactly the

same system state (same molecular speed, location and direction of every atom) as one in the past is impossible considering realistic timescales. The monotonic variable that gives rise to the random arrangements of the system in the real world is the time dimension (t_{real}). As such, in order to recreate the various system states that will model a realistic process, the randomisation routine has to reproduce a different and unique initial state for each complete simulation under account. This was achieved by seeding the native randomisation routine by a unique number (t_{real}), which links the domain time evolution ($state_i$) to the real time dimension.

The seeding process is using the high resolution timing facility of Windows 7 environment, which has a time resolution of 100ns to retrieve the date-stamp (t_{real}) of the execution of the code (date and time are included). The seeder is hence a unique variable that contains the instance of execution up to a resolution of 100ns. Caution in assigning the simulations to the supercomputer has been taken so that each job is assigned sequentially to each core processor with a maximum period of job submission of the order of at least 30ms (namely t_{real} is always a unique number which increases monotonically). The core processors are synchronised with the Windows 7 environment time servers, hence it is assumed that they are all following the same timeline reference. It is hence possible to initialise the domain at a unique state ($state_i$) for the number of simulations performed for each parametric study. A diagram of the process described in this section can be found in Figure 7.6.

7.3 HTCondor® set up

In order to be able to extract the macroscopic thermodynamic phenomena from the MDS calculations, the code requires millions of CPU hours to run. It was estimated that for every data point created in the parametric study to be completed, a total of 1500 realisations are required. This means that for every comparison data point (baseline atom and nanoparticle comparison) a total of 3000 realisations are required in order to retrieve statistically valid results. This presents an immense CPU work load and hence alternative computational platforms are required to carry it through.

It was decided to employ a novel technique to run the vast amounts of simulations required for this study. The current author believes that the development of this path will enable institutions to proceed with high CPU load simulations using cheaper and more user approachable platforms than the ones traditionally used (Supercomputing clusters) which might be otherwise out of reach. HTCondor® is a workload management computing system invented by the High Throughput Computing division of the Department of Computing Sciences of the university of Wisconsin-Madison (UW-Madison) around 1988 (renamed "HTCondor®" from 2012 onwards from "Condor"). The system is able to take advantage of the idling time of networked computer systems (such as ordinary desktop machines) in order to run batch jobs and return the results via the local network. Such system is under trial at the South Kensington university campus of Imperial College London and in collaboration with the Information and Communication Technologies division it was decided to co-develop and test parts of the system to enable computing the lengthy MDS required for the current study.

The system is installed campus wide and has a current maximum capacity of around 4000 cores with a current nominal operational capacity of 3000-3500 cores depending on usage (green saving energy higher order policies of the campus are restricting the maximum usage during the current deployment and testing phase of the HTCondor® system). The machines employed to form the HTCondor® bank of nodes/core processors are 64bit Windows 7 machines incorporating multicore or/and hyper threaded processors that can be employed individually for each job assignment. The machines utilised for this purpose are the same machines located inside computational cluster rooms of the campus used for teaching by students. Automatic HTCondor® script cut off (suspend and vacation routines) provide priority of node utilisation to physical users or higher order functions sent from the ICT division (e.g. for maintenance, updates etc.) over any batch job sent to the system. The HTCondor® is provided under an open source license.

The current campus installation utilises the "vanilla universe" under the HTCondor® 7.8.2 version. This is an operational mode which provides flexibility for running scripts but has limited administrative services. The main limitations of the "vanilla universe" are the lack of check pointing services and remote system calling. This presents

an issue for longer code runs that get interrupted and cannot be resumed on the same node as all progress is lost and the run has to be restarted. As a result, the system was not responding well to increased node user activity.

7.3.1 MDS core code and HTCondor® configuration file adjustment

In order to reach to the final version of the Fortran 90 MDS code for this study, significant alterations had to be performed to suit the HTCondor® node environment compared to the initially developed desktop version. These changes mainly revolved around system performance increase by changing the operational profiles of the code as well as altering the handling routines for the inputs and outputs of the code. The MDS code was compiled into an executable 64bit Windows 7 compatible file and along with the input files it was sent by an HTCondor® function to a temporary storage space on the nodes for execution. The Fortran 90 code had hence to adapt to use dynamic paths for the input and output functions as the paths changed from node to node. The code was also adjusted so as the solution was performed into short blocks, namely, it was preferred to break up the solution into shorter runs of 100k iterations than having a node running multiple simulations from the same execution file. This provides a dynamic and more reliable environment for collecting the required data as a failure to complete a short run will only cause a loss of data for the particular run instead of a series of simulations. Specific hard-kill commands are also incorporated into the MDS code to increase system performance. These routines detect when a case might become unstable and terminate it in a controlled manner in order to retrieve the results produced and free up the available nodes; something which was of great use especially during the designing and debugging process.

The HTCondor® configuration files also had to be tuned to be able to increase the overall performance of the system. Taking account of the large volume of jobs required to monitor by the administration machines, the settings had to be altered from their generic profile to accommodate the specific use for the MDS code. The allocation of jobs was performed sequentially in order of the shorter to the longest runs to increase system utilisation, data retrieval and postprocessing optimisation.

7.3.2 Hardware requirements

The cluster was required to run a large number of jobs (order of thousands) at any given time. This presented one of the largest challenges in setting up the system as there were many limitations on the simultaneous operation, monitoring, assignment and retrieval of the thousands of instances of the MDS code running. It was discovered that several bottlenecks existed, which halted the full deployment of the system. Real time monitoring of the nodes requires fast response from the administration machines to their corresponding nodes. A continuous communication of the nodes is required to keep track of the job assignment and completion as well as dynamically responding to node availability and priority system functions. The communication is performed by having the nodes "touching" periodically their progress files, which are located under the administration machine storage system (pulse check). By increasing the number of nodes, the responsiveness of the storage space of the administration machine appeared to be lagging to the amount of request received. This presented a hardware issue as the hard disks used, the network response and processor response of the administration was insufficient to perform these tasks. An additional problem arose from the lack of Random Access Memory (RAM) required by the HTCondor® administrators to keep track of each MDS run as the amount of memory required was beyond the maximum capacity of the administration machine.

As a result, it was not possible to run more than a couple of hundreds of concurrent simulations on HTCondor® from a single administration machine. It was hence decided to split up the administration of the nodes into six individual machines. Each machine was equipped with a fast Solid State Drive (SanDisk SDSSDP-064G-G25, 64GB, SATA 6GB/s, 2.5inch Internal SSD), where the job communication files are stored and 6GB of RAM. Each administration machine is a 64bit, dual core machine running Windows 7 with a 1Gbit network connection. A shared 1Gbit network space of 180GB for the input, execution and output files was used where each node had access to read and write hence reducing significantly the data transfer load from/to the local administrators. The current hardware provides a maximum simultaneous handling support capacity of 1200 jobs per administration machine (7200 jobs in total from the administration bank), which provides

multiple redundancies for the current system operation as well as accommodating future system expandability. Each administrator is limited to a maximum number of jobs to run under normal operation according to equation (7.18). This limitation is necessary to keep the administration bank load utilisation balanced for long periods of running time.

$$M_{jobs} = \frac{N_{nodes}}{N_{admin}} \tag{7.18}$$

where,

M_{jobs} : maximum number of jobs to assign on each administration machine

N_{nodes} : number of available nodes

N_{admin} : number of administration machines in operation

7.4 Matlab post processing routines

It was decided the extended post processing and assessment of results to be implemented through Matlab scripting. This provides a wide flexibility of postprocessing tools, which are not available or are hard to employ using Fortran 90. The visualisation routines were also implemented through Matlab that aided code development. The main postprocessing routine uses locational data from the trajectory of the central atom inside the nanoparticle as well as the current domain set up of each data set and compares it to the trajectory data of a fluid atom released from the same location as the nanoparticle without the activation of the nanoparticle assembly routine. This is in order to extract the required path statistics for the reference baseline atom and the nanoparticle.

Traditional statistical quantities such as means and their variances are hence required to quantify the change in the properties investigated across every simulation and every iteration. A method of collecting statistical data from each iteration across the range of simulations and iterations performed is followed. This presented challenges as data compression routines were required to preserve the data recorded and allow the execution of the code without overwhelming the RAM capacity of the machine running the postprocessing jobs. The statistics compression algorithm derived uses recursive processes, equations (7.19) to (7.23) to calculate the statistics cumulatively instead of collectively. The entire range of data is not required to estimate the final mean and variance of the

population as this is calculated incrementally. This tactic makes it possible to perform the statistical analysis with minimal memory requirements.

$$\mu_{y_i} = \frac{\sum y_i}{N_{y_i}} \tag{7.19}$$

$$\mu_{y_n} = \frac{1}{N_{y_n}}(\sum y_i + y_n) = \frac{1}{N_{y_n}}\left(N_{y_i}\mu_{y_i} + y_n\right) \tag{7.20}$$

$$\sigma^2_{y_i} = \frac{1}{N_{y_i}}\sum\left(y_i - \mu_{y_i}\right)^2 \tag{7.21}$$

$$\sigma^2_{y_n} = \frac{1}{N_{y_n}}(\sum y_i^2 - \mu^2_{y_n}) \tag{7.22}$$

$$\sum y_i^2 = N_{y_{n-1}}\left(\sigma^2_{y_{n-1}} + \mu^2_{y_{n-1}}\right) + y_i^2 \tag{7.23}$$

where,

y : atomic property y

μ_{y_i} : mean of the 1st up to the ith value of population property y

μ_{y_n} : mean of the 1st up to the nth value of population property y (n>i)

$\sigma^2_{y_i}$: variance of the 1st up to the ith value of population property y

$\sigma^2_{y_n}$: variance of the 1st up the nth value of population property y (n>i)

The Matlab routines also offer automatic incremental backup, stop and resume functions in order to minimise data and computational time losses in case of a system crash when they are implemented on a desktop machine. The routines are also adjusted and compatible to run on HTCondor® should an increased load of post processing is required. The incremental backup, stop and resume functions are unavailable when they are deployed through the condor system due to aforementioned limitations of the “vanilla universe”.

7.5 Results and discussion

7.5.1 System operation and performance

The preliminary test cases investigated how the code and HTCondor® react to long and short code runs. It is estimated that the process of designing, debugging and testing all of the systems as well as obtaining the first showcase results documented in this study to have taken an equivalent running time of about 5 million CPU hours. It was discovered that the performance of the system drops significantly for runs of the order of 16hrs and over. The performance was also moderately reduced for short runs (runs shorter than 1hr). A further investigation indicated that the bottlenecks encountered for the longer runs were due to the lack of checkpointing and network drive speed limitations upon batches of runs reaching completion. The longer runs have higher probability of getting interrupted by priority functions or users at the node systems and with the lack of a checkpointing facility the runs are cancelled and restarted.

Moreover, even if the longer runs do reach completion – even though countermeasures are taken to limit this case up to a permissible degree by randomising the write intervals after completion – there is still a high probability that a large number of nodes is simultaneously trying to transfer and write up data to a single network storage node which gets overwhelmed and discards connections. As such, the system will cancel the nodes that fail to write up the data in a pre-allocated time interval and restart them on a different node. These two competing factors are hampering significantly the overall system performance. Shorter runs present a similar problem however; the countermeasures in place (random assigned time delays in data transfer) as well as the distribution, allocation and running time of very short jobs reduce the impact of the problem compared to the longer runs. A maximum performance was reached for runs taking around 5 hours to complete at which the problems of data transfer and the probability of simulation interruption are minimised.

The problems concerning interruptions by a priority service or a user at the node machines can be resolved by forming up a checkpointing facility. This is not offered by the native HTCondor® software as an option for the “vanilla universe” running on Windows

platforms. In this case the only way to resolve the issue (without affecting the primary user functions of the nodes at the campus) is by changing the universe HTCondor® is running the jobs in to a different one which provides more services (for example the "standard universe"). Nevertheless, this will have as a result to limit up to a large degree the flexibility the node platforms present to run scripts through the system. There is also the possibility of hard coding checkpointing functions in the "vanilla universe" however; the first attempts performed for this study indicated extensive problems with the stability of the system due to the extensive higher order campus network security and operation policies. A tertiary solution would be to abolish the singular network storage scheme and employ a clustered storage scheme with fast SSD drives. HTCondor® offers this facility by disabling network storage and setting up for the files each node produces to be returned back to the administration machine. This is something to be tried in the future before larger scale changes are attempted however; this solution will impair a large CPU use of the administration machines to write the high volume and short response rate network data required which might as a result limit the overall node volume handling capacity by the administrators.

7.6 MDS showcase results

The results from an example run are included in this section as a showcase for the MDS, Matlab and Condor scripts and hardware. The study focuses on a 3136 atom domain (56x56) with an applied temperature gradient of 0.02 NDU of temperature per NDU of length. The nanoparticle has a radius of 7 non-dimensional length units, which corresponds to a physical mapped size of 2nm (diameter). The coordinate system is placed at the release point of the baseline atom and nanoparticle which is the middle of the domain as shown in Figure 7.7. The vertical coordinate is aligned with the temperature gradient while an arbitrary alignment is chosen for the horizontal coordinate.

Figure 7.8 shows a plot of the average one dimensional distance vector (against the temperature gradient) followed by a fluid atom and a nanoparticle both released from the same domain location (middle of the domain). The plot indicates a clear distinction between the average behaviour of a nanoparticle and a fluid atom (baseline atom). The

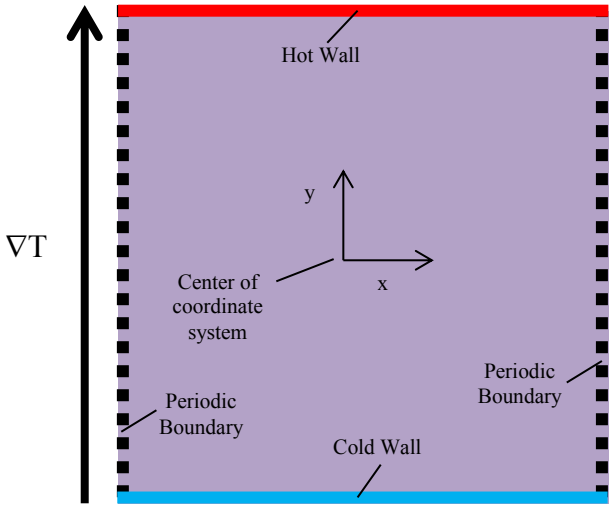

Figure 7.7. Domain analysis set up schematic.

largest differences appear to become evident in the region where the nanoparticles and baseline atoms begin moving along the temperature gradient (the gradient of the distance plot becomes positive) which might be an indication for the enhancement observed in nanofluids. In depth analysis on the distance vector plot and the parametric investigation followed are described in chapter 8.

The self-diffusion coefficient for the calibration and nanoparticle cases as described in section 7.2 were found to be 0.0472 and 0.1208 non-dimensional length units squared over non-dimensional time units respectively. For the given interval, the self-diffusion coefficient is 156% larger compared to a baseline atom in the domain, which might be accounted for the thermal phenomena observed in a real nanofluid.

7.7 Conclusions

A Fortran 90 MDS code has been composed to model a simplified nanofluid containing a single nanoparticle. The code is based on the Lennard-Jones potential model. The code was evaluated using three test cases; namely a randomness function test, a RDF test and a normalised VACF test. The results were cross-checked and were in good agreement with the literature. This provides confidence into the subsequent results obtained from the simulations.

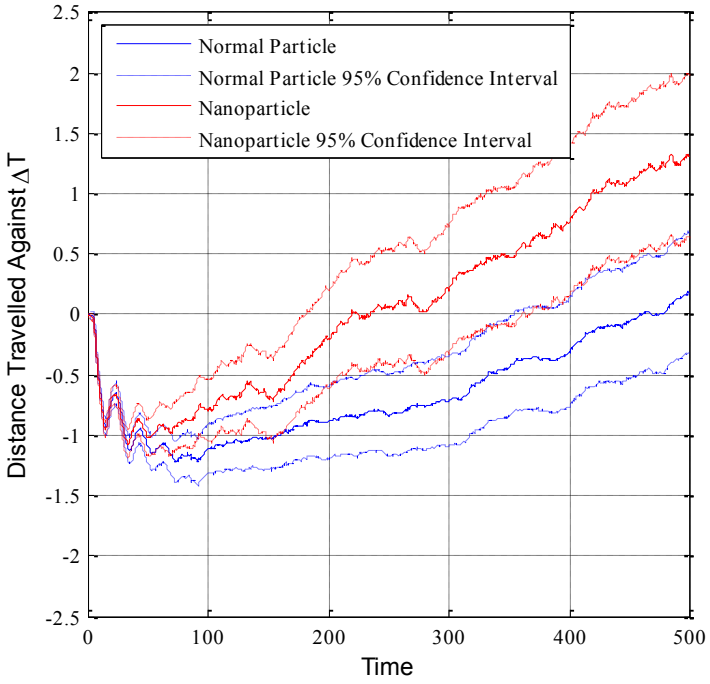

Figure 7.8. Distance vector plots for a baseline atom and a 2nm nanoparticle released from the same location in a domain with a fixed temperature gradient

The code was developed to run on the HTCondor® cluster and effort has been put into developing both the software and hardware to enable a large scale deployment and control of the simulations. Due to the magnitude of the raw data received, postprocessing routines were composed on Matlab and special compression techniques applied to enable handling the large volume of data recorded. Five million CPU hours were used for the design, testing and production of the different pieces of MDS code, as well as for the showcase results.

Showcase results for a 2nm nanoparticle in a 56x56 atom domain with 0.02 non-dimensional temperature gradient units are obtained. The 1 dimensional distance vector results indicate that on average the nanoparticle appears to cover more distance compared to a fluid atom (baseline atom) during its motion along the temperature gradient – recovery (from a time of 80 NDU and onwards). The self-diffusion coefficients for the nanoparticle and baseline atoms were also calculated using the Green-Kubo relationship at a starting time reference of 250non-dimensional time units. It was discovered that the nanoparticle self-diffusivity has an enhancement of 156% over a baseline atom released from the same location (middle of the domain) for the particular time interval investigated. This study

presents the prologue of the parametric investigation performed towards understanding the conductive heat transfer modes employed by nanofluids in chapter 8.

Chapter 8

Molecular Dynamic Simulation Calculations of Nanoparticle Surrounded by Fluid

8.1 Introduction

This chapter attempts to decipher the elusive heat transfer mechanism for the conductive heat transfer mode of nanofluids via a MDS code. A size parametric test was conducted involving four nanoparticle sizes – 0.6nm, 1.1nm, 2nm and 2.9nm in diameter. The domain size scales linearly with the diameter of the nanoparticle to ensure that the effect of the domain size on the results is minimised as well as preserving computational time efficiency. The minimum domain size was kept at 1600 atoms and it was valid for the lowest two nanoparticle sizes tested. The analysis followed is described in Chapter 7 with the addition of a domain temperature study as required by the new findings. The findings of this study are the first of their kind and suggest a conflict of the so far theories and trends applying to heat transfer propagation through micron sized slurries and pure matter. The findings provide a proposal for the formulation of a complex new type of heat transfer mechanism which might explain the abnormal heat transfer augmentation observed.

8.2 Results and discussion

8.2.1 MDS results

Figure 8.1a shows a plot of the average distance vector comparison between a 2.9nm nanoparticle and a fluid atom (baseline atom). Figure 8.1b shows the results of the difference in the distance vector between a nanoparticle and the baseline atom for different nanoparticle sizes. Figure 8.1a and the derived Figure 8.1b contain distinctive features. On average, both the nanoparticle and baseline atom display a sharp movement towards the cold region of the domain (kick) followed by a slow recovery into the hot region. For the entire duration of the kick, the nanoparticle seems to lack behind the baseline atom while for the recovery the nanoparticles are ahead of the baseline atom. Additionally, for both cases there appears to exist an oscillation for a range of zero up to 100-150 time units which corresponds to the system heating up duration.

The initial kick might be accounted due to Thermophoresis. Thermophoresis is a force which acts to cause migration of atoms and particles against the temperature gradient of their surroundings according to equation (8.1) – macroscopically and ignoring

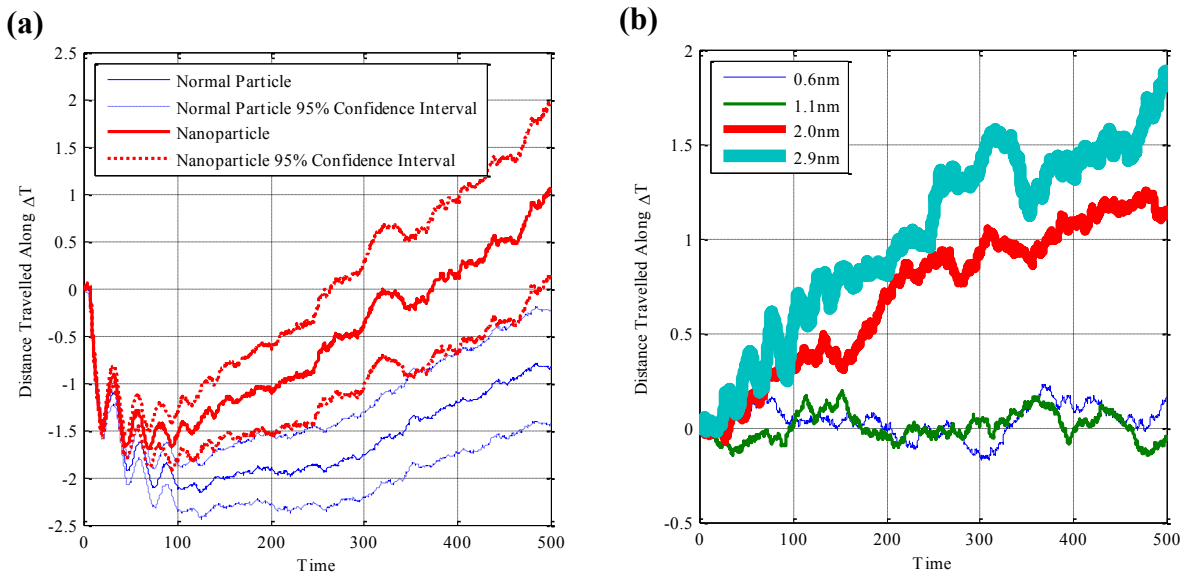

Figure 8.1. (a) depicts the average distance vector for the 2.9nm particle and baseline while (b) shows the parametric study results on all sizes tested and shows the differences in distance covered by the nanoparticle and baseline atom.

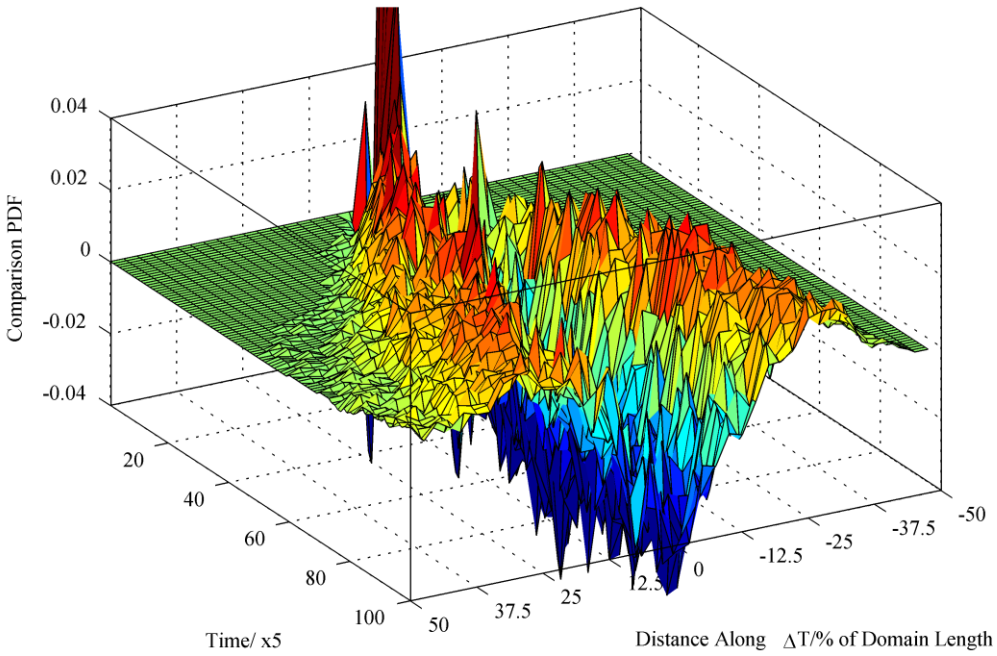

Figure 8.2. Comparison of 3D PDF histograms between a 2.9nm Nanoparticle and the baseline atom. Positive values indicate that the PDF of the nanoparticle is larger than the PDF of the baseline atom.

temperature variations inside a particle itself [218-220] – and is hence responsible for causing an initial average motion of atoms and particles towards the cold region of the domain. The nanoparticle seemingly lacks behind the baseline atom perhaps due to the larger mass it possesses hence inertia effects come into play to reduce the effects of Thermophoresis on the trajectory followed.

$$F_{TP} \propto \frac{d_p \nabla T}{T} \tag{8.1}$$

where,

F_{TP} : Thermophoresis force

d_p : atomic/particle diameter and

T : temperature of the domain.

The Thermophoresis looks to be initially dominant as the local ∇T is large during the system heat up period while T is small. When the system reaches a constant global average temperature, the thermophoretic effects are expected to reduce as the local ∇T reduces to the global value and the average temperature of the system increases. The Thermophoresis in this case shows a global number density increase towards the cold region of the domain.

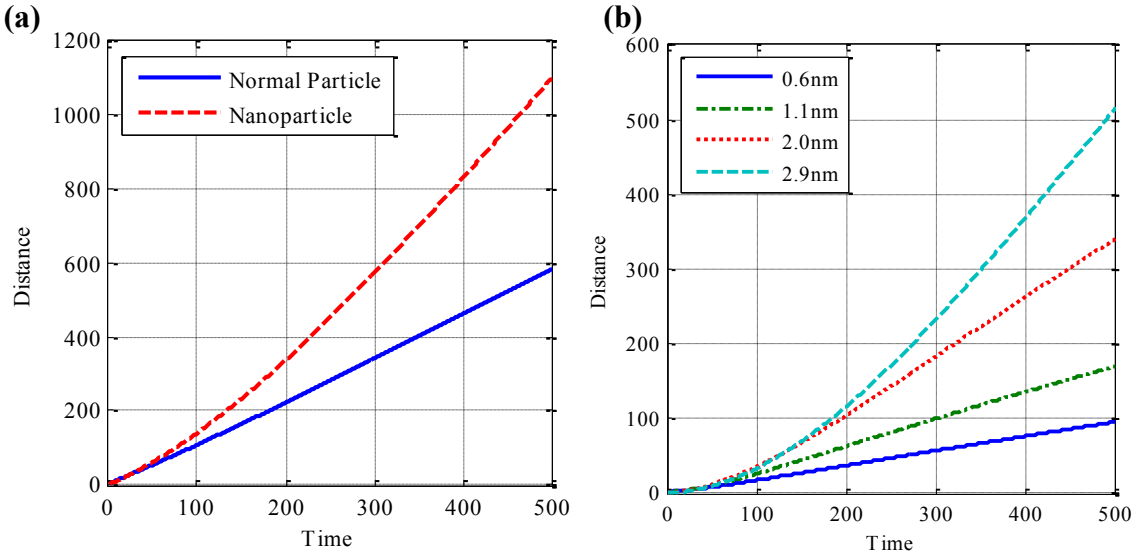

Figure 8.3. Absolute distance covered plots for a 2.9nm particle and the baseline in (a) and a size parametric study of the absolute distances covered comparison between the nanoparticle and the baseline atom (b).

A number density gradient is formed with an opposite sign to the temperature gradient established in the domain. According to Fick's first law of diffusion, equation (8.2), a diffusion force is expected to be established which acts to the opposite direction as the number density gradient initially established. This force becomes dominant over the Thermophoresis force and hence it might be responsible for the slow recovery – evident for both the nanoparticle and baseline atom – back to the hot side of the domain.

$$J = -D_F \nabla \Phi_p \tag{8.2}$$

where,

J : diffusion flux

D_F : diffusion factor/coefficient

Φ_p : concentration of atoms/particles in consideration.

However, this cannot still explain the apparent increased distance covered by the nanoparticle compared to the baseline atom and how this correlates with the size of the nanoparticle.

The initialisation of the simulation and the application of the hot wall on a "cold" system induces a large perturbation which then propagates through the system as a thermal wave. The perturbation dies out as the system reaches a constant global temperature as the local temperature gradients are smoothed out to the steady state ones. This has as an

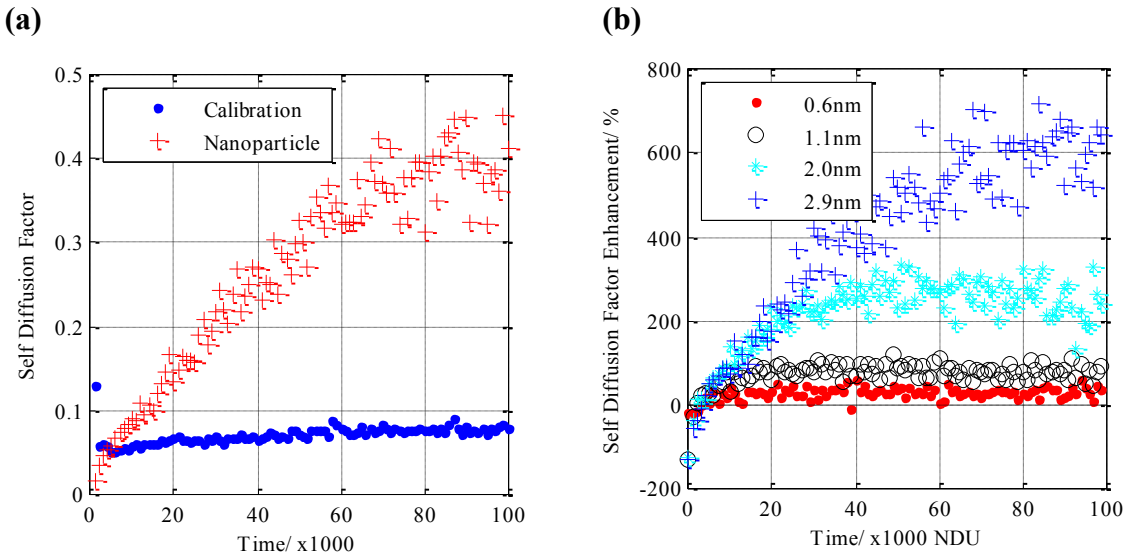

Figure 8.4. Self-diffusion coefficient for a 2.9nm particle and the baseline in (a) and a size parametric study comparison of the self-diffusion coefficients comparison between nanoparticles and the baseline atom (b).

indicative result the oscillatory behaviour of atoms and particles seen from time 0 up to 100-150 non-dimensional time units in Figure 8.1. The effects are observed to be larger for larger systems as by keeping a constant temperature gradient across the domain results in higher hot wall temperatures – hence making the initial local perturbation larger. The increase of domain size has also a direct effect on the duration of oscillations in time as the larger perturbations require longer times to traverse and eventually die out in a larger domain upon reaching steady state.

Focusing on the one dimensional spread of atoms and particles along the temperature gradient, Figure 8.2 shows an example comparison plot of the 3D histogram probability density function (PDF) of a 2.9nm nanoparticle and the baseline atom (positive peaks indicate an increased probability for a nanoparticle to occupy the investigated position whilst negative peaks indicate that the baseline atom is most probable to occupy the investigated position). The 3D histograms quantified the effects of the temperature gradient and confirmed that there appears to be an increased probability that the nanoparticles will travel further away from their initial release point compared to the baseline atom. The effect is more pronounced as the nanoparticle size is increased. The comparison produces a noisy profile near the hot wall as the probability of differential

atomic and particle distributions in this more active region is higher (hence the wrinkling of the zero-difference sheet closer to the hot wall in Figure 8.2).

Spread plot studies were performed indicating that in two dimensions the nanoparticles appear to have larger probabilities to travel further away from their release point compared to the baseline atom. The spreads appeared isotropic which indicated that the mechanism employed might give rise to an increased mobility in all directions including those that do not contain any thermal boundaries (horizontal x-direction in this study).

Absolute distance covered plots showed the activity of the atoms and particles. Figure 8.3a shows an example plot from the 2.9nm case whilst Figure 8.3b shows a parametric size study plot indicating the differences found between the absolute distance covered by a nanoparticle and the baseline atom. The plots indicate significant differences with the nanoparticle covering up to twice the distance of a baseline atom for the same time interval. The effect is more pronounced as the nanoparticle size is increased. This also reflects on the residence time studies performed which indicate that even though overall the baseline atom and particle spend most of their time in the cold region (as their effective velocities are expected to be lower in that region), the nanoparticle case can spend up to 6.3% more time inside the hot region compared to the baseline atom with a tendency of the time spend for longer times inside each region reaching a 50-50 distribution for the nanoparticle case.

The latter results on the increased activity of nanoparticles are also confirmed by calculating the self-diffusion coefficient for the nanoparticle and baseline atom (Figure 8.4). Figure 8.4a shows the self-diffusion coefficient for a 2nm nanoparticle and the corresponding baseline atom while Figure 8.4b shows a comparison on the parametric size investigation of the self-diffusion coefficients between a nanoparticle and the baseline atom. As expected, the baseline atom has a fixed self-diffusion coefficient throughout the simulation at longer computational times. The nanoparticle indicates a transient behaviour at which the particle reaches its maximum self-diffusion coefficient value after a significant amount of time. The effect is more profound for larger nanoparticles; particularly, for the 2.9nm nanoparticle, the duration of the simulation is not enough for the nanoparticle to reach its maximum value. This is an indication that the nanoparticle

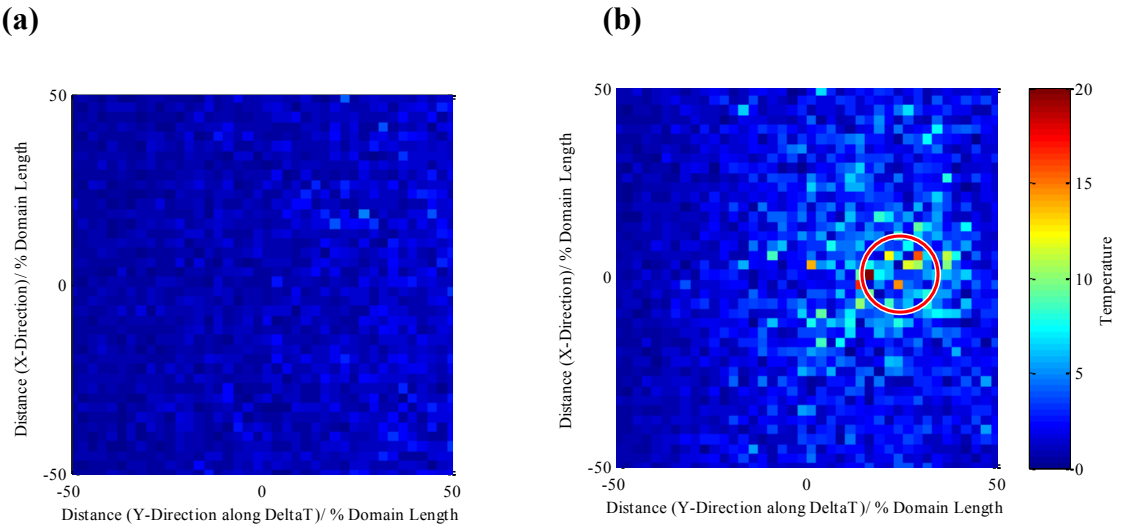

Figure 8.5. Instantaneous temperature profiles for the baseline atom in (a) and a 2.9nm Nanoparticle in (b) in the domain. The temperature scale colour map has been preserved for both images. The red circle in (b) represents the nanoparticle crystallic boundaries.

appears to be dramatically more active compared to the baseline atom cases which goes against the classical theories for the associated mean squared displacement of large particles compared to small micron sized particles [221].

The local instantaneous temperature profiles (averaged over 10 consecutive iterations which can be considered a very short time for considerable particle dynamic changes) of the baseline atom and the 2.9nm nanoparticle case are plotted in Figure 8.5 (the grid cell resolution for temperature calculations is 0.625% of the domain length). The same domain with the nanoparticle assembly routines inactivated (Figure 8.5a) and activated (Figure 8.5b) are plotted. The nanoparticle appears to become a hotspot which affects the surrounding area creating areas of mismatching surface temperatures between the nanoparticle and the surrounding argon atoms.

8.2.2 Formulation of a new type of heat transfer mechanism valid for nanofluids

There is a suggestion for the existence of a complex heat transfer mechanism employed by nanoparticles as indicated by the findings of the study. The nanoparticle, even though it is larger in size appears to be more active compared to smaller particles when placed in a

temperature gradient. This goes against the classical thermodynamic theories for diffusing particles. Previous investigations on the self-diffusion coefficient of nanoparticles in domains without the presence of a temperature gradient also indicated departure from the Einstein's diffusion relationship for micron sized particles however, they were in agreement with the inverse proportionality relationship of the self-diffusion coefficient with the particle radius [217]. In addition, other studies with hard sphere or/and assembled nanoparticles using similar assembly models as the current investigation but without the presence of a temperature gradient; indicated an overall lower self-diffusion coefficient for nanoparticles [210] compared to baseline atoms. The literature comes in direct disagreement with the findings of this study concerning the activity of nanoparticles in isothermal domains and excluding thermal quantum effects.

Given the results of the current analysis, it can be proposed that the effects of increased nanoparticle activity observed are perhaps due to a complex mechanism arising from the apparent mismatch of the temperature (kinetic energy ensemble) across parts of the surface of the nanoparticles and the surrounding atoms. The temperature disparity possibly induces a local thermophoretic force which might cause the enhanced mobility effects observed on the nanoparticle. The mismatch is the outcome of different heat transfer coefficients across the crystallic structure of the nanoparticle and the fluid as well as the ability of the nanoparticle to translate and rotate which as a result give rise to a different collective atomic activity (local temperature) between certain regions of the particle and the surrounding fluid atoms (this is observed in Figure 8.5). The increased nanoparticle temperature arises from the fluid to solid incompatibility of energy transfer at which the energy inside the nanoparticle (apart from part of it getting converted into potential energy, translational and rotational motion of the nanoparticle) is accumulated in the form of high frequency and small amplitude vibrations. On the contrary, the energy in the fluid domain is stored in the form of translational motion whilst part of it converted into potential in between the atomic bonds. The collective effect of this classical mechanical model is manifested as the Kapitza resistance found in the literature [1, 12, 13].

The nanoparticle apparently becomes more active for larger nanoparticle sizes. This might be explained via the new mechanism proposed as the size increase of the nanoparticle increasing the probability of a temperature mismatch to occur across certain

parts of the nanoparticle. In addition, translational and rotational events are expected to enhance even further the mismatching phenomena. Although the size parametric study was limited to smaller nanoparticle sizes due to the lack of further computational time to conclude the investigation, it is expected that the phenomenon will reach a maximum when the inertial effects of the nanoparticle will overcome the diffusive phenomena observed. This mechanism appears to be in agreement with the experimental observations recorded linking nanoparticle size and thermal conductivity of a nanofluid and it might hence explain the heat transfer enhancement exhibited by nanofluids.

In essence, the mechanism proposed links several speculations regarding the various physical heat transfer mechanisms involved that give rise to the heat augmentation phenomena observed. Earlier studies (section 2.1) indicated that most researches explain the augmentation observed in this type of study (conductive mode) via the enhancement of Brownian motion, the interfacial layer theory (Kapitza resistance) or a combination of enhanced Brownian motion and an aggregation and diffusion enhancement mechanism. The proposed new theory appears to merge all three most popular mechanisms into a single one. The increased mobility of the nanoparticle observed gives rise to an enhanced Brownian motion and diffusion while the temperature mismatching gives rise to a Kapitza resistance around the nanoparticle which increases the mobility of the surrounding fluid atoms. Aggregation phenomena cannot be verified as a single nanoparticle study was considered. An addition to the three most popular mechanisms would be the thermophoretic effect in a local scale which might explain the origin of the increased mobility. The suggested findings are also supported by an order of magnitude analysis performed by Buonjiorno J. (2006)[138]. In that study, seven velocity slip mehanisms were considered to investigate their effect on the increased heat transfer phenomena observed in nanofluids. These were: inertia, Brownian diffusion, Thermophoresis, diffusionphoresis, Magnus effect, fluid drainage and gravity settling. Out of the seven mechanisms investigated it was proposed that the Brownian motion and Thermophoresis velocity slip mechanisms are important and can be held accountable for giving rise to the anomalous heat transfer phenomena observed in nanofluids.

8.3 Conclusions

A MDS code was developed to simulate a single nanoparticle nanofluid with a temperature gradient to study, at a molecular level, the conductive heat transfer mechanisms involved. The code accuracy was successfully verified using a variety of common to the field MDS tests. The results suggested the possible presence of a complex heat transfer mechanism that might give rise to increased thermo diffusion phenomena which appear to intensify over the range of nanoparticle sizes analysed. The resulting trends observed are against the classical thermodynamic theories and propose the possible presence of a new type of complex heat transfer mechanism. The new type of heat transfer mechanism suggested supports the experimental results found in the literature.

Chapter 9

Conclusions and Future Research Needs

9.1 Conclusions

Nanofluids are two phase mixtures of a solid (nanoparticles) and a fluid (carrier fluid). The concentrations of Nanoparticles are usually small (of the order of sub-one to 10%vol) and their size usually does not exceed 100nm. The carrier fluids employed are typical coolants found in heat transfer applications. Nanofluids were discovered by Choi around the mid-1990s [4] and started attracting large attention from the scientific community from 2000 and onwards because of the heat transfer enhancement modes they exhibit [7, 81, 102, 126, 147, 149, 222-228]. The analysis performed in section 2.1 indicated that the expected heat transfer enhancement of nanofluids over their conventional coolants to be 5-9%, 10-14%, 40-44% and 100-200% for the conductive, convective/mixed conductive, pool boiling heat transfer (PBHT) and Critical Heat Flux (CHF) heat transfer modes. These enhancements could potentially revolutionise the industry by providing a step change in the performance level of heat transfer applications. The analysis of section 2.1 also indicated the absence of a definite answer in the literature to explain the enhancements observed by the scientific community.

The motivating tasks behind this thesis were to investigate the physical heat transfer mechanisms employed by nanofluids and test their applicability for high heat flux devices. The study was hence divided into two large groups. The experimental and numerical

investigations. The experimental investigations (chapters 4 to 6) revolved around a cold flow Particle Image Velocimetry (PIV) experiment to investigate the coolant flows exhibited by HyperVapotrons operating with water and a dilute nanofluid. HyperVapotrons are High Heat Flux (HHF) devices which are strong candidates to be used as the primary heat exchanging devices of a future nuclear fusion reactor. The numerical studies (chapters 7 and 8) involved the formulation of a MDS code to study from first principles and minimal assumptions the conductive heat transfer mode of a simplified nanofluid.In short, the main conclusions of both set of studies indicated the following:

1. The High spatial resolution optical method (PIV) mapped for the first time the flow structures inside two HV geometries in very high spatial resolution (30μm). The results indicated mean and instantaneous device behaviour. The main outcomes of the results presented aid to understand better the Vapotron effect, the HyperVapotron design parameters as well as to provide a benchmark analysis for future CFD studies as the findings are missing from the literature.
2. Nanofluid and conventional coolant (water) comparison runs in two HyperVapotron geometries using the optical method merits outlined above allowed for the first time to obtain quantitative data regarding the applicability of nanofluids in such devices. It appears that the best candidate to perform a HHF experiment with nanofluids will be the MAST geometry as the JET geometry indicated severe departures from the nominal designed operations with the use of nanofluids.
3. The MDS code demonstrated a large scale study using a more versatile and economically affordable methodology something which will be crucial for research groups in the field with no access to traditional computational clusters (Supercomputers).
4. The results from the MDS code suggest the possible presence of a complex heat transfer mechanism that might give rise to increased thermo diffusion phenomena which appear to intensify over the range of nanoparticle sizes analysed. The new type of heat transfer mechanism proposed justifies the experimental results found in the literature. The proposed new theory appears to merge all three most popular mechanisms into a single one with an additional local thermophoretic component

which might explain the increased mobility and thermo diffusion phenomena observed in nanofluids.

9.2 Epilogue

From the numerical and experimental investigations, it was confirmed that nanofluids do not behave in the way classical fluids do. The cold flow measurements, apart from documenting for the first time in high resolution the flow structures inside HyperVapotrons, indicated that nanofluids appear to exhibit non-Newtonian behaviour. Shear thinning behaviour and effective viscosity changes appear to be present even at the lowest concentrations experimented with. These mechanical property changes of nanofluids have a significant effect on the coolant flow structures and probably will have a significant impact on the overall heat transfer performance of the devices tested. These effects could be taken into account upon designing heat exchangers in order to alter the traditional patterns of coolant and enhance the heat transfer capabilities of the device. Smart heat exchangers can be actively designed to take advantage of the mechanical properties of the fluid in order to maximise their heat transfer performance levels.

On the other hand, the numerical investigations supported the possible existence of an anomalous heat transfer mode which has not been documented so far in classical thermodynamics and has been widely disputed in the literature [119, 229]. This is a passive mode of heat transfer augmentation employed by nanofluids without the need to actively design for (unless the mechanical flow properties of the fluids are going to impart on the overall performance of the device). As such, the passive mode could enable a variety of devices to reach higher performance levels without actively changing their design.

Even though the numerical investigations considered a single nanoparticle nanofluid, never-the-less, it can be extrapolated that they will possibly also hold valid in nanofluids with low agglomerations (unless an agglomeration heat transfer mechanism is revealed/applies in certain mixtures). This is expected as the nanoparticle concentrations used in nanofluids are low and hence the small probability and short duration of interaction between nanoparticles should not affect the overall predicted conductive behaviour of the fluid. The enhancement of the conductive mode is also expected to improve the natural

convection heat transfer mode of in nanofluids. The conductive mode is responsible for the heat transfer between the heater and the fluid in every convective heat transfer application. Given that the nanoparticles have negligible gravitational effects (negligible mass) while the natural convection fluid mobility induced has low shear stresses (hence no effective viscosity change), the augmentation of the conductive mode is anticipated in its turn to boost this mode as well.

9.2.1 Future research needs

Nanofluids are a rather recent invention and as a result, due to the high complexity of the heat transfer mechanisms employed in this seemingly simple mixture, it can be concluded that the study field is rather novel. From the study of the literature as well as the experimental and numerical investigations performed in this thesis, it can be deduced that the research field efforts need to be aligned towards achieving the following main tasks.

Firstly, more convection, pool boiling and critical heat flux heat transfer mode studies are needed as it appears that these modes have not yet been investigated at the degree the purely conductive heat transfer mode has. Starting with the convective heat transfer mode, researchers need to focus on simple experiments to identify the basic changes a nanofluid can impart on the convective flow structures developed in simple geometries. There are a lot of unanswered questions regarding how nanofluids might perform in the convective mode. The first comes from the fact that nanofluids exhibit non-Newtonian effects which might be triggered and come in action by strong shear stresses in flows. These shear stresses are expected to be low in natural convection experiments and hence the non-Newtonian effects are predicted to be negligible. However, if a forced convection is imparted, the local effective viscosity or alteration of wetted surfaces due to nanoparticle coating might have a large impact on the convective flow patterns established in the fluids which in extend will be affecting the overall heat transfer capabilities of nanofluids. There is not a lot of information regarding the behaviour of this mode and hence researchers must focus their efforts in mapping the convective structures induced in the natural and forced mode via PIV investigations while simultaneously using a thermometry method e.g. using temperature sensitive dyes to discover the heat distribution

field evolution. Regarding the PBHT and CHF heat transfer modes, this is a different sub category and similar experiments should be performed in conjunction with TEM measurements to confirm if the main mechanism of particle deposition and alteration of the heating surface as proposed in the literature plays an important role in heat transfer augmentation. The surfaces and nano structures formed during boiling and critical heat flux on the heating elements must be investigated and linked to the changes imparted to the boiling properties of the fluid. These involve the frequency of bubble departure, the size of bubbles and angle of detachment from the heating element as well as assessing the wetting properties of the heated surface near the CHF limit. In case of forced conditions (namely flow over heating element), it will be interesting to see the evolution of the thermal boundary layer induced in conjunction with the viscous boundary layer and their effects on heat transfer.

Secondly, more studies need to be performed which take into account simultaneously all of the by-part mixture properties and assess their impact on the thermal performance obtained. This study will contain a high technical workload of performing simple experiments (for example simple stationary hot wire experiments such as those widely found in the literature as well as simple heated pipe flow experiments) and building large databases with the parameters to be processed. The mixture properties to be investigated are the nanoparticle concentration, size and shape, nanoparticle and basefluid material, temperature of heat transfer and flow type of application. Various studies exist already on the effect of nanoparticle concentration hence there is a need to investigate the rest of the parameters mentioned to find their effect on the heat transfer exhibited. The most interesting of these parameters will be to find the relationship between the nanoparticle material and shape with the heat augmentation measured and also discover the effects of turbulent or multiphase flow heat transfer with nanofluids. For example, high and low heat conductive nanoparticles could be used at a time to see if the conductivity of the particles themselves will cause significant effects on the heat transfer or mechanical properties of the fluid for the former parameter. Other material properties such as shape and surface treatment of nanoparticle will also be of interest. For the flow type application studies, experiments involving heat transfer at a fixed turbulent profile (length scale and intensity) or a multiphase cycle will reveal more on the mechanical and – as an effect –

thermal properties evolving, which will be useful for forced flow heat transfer applications widely used in the industry. These studies will be necessary to understand better the physics behind the mechanisms nanoparticles employ which might have a direct relation to the nanoparticle material, shape and the flow type used.

Thirdly, an assessment of the nanofluid quality before and after its application based on standardized preparation method guidelines is required to normalise the experimental results from different research groups. In this thesis it was confirmed that the preparation method plays an important role to the final nanofluid quality. Taking account of the sensitivity of the parameters on the creation of nanofluids and their possible impact on the overall heat transfer capability, it is mandatory to create a standardise framework of nanofluid preparation methods which will ensure uniformity across the results from different research groups around the world. This will result to a dissemination of the technical labour to prepare the large databases required for assessing the nanofluid properties and their effects on heat transfer. The standardize framework will allow easier and more reliable cross comparison of experimental results between different groups without the danger of mismatching nanofluid qualities that might affect the final outcome of the study.

Fourthly, more erosion experiments to quantify the effects of long term nanofluid runs instead of conventional coolants in traditional heat exchangers are also necessary. The initial idea of inventing nanofluids was that the nanoparticles will be small enough so as to avoid eroding their flowing channels, themselves and reduce or eliminate heavy precipitation effects found in their micron sized counterparts. Unfortunately, even though in theory this is a sound assumption, there has been no study to confirm this due to the difficulty in setting up a relevant laboratory experiment. The difficulty arises from the fact that the experiment needs to be left running for years at a time with frequent and consistent erosion quantification studies. This part is important to be able to persuade the industry to adopt nanofluids as a new cooling technology.

Fifthly, hot flow parametric experiments with nanofluids and water on HyperVapotron devices are required. In this thesis a cold flow PIV study was carried out to quantify the effects of nanoparticles on the flow structures evolution inside these devices and hence extrapolate these effects on the heat transfer profile of the devices during actual

hot flow runs (pre or inter boiling regime). Even though the current study is considered as a preliminary test, it is still necessary to proceed with full scale, hot flow experimentation on HyperVapotrons with nanofluids. The intermediate step of the experiments could be to use a low heat flux PIV method to investigate any possible changes on the flow structures investigated with the cold flow before proceeding with the full magnitude of high heat fluxes (10-20 MW/m^2) encountered in future nuclear fusion reactors. The flow environment inside the device under these high heat fluxes is expected to change as boiling and critical heat flux events, as well as buoyancy effects due to localized coolant density changes come into play. The latter test will prove the applicability of nanofluids in HyperVapotron devices and will allow the collection of valuable data to aid understanding more the forced convective and forced critical heat flux heat transfer modes in high heat flux applications. Moreover, irradiation studies must also be carried out to define the safest and most economically viable (considering disposal processes required of irradiated materials) nanoparticle material that could be used in such nuclear fusion applications.

Finally, there is an imperative need to look more into the physics of heat transfer in nanofluids in order to decipher in full the complex mechanisms employed and their controlling parameters. This will be carried out initially via MDS calculations using multiple nanoparticles and by expanding the parametric study already performed to include calculations of thermophysical nanofluid properties such as thermal conductivity, viscosity and density as well as comparing the time constants for particle relaxation for both the fluid atoms and nanoparticles. The necessary computational cost and resourced employed in such large scale studies will be significant and the HTCondor® proved promising yet at its current form limiting. Alternative platforms (such as GPU stations) or further development of the HTCondor® are worth investing to allow more freedom in the high throughput calculations required. However, this will be the first step to understand the underlying mechanisms involved in the molecular level something which is technologically very hard to impossible to achieve in certain modes. The outlook of the study will be to perform an actual experiment to investigate these mechanisms at a molecular level. This might be possible via the development of further laser diagnostic techniques.

Bibliography

1. Sergis, A. and Hardalupas, Y., *Anomalous heat transfer modes of nanofluids: a review based on statistical analysis.* Nanoscale Research Letters, 2011. **6**(1): p. 391.
2. Sergis, A. and Hardalupas, Y. *Anomalous Heat Transfer Modes of Nanofluids: A Statistical Analysis Approach Review*. in *HSTAM 2010 Conference,* 2010. Limassol.
3. Buongiorno, J., Venerus, D.C., Prabhat, N., McKrell, T., Townsend, J., Christianson, R., Tolmachev, Y.V., Keblinski, P., Hu, L.W. Alvarado, J.L., Bang, I.C., Bishnoi, S.W., Bonetti, M., Botz, F., Cecere, A., Chang, Y., Chen, G., Chen, H., Chung, S.J., Chyu, M.K., Das, S.K., R. Di Paola, Ding, Y., Dubois, F., Dzido, G., Eapen, J., Escher, W., Funfschilling, D., Galand, Q., Gao, j., Gharagozloo, P.E., Goodson, K.E., Gutierrez, J.G., Hong, H., Horton, M., Hwang, K.S., Iorio, C.S., Jang, S.P., Jarzebski, A.B., Jiang, Y., Jin, L., Kabelac, S., Kamath, A., Kedzierski, M.A., Kieng, L.G., Kim, C., Kim, J.H., Kim, S., Lee, S.H., Leong, K.C., Manna, I., Michel, Ni, R., Patel, H.E., Philip, J., Poulikakos, D., Reynaud, C., Savino, R., Singh, P.K., Song, P., Sundararajan, T., Timofeeva, E., Tritcak, T., Turanov, A.N., Vaerenbergh, S.V., Wen,D., Witharana, S., Yang, C., Yeh, W.H., Zhao, X.Z. and Zhou, S.Q., *A benchmark study on the thermal conductivity of nanofluids.* Journal of Applied Physics, 2009. **106**(9): p. 094312-094312.
4. Das S.K., Choi S.U.S., Yu W., Pradeep T., *Nanofluids: Science and Technology*. First ed. 2007, Hoboken, NJ, USA: John Wiley & Sons, Inc.
5. Kakaç, S. and Pramuanjaroenkij A., *Review of convective heat transfer enhancement with nanofluids.* International Journal of Heat and Mass Transfer, 2009. **52**(13-14): p. 3187-3196.

6. Taylor, R.A. and Phelan, P.E., *Pool boiling of nanofluids: Comprehensive review of existing data and limited new data.* International Journal of Heat and Mass Transfer, 2009. **52**(23-24): p. 5339-5347.
7. Wang, X.-Q. and Mujumdar, A.S., *Heat transfer characteristics of nanofluids: a review.* International Journal of Thermal Sciences, 2007. **46**(1): p. 1-19.
8. Yu, W.H., France, D.M., Smith, D.S., Singh, D., Timofeeva, E.V. and Routbort, J.L., *Heat transfer to a silicon carbide/water nanofluid.* International Journal of Heat and Mass Transfer, 2009. **52**(15-16): p. 3606-3612.
9. Trisaksri, V. and Wongwises, S., *Critical review of heat transfer characteristics of nanofluids.* Renewable and Sustainable Energy Reviews, 2007. **11**(3): p. 512-523.
10. Sarit K. Das, Wenhua, Y., Pradeep, T., *Nanofluids: Science and Technology*. First ed. 2007, Hoboken, NJ, USA: John Wiley & Sons, Inc. 397.
11. Bang, I. and Heungchang, S., *Boiling heat transfer performance and phenomena of Al_2O_3–water nano-fluids from a plain surface in a pool.* International Journal of Heat and Mass Transfer, 2005. **48**(12): p. 2407-2419.
12. Yu, W. and Choi, S.U.S., *The Role of Interfacial Layers in the Enhanced Thermal Conductivity of Nanofluids: A Renovated Maxwell Model.* Journal of Nanoparticle Research, 2003. **5**(1/2): p. 167-171.
13. Yu, W. and Choi, S.U.S., *The role of interfacial layers in the enhanced thermal conductivity of nanofluids: A renovated Hamilton-Crosser model.* Journal of Nanoparticle Research, 2004. **6**(4): p. 355-361.
14. Huang, K.D. and Hua, C., *Acta Mechanica.* Acta Mechanica, 2005. **23**: p. 11-23.
15. Quaresma, J., Macedo, E., Henrique, H. Orlande and R. Cotta, *An Analysis of Heat Conduction Models for Nanofluids.* Heat Transfer Engineering, 2010. **31**(14): p. 1125-1136.
16. Hung, Y.M., *Analytical Study on Forced Convection of Nanofluids With Viscous Dissipation in Microchannels.* Heat Transfer Engineering, 2010. **31**(14): p. 1184-1192.
17. Eastman, J.A., Choi, S.U.S., Li, S., Yu, W. and Thompson, L.J., *Anomalously increased effective thermal conductivities of ethylene glycol-based nanofluids containing copper nanoparticles.* Applied Physics Letters, 2001. **78**(6): p. 718-720.
18. Kulkarni, D.P., Vajjha, R.S., Das, D.K. and Oliva, D., *Application of aluminum oxide nanofluids in diesel electric generator as jacket water coolant.* Applied Thermal Engineering, 2008. **28**: p. 1774-1781.

19. Abu-Nada, E., *Application of nanofluids for heat transfer enhancement of separated flows encountered in a backward facing step.* International Journal of Heat and Fluid Flow, 2008. **29**(1): p. 242-249.
20. Bi, S.S., Shi, L. and Zhang, L.L. *Application of nanoparticles in domestic refrigerators.* Applied Thermal Engineering, 2008. **28**: p. 1834-1843.
21. Chen, G., Yu, W., Singh, D., Cookson, D. and Routbort, J *Application of SAXS to the study of particle-size-dependent thermal conductivity in silica nanofluids.* Journal of Nanoparticle Research, 2008. **10**(7): p. 1109-1114.
22. Mudawar, I., *Assessment of the effectiveness of nanofluids for single-phase and two-phase heat transfer in micro-channels.* International Journal of Heat and Mass Transfer, 2007(50): p. 452-463.
23. Bang, I.C. and Heo, G., *An axiomatic design approach in development of nanofluid coolants.* Applied Thermal Engineering, 2009. **29**(1): p. 75-90.
24. Liu, Z., Xiong, J. and Bao, R., *Boiling heat transfer characteristics of nanofluids in a flat heat pipe evaporator with micro-grooved heating surface.* International Journal of Multiphase Flow, 2007. **33**(12): p. 1284-1295.
25. Lotfi, H. and Shafii, M.B., *Boiling heat transfer on a high temperature silver sphere in nanofluid.* International Journal of Thermal Sciences, 2009. **48**(12): p. 2215-2220.
26. Jain, S., Patel, H.E. and Das, S.K., *Brownian dynamic simulation for the prediction of effective thermal conductivity of nanofluid.* Journal of Nanoparticle Research, 2008. **11**(4): p. 767-773.
27. Vasiliev, L., Hleb, L., Shnip, A. and Lapotko, D., *Bubble generation in micro-volumes of "nanofluids".* International Journal of Heat and Mass Transfer, 2009. **52**(5-6): p. 1534-1539.
28. Khanafer, K., Vafai, K. and Lightstone, M., *Buoyancy-driven heat transfer enhancement in a two-dimensional enclosure utilizing nanofluids.* Int. J. Heat Mass Transfer, 2003. **46**: p. 3639-3653.
29. Avsec, J., *The combined analysis of phonon and electron heat transfer mechanism on thermal conductivity for nanofluids.* International Journal of Heat and Mass Transfer, 2008. **51**(19-20): p. 4589-4598.
30. Murshed, S.M.S., Leong, K.C. and Yang, C., *A combined model for the effective thermal conductivity of nanofluids.* Applied Thermal Engineering, 2009. **29**(11-12): p. 2477-2483.

31. Doroodchi, E., Evans, T.M. and Moghtaderi, B., *Comments on the effect of liquid layering on the thermal conductivity of nanofluids.* Journal of Nanoparticle Research, 2008. **11**(6): p. 1501-1507.
32. Trisaksri, V. and Wongwises, S., *Critical review of heat transfer characteristics of nanofluids.* Renewable Sustainable Energy Reviews, 2007. **11**(3): p. 512-523.
33. Vajjha, R.S., Das, D.K. and Kulkarni, D.P., *Development of new correlations for convective heat transfer and friction factor in turbulent regime for nanofluids.* International Journal of Heat and Mass Transfer, 2010. **53**(21-22): p. 4607-4618.
34. Kenneth, E.G., *Diffusion, Aggregation and the thermal conductivity of nanofluids.* Applied Physics Letters, 2008. **93**.
35. Kondaraju, S., Jin, E.K. and Lee, J.S., *Direct numerical simulation of thermal conductivity of nanofluids: The effect of temperature two-way coupling and coagulation of particles.* International Journal of Heat and Mass Transfer, 2010. **53**(5-6): p. 862-869.
36. Pantzali, M.N., Antoniadis, K.D. and Paras, S.V., *Effect of nanofluids on the performance of a miniature plate heat exchanger with modulated surface.* International Journal of Heat and Fluid Flow, 2009. **30**(4): p. 691-699.
37. Mirmasoumi, S. and Behzadmehr, A., *Effect of nanoparticles mean diameter on mixed convection heat transfer of a nanofluid in a horizontal tube.* International Journal of Heat and Fluid Flow, 2008. **29**(2): p. 557-566.
38. Kim, H., Kim, J,. and Kim, M.H., *Effect of nanoparticles on CHF enhancement in pool boiling of nano-fluids.* International Journal of Heat and Mass Transfer, 2006. **49**(25-26): p. 5070-5074.
39. You, S.M., Kim, J.H. and Kim, K.H., *Effect of nanoparticles on critical heat flux of water in pool boiling heat transfer.* Applied Physics Letters, 2003. **83**(16): p. 3374.
40. Anoop, K.B., Sundararajan, T. and Das, S.K., *Effect of particle size on the convective heat transfer in nanofluid in the developing region.* International Journal of Heat and Mass Transfer, 2009. **52**(9-10): p. 2189-2195.
41. Beck, M.P., Yuan, Y., Warrier, P. and Teja A.S., *The effect of particle size on the thermal conductivity of alumina nanofluids.* Journal of Nanoparticle Research, 2009. **11**(5): p. 1129-1136.
42. Bergman, T.L., *Effect of reduced specific heats of nanofluids on single phase , laminar internal forced convection.* International Journal of Heat and Mass Transfer, 2009. **52**(5-6): p. 1240-1244.

43. Lin, Y.H. and Chen, H.L. *Effect of silver nano-fluid on pulsating heat pipe thermal performance.* Applied Thermal Engineering, 2008. **28**: p. 1312-1317.

44. Prakashnarayan, G., Anoop, K., Sateesh, G. and Das, S., *Effect of surface orientation on pool boiling heat transfer of nanoparticle suspensions.* International Journal of Multiphase Flow, 2008. **34**(2): p. 145-160.

45. Abu-Nada, E., *Effects of variable viscosity and thermal conductivity of Al_2O_3-water nanofluid on heat transfer enhancement in natural convection.* International Journal of Heat and Fluid Flow, 2009. **30**(4): p. 679-690.

46. Chon, C.H., Kihm, K.D., Lee, S.P., Choi, S.U.S., *Empirical correlation finding the role of temperature and particle size for nanofluid Al_2O_3 thermal conductivity enhancement.* Applied Physics Letters, 2005. **87**(15): p. 2005-2007.

47. Le Goff, C., Ben-Abdallah, P., Domingues, G. and Moctar, A.O.E., *Enhanced thermal conductivity in nanofluids under the action of oscillating force fields.* Journal of Nanoparticle Research, 2008. **10**(7): p. 1115-1120.

48. Singh, P.K., Anoop, K.B., Sundararajan, T. and Das, S.K., *Entropy generation due to flow and heat transfer in nanofluids.* International Journal of Heat and Mass Transfer, 2010. **53**(21-22): p. 4757-4767.

49. Vajjha, R.S. and Das, D.K., *Experimental determination of thermal conductivity of three nanofluids and development of new correlations.* International Journal of Heat and Mass Transfer, 2009. **52**(21-22): p. 4675-4682.

50. Ding, Y, Wen, D., *Experimental investigation into the pool boiling heat transfer of aqueous based γ-alumina nanofluids.* Journal of Nanoparticle Research, 2005. **7**(2-3): p. 265–274.

51. Zeinali, H.S., Esfahany, M.N. and Etemad, S.G., *Experimental investigation of convective heat transfer of Al_2O_3/water nanofluid in circular tube.* International Journal of Heat and Fluid Flow, 2007. **28**(2): p. 203-210.

52. Nayak, A.K., Gartia, M.R. and Vijayan, P.K., *An experimental investigation of single-phase natural circulation behavior in a rectangular loop with Al_2O_3 nanofluids.* Experimental Thermal and Fluid Science, 2008. **33**(1): p. 184-189.

53. Godson, L., Raja, B., Lal, D.M. and Wongwises, S., *Experimental Investigation on the Thermal Conductivity and Viscosity of Silver-Deionized Water Nanofluid.* Experimental Heat Transfer, 2010. **23**(4): p. 317-332.

54. Chein, R. and Chuang, J., *Experimental microchannel heat sink performance studies using nanofluids.* International Journal of Thermal Sciences, 2007. **46**: p. 57-66.

55. Phuoc, T.X. and Massoudi, M., *Experimental observations of the effects of shear rates and particle concentration on the viscosity of Fe_2O_3-deionized water nanofluids.* International Journal of Thermal Sciences, 2009. **48**(7): p. 1294-1301.

56. Kim, H., Kim, J. and Kim, M., *Experimental studies on CHF characteristics of nano-fluids at pool boiling.* International Journal of Multiphase Flow, 2007. **33**(7): p. 691-706.

57. Nguyen, C., Galanis, N., Polidori, G., Fohanno, S., Popa, C.V., LeBechec, A., *An experimental study of a confined and submerged impinging jet heat transfer using Al_2O_3-water nanofluid.* International Journal of Thermal Sciences, 2009. **48**(2): p. 401-411.

58. Seon, H., Kim, H., Jo, H., Kang, S., Chang, W. and Hwan, M., *Experimental study of critical heat flux enhancement during forced convective flow boiling of nanofluid on a short heated surface.* International Journal of Multiphase Flow, 2010. **36**(5): p. 375-384.

59. Kim, H. and Kim, M., *Experimental study of the characteristics and mechanism of pool boiling CHF enhancement using nanofluids.* Heat and Mass Transfer, 2007. **45**(7): p. 991-998.

60. Sik, K., Pil, S. and Choi, S.U.S., *Flow and convective heat transfer characteristics of water-based Al_2O_3 nanofluids in fully developed laminar flow regime.* International Journal of Heat and Mass Transfer, 2009. **52**(1-2): p. 193-199.

61. Wen, D., Zhang, L. and He, Y., *Flow and migration of nanoparticle in a single channel.* Heat and Mass Transfer, 2009. **45**(8): p. 1061-1067.

62. Liao, L. and Liu, Z.H., *Forced convective flow drag and heat transfer characteristics of carbon nanotube suspensions in a horizontal small tube.* Heat Mass Transfer, 2009. **45**(8): p. 1129-1136.

63. Jung, J.Y., Oh, H.S. and Kwak, H.Y., *Forced convective heat transfer of nanofluids in microchannels.* International Journal of Heat and Mass Transfer, 2009. **52**(1-2): p. 466-472.

64. Wen, D. and Ding, Y., *Formulation of nanofluids for natural convective heat transfer applications.* International Journal of Heat and Fluid Flow, 2005. **26**(6): p. 855-864.

65. Akbari, M., Behzadmehr, A. and Shahraki, F., *Fully developed mixed convection in horizontal and inclined tubes with uniform heat flux using nanofluid.* International Journal of Heat and Fluid Flow, 2008. **29**(2): p. 545-556.
66. Turanov A. and Tolmachev, Y.V., *Heat- and mass-transport in aqueous silica nanofluids.* Heat Mass Transfer, 2009. **45**(12) p. 1583-1588.
67. Tiwari, R. and Das, M., *Heat transfer augmentation in a two-sided lid-driven differentially heated square cavity utilizing nanofluids.* International Journal of Heat and Mass Transfer, 2007. **50**(9-10): p. 2002-2018.
68. Duangthongsuk, W. and Wongwises, S., *Heat transfer enhancement and pressure drop characteristics of TiO_2–water nanofluid in a double-tube counter flow heat exchanger.* International Journal of Heat and Mass Transfer, 2009. **52**(7-8): p. 2059-2067.
69. Noie, S.H., Heris, S.Z., Kahani, M., Nowee, S.M., *Heat transfer enhancement using Al_2O_3/water nanofluid in a two-phase closed thermosyphon.* International Journal of Heat and Fluid Flow, 2009. **30**(4): p. 700-705.
70. Ding, Y., Alias, H., Wen, D. and Williams, R.A., *Heat transfer of aqueous suspensions of carbon nanotubes (CNT nanofluids).* International Journal of Heat and Mass Transfer, 2006. **49**: p. 240-250.
71. Chow, L. *High Thermal Conductivity, CTE Matched Nanocomposite*. in *AIAA Aerospace Sciences Meeting*. 2006. University of Central Florida.
72. Hadjov K. and Dontchev D., *Influence of the particle size distribution on the thermal conductivity of nanofluids.* Journal of Nanoparticle Research, 2009. **11**(7): p. 1713-1718.
73. Akbarinia, A. and Laur, R., *Investigating the diameter of solid particles effects on a laminar nanofluid flow in a curved tube using a two phase approach.* International Journal of Heat and Fluid Flow, 2009. **30**(4): p. 706-714.
74. Pantzali, M.N., Mouza, A.A. and Paras, S.V., *Investigating the efficacy of nanofluids as coolants in plate heat exchangers (PHE).* Chemical Engineering Science, 2009. **64**: p. 3290-3300.
75. Leong, K.C. and Yang, C., *Investigations of thermal conductivity and viscosity of nanofluids.* International Journal of Thermal Sciences, 2008. **47**: p. 560-568.
76. Murshed, S.M.S., Leong, K.C. and Yang, C., *Investigations of thermal conductivity and viscosity of nanofluids.* International Journal of Thermal Sciences, 2008. **47**: p. 560-568.

77. Rea, U., McKrell, T., Hu, L.W. and Buongiorno, J., *Laminar convective heat transfer and viscous pressure loss of alumina – water and zirconia – water nanofluids.* International Journal of Heat and Mass Transfer, 2009. **52**(7-8): p. 2042-2048.

78. Xuan Y. and Yao Z., *Lattice Boltzmann model for nanofluid.* Heat Mass Transfer, 2005. **41**: p. 199-205.

79. Liao, J., Zhang, Y., Yu, W., Xu, L., Ge, C., Liu, J. and Gu, N., *Linear aggregation of gold nanoparticles in ethanol.* Colloids and Surfaces A: Physicochemical and Engineering Aspects, 2003. **223**(1-3): p. 177-183.

80. Duangthongsuk, W. and Wongwises, S., *Measurement of temperature-dependent thermal conductivity and viscosity of TiO_2-water nanofluids.* Experimental Thermal and Fluid Science, 2009. **33**(4): p. 706-714.

81. Wen, D., *Mechanisms of thermal nanofluids on enhanced critical heat flux (CHF).* International Journal of Heat and Mass Transfer, 2008. **51**(19-20): p. 4958-4965.

82. Li C. H., Peterson G. P., *Mixing effect on the enhancement of the effective thermal conductivity of nanoparticle suspensions (nanofluids).* International Journal of Heat and Mass Transfer, 2007. **50**(23-24): p. 4668-4677.

83. Leong, K.C., Yang, C. and Murshed, S.M.S., *A model for the thermal conductivity of nanofluids-the effect of interfacial layer.* Journal of Nanoparticle Research, 2006. **8**: p. 245-254.

84. Hadjov, K.B., *Modified self-consisted scheme to predict the thermal conductivity of nanofluids.* International Journal of Thermal Sciences, 2009. **48**(12): p. 2249-2254.

85. Zhou, L.J., Xuan, Y.M. and Li, Q., *Multiscale simulation of flow and heat transfer of nanofluid with lattice Boltzmann method.* International Journal of Multiphase Flow, 2010. **36**(5): p. 364-374.

86. Feng, Y. and Kleinstreuer, C., *Nanofluid convective heat transfer in a parallel-disk system.* International Journal of Heat and Mass Transfer, 2010. **53**(21-22): p. 4619-4628.

87. Golubovic M.N., Madhawa H.D., Worek W.M. and Minkowycz W.J., *Nanofluids and critical heat flux, experimental and analytical study.* Applied Thermal Engineering, 2009. **29**(7): p. 1281-1288.

88. Xie, H., Lee, H., Youn, W. and Choi, M., *Nanofluids containing multiwalled carbon nanotubes and their enhanced thermal conductivities.* Journal of Applied Physics, 2003. **94**(8).

89. Sefiane, K. and Bennacer, R., *Nanofluids droplets evaporation kinetics and wetting dynamics on rough heated substrates.* Advances in colloid and interface science, 2009. **147-148**: p. 263-71.

90. Büyük Öğüt, E., *Natural convection of water-based nanofluids in an inclined enclosure with a heat source.* International Journal of Thermal Sciences, 2009. **48**(11): p. 2063-2073.

91. Mintsa, H.A., Roy, G., Nguyen, C.T. and Doucet, D., *New temperature dependent thermal conductivity data for water-based nanofluids.* International Journal of Thermal Sciences, 2009. **48**(2): p. 363-371.

92. Koo, J. and Kleinstreuer, C., *A new thermal conductivity model for nanofluids.* Journal of Nanoparticle Research, 2005. **6**(2004): p. 577-588.

93. Polidori, G., Fohanno, S. and Nguyen, C.T., *A note on heat transfer modelling of Newtonian nanofluids in laminar free convection.* Heat and Mass Transfer, 2007. **46**: p. 739-744.

94. Walsh, P.A., Egan, V.M. and Walsh, E.J., *Novel micro-PIV study enables a greater understanding of nanoparticle suspension flows: nanofluids.* Microfluidics and Nanofluidics, 2009. **8**(6): p. 837-842.

95. Trisaksri, V. and Wongwises, S., *Nucleate pool boiling heat transfer of TiO_2-R141b nanofluids.* International Journal of Heat and Mass Transfer, 2009. **52**(5-6): p. 1582-1588.

96. He, Y., Men, Y., Zhao, Y., Lu, H., Ding, Y., *Numerical investigation into the convective heat transfer of TiO_2 nanofluids flowing through a straight tube under the laminar flow conditions.* Applied Thermal Engineering, 2009. **29**(10): p. 1965-1972.

97. Bianco, V., Chiacchio, F., Manca, O. and Nardini, S., *Numerical investigation of nanofluids forced convection in circular tubes.* Applied Thermal Engineering, 2009. **29**(17-18): p. 3632-3642.

98. Jou, R.Y. and Tzeng, S.C., *Numerical research of nature convective heat transfer enhancement filled with nanofluids in rectangular enclosures.* International Communications in Heat and Mass Transfer, 2006. **33**(6): p. 727-736.

99. Mirmasoumi, S. and Behzadmehr, A., *Numerical study of laminar mixed convection of a nanofluid in a horizontal tube using two-phase mixture model.* Applied Thermal Engineering, 2008. **28**(7): p. 717-727.

100. Oztop, H. and Abunada, E., *Numerical study of natural convection in partially heated rectangular enclosures filled with nanofluids.* International Journal of Heat and Fluid Flow, 2008. **29**(5): p. 1326-1336.

101. Namburu, P.K., Das, D.K., Tanguturi, K.M. and Vajjha, R.S., *Numerical study of turbulent flow and heat transfer characteristics of nanofluids considering variable properties.* International Journal of Thermal Sciences, 2009. **48**(2): p. 290-302.

102. Kim, H., DeWitt, G., McKrell, T., Buongiorno, J. and Hu, L.W., *On the quenching of steel and zircaloy spheres in water-based nanofluids with alumina, silica and diamond nanoparticles.* International Journal of Multiphase Flow, 2009. **35**(5): p. 427-438.

103. Soltani, S., Etemad, S.G. and Thibault, J., *Pool boiling heat transfer performance of Newtonian nanofluids.* Heat and Mass Transfer, 2009. **45**(12): p. 1555-1560.

104. Santra, A.K., Chakraborty, N. and Sen, S., *Prediction of heat transfer due to presence of copper–water nanofluid using resilient-propagation neural network.* International Journal of Thermal Sciences, 2009. **48**(7): p. 1311-1318.

105. Behzadmehr, A., Saffar-Avval, M. and Galanis, N., *Prediction of turbulent forced convection of a nanofluid in a tube with uniform heat flux using a two phase approach.* International Journal of Heat and Fluid Flow, 2007. **28**(2): p. 211-219.

106. Kim, D., Hwang, Y., Cheong, S.I., Lee, J.K., Hong, D., Moon, S., Lee, J.E. and Kim, S.H., *Production and characterization of carbon nano colloid via one-step electrochemical method.* Journal of Nanoparticle Research, 2008. **10**(7): p. 1121-1128.

107. Sharma, N.N., *Radiation model for nanoparticle: extension of classical Brownian motion concepts.* Journal of Nanoparticle Research, 2007. **10**(2): p. 333-340.

108. Zhang, Z. *Radiative Properties of Nanomaterials and Radiative Heat Transfer at the Nanoscale*. in *44th AIAA Aerospace Sciences Meeting and Exhibit*. 2006. Georgia Institude of Technology, Atlanda, Georgia.

109. Chen, H., Ding, Y., Lapkin, A. and Fan, X., *Rheological behaviour of ethylene glycol-titanate nanotube nanofluids.* Journal of Nanoparticle Research, 2009. **11**(6): p. 1513-1520.

110. Pil, S. and Choi, S.U.S., *Role of Brownian motion in the enhanced thermal conductivity of nanofluids.* Applied Physics Letters, 2004. **84**(21): p. 4316-4318.

111. Milanova, D. and Kumar, R., *Role of ions in pool boiling heat transfer of pure and silica nanofluids.* Applied Physics Letters, 2005. **87**(23): p. 233107.

112. Coblenz, W.S. *Role of Nanotechnology in Thermal Management*. in *DARPA Disruptive Investment Strategies, AIAA Panel Session*. 2006.

113. Meibodi, M.E., Rashidi, A.M., Amrollahi, A., Tabasi, M. and Kalal, H.S., *Simple model for thermal conductivity of nanofluids using resistance model approach.* International Communications in Heat and Mass Transfer, 2010. **37**(5): p.555-559.

114. Santra, A.K., Sen, S. and Chakraborty, N., *Study of heat transfer due to laminar flow of copper–water nanofluid through two isothermally heated parallel plates.* International Journal of Thermal Sciences, 2009. **48**(2): p. 391-400.

115. Hong, T., Yang H. and Choi C., *Study of the enhanced thermal conductivity of Fe nanofluids.* Physics, 2005. **97**(6) p. 4-7.

116. Das, S.K. and Baby, A.K., *Survey on nucleate pool boiling of nanofluids: the effect of particle size relative to roughness.* Journal of Nanoparticle Research, 2008. **10**(7): p. 1099-1108.

117. Wei, X., Zhu, H., Kong, T., Wang, L., *Synthesis and thermal conductivity of Cu_2O nanofluid.* International Journal of Heat and Mass Transfer, 2009. **52**(19-20): p. 4371-4374.

118. Nguyen, C., Desgranges, F., Roy, G., Galanis, N., Mare, T., Boucher, S. and Anguemintsa, H., *Temperature and particle-size dependent viscosity data for water-based nanofluids – Hysteresis phenomenon.* International Journal of Heat and Fluid Flow, 2007. **28**(6): p. 1492-1506.

119. Keblinski, P., Prasher, R. and Eapen, J., *Thermal conductance of nanofluids: is the controversy over?* Journal of Nanoparticle Research, 2008. **10**(7): p. 1089-1097.

120. Patel, H.E., Das, S.K., Sundararajan, T., Nair, A.S., George, B. and Pradeep, T., *Thermal conductivities of naked and monolayer protected metal nanoparticle based nanofluids: Manifestation of anomalous enhancement and chemical effects.* Applied Physics Letters, 2003. **83**(14): p. 2931-2933.

121. Jung, J.Y. and Yoo, J.Y., *Thermal conductivity enhancement of nanofluids in conjunction with electrical double layer (EDL).* International Journal of Heat and Mass Transfer, 2009. **52**(1-2): p. 525-528.

122. Lee, J.S., *Thermal conductivity measurement and sedimentation detection of aluminum oxide nanofluids by using the 3ω method.* International Journal of Heat and Fluid Flow, 2008. **29**(5): p. 1456-1461.

123. Khandekar, S., Joshi, Y.M. and Mehta, B., *Thermal performance of closed two-phase thermosyphon using nanofluids.* International Journal of Thermal Sciences, 2008. **47**: p. 659-667.

124. Li, J. and Kleinstreuer, C., *Thermal performance of nanofluid flow in microchannels.* International Journal of Heat and Fluid Flow, 2008. **29**: p. 1221-1232.

125. Ponnappan, P.R. *Thermophysics Panel Session 113-TP-8 Introduction : Impact of Nanotechnology in Thermal Management*. in *44th AIAA Aerospace Sciences Meeting and Exhibit*. 2006. Reno, NV.

126. Wang, G.S. and Bao, R., *Two-phase flow patterns of nitrogen and nanofluids in a vertically capillary tube.* International Journal of Thermal Sciences, 2009. **48**(11): p. 2074-2079.

127. Nguyen, C.T., Desgranges F., Galanis, N., Roy, G., Mare, T., Boucher, S., *Viscosity data for Al_2O_3-water nanofluid-hysteresis: is heat transfer enhancement using nanofluids reliable.* International Journal of Thermal Sciences, 2008. **47**(2): p. 103-111.

128. Hong, T.K., Yang, H.S. and Choi, C.J., *Study of the enhanced thermal conductivity of Fe nanofluids.* Journal of Applied Physics, 2005. **97**(6): p. 064311.

129. Meibodi, M.E., Vafaie-Sefti, M., Rashidi, A.M., Amrollahi, A., Tabasi, M. and Kalal, H.S., *Simple model for thermal conductivity of nanofluids using resistance model approach.* International Communications in Heat and Mass Transfer, 2010. **37**(5): p. 555-559.

130. Hwang, K.S., Jang, S.P. and Choi, S.U.S., *Flow and convective heat transfer characteristics of water-based Al_2O_3 nanofluids in fully developed laminar flow regime.* International Journal of Heat and Mass Transfer, 2009. **52**(1-2): p. 193-199.

131. Fu, C.J. and Zhang, Z.M., *Nanoscale radiation heat transfer for silicon at different doping levels.* International Journal of Heat and Mass Transfer, 2006. **49**(9-10): p. 1703-1718.

132. Ding, Y., Alias, H., Wen, D. and Williams, R.A., *Heat transfer of aqueous suspensions of carbon nanotubes (CNT nanofluids).* International Journal of Heat and Mass Transfer, 2006. **49**(1-2): p. 240-250.

133. Li, J. and Kleinstreuer, C., *Thermal performance of nanofluid flow in microchannels.* International Journal of Heat and Fluid Flow, 2008. **29**(4): p. 1221-1232.

134. Yang, B. and Han, Z.H., *Thermal conductivity enhancement in water-in-FC72 nanoemulsion fluids.* Applied Physics Letters, 2006. **88**(26): p. 261914.

135. Sul, H.Y., Jung, J.Y. and Kang, Y.T., *Thermal conductivity enhancement of binary nanoemulsion (O/S) for absorption application.* International Journal of Heat and Mass Transfer, 2011. **54**(7-8): p. 1649-1653.

136. Chiesa, M., Garg, J., Kang, Y.T. and Chen, G., *Thermal conductivity and viscosity of water-in-oil nanoemulsions.* Colloids and Surfaces A: Physicochemical and Engineering Aspects, 2008. **326**(1-2): p. 67-72.

137. Babaei, H., Keblinski, P. and Khodadadi, J.M., *A proof for insignificant effect of Brownian motion-induced micro-convection on thermal conductivity of nanofluids by utilizing molecular dynamics simulations.* Journal of Applied Physics, 2013. **113**(8): p. 084302-084302.

138. Buongiorno, J., *Convective Transport in Nanofluids.* Journal of Heat Transfer, 2006. **128**(3): p. 240-240.

139. Eapen, J., Li, J. and Yip, S., *Beyond the Maxwell limit: Thermal conduction in nanofluids with percolating fluid structures.* Physical Review E, 2007. **76**(6): p. 062501-062501.

140. Keblinski, P., Phillpot, S.R., Choi, S.U.S. and Eastman, J.A., *Mechanisms of heat flow in suspensions of nano-sized particles (nanofluids).* 2002. **45**: p. 855-863.

141. Keblinski, P. and Thomin, J., *Hydrodynamic field around a Brownian particle.* Physical Review E, 2006. **73**(1): p. 010502-010502.

142. Pustovalov, V.K., *Theoretical study of heating of spherical nanoparticle in media by short laser pulses.* Chemical Physics, 2005. **308**(1-2): p. 103-108.

143. Venerus, D.C., Buongiorno, J., Christianson, R., Bang, I.C., Chen, G., Chung, S.J., Chyu, M., Chen,H., Ding, Y., Dubois, F., Dzido, G., Funf, D., Galand, Q., Gao, J., Hong, H., Horton, M., Iorio, C.S., Jarzebski, A.B., Jiang, Y., Kabelac, S., Kedzierski, M.A., Kim, C., Kim, J.H., Kim, S., Ni, R., Philip, J., Prabhat, N., Song, P. and Van, S., *Viscosity Measurements on Colloidal Dispersions (Nanofluids) for Heat Transfer Applications.* 2010. **20**(4): p. 2-8.

144. Xuan, Y. and Li, Q., *Heat transfer enhancement of nanofluids.* International Journal of Heat and Fluid Flow, 2000. **21**(1): p. 58-64.

145. Xuan, Y. and Li, Q., *Investigation on Convective Heat Transfer and Flow Features of Nanofluids.* Journal of Heat Transfer, 2003. **125**(1): p. 151-151.

146. Liao, L. and Liu, Z.H., *Forced convective flow drag and heat transfer characteristics of carbon nanotube suspensions in a horizontal small tube.* Heat and Mass Transfer, 2009. **45**(8): p. 1129-1136.

147. Xie, H., Lee, H., Youn, W. and Choi, M., *Nanofluids containing multiwalled carbon nanotubes and their enhanced thermal conductivities.* Journal of Applied Physics, 2003. **94**(8): p. 4967.

148. Chon, C.H., Kihm, K.D., Lee, S.P., Choi, S.U.S., *Empirical correlation finding the role of temperature and particle size for nanofluid (Al_2O_3) thermal conductivity enhancement.* Applied Physics Letters, 2005. **87**(15): p. 153107.

149. Wei, X., Zhu, H., Kong, T., Wang, L., *Synthesis and thermal conductivity of Cu_2O nanofluids.* International Journal of Heat and Mass Transfer, 2009. **52**(19-20): p. 4371-4374.

150. Koo, J. and Kleinstreuer, C., *A new thermal conductivity model for nanofluids.* Journal of Nanoparticle Research, 2005. **6**(6): p. 577-588.

151. Eastman, J.A., Choi, S.U.S., Li, S., Yu, W., Thompson, L.J., *Anomalously increased effective thermal conductivities of ethylene glycol-based nanofluids containing copper nanoparticles,* Applied Physics Letters, 2001. **78**(6): p. 718-720.

152. Leong, K.C., Yang, C. and Murshed, S.M.S., *A model for the thermal conductivity of nanofluids-the effect of interfacial layer.* J. Nanoparticle Res., 2006. **8**: p. 245-254.

153. Doroodchi E., Evans T., Moghtaderi B., *Comments on the effect of liquid layering on the thermal conductivity of nanofluids.* Journal of Nanoparticle Research, 2008. **11**(6): p.1401-1507

154. Avsec, J., *The combined analysis of phonon and electron heat transfer mechanism on thermal conductivity for nanofluids.* International Journal of Heat and Mass Transfer, 2008. **51**: p. 4589-4598.

155. Yu, W. and Choi, S.U.S., *The role of interfacial layers in the enhanced thermal conductivity of nanofluids: a renovated Hamilton-Crosser model.* Journal of Nanoparticle Research, 2004. **6**(4): p. 355-361.

156. Yang, C., *A combined model for the effective thermal conductivity of nanofluid.* Applied Thermal Engineering, 2009(29): p. 2477-2483.

157. Bhattacharya P., *Brownian dynamics simulation to determine the effective thermal conductivity of nanofluid.* Journal of Applied Physics, 2004. **95**(11):6992.

158. Huang, K.D. and Hua, C., *Heat transfer enhancement of nanofluids in rotary blade coupling of four-wheel-drive vehicles.* Acta Mechanica, 2005. **23**: p. 11-23.

159. Behzadmehr, A., Saffar-Avval, M. and Galanis, N., *Prediction of turbulent forced convection of a nanofluid in a tube with uniform heat flux using a two-phase approach.* International Journal of Heat and Fluid Flow, 2007. **28**(2): p. 211-219.

160. Zeinali, H.S., Nasr, E.M., Etemad, S.G., *Experimental investigation of convective heat transfer of Al_2O_3 /water nanofluid in circular tube.* International Journal of Heat and Fluid Flow, 2007. **28**(2): p. 203-210.

161. Mirmasoumi, S. and Behzadmehr, A., *Numerical study of laminar mixed convection of a nanofluid in a horizontal tube using two-phase mixture model, Journal of* Applied Thermal Engineering, 2008.

162. Abu-Nada, E., *Application of nanofluids for heat transfer enhancement of separated flows encountered in a backward facing step.* International Journal of Heat Fluid Flow, 2008. **29**: p. 242-249.

163. Jou, R.Y. and Tzeng, S.C., *Numerical research of nature convective heat transfer enhancement filled with nanofluids in rectangular enclosures,* International Communincation of Heat and Mass Transfer, 2006. **33**: p. 727-736.

164. Kim, H., Kim, J. and Kim, M.H., *Effect of nanoparticles on CHF enhancement in pool boiling of nano-fluids.* International Journal of Heat and Mass Transfer, 2006. **42**: p. 2003-2013.

165. You, S.M., Kim, J.H. and Kim, K.H., *Effect of nanoparticles on critical heat flux of water in pool boiling heat transfer.* Applied Physics Letters, 2003. **83**: p. 3374-3376.

166. Barrett, T.R., Robinson, S., Flinders, K., Sergis, A. and Hardalupas, Y., *Investigating the use of Nanofluids to Improve High Heat Flux Cooling Systems*. in *27th Symposium on Fusion Technology*. 2012. Liege: SOFT.

167. Barrett, T.R., Robinson, S., Flinders, K., Sergis, A. and Hardalupas, Y., *Investigating the use of nanofluids to improve high heat flux cooling systems.* Fusion Engineering and Design, 2013. **88**(9-10): p. 2594-2597.

168. Sergis, A., Hardalupas, Y. and Barrett, T.R., *Potential for improvement in high heat flux HyperVapotron element performance using nanofluids.* Nuclear Fusion, 2013. **53**(11).

169. Sergis, A., Hardalupas, Y. and Barrett, T.R., *Potential for Improvement in High Heat Flux HyperVapotron Element Performance Using Nanofluids*. in *24th IAEA Fusion Energy Conference*. 2012. San Diego: IAEA.

170. Escourbiac, F., *Experimental optimisation of a hypervapotron® concept for ITER plasma facing components.* Fusion Engineering and Design, 2003. **66-68**: p. 301-304.

171. Falter, H.D. and Thompson, E., *Performance of hypervapotron beam-stopping elements at JET.* Fusion Technology, 1996. **29**(4): p. 584-598.

172. Pascal-Ribot, S., Saroji, A.F., Grandotto, M., Spitz, P. and Escourbiac, F., *3D numerical simulations of hypervapotron cooling concept.* Fusion Engineering and Design, 2007. **82**(15-24): p. 1781-1785.

173. Cattadori, G., Gaspari, G., Celata, G., Cumo, M., Mariani, A. and Zummo, G., *Hypervapotron technique in subcooled flow boiling CHF.* Experimental Thermal and Fluid Science, 1993. **7**(3): p. 230-240.

174. Boscary, J., *Dimensional analysis of critical heat flux in subcooled water flow under one-side heating conditions for fusion application.* Fusion Engineering and Design, 1998. **43**(2): p. 147-171.

175. D. Youchison, *Research and Development Task - Engineering Design Activity Final Report - Manufacturing and Testing of Permanent Components - USA home Team*. 1998: USA Home Team - ITER Report.

176. Raffray, A., *Critical heat flux analysis and R&D for the design of the ITER divertor.* Fusion Engineering and Design, 1999. **45**(4): p. 377-407.

177. Di Pietro, E., *The high heat flux components for ITER neutral beam system.* Fusion Engineering and Design, 2000. **49-50**(1-4): p. 177-182.

178. Baxi, C., *Thermal hydraulics of water cooled divertors.* Fusion Engineering and Design, 2001. **56-57**: p. 195-198.

179. Ezato, K., *Critical heat flux test on saw-toothed fin duct under one-sided heating conditions.* Fusion Engineering and Design, 2001. **56-57**: p. 291-295.

180. Komarov, V., Labusov, I. and Makhankov, A., *Hypervapotron Analysis*. 2001: St. Petersburg, Russia. p. 1-62.

181. Nightingale, M., *The MAST neutral beam injection system.* Fusion Engineering and Design, 2001. **56-57**: p. 529-532.

182. Tivey, R., *ITER R&D: Vacuum Vessel and In-Vessel Components: Divertor Cassette.* Fusion Engineering and Design, 2001. **55**(2-3): p. 219-229.

183. Emetteur, V. and Grosman, A., *Critical Heat Flux Testing of Hypervapotron*. 2002. CEA report, p. 1-15.

184. Chang, S.H. and Baek, W.P., *Understanding, Predicting and Enhancing Critical Heat Flux.* The 10th International Topical Meeting on Nuclear Reactor Thermal Hydraulics (NURETH-10), 2003: p. 1-20.

185. Escourbiac, F., Bobin-Vastra, I., Kuznetsov, V., Missirlian, M., Schedler, B. and Schlosser, J., *A mature industrial solution for ITER divertor plasma facing components: Hypervapotron cooling concept adapted to Tore Supra flat tile technology.* Fusion Engineering and Design, 2005. **75-79**: p. 387-390.

186. Ezato, K., Suzuki, S., Dairaku, M. and Akiba, M., *Experimental examination of heat removal limitation of screw cooling tube at high pressure and temperature conditions.* Fusion Engineering and Design, 2006. **81**(1-7): p. 347-354.

187. Chen, P., *An experimental investigation of critical heat flux performance of Hypervapotron in subcooled boiling*. 2007. PhD Thesis, University of Illinois at Urbana-Champaign

188. Milnes, J., Chuilon, B., Xue, Y., Martin, D. and Waldon, C., *High heat flux (HHF) elements for negative ion systems on ITER.* Fusion Engineering and Design, 2007. **82**(5-14): p. 945-952.

189. Chen, P., Newell, T.A. and Jones, B.G., *Heat transfer characteristics in subcooled flow boiling with hypervapotron.* Annals of Nuclear Energy, 2008. **35**(6): p. 1159-1166.

190. Bullock, J.H., Youchison, D.L. and Ulrickson, M.A., *A comparison of two-phase computational fluid dynamics codes applied to the ITER first wall hypervapotron.* IEEE Transactions on Plasma Science, 2009. **38**(7): p. 1704-1708.

191. Schlosser, J., Escourbiac, F., Merola, M., Schedler, B., Bayetti, P., Missirlian, B., Mitteau, R. and Bobin-Vastra, I., *Flat Tile Armour Cooled by Hypervapotron Tube: a Possible Technology for ITER.* Physica Scripta, 2010. **81**(1): p. 011001.

192. Milnes, J., *Computational modelling of the HyperVapotron cooling technique for nuclear fusion applications*. 2010, PhD Thesis, Cranfield University.

193. Youchison, D.L., *Prediction of critical heat flux in water-cooled plasma facing components using Computational Fluid Dynamics.* Fusion Science and Technology, 2011. **60**(July): p. 177-184.

194. Youchison, D.L., *Effects of Hypervapotron Geometry on Thermalhydraulic Performance.* IEEE Transactions on Plasma Science, 2012. **40**(3): p. 653-658.

195. Milnes, J., Ciric, D., Forner, M., Gee, S., Martin, D., Nightingale, M. and Sauer. M., *Hypervapotron design for the long pulse upgrades on MAST NBI*. in *20th IEEE/NPSS Symposium on Fusion Engineering*. 2003. San Diego, California.

196. Rapaport, D.C., *The Art of Molecular Dynamics Simulation*. 1995, Cambridge: Cambridge University Press.

197. Lee, J.H., Hwang, K.S., Jang, S.P., Lee, B.H., Kim, J.H., Choi, S.U.S. and Choi, C.J., *Effective viscosities and thermal conductivities of aqueous nanofluids containing low volume concentrations of Al_2O_3 nanoparticles.* International Journal of Heat and Mass Transfer, 2008. **51**(11-12): p. 2651-2656.

198. White, F.M., *Fluid mechanics*. 1st Edition, 1986. McGraw-Hill Ryerson, Limited.

199. Mehta, R.D. and Bradshaw, P., *Design Rules for Small Low-Speed Wind Tunnels.* Aeronautical Journal, 1979. **83**(827): p. 443-449.

200. Morel, T. *Comprehensive design of axisymmetric wind tunnel contractions*. Journal of Fluids Engineering. 1975. **97**(2): p. 225-233.

201. Tulapurkara, E.G. and Bhalla, V.V.K., *Experimental Investigation of Morel's Method for Wind Tunnel Contractions.* Journal of Fluids Engineering, 1988. **110**: p. 45-47.

202. Thole, K.A., Bogard, D.G. and Whan-Tong, J.L., *Generating high freestream turbulence levels.* Experiments in Fluids, 1994. **17**: p. 375-380.

203. Jeans, A.H. and Johnston, J.P., *The effects of streamwise concave curvature on turbulent boundary layer structure*. 1982, Massachusetts Institude of Technology (MIT): Cambridge, USA.

204. Bradshaw, P., *The effect of wind-tunnel screens on nominally two-dimensional boundary layers.* Journal of Fluid Mechanics, 1965. **22**(4): p. 679.

205. Bell, J.H. and Mehta, R.D., *Contraction Design for Small Low-Speed Wind Tunnels*, in *NASA Technical Report*. 1988, Stanford University: Stanford, California, USA.

206. Raffel, M., Willert, C.E., Wereley, S.T. and Kompenhans, J., *Particle Image Velocimetry: A Practical Guide*. 2nd Edition, 2007, Springer.

207. Pope, S.B., *Turbulent Flows*. 2000: Cambridge University Press.

208. Youchison, D.L. and Ulrickson, M., *Research and Development Task - Engineering Design Activity Final Report - Manufacturing and Testing of Permanent Components - USA home Team*. 1998: USA Home Team - ITER Report.

209. Domalapally, P. and Rizzo, E., *CFD analysis of flow boiling in the ITER first wall.* Fusion Engineering and Design 2012. **87**(5-6): p. 556-560.

210. Heyes, D.M., Nuevo, M.J. and Morales, J.J., *Self-diffusion of large solid clusters in a liquid by molecular dynamics simulation.* Molecular Physics, 1996. **88**(6): p. 37-41.

211. Hardalupas, Y. and Horender, S., *Fluctuations of particle concentration in a turbulent two-phase shear layer.* International Journal of Multiphase Flow, 2003. **29**(11): p. 1645-1667.

212. Eaton, J.K. and Fessler, J.R., *Preferenctial Conventration of particles by turbulence.* International Journal of Multiphase Flow, 1994. **20**(94): p. 169-209.

213. Bamdad, M., Alavi, S., Najafi, B. and Keshavarzi, E., *A new expression for radial distribution function and infinite shear modulus of Lennard-Jones fluids.* Chemical Physics, 2006. **325**(2-3): p. 554-562.

214. Korsunskii, V.I., Neder, R., Hradil, K., Neuefeind, J., Barglik-Chory, K. and Miller, G., *Investigation of the local structure of nanosized CdS crystals stabilized with glutathione by the radial distribution function method.* Journal of Structural Chemistry, 2004. **45**(3): p. 427-436.

215. Wilson, D.S. and Lee, L.L., *Molecular recognition and adsorption equilibria in starburst dendrimers: gas structure and sensing via molecular theory.* Fluid Phase Equilibria, 2005. **228-229**: p. 197-205.

216. Kowsari, M.H., Alavi, S., Ashrafizaadeh, M. and Najafi, B., *Molecular dynamics simulation of imidazolium-based ionic liquids. I. Dynamics and diffusion coefficient.* The Journal of chemical physics, 2008. **129**(22): p. 224508-224508.

217. Rudyak, V.Y. and Belkin, A.A., *Self-diffusion and viscosity coefficient of fluids in nanochannels.* 3rd Micro and Nano Flows Conference, 2011(August): p. 22-24.

218. Savithiri, S., Pattamatta, A. and Das, S.K., *Scaling analysis for the investigation of slip mechanisms in nanofluids.* Nanoscale Research Letters, 2011. **6**(11): p. 471.

219. Han, M., *Thermophoresis in liquids: a molecular dynamics simulation study.* J Colloid Interface Sci, 2005. **284**(1): p. 339-48.

220. Sung, C.J. and Law, C.K., *Thermophoretic Effects on Seeding Particles in LDV Measurements of Flames.* Combustion Science and Technology, 1994. **99**: p. 119-132.

221. Einstein, A., *On the movement of small particles suspended in stationary liquids required by the molecular-kinetic theory of heat.* Annalen der Physik, 1905. **17**: p. 549-560

222. Rea, U., McKrell, T., Hu, L.W. and Buongiorno, J., *Laminar convective heat transfer and viscous pressure loss of alumina–water and zirconia–water nanofluids.* International Journal of Heat and Mass Transfer, 2009. **52**(7-8): p. 2042-2048.

223. Zhu, H., Han, D., Meng, Z., Wu, D., Zhang, C., *Preparation and thermal conductivity of CuO nanofluid via a wet chemical method.* Nanoscale Research Letters, 2011. **6**(1): p. 181.

224. Xuan, Y. and Z. Yao, *Lattice Boltzmann model for nanofluids.* Heat and Mass Transfer, 2004. **(41)**: p. 199-205

225. Wen, D., Lin, G., Vafaei, S. and Zhang, K., *Review of nanofluids for heat transfer applications.* Particuology, 2009. **7**(2): p. 141-150.

226. Wen, D. and Ding, Y., *Experimental investigation into the pool boiling heat transfer of aqueous based γ-alumina nanofluids.* Journal of Nanoparticle Research, 2005. **7**(2-3): p. 265-274.

227. Warrier, P. and Teja, A., *Effect of particle size on the thermal conductivity of nanofluids containing metallic nanoparticles.* Nanoscale Research Letters, 2011. **6**(1): p. 247.

228. Wang, X.B., Liu, Z.M., Hu, P.A., Liu, Y.Q., Han, B.X. and Zhu, D.B., *Nanofluids in carbon nanotubes using supercritical CO_2: a first step towards a nanochemical reaction.* Applied Physics, 2003. **80**(3): p. 637-639.

229. Michaelides, E.E., *Transport properties of nanofluids. A critical review.* Journal of Non-Equilibrium Thermodynamics, 2013. **38**(1): p. 1-79.

Appendix A

Methodology of Nanofluid Preparation

Two methods of nanofluid preparation were used in this study. The first method (Method 1) was used for the Nanofluids quality assessment (section 3.1) and the Nanofluid laser absorbance assessment (section 3.2) while the second method (Method 2) was used for Particle Image Velocimetry (PIV) (section 3.4.1). The same nanoparticles in water are used for both methods (Al_2O_3 at 50nm) however. Method 2 offered a lower purity nanofluid due to the presence of impurities inside the large scale PIV experimentation rig. This is in par with the assessment of the preparation methods stated in the literature review (chapter 2). However, the sonication times which link to the nanoparticle cluster break up are expected to be the same for both nanofluid preparation methods. As a result, the optimum derived sonication timings found in section 3.1 under Method 1 are also used for Method 2.

The reason for employing two different nanofluid manufacturing methods come down to practicality and costs associated with the large volumes of nanofluid required for the large scale PIV experimentation (220 litres of nanofluid were required for the experiment). The preparation methods are described in more detail below:

Method 1

A multi-step method was employed at which a dense Al_2O_3-water nanofluid (Sigma Aldrich, 50nm Aluminium Oxide Dispersion, Product Number: 642991) was diluted to 1%

concentration using deionized water and placed in separate test tubes. The samples are subsequently positioned into an ultrasonic bath (38kHz, Kerry Ultrasonic bath, model number: V10951) and left for a variable amount of time in order to break up any agglomerates and ensure even nanoparticle distribution into the carrier fluid.

Method 2

A multistep method is also followed to produce the nanofluids for Method 2. Al_2O_3 dry particles of 50nm in diameter (Sigma Aldrich, 50nm Aluminium Oxide Particles, Product Number: 544833) were mixed with water inside sealed containers and then immersed in an ultrasonic bath for at least 5 hours to ensure good and even dispersion of the particles in the water (see section 3.1). The solutions in the containers ranged from 0.1032% up to 0.4000% in nanoparticle volumetric concentrations. The dense solutions were then transferred to the PIV experimental rig and diluted further to a concentration of 0.0001%vol.